The AzTEC Millimeter-wave Camera: Design, Integration, Performance, and the Characterization of the (sub-)millimeter Galaxy Population

THE AZTEC MILLIMETER-WAVE CAMERA: DESIGN, INTEGRATION, PERFORMANCE, AND THE CHARACTERIZATION OF THE (SUB-)MILLIMETER GALAXY POPULATION

A Dissertation Presented

by

JASON EDWARD AUSTERMANN

Submitted to the Graduate School of the
University of Massachusetts Amherst in partial fulfillment
of the requirements for the degree of

DOCTOR OF PHILOSOPHY

May 2009

Astronomy

THE AZTEC MILLIMETER-WAVE CAMERA: DESIGN, INTEGRATION, PERFORMANCE, AND THE CHARACTERIZATION OF THE (SUB-)MILLIMETER GALAXY POPULATION

A Dissertation Presented

by

JASON EDWARD AUSTERMANN

Approved as to style and content by:

Grant W. Wilson, Chair

Guy Blaylock, Member

Mark Heyer, Member

Houjun Mo, Member

Ron Snell, Department Chair
Astronomy

To all the moments and people that made my grad school experience unforgetable and unregretable.

ACKNOWLEDGMENTS

I sincerely thank Grant Wilson for his guidance, patience, insight, and unwavering support. I thank him for the boundless freedom and healthy environment he provided me, both of which helped nurture my independent spirit and confidence. I thank him for his leadership, both in words and by example. Finally, I thank him for what he was under no obligation to give: his friendship.

I am also indebted to the other core AzTEC instrument team members: Kimberly Scott and Thushara Perera. I am very thankful to the UMass astronomy department for the opportunities and education. I am especially thankful to the department staff who made absolutely vital contributions to the AzTEC project, including: John Karakla, Kamal Souccar, Gary Wallace, Don Lydon, and Tom Scott.

I thank the following collaborators for their varied contributions to my work, education and development: David Hughes, Min Yun, Itziar Aretxaga, Sunil Golwala, and James Lowenthal. I thank the following observers and telescope staff who helped make AzTEC such a success and often helped keep me sane on various mountain tops: Tai Oshima, Masao Uehara, Hajime Ezawa, Douglas Haig, Simon Doyle, Kunihiko Tanaka, Ian Coulson, Russel Kackley, Per Friberg, Remo Tilanus, and many others.

Last, but not least, I thank my friends and peers who, in addition to many of the contributions above, gave me so much, both professionally and personally: Cara Battersby, Kimberly Scott, Will Fischer, Thushara Perera, Bastien Aracil, Stefan Kraus, Joshua Snyder, Dan Logan, and Craig West.

Support for this work was provided in part by the NSF grant AST 05-40852 and a grant from the Korea Science & Engineering Foundation (KOSEF) under a

cooperative Astrophysical Research Center of the Structure and Evolution of the COSMOS (ARCSEC).

Finally, I thank David Hughes and Itziar Aretxaga for having a small tank for a car, without which this work may never have been concluded.

ABSTRACT

THE AZTEC MILLIMETER-WAVE CAMERA: DESIGN, INTEGRATION, PERFORMANCE, AND THE CHARACTERIZATION OF THE (SUB-)MILLIMETER GALAXY POPULATION

MAY 2009

JASON EDWARD AUSTERMANN

B.S. Physics, UNIVERSITY OF MISSOURI, ST. LOUIS

M.S. Astronomy, UNIVERSITY OF MASSACHUSETTS, AMHERST

Ph.D., UNIVERSITY OF MASSACHUSETTS AMHERST

Directed by: Professor Grant W. Wilson

One of the primary drivers in the development of large format millimeter detector arrays is the study of sub-millimeter galaxies (SMGs) – a population of very luminous high-redshift dust-obscured starbursts that are widely believed to be the dominant contributor to the Far-Infrared Background (FIB). The characterization of such a population requires the ability to map large patches of the (sub-)millimeter sky to high sensitivity within a feasible amount of time. I present this dissertation on the design, integration, and characterization of the 144-pixel AzTEC millimeter-wave camera and its application to the study of the sub-millimeter galaxy population. In particular, I present an unprecedented characterization of the "blank-field" (fields with no known mass bias) SMG number counts by mapping over $0.5\,\mathrm{deg}^2$ to $1.1\,\mathrm{mm}$ depths of $\sim$1 mJy – a previously unattained depth on these scales. This survey provides

the tightest SMG number counts available, particularly for the brightest and rarest SMGs that require large survey areas for a significant number of detections. These counts are compared to the predictions of various models of the evolving mm/sub-mm source population, providing important constraints for the ongoing refinement of semi-analytic and hydrodynamical models of galaxy formation. I also present the results of an AzTEC $0.15\,\mathrm{deg}^2$ survey of the COSMOS field, which uncovers a significant over-density of bright SMGs that are spatially correlated to foreground mass structures, presumably as a result of gravitational lensing. Finally, I compare the results of the available SMG surveys completed to date and explore the effects of cosmic variance on the interpretation of individual surveys.

TABLE OF CONTENTS

LIST OF TABLES

LIST OF FIGURES

Figure **Page**

CHAPTER 1

INTRODUCTION

The advance of ground-based multi-pixel bolometer cameras have facilitated significant advances in many areas of (sub-)millimeter astronomy, with one of the most striking being the discovery of a population of high-redshift, FIR ultra-luminous starburst galaxies (Smail et al., 1997; Hughes et al., 1998; Barger et al., 1998), now commonly referred to as Sub-Millimeter Galaxies (SMGs). These objects were initially discovered using the highly successful Submillimeter Common-User Bolometer Array (SCUBA; Holland et al., 1998, 1999) on the James Clerk Maxwell Telescope (JCMT). SCUBA was a dual-frequency camera that operated simultaneously with 37 and 91 pixels at 450 and 850 microns, respectively. In the years following their discovery, SCUBA undertook many blank-field (fields with no known foreground contamination or mass bias) surveys to characterize the SMG population (e.g. Scott et al., 2006, and references therein). Recently, other large-format (sub-)millimeter continuum cameras have come online and performed SMG surveys (e.g. Laurent et al., 2005; Greve et al., 2004), including the ∼144 pixel BOLOCAM (Glenn et al., 2003; Haig et al., 2004) operating at 1.1mm on the Caltech Submillimeter Observatory (CSO) and the 37/117 pixel MAMBO/MAMBO-2 cameras (Kreysa et al., 1998) operating at 1.2 mm at the IRAM 30-m telescope.

Why are SMGs important? These presumably massive galaxies are found primarily at high redshift (median redshift of $z \sim 2.2$ for the radio-bright SMG population; Chapman et al., 2005) and provide a unique tracer to structure formation and evolution. The distribution of SMGs in redshift and when they formed can provide

important constraints and challenges to current structure formation and galaxy evolution models. The intense levels of FIR radiation from these objects infer that they are undergoing extreme levels of dust enshrouded star formation ($\sim 1000 M_{\odot}\mathrm{yr}^{-1}$; Blain et al., 2002), thus potentially providing a significant component to the star formation history of the universe at high redshift. The expected emissivity of the dust causes these galaxies to have a strong negative K-correction at millimeter wavelengths that roughly compensates for cosmological dimming (see Figure 1.1; thus, any SMG of a given luminosity is roughly equally detectable between redshifts of 1 to 10 at wavelengths of $\sim 1\,\mathrm{mm}$ and resulting in blind surveys that are effectively volume unlimited. These hyper-luminous star forming galaxies are not seen in the local universe, which begs important evolutionary questions. What modern day objects are the products/remnants of SMGs? Is their star formation episodic or relatively continuous? How are these massive galaxies associated with modern day clusters and cluster formation?

Existing blank-field (sub-)millimeter SMG surveys have discovered a few hundred sources at moderate significance ($S/N \geq 3.5$) and have done well to constrain the intermediate flux population ($2 < S_{850\mu\mathrm{m}} < 10$ mJy). Other surveys (e.g. Blain et al., 1999; Smail et al., 2002; Cowie et al., 2002; Knudsen et al., 2006; Wilson et al., 2008b) have targeted gravitationally lensed fields to probe the faint end of the SMG population ($S_{850} < 2$ mJy). However, most published surveys cover a relatively small patch of sky (typically less than 150 arcmin^2), rendering them insensitive to the bright and rare end of the SMG population. Some larger surveys exist (Borys et al., 2003; Greve et al., 2004; Laurent et al., 2005; Coppin et al., 2006), with the largest and deepest (most sensitive) contiguous maps being the SHADES Lockman Hole and Subaru/XMM-Newton Deep Field (SXDF) surveys, with each covering ~ 360 arcmin^2 (Coppin et al., 2006). However, even the combined area of the SCUBA/SHADES

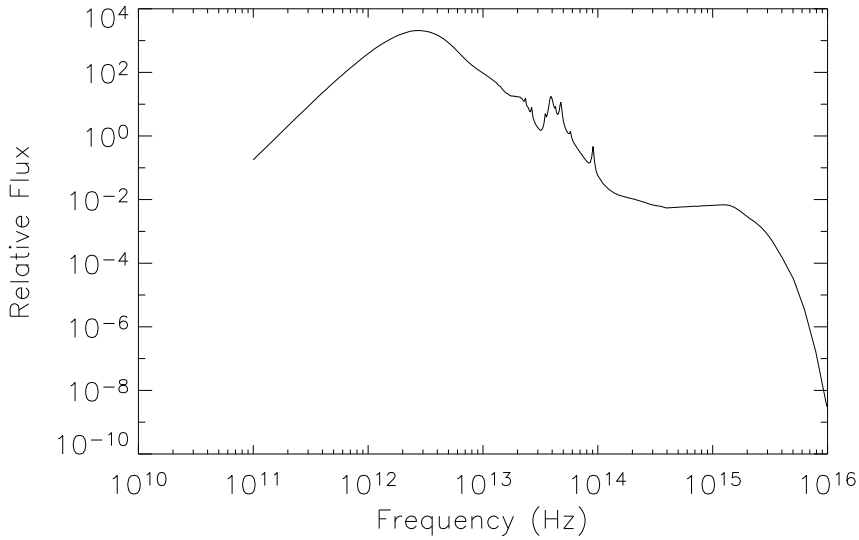

(a) Model Starburst SED

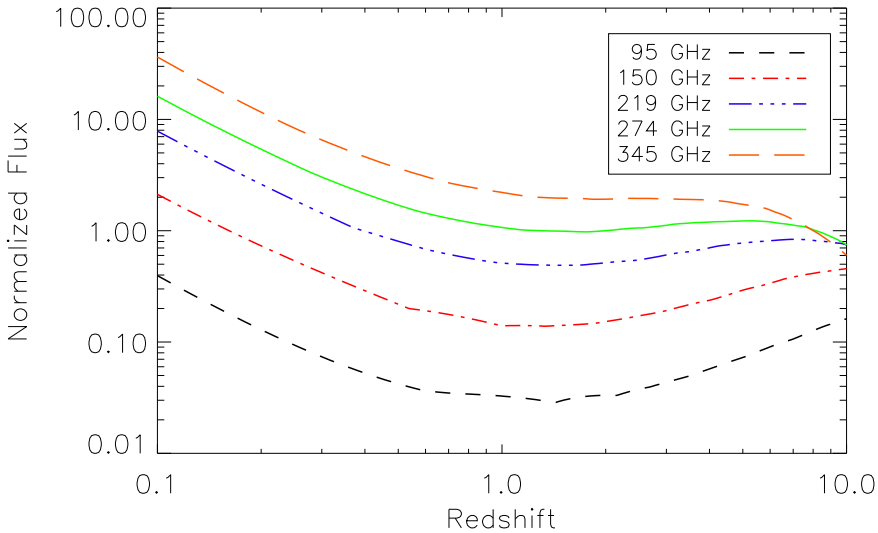

(b) Observed Flux vs. Redshift

Figure 1.1. SMG detectability as a function of redshift. **Top:** Modeled dusty starburst rest-frame SED from Siebenmorgen & Krügel (2007). Modeled data points end at 2 mm (150 GHz) and are extended to 3 mm assuming a purely Rayleigh-Jeans spectrum in that regime. **Bottom:** Observed flux of the modeled source at typical (sub-)mm wavelengths as a function of redshift. Flux values have been normalized to the 274 GHz ($\sim$ 1.1 mm) value at the typical SMG redshift of $z = 2$. Calculations are made assuming a flat ΛCDM model with $\Omega_\Lambda = 0.7$ and $\Omega_M = 0.3$. Anomalous small scale ripples seen in the lower frequency bands are due to the quadratic interpolation between the sparsely sampled portions of the model SED.

maps is insufficient to significantly constrain the brightest portion of the population ($S_{850} \gtrsim 15\,\mathrm{mJy}$).

Small area surveys are also susceptible to clustering and cosmic variance. By performing a uniform re-analysis of most the pre-SHADES SCUBA blank field surveys (resulting in ~ 500 arcmin^2 of disjointed survey area), Scott et al. (2006) have found evidence for clustering of bright sources on scales of $\sim$1 arcminute, although the statistics (number of bright sources) are too small to constrain or parametrize the level of this potential clustering. In addition, spatial correlations with low-redshift large-scale structure has been detected in three disjoint SCUBA fields, which is attributed to lensing by the foreground structure (Almaini et al., 2003, 2005) that could induce an apparent clustering by amplifying the more numerous dimmer SMG population around foreground mass structures. The lack of a large contiguous survey area leaves these analyses powerless to address clustering and variance on large scales. Clustering analysis is expected on the recently published SCUBA SHADES fields (Coppin et al., 2006), although these fields are likely too small to significantly advance the understanding of SMG clustering alone. BOLOCAM has performed large survey of the COSMOS field (~ 0.25 deg^2) that has yet to be published, however, the map is expected to be rather shallow (1-sigma depth of $\sim$2 mJy), resulting in marginal significance of even the brightest detections and diminishing the survey's power to discern clustering strengths.

Several large (many hundreds of square arcminutes) contiguous surveys covering different patches of sky to a moderate depth ($\sigma_{1.1\mathrm{mm}} \sim 1\,\mathrm{mJy}$) and totaling on order of $1\,\mathrm{deg}^2$ are necessary to characterize the brightest SMG population while also measuring clustering and variance. This is one of the primary science goals of AzTEC; a new mm-wave camera developed at the University of Massachusetts, Amherst. Construction and design of AzTEC is described in Chapter 2. Integration, characterization, and performance of the instrument are detailed in Chapter 3. An AzTEC survey of

a $0.15\,\mathrm{deg}^2$ portion of the COSMOS field (Scott et al., 2008) discovered a significant over-density of SMGs that are spatially correlated with the low-redshift structure ($z \lesssim 1.1$), as described in Chapter 5. Finally, I describe AzTEC's significant contribution to the overall characterization of the 1.1 mm SMG population in Chapter 6. Additional details and discussion pertaining to the AzTEC instrument and SMG surveys are found in the Appendices.

These and other recent AzTEC surveys have produced a collection of maps of unprecedented size and depth at 1.1 mm. When coupled with the 50-m Large Millimeter Telescope, AzTEC will be capable of producing maps at high-resolution (5 arcseconds at 1.1 mm), thus allowing survey depths previously unattainable because of source confusion – the AzTEC/LMT 1.1 mm confusion limit is expected to be < 0.1 mJy using an extrapolation of the known SMG number counts at larger fluxes.

While this dissertation focuses on the SMG applications of AzTEC, it should be noted that AzTEC proves to be a powerful tool in many other areas of (sub-)millimeter astronomy, such as the study of galactic star-forming regions, brown dwarfs, evolved stars, comets, clusters via the Sunyaev-Zeldovich effect (Sunyaev & Zeldovich, 1970) and the mapping of dust in nearby galaxies. Many projects in these fields have already been undertaken using AzTEC, with analysis and publications in preparation.

CHAPTER 2

INSTRUMENT DESIGN AND CONSTRUCTION

2.1 Introduction and History

The AzTEC instrument represents the second realization of the greater BOLOCAM project (Glenn et al., 1998, 2003; Haig et al., 2004; Wilson et al., 2008a); an effort to develop a new generation of large-format ($\sim$ 150 detectors) mm-wave continuum cameras. The original BOLOCAM instrument was first commissioned in 2000 with a set of engineering-grade (non-optimized) detectors and began full scientific observations at the 10-meter Caltech Submillimeter Observatory (CSO) with the science-grade detector array in 2004 (Haig et al., 2004). BOLOCAM is still in part-time use at the CSO and has been a success in its own right. However, as with any instrument, lessons are learned and technology advances through experience and time. AzTEC has been re-designed and improved in many areas of weakness found in BOLOCAM, including aspects of the cryogenics, optics, electronics, operation and control. In the end, everything but the focal plane array was improved or radically re-designed in significant ways.

The design and construction of AzTEC began in earnest in 2002, culminating with first light at the 15-m James Clerk Maxwell Telescope (JCMT) in the summer of 2005 using an existing BOLOCAM engineering-grade array for 1.1 mm observations. The fabrication (Caltech/JPL) of the final AzTEC science-grade detector array was completed in the fall of 2005, leading to drastically improved sensitivities during AzTEC's first scientific observing run at the JCMT, which lasted 3 months during the North American winter of 2005-2006 and proved to be highly successful

(Chapters 3–6). AzTEC was then moved to the Atacama Submillimeter Telescope Experiment (ASTE), a ten-meter diameter ALMA prototype telescope, where surveys of the southern sky would be possible. AzTEC has since enjoyed roughly 12 months of full-time operation at ASTE, which were split into two continuous observing runs that spanned the southern hemisphere winters of 2007 and 2008, respectively. Ultimately, the AzTEC instrument is designed as a facility instrument at the Large Millimeter Telescope (LMT;Schloerb, 2008), a new 50-m (sub-)millimeter telescope entering the latter stages of construction and characterization and potentially beginning science-grade observations in late 2009 or early 2010.

2.2 Cryogenics

New custom cryogenics were designed for the AzTEC system. When compared to its predecessor, these designs resulted in improved cryostat efficiency, accessibility, flexibility, and increased 4 K working volume.

2.2.1 Cryostat

The cryostat of the original BOLOCAM instrument is limited in both cryogen capacity and nominal 4 K workspace. The liquid helium (LHe) stage has also proven to be poorly isolated, resulting in a high rate of cryogen usage and making refills both expensive and difficult to schedule (often requiring a refill on $<$ 24hour intervals).

An all new custom cryostat was designed for AzTEC, which incorporates several features to combat the issues incurred by BOLOCAM. First, the new cryostat has larger liquid helium (23 liters) and liquid nitrogen (26 liters) tanks, thus ensuring the cryogens will last more than 1 day in even the worst case scenario. Larger tanks also increase the transfer efficiency – liquid helium loss during a transfer is dominated by the cooling of the transfer line and is thus roughly independent of the total volume transferred. Secondly, a significant effort was made to insulate the cryostat

post manufacture. Low-emissivity aluminized mylar multi-layered insulation (MLI) was installed at both the LN_2 ($\sim$ 30 layers) and LHe ($\sim$ 10 layers) levels. Within the evacuated cryostat, this insulation acts as a series of radiatively coupled plates, linearly reducing the power load between two surfaces of different temperature as a function of the total number of insulation layers. Empirically, it has been found that this linear relationship begins to breakdown at about 30 layers of MLI between the 300 K and 77 K surfaces, and 10 layers between the 77 K and 4 K surfaces, at which point the application of additional layers provides little benefit. However, the truly limiting factor for any application is the quality and care with which the MLI is applied. Additionally, most internal surfaces of the AzTEC cryostat have been covered with low-emissivity aluminum tape to reduce radiation and absorption between surfaces. This design and preparation of the cryostat resulted in operational (full loading, including daily fridge cycles) hold times of approximately 3 days for liquid helium and over 7 days for a full tank of liquid nitrogen. The relatively long hold times for cryogens and the millikelvin refrigerator (Section 2.2.2) allow for regularly scheduled maintenance and minimizes cryogen costs.

The liquid helium evaporation rate for AzTEC when optically open and fully operational is $\sim$ 5 L/day (excluding fridge cycles). In practical units, the latent heat of evaporation of liquid helium is $\sim$ 0.72 W·hour/L, thus giving $\sim$ 0.15 W of total loading on the AzTEC 4 K stage. The primary components of this loading includes the parasitic loading conducted between the 4 K and 77 K stages through the G-10 support cylinders ($\sim$ 70 mW), the two stainless steel LHe fill tubes (difficult to estimate due to cooling by exhaust), and the $\sim$ 400 signal/bias/housekeeping manganin wires ($\sim$ 15 mW). Relatively hot (130 K) internal JFET amplifiers (Section 2.5.1) contribute a combined $\sim$ 30 mW (1 L/day) to the total loading. The remaining radiation load on the 4 K stage is expected to be sub-dominant ($<$ 35 mW) to these combined parasitic loads, thanks largely to the careful insulation discussed previously.

Operation of the millikelvin refrigerator (Section 2.2.2) requires $\sim 3\,\mathrm{L_{LHe}}$/cycle. When AzTEC was at the JCMT, the refrigerator was cycled daily, resulting in a total daily LHe consumption rate of $\sim 8\,\mathrm{L/day}$, thus the cryostat required LHe refills every two days. At the ASTE telescope, the refrigerator was cycled every other day (total average consumption $\sim 6.5\,\mathrm{L/day}$), thus allowing a more relaxed filling schedule of every 3 days.

AzTEC's cryogen tanks are concentric cylinders, with the inner liquid helium tank leaving a 6-inch diameter hollow center. This design adds valuable volume and accessibility to the 4 K workspace without severely compromising the cryogen capacity, thus offering tremendous flexibility and allowing for significant improvements in the optical and electronic designs and layout. The overall layout of the AzTEC cryostat and placement of vital components are depicted in Figure 2.1.

2.2.2 Millikelvin refrigeration and design

For optimum detector sensitivity (i.e. inherent noise properties of detectors are negligible or, at least, sub-dominant), the AzTEC bolometers must be cooled to sub-Kelvin temperatures. To achieve these temperatures, the AzTEC bolometer array is cooled by a three-stage, closed-cycle sub-Kelvin ^{3}He refrigerator that was custom built by Chase Research Cryogenics LTD[1]. The fridge utilizes the temperature-dependent adsorptive qualities of activated charcoal to operate its three helium pumps (^{4}He/^{3}He/^{3}He) and can operate from the ambient pressure (non-pumped) liquid helium bath temperature ($\sim 4\,\mathrm{K}$). Each stage is initially charged with an overpressure of helium gas at room temperature and when the charcoal is cold ($\sim 4\,\mathrm{K}$), nearly all the helium molecules are adsorbed to the charcoal's surface. The amount of adsorption is temperature dependent such that when the charcoal is heated (e.g. $\gtrsim 20\,\mathrm{K}$) it expels helium molecules to the stage's working volume. When the volume is sufficiently over-

[1] www.chasecryogenics.com

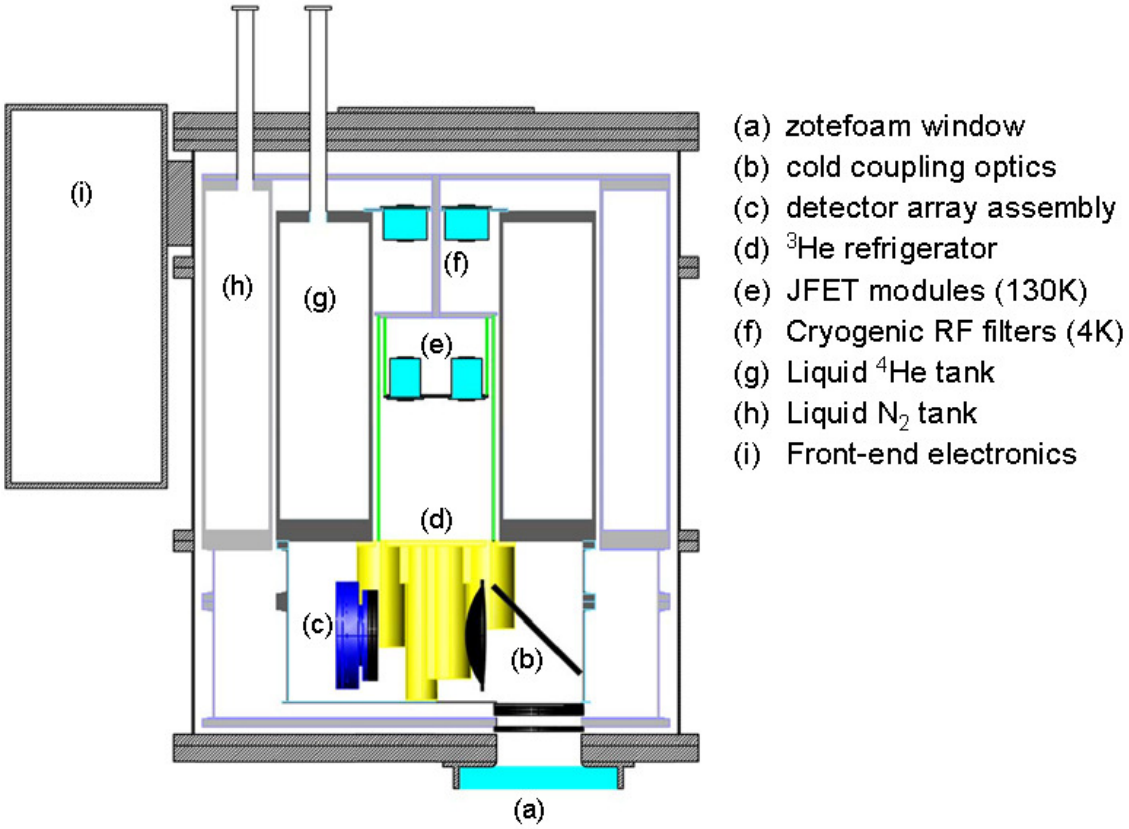

Figure 2.1. Cross-sectional view of the AzTEC cryostat including prominent optical and electronic components. Some mechanical, thermal, and electronic components are omitted for clarity. The effective signal chain runs from the detectors (c), up through the center of the cryostat (e and f), and out to the front-end electronics (i). Figure reproduced from Wilson et al. (2008a).

pressured and cooled by another bath (e.g. the cryostat's liquid helium bath and/or an another stage of the refrigerator), condensation and liquefaction occurs. When liquefaction is maximized, the activated charcoal is cooled back to 4 K at which point it acts as a pump, thus reducing the vapor pressure above the liquefied helium and reducing its temperature. Through a coordinated timed sequence (generally referred to as "cycling" the refrigerator) of heating and cooling of the various charcoal pumps, millikelvin temperatures are achieved. Further details of this type of refrigerator can be found in Bhatia & Saba (2001).

The three-stage approach results in two vacuum-pumped baths of liquefied ^{3}He: (a) the Ultracold (UC) stage at a temperature of $\sim$ 250 mK (under typical loading conditions); and (b) the Intercooler (IC) stage at $\sim$ 360 mK, which acts to pre-cool and buffer the UC stage. Under typical operational and loading conditions, AzTEC's UC stage comes to an equilibrium temperature of $256.5 \pm 1.9 \pm 10$ mK, where the latter error represents the systematic uncertainty of the calibrated germanium resistance thermometer (GRT). The equilibrium UC and IC temperatures show no correlation with cryostat tilt or atmospheric optical depth, resulting in a stable temperature regardless of the observed elevation on the sky. The AzTEC detector array is thermally sunk to the UC stage using solid OFHC copper that is thin enough to allow easy flexing due to differential thermal contraction.

The detector array is mechanically supported from the cryostat's 4 K plate using a series of Vespel[2] standoffs and an intermediate insulating stage sunk to the refrigerator's 360 mK IC. Each mechanical stage is supported by a radial configuration of three 1 inch long cylindrical Vespel legs of diameter 0.25 inches that are hollowed to a 0.01 inch thickness. The detector array is supported using Vespel type SP-22 (black), resulting in a total parasitic load through the legs of $\sim$ 10 nW to the UC. The in-

[2]Vespel is a type of polymer that is mechanically strong while having very low thermal conductivities at cryogenic temperatures; www2.dupont.com

termediate mechanical stage is thermally isolated using Vespel type SP-1 (brown), resulting in a total conducted loading of $\sim 14\,\mu$W to the IC. All signal and bias cables are thermally sunk to the 360 mK mechanical stage to further insulate the array from the 4 K bath. AzTEC signal and bias lines consist of 300 SWG-44 gauge wires, resulting in thermal loads of ~ 20 nW and $\sim 12\,\mu$W for the UC and IC stages, respectively.

The refrigerator is designed to have a 24 hour hold time with excess loads (in addition to inherent parasitic loads of the refrigerator) of $3\,\mu$W and $115\,\mu$W for the UC and IC stages, respectively (Bhatia & Saba, 2001). The relatively constant parasitic loading through the refrigerator structure and wiring is expected to be $\sim 1\,\mu$W for the UC stage, and considerably higher for the IC. In typical configurations (including a no-load situation, i.e. parasitic only), the IC stage typically determines the system hold time as it exhausts it's cooling capacity (no more liquid helium) before the UC stage. Once the IC is exhausted, the UC stage remained cold for 10–12 hours, but at a higher equilibrium temperature (~ 320 mK).

In practice, I find there are three primary aspects of the system configuration and operation that strongly affect the resulting cooling capacity: (a) the cryostat's bath temperature (4.2 K for a liquid ^{4}He cooled system at sea level); (b) the angle between the vertical axis of the refrigerator and the gravity vector; and (c) the timing of the various steps in the refrigerator cycle. The resulting hold time of the system is a strong function of bath temperature, as a colder bath (e.g. cryocooled, pumped liquid bath or lower atmospheric pressure) will more efficiently pre-cool and liquefy the over-pressured gasses in the various stages of the refrigerator. For AzTEC, the hold time (cooling capacity) doubled when going from sea level ($T_{\rm LHe} \approx 4.2$ K) to the ASTE site at 16,000 feet ($T_{\rm LHe} \sim 3.6$ K). The angle, or tilt, of the refrigerator during the cycle can drastically affect the convection of the gas within each stage which affects the cooling and isolation of the liquefaction stage. For the AzTEC system, I found

that an angle of 20–45 degrees with respect to gravity (tilt necessary only during cycle procedure) resulted in the longest hold times, with up to a 50% improvement from vertical (i.e. the orientation depicted in Figure 2.1). AzTEC was mounted such that the system was at 30 and 45 degrees when the JCMT and ASTE were at zenith, respectively, thus allowing for cycles even when the respective telescope was undergoing maintenance. Finally, the fridge cycling sequence and timing is optimized such that the system hold time was 22, 38, and 44 hours for the lab (sea level), JCMT (14,000 feet), and ASTE (16,000 feet), respectively. Achieving hold times of $\gtrsim 40$ hours is highly beneficial for liquid cooled cryostats as it allows refrigerator cycles to be scheduled every 2 days, rather than every day, thus saving on liquid helium usage (i.e. monetary and manpower costs).

The optimized AzTEC refrigerator cycle takes approximately 2 hours to cycle and another ~ 1 hour to fully settle to the equilibrium temperature (e.g. exponential settling/cooling falls below inherent noise fluctuations in temperature, or $< 1\,\mathrm{mK}$), given the final AzTEC configuration and thermal mass. The sequence of actions that comprise the cycle have been fully automated into a single script that can be remotely controlled using the Large Millimeter Telescope Monitor and Control (LMTMC) program. The various pump and stage temperatures during a typical cycle are plotted in Figure 2.2. The entire cycle results in approximately 3 liters of liquid helium usage in the cryostat's 4 K bath as a result of the power used to heat the various charcoal pumps. An alternative cycle procedure in which the first stage (^{4}He) pump is cycled twice (Runyan, 2003) in order to liquefy more ^{3}He in the IC can result in longer hold times at the expense of more power dumped to the 4 K bath (i.e. more helium usage). If using a cryocooled (e.g. pulse tube cooler) rather than liquid cryogens, this may be an attractive option for increasing hold times.

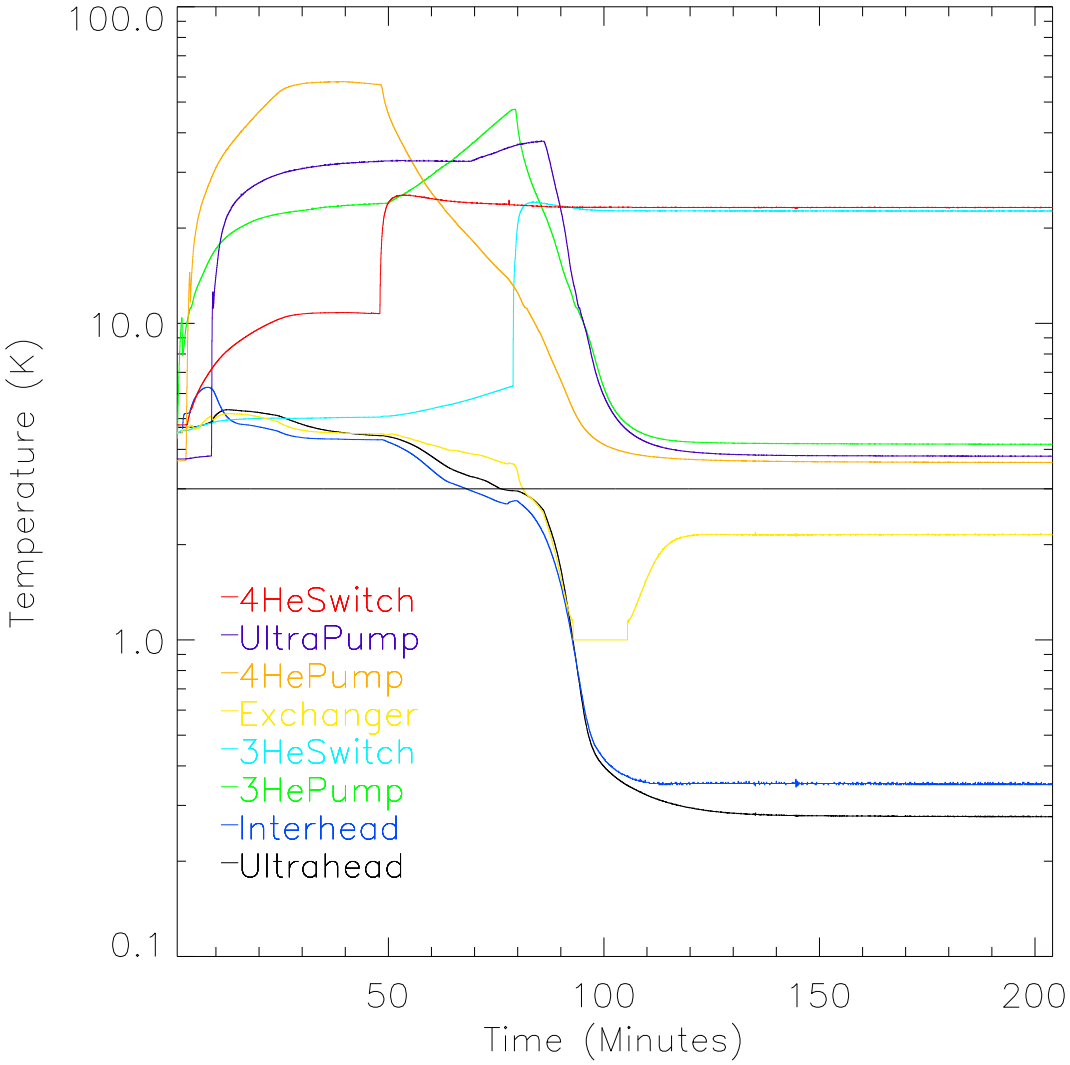

Figure 2.2. Temperature sequence of pumps, switches, and stages during a typical cycle of the three-stage millikelvin refrigerator. Heat switches are effectively on/off when above/below 10 K. The heat exchanger (labeled 'Exchanger') thermometry is uncalibrated below 1 K and, therefore, appears to bottom out at 1 K when actually at lower temperatures during the final stages of cooling.

2.3 Detectors

At the heart of AzTEC lies its hexagonal array of 151 Silicon Nitride (Si_3N_4) micromesh "spider-web" bolometers, fabricated at the Jet Propulsion Laboratory (JPL) as a single, 76 mm diameter monolithic wafer (Bock et al., 1996; Mauskopf, 1997; Turner et al., 2001). Each bolometer is fitted with a Neutron Transmutation Doped (NTD) germanium thermistor (temperature dependent resistor) that is indium bump-bonded to the mesh absorbers. The detectors are optically coupled to an array of 151 straight-walled conical feedhorns through single-mode waveguides that are all machined as a single piece. An integrating cavity is formed for each bolometer by sandwiching the detector array between the machined cavities on the back of the feedhorn/waveguide array ("frontshorts") and a rear plate with reflective cavities that provide the "backshorts". The BOLOCAM team has optimized the parameters of the integrating cavity and absorber through numerical simulations of the electromagnetic fields within the cavity (Glenn et al., 2002) and this general design was adopted for the AzTEC focal plane.

The absorber and thermistor of each bolometer are thermally distant from the wafer substrate (wafer sunk to the UC bath temperature), thus allowing the thermistor/absorber to be heated to temperatures that are a strong function of the incident power (optical and electrical). Each device's' thermal and electrical response to incident power and bath temperatures can be modeled through the parameters (R_0, Δ, g and α) and relationships outlined in Glenn et al. (2003), where the detector resistance is

$$R_{\rm d}(T_{\rm d}) = R_0 \exp(\Delta/T_{\rm d})^{1/2}, \tag{2.1}$$

with the values of R_0 and Δ determined by the doping concentration of the thermistor; the total power conducted through the device's weak thermal link is described as

$$P = g(T_{\rm d}^{\alpha} - T_{\rm bath}^{\alpha}), \tag{2.2}$$

which also represents the total incident (optical + electronic) power when in equilibrium; and the thermal conductance

$$G(T_{\rm d}) = g\alpha T_{\rm d}^{\alpha-1}, \tag{2.3}$$

where g is defined by the thermal link to the bath and α has been measured to be $\alpha = 2.47 \pm 0.08$ for these types of detectors (Haig et al., 2004).

The optimal achievable parameters are a function and balance of several factors, including expected loading (itself a function of bandpass, atmospheric conditions, parasitics, bias current, etc), necessitated noise (sensitivity) characteristics, and the desired speed of the detectors (thermal time constant is a function of the heat capacity of the device, C, and its conductance to the bath, G, i.e. $\tau = C/G$). In manufacturing, these factors are typically taken into account when defining the device conductance parameter, g, which is dictated and controlled by the thickness of Au deposited on one of the micromesh support legs. Since AzTEC is designed to be capable of observing at various frequencies (but only one available per installation due to the unique feedhorns, backshorts, and lens needed for each band), a compromise value of g had to be chosen that could accommodate the expected optical loading for various passbands in the 1.1–2.1 mm range. From this range, a conservatively high value value was chosen ($g \approx 407\,\mathrm{pW/K^{\alpha-1}}$) to account for any unanticipated loads that may arise (e.g. underestimated atmospheric or optical component emission). Target parameters for the AzTEC detectors are given in Table 2.1, followed by a set of example characteristic values and noise estimates when assuming the bolometer model and a nominal atmospheric opacity of $\tau_{225\mathrm{GHz}} = 0.11$.

Once defined and installed (i.e. post-manufacture), further optimization of detector effective sensitivity can be achieved through tuning of the electrical bias current through the thermistor, which gives the user some control over the total loading (and consequently temperature, resistance, etc) of the device. Such tuning may be de-

Table 2.1 Target Bolometer Model Parameters, JCMT Operating Points and Noise Estimates

Target Bolometer Parameters	
R_0 (Ohms)	100
Δ (K)	42
α	2.5
g (pW/K$^{\alpha-1}$)	407
Resulting JCMT Operating Points (at example opacity)	
$\tau_{225\mathrm{GHz}}$	0.11
T (mK)	438
R (MΩ)	1.79
G (pW/K)	295
S (V/W)	1.22×10^8
Resulting Noise Estimates (from model)	
Johnson noise	34 aW/$\sqrt{\mathrm{Hz}}$
Phonon noise	44 aW/$\sqrt{\mathrm{Hz}}$
Amplifier (JFET pair)	58 aW/$\sqrt{\mathrm{Hz}}$
Load resistor	4 aW/$\sqrt{\mathrm{Hz}}$
Photon noise	102 aW/$\sqrt{\mathrm{Hz}}$
Total:	**130 aW/$\sqrt{\mathrm{Hz}}$**

Targeted bolometer model parameters, followed by the predicted set of 1.1 mm operational characteristics and noise estimates for an example atmospheric opacity of $\tau_{225\mathrm{GHz}} = 0.11$, given the JCMT optical parameters of Section 2.4 and nominal operating bias (62.5 mV). Various noise contributions are estimated using the given operating parameters and the equations of Mather (1984).

sirable when using the same device in significantly different weather conditions or when changing the optical bandpass fed to the device (both can drastically affect the optical loading on the absorber). An optimum bias current can be found by minimizing the inherent detector noise through a minimized balance of phonon noise, which rises with increasing T, and Johnson noise, which falls steeply with rising T because the resistance of NTD-Ge thermistors declines exponentially with temperature. For AzTEC, all 24 bolometers of a hextant share a common bias source and, in practice, a single bias current is applied to the entire array. Therefore, a compromise bias setting was chosen to accommodate the inherent spread in detector properties across the array and the unpredictable optical loading from the ever changing atmosphere.

For all JCMT and ASTE observing runs using the science-grade array, the bias voltage was set to 62.5 mV, which is put across two 10 MΩ load resistors that are in series with each bolometer (typically 1.5–2.0 MΩ) to produce a roughly constant bias current of ~ 2.8 nA. This compromise value results in sensitivities (total NEP) within 7% of the optimal bias setting for any typical observing conditions, i.e. $0.02 < \tau_{225\mathrm{GHz}} < 0.30$, assuming the detector parameters of Table 2.1. Experimentally, it is found that this choice of bias was near optimum, as confirmed through nightly load curves, noise measurements, and beam map observations taken at each telescope (see Section 3.3.2.3). Ultimately, AzTEC's sensitivity at 1.1 mm has proven to be limited by photon noise and signal induced through slowly changing (low frequency) fluctuations in the atmospheric emission, thus the choice of bias voltage is effectively optimal.

NTD-Ge spider-web bolometers have proven to be a very successful and reliable detector technology (e.g. BOOMERANG; Crill et al., 2003). The AzTEC detector array is physically the same as BOLOCAM's (and similar to the arrays produced for SPIRE; Griffin et al., 2003) and its fabrication benefited from the production experiences of the BOLOCAM arrays. Consequently, the AzTEC array was the first

detector array of its kind to be produced without any open-circuit (explicitly "broken") detectors. However, it appears that a few of the AzTEC detector circuits contain electrical shorts or have bad JFET amplifiers (Tables A.2–A.3) in series that render the bolometer channel unusable. For readout symmetry (Section 2.5.1), only 144 detectors are electrically active and available for a particular run. When considering all possible points of detector channel failure, there were typically 107 and 114 stable, high-sensitivity channels available during the JCMT05B and ASTE observing runs, respectively.

2.4 Optics

The AzTEC micromesh bolometers are inherently broadband devices that can used at a variety of sub-millimeter and millimeter bands; therefore, the desired AzTEC bandpass is defined through a series of filtering components along the optical path. The high frequency edge of the AzTEC bandpass is defined through a series of low-pass metal mesh filters (Ade et al., 2006) that are placed at the 77 K, 4 K, and 300 mK barriers along the optical path, with relative positions and filter characteristics outlined in Figure 2.3. The series approach to filtering is necessary to suppress harmonic response from the final 250 mK edge defining filters and to minimize optical loading on the cold (0.25–4 K) stages. The low frequency bandpass edge is defined by the cutoff frequency of a short section of single-mode circular waveguide located at the detector end of the feedhorn array.

There are several necessary considerations when choosing an experiment's bandpass, which include, but are not limited to, atmospheric transmission and emission characteristics (for ground based experiments), sensitivity (wider band generally corresponds to higher signal-to-noise, if atmosphere/noise/source characteristics are constant over band), and spectral resolution needed for field(s) of study. These and other practical considerations led to the chosen filtering components of the AzTEC 1.1 mm

configuration, resulting in the bandpass shown in Figure 2.4. The bandpass was measured before deployment using the UMass Fourier Transform Spectrometer (FTS), which is similar in concept and design to that outlined in Bin et al. (1999). This configuration has an effective bandwidth of 49 GHz, which is 18% of the nominal band center frequency of 270.5 GHz.

The AzTEC system was designed with flexibility in bandpass in mind. In particular, AzTEC was designed to have near-optimum sensitivity for bandpasses centered at 1.1 mm, 1.4 mm, and 2.1 mm – wavelengths corresponding to the increment, null, and decrement of the Sunyaev-Zel'Dovich effect (Sunyaev & Zeldovich, 1970), respectively. To change bandpasses, AzTEC simply requires changing of the feedhorn/backshort assembly, some of the optical low-pass filters, and the UHMWPE cold lens. The necessary swapping of cold components means only one bandpass is available per observing run. A full warm-up, part swap, and cooldown would take a minimum of 4 days. To date (early 2009), AzTEC has only operated at 1.1 mm. The AzTEC electronics (Section 2.5) incorporate digitally controlled variable components, thus readily allowing for optimal tuning to the particular band in use. The Focal plane array and optics (e.g. feedhorns and backshorts) are discussed further in Section 2.3.

Light enters AzTEC through the cryostat's vacuum window (Figure 2.1) and is made of closed-cell Zotefoam[3] (type PPA30; nitrogen expanded polypropylene), which, thanks to its small cell size and low density, has very low absorption and scattering properties at millimeter wavelengths (>99% transmission at 1.1 mm, as measured using the UMass FTS). The Zotefoam window also acts as an optical and IR blocker. A cold Lyot stop is placed at the image of the primary mirror and sunk to the 4 K bath (Figure 2.5). This optical stop truncates the detector beams before

[3]http://zotefoams.com. However, Zotefoams no longer actively manufactures this material and existing quantities are limited to large volume purchases. Limited smaller quantities may be available through the distributor Technifab Inc., http://technifabfoam.com.

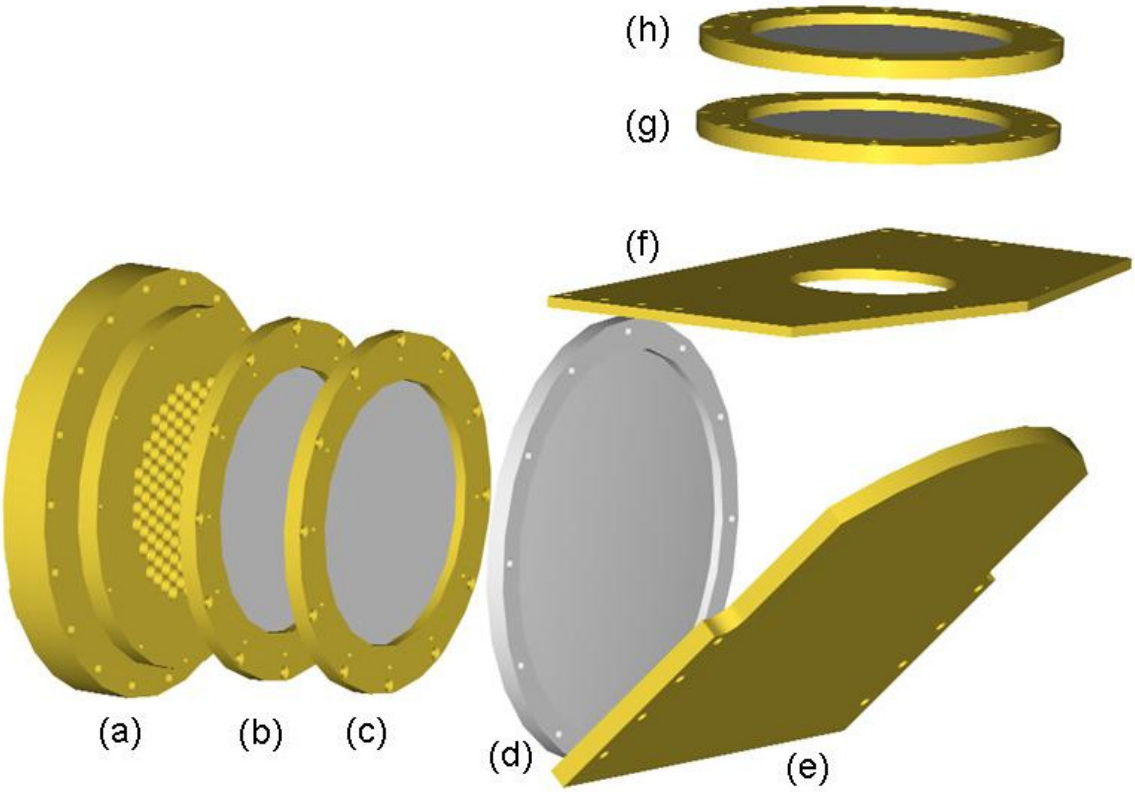

Figure 2.3. Cartoon layout of the internal AzTEC optics. Relative component placements are not to scale. Components are: (a) integrated detector array, back-shorts and conical feedhorns (250 mK); (b) 310 GHz low-pass filter (250 mK); (c) 360 GHz low-pass filter (250 mK); (d) bi-convex ultra-high molecular weight polyethylene lens (4 K); (e) folding flat (4 K); (f) 50 mm diameter Lyot stop (4 K); (g) 390 GHz low-pass filter (4 K); and (h) 1050 GHz low-pass filter (4 K). Not shown are an additional 77 K 540 GHz low-pass filter and a Zotefoam PPA-30 cryostat vacuum window that also serves as an IR blocker (see Figure 2.1). Figure reproduced from Wilson et al. (2008a).

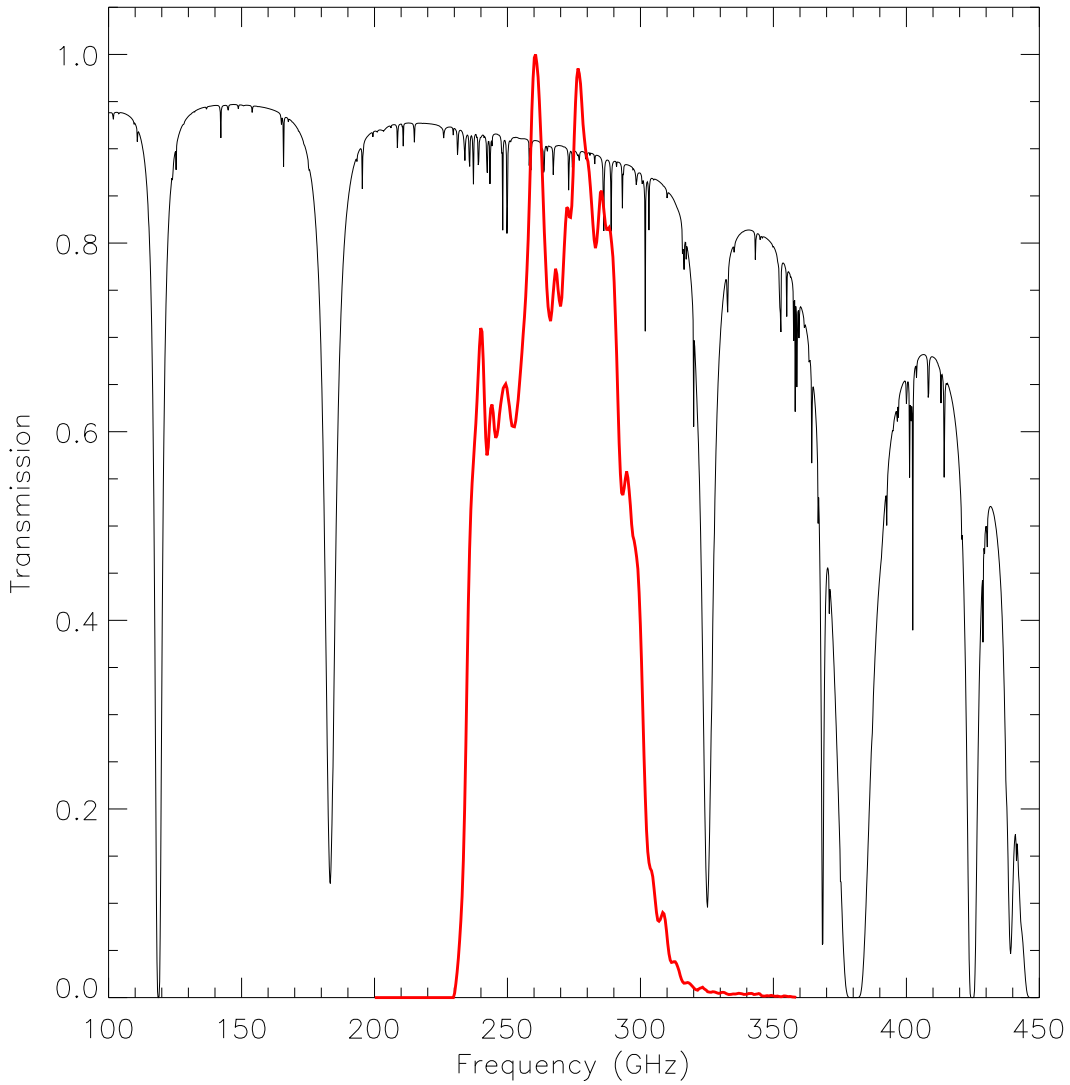

Figure 2.4. AzTEC 1.1 mm bandpass and relevant atmospheric transmission function. The peak normalized AzTEC bandpass (red) was measured using the Fourier Transform Spectrometer (FTS) at the UMass Continuum Detector Laboratory (CDL). Over-plotted is the atmospheric transmission model (black) of Schneider et al. (2009) for 1 mm of precipitable water vapor at the Mauna Kea site.

the edge of the primary to reduce illumination of the warm ground (i.e. spillover) lying beyond the primary mirror's extent.

The original BOLOCAM cryostat natively lacked the necessary 4 K working volume for the necessary internal optics and required a long on-axis extension. This caused many of the optical components to be spatially distant from the 4 K cryogen bath, making them difficult to keep cold and adding overall loading to the liquid helium bath. If these components and supports were allowed to heat significantly beyond 4 K, it would show up as excess loading on the detectors and reduce their sensitivity. To avoid such problems in AzTEC, significant optical and mechanical modifications were undertaken to make the internal optical path more compact. First, several components of the readout electronics were moved into the excess 4 K volume formed by the the concentric liquid helium tank. This effectively freed space "behind" the detector array, thus rendering BOLOCAM's long on-axis thermal and mechanical standoffs obsolete and wasteful. Therefore, a novel, off-axis support design was adopted that required fewer and smaller standoffs. This made the array support more compact, freeing up more optical path length within the nominal cryostat working area. It also makes the support system more rugged by reducing the lever arm on which the relatively massive focal plane components are mounted. The array support is stiffer in this configuration, hence raising the frequency of any vibrational modes. The standoffs support the array radially at 90 degrees from the optical axis, making the array extremely rigid along the focal plane and reduces the structure's sensitivity to thermal differential contraction, thus reducing susceptibility to pointing and alignment errors due to movement of the detector array relative to the optical axis. The weakest vibrational mode of the support is along the optical axis, which only acts to negligibly affect the focus, and the structure has been verified to have no resonant frequencies below 400 Hz (i.e. faster than the relevant signal frequencies). Finally, the optical path was 'folded' into the cryostat by rotating the detector array optical

Table 2.2. AzTEC Optical Design Parameters at the JCMT

Optical Parameter	
ellipsoid focal length	645.2 mm
ellipsoid reflection angle	37°
UHMWPE lens focal length	163.6 mm
$f/\#_{\mathrm{cass}}$	12.0
$f/\#_{\mathrm{Lyot}}$	11.8
$f/\#_{\mathrm{horns}}$	3.2
Lyot stop diameter	50 mm
edge taper at Lyot stop	-5.2dB
image of primary mirror dia.	52 mm
plane wave coupling efficiency at Lyot stop	0.62
detector spacing	$1.4f\lambda$

Note. — The calculation of the plane wave coupling efficiency at the Lyot stop is made assuming Gaussian optics and following the prescription of (Goldsmith, 1998). Table reproduced from Wilson et al. (2008a).

axis 90 degrees and incorporating a flat mirror at 4 K. This allowed the Lyot stop to fall just inside the nominal, and thermally well sunk, 4 K working area of the cryostat (Figure 2.5).

The rest of the coupling optics are generally telescope specific. This typically includes a set of external (300 K) ellipsoidal and flat mirrors (one each at the JCMT) to couple and manipulate the detector beams, their path, and path length relative to the telescope optics. Within the cryostat, AzTEC uses a 4 K ultrahigh molecular weigh polyethylene (UHMWPE) lens (index of refraction, $n = 1.52$) to remove field curvature and convert the detector beams to the desired f-number of the feedhorns ($f/3.2$). An anti-reflection surface is produced on the lens through a series of narrow concentric grooves tuned to the system passband, i.e. grooved to a depth of $\lambda/4\sqrt{n}$. Detailed specifications of the AzTEC/JCMT optical coupling are listed in Table 2.2.

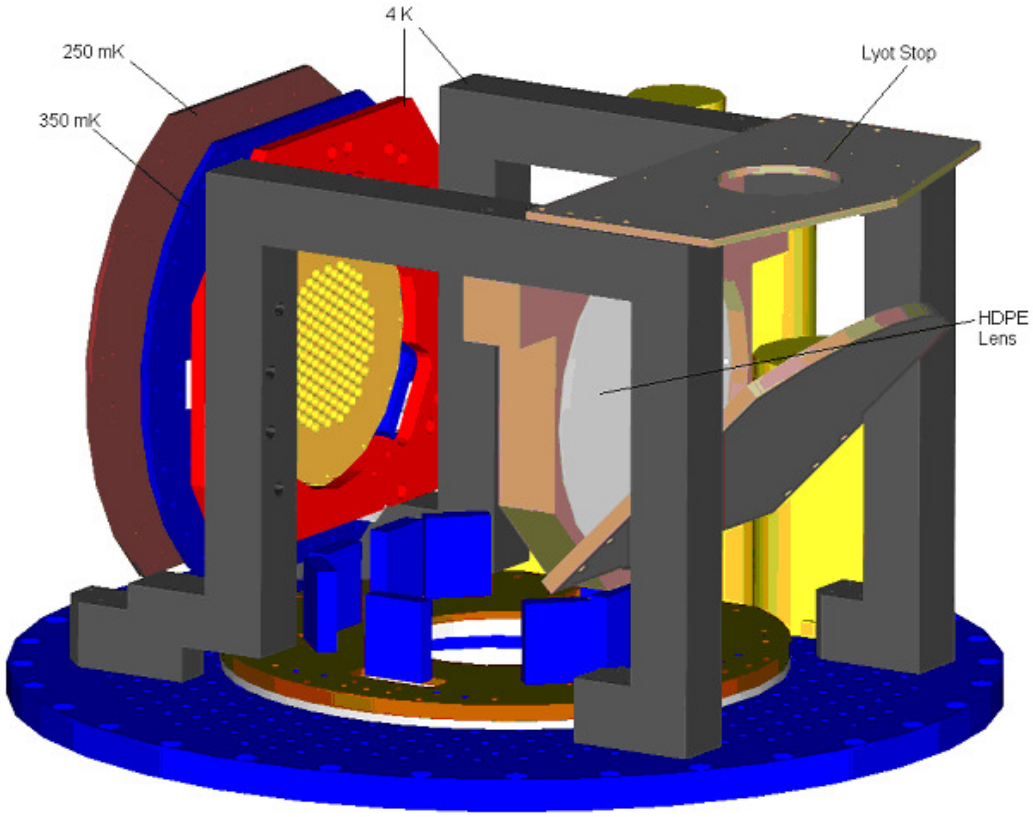

Figure 2.5. Mechanical design and layout of millikelvin and 4 K components. The thermal isolation stack for the detector array can be seen on the left, with 250 mK, 350 mK, and 4 K plates mechanically supported by low thermal conductivity Vespel. In this orientation, light enters the cryostat from above and comes through the cold aperture (Lyot) stop. The light is reflected off of a 45-degree flat mirror and through the HDPE lens to the feedhorn array seen on the left. The $\sim$ 130 K JFETs reside in the hollow 4 K cylinder located below the components depicted in this diagram. Signal cables come up through this hidden volume via 51-pin micro-D connectors (depicted as blue boxes). The three stage ^{3}He millikelvin refrigerator is roughly depicted by the yellow cylinders in the back of the drawing. Low-pass optical filters, millikelvin thermal straps, and signal cables are omitted for clarity.

2.5 Signal Chain

2.5.1 Internal (cold) readout electronics

The cold readout electronics (internal bolometer circuit) for AzTEC and BOLOCAM are identical in electronic design, but differ in implementation. The detector array is wired into six "hextants" of 25 bolometers each. Only 24 bolometers of each hextant are read out at any given time, due to practical wiring limitations (standard 51-pin connectors are used; two wires for each bolometer readout and two common bias lines per hextant) coupled with the fact that 100% yield is not expected of the detector array, leaving AzTEC/BOLOCAM with a maximum of 144 simultaneously operational detectors.

Common observing strategies result in relatively slow modulations of the astronomical signal, therefore, the bolometers are AC biased to achieve low frequency stability. Two 10 MΩ load resistors are placed in series with each bolometer ($\sim$ few MΩ) to transform the applied sine-wave voltage bias to a near constant current bias. A current bias is necessary due to the negative electro-thermal feedback (ETF) of the thermistors (i.e. resistance decreases with increasing temperature).

The range of appropriate bias frequencies is restricted by three major concerns. First, it is important that the bolometers see an effectively constant bias power; therefore, the bias frequency must be relatively fast compared to the detector time constant ($f_c = 1/(2\pi\tau) \sim 40\,\mathrm{Hz}$). The bias frequency must also be slow enough to avoid attenuation from an effective RC filter that arises from the resistive bolometers and capacitance between the wires (e.g. for $R_{\mathrm{bolo}} \sim 2$–$3\,\mathrm{M\Omega}$ and $C \sim 100\,\mathrm{pF}$, the cutoff frequency is $f_c = 1/(2\pi RC) \sim 320$ Hz). Finally, the bias frequency may not be near any resonant frequency within the system to avoid signal (noise) induced through microphonic pickup (all resonant frequencies of AzTEC measured to be $> 400\,\mathrm{Hz}$). Taking these restrictions into consideration, a bias frequency of 200 Hz was chosen for AzTEC.

Following each bolometer is a low-noise, unity-gain JFET amplifier that transforms the differential detector output from the bolometer resistance (several MΩ) to much lower impedance ($\sim 350\,\Omega$), thus reducing the circuit's susceptibility to microphonics, EMI noise, and RC attenuation from that location outward. The U401 JFETs used in the bolometer readout chain demonstrate optimal low-noise performance at temperatures of $\sim 130\,\mathrm{K}$. These relatively hot JFETs must be kept thermally isolated from the bolometers while remaining physically close to avoid the noise and attenuation problems associated with the high impedance portions of the circuit. AzTEC takes advantage of the added 4 K workspace in the cryostat by suspending the JFET modules (each module contains the 48 JFETs, i.e. 24 matched pairs, required for a single hextant of the bolometer array) within the center cavity of the cryostat. The two-stage suspension system is built primarily of G-10, which acts to thermally isolate the warm JFETs from the 4 K bath. An intermediate stage of the suspension is sunk to the 77 K bath and acts to intercept the heat dissipated by the powered JFETs. These 130 K and 77 K components are radiatively insulated with several layers of MLI and the walls of the 4 K cavity are painted black to absorb any stray thermal radiation.

A gold-plated copper shield caps the cavity containing the $\sim 130\,\mathrm{K}$ JFETs and shields the nominal workspace containing the focal plane. An FR4 printed circuit board with MDM-51 connectors is attached to the copper shield, and together they act as a transitional feedthrough for the signal cables connecting the detector array and JFET amplifiers. The primary purpose of this circuit board is to couple the bolometer bias to the same 51-pin connectors and cables connecting to the load resistor modules (i.e. 250 mK bolometer circuit) [4]. This circuit board also serves as a convenient

[4]The bias signal represents a completely separate set of electronics and cables from the readout electronics until this circuit board; however, with the primary signal cables no longer needing to carry the JFET power lines at this point, two wires are now 'free' for the bias to be coupled to the standard 51-way cables via this PCB.

and effective thermal sink for the relatively hot wires coming from the 130 K JFET modules. This is accomplished by epoxying (using Emerson & Cumming Stycast 2850FT) the board to the 4 K copper shield at the top of the cryostat's inner cavity. On the circuit, each conductor path has a length of trace that is extra-wide to create a heat sink and improve its thermal connection to 4 K. The thermal conductance of each trace's sink is $G \sim 5\,\mathrm{mW/K}$, which is more than enough to handle the small power loads ($\ll 1\,\mathrm{mW}$) carried through each of the manganin wires. The capacitance between the traces and copper plate is $< 1\,\mathrm{pF}$ and is inconsequential. The copper plate also acts as a radiation shield for the bolometers, blocking the thermal radiation from the relatively hot JFETs and cables below.

Electromagnetic/radio-frequency interference (EMI/RFI) shielding is also necessary due to noise sources that enter the cryostat through the vacuum window and couple to the wires between the 4 K and 300 K stages. Therefore, all signal, power, bias, and housekeeping (thermometry and fridge operation) wires are RFI/EMI filtered as they enter the 4 K workspace (see Figure 2.1), which, together with the high conductivity shields/tanks, form an effective Faraday cage around the 4 K volume. For AzTEC, custom compact filter modules with in-line pi-filters circuits were designed in coordination with the manufacturer, Cristek Interconnects Inc[5].

2.5.2 External (warm) readout electronics

Perhaps the most significant design advances for AzTEC involve the warm (external) electronics that perform the real-time data conditioning, processing (e.g. demodulation, filtering, decimation) and acquisition. Traditionally, this processing has required large quantities of identical and parallel analog components (one for each detector) before the data is digitized and stored. With a large number of detectors, such a design quickly becomes complicated, cumbersome, inflexible, expensive, and more

[5] www.cristek.com

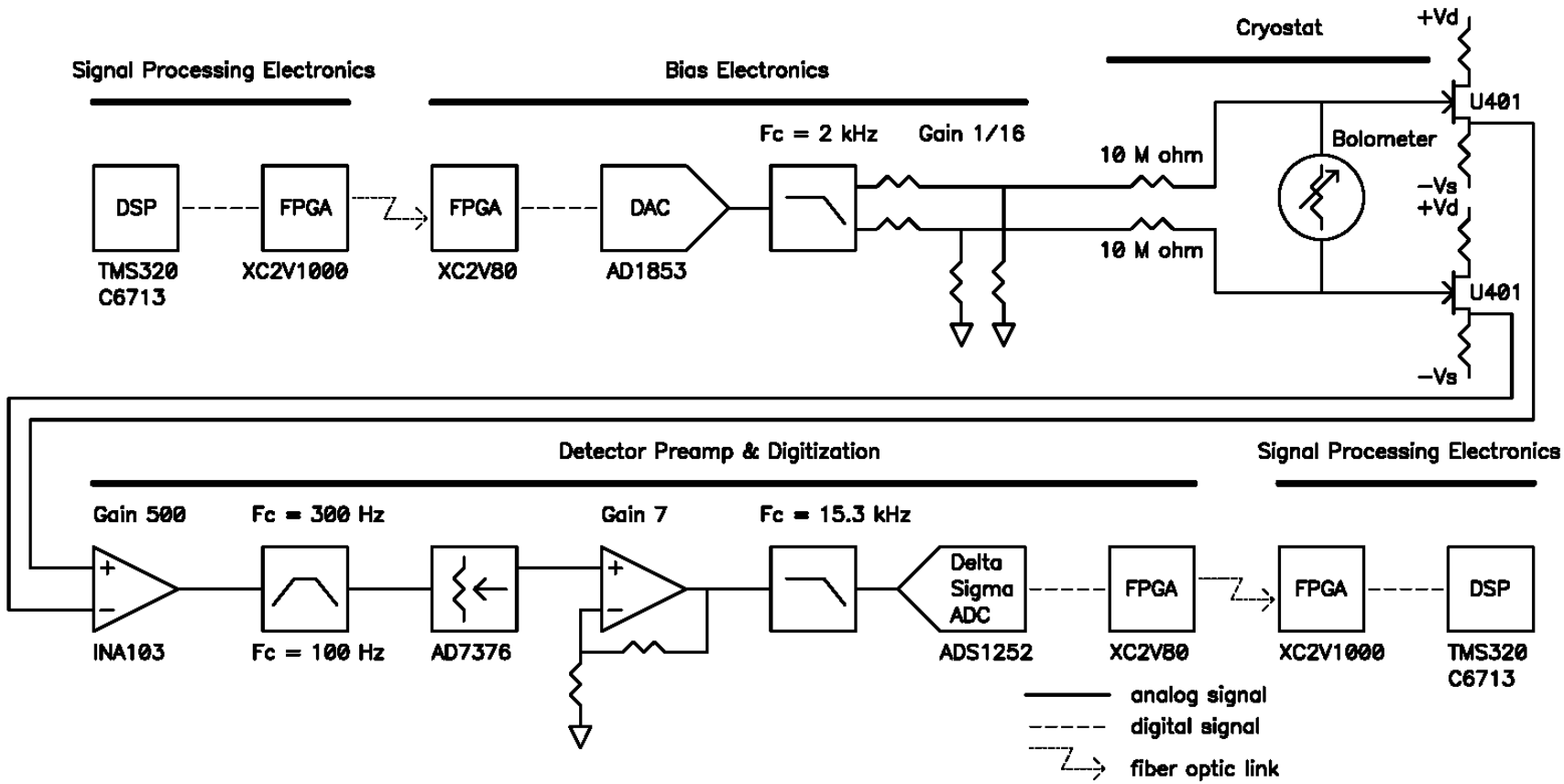

Figure 2.6. AzTEC readout electronics schematic and signal path. Schematic representation of the signal path of a single bolometer channel through the AzTEC readout electronics. All analog components listed under "Cryostat" and "Detector Preamp" (and analog connections) are repeated 144 times, i.e. one set for each detector. Note that the "Signal Processing Electronics" seen at both the beginning and end of the signal chain represent the same set of external digital electronics. Figure reproduced from Wilson et al. (2008a).

prone to failures. Fortunately, advances in the speed and resolution of modern digital electronics have allowed for a new approach undertaken for AzTEC. Now, nearly all of the real-time processing is done digitally and in software/firmware, thus adding a tremendous amount of flexibility and power. A schematic diagram of the AzTEC signal path, which includes all prominent electronic components, is represented in Figure 2.6.

The first set of external components is mounted directly to the cryostat and represents the "frontend" electronics. Upon exiting the cryostat, the differential signals (voltage across each bolometer) are EMI/RFI filtered and sent to the signal conditioning electronics. The custom frontend electronics box is well shielded and grounded to the cryostat's exterior, representing another "clean" Faraday cage. For optimum noise characteristics, it is usually important to provide power to the frontend electronics from a clean power source (e.g. a conditioned, battery buffered, UPS or other low-noise source). Upon entering the frontend, the bolometer signals are immediately applied to low-noise (1.7 $\mathrm{nV/Hz^{1/2}}$) instrumentation amplifiers (Texas Instruments INA103) with a fixed gain of 500. Each detector channel is high-pass filtered at 100 Hz and low-pass filtered at 300 Hz. Further amplification and a resistive divider with a digitally controlled resistor provide a final programmable analog gain of $\sim$ 100–10000. The resulting transfer function of select channels at a particular gain setting can be seen in Figure 2.7. The circuit is designed to have a relatively flat maximum gain near the modulation frequency (typically set to 200 Hz for AzTEC). The gain of the various bolometer channels (144 in total) are consistent within $\sim$ 1%. In practice, the channels are treated as having identical gain and the small differences between channels are intrinsically accounted for in the power calibration (i.e. responsivity calibration; see Section 3.3.2.2).

After amplification and conditioning, the signals are digitized by high-precision 24-bit sigma-delta analog to digital converters (ADCs) (Texas Instruments ADS1252)

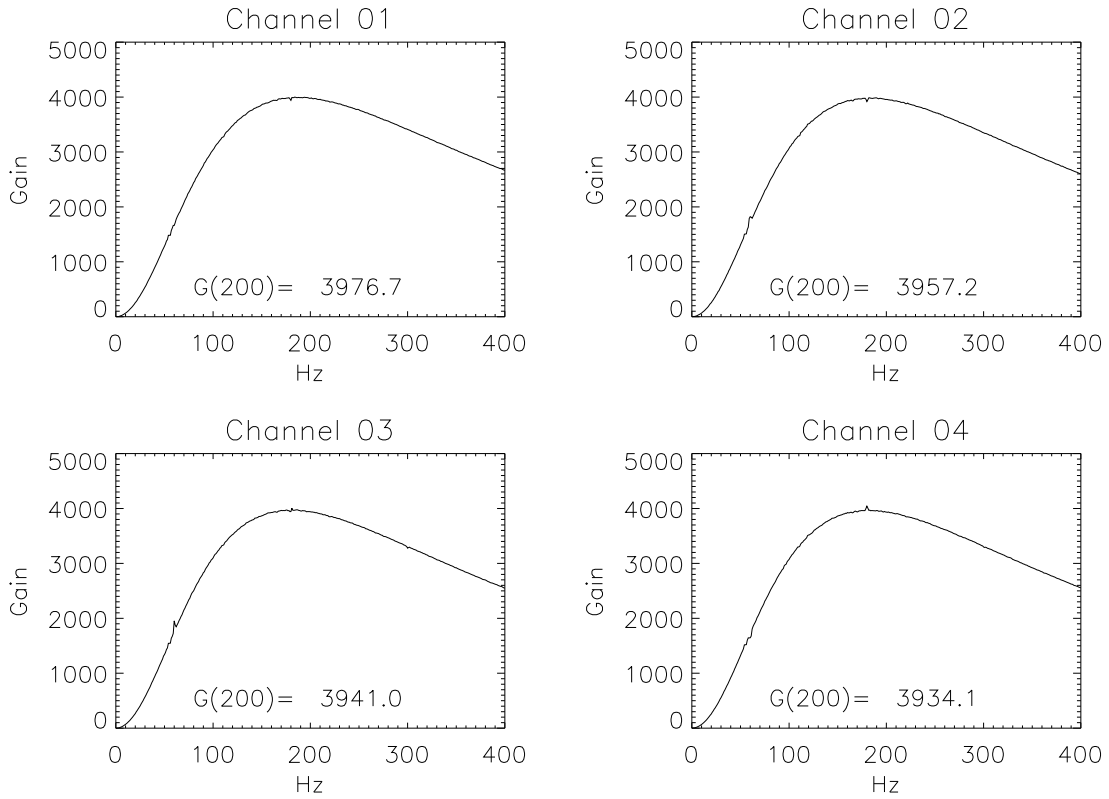

Figure 2.7. Transfer function of AzTEC's external analog readout electronics for four sample channels. The maximum gain is tunable through a digital remote-controlled variable resistor, allowing the gain at 200 Hz to be adjusted to various points between $\sim$ 100–10000. Data was taken during diagnostic testing of prototype readout boards during development. Small features due to pickup of 60Hz noise, and it's harmonics, are present during these open-air (unshielded) tests but are not significant when the electronics are in their full operational configuration.

at an output rate of 16 kHz. The analog part of the circuit includes a digitally controlled switch that allows the readout of an alternate, low-passed DC signal for engineering and bolometer characterization measurements. The variable gain of the analog electronics is necessary to maintain utilization of the full dynamic range of the ADCs when adjusting the bolometer bias voltage (i.e. when 'tuning' AzTEC to maximum sensitivity for the given optical loading conditions).

Once digitized, a Field Programmable Gate Array (FPGA) serializes each hextant (24 channels) worth of data into a single data stream. This data is sent via fiber optic to the off-cryostat "backend" electronics for processing and storage where a

single FPGA collects all six of the hextants' data streams, along with the digital bias signal. This FPGA feeds this data to a single Digital Signal Processor (DSP) that demodulates each channel using the reference bias signal. The DSP caches the demodulated data in memory and applies (in software) a sharp block FIR (Finite Impulse Response) filter, whose cutoff begins just below the Nyquist frequency of the final desired decimated and stored sampling rate. Since astronomical signals are typically much slower than the intrinsic ADC sampling rate of 16 kHz, the final decimated sampling rate can be significantly smaller without losing any sensitivity. In practice, the default decimated AzTEC sampling rate has been 64 Hz, which can be modified in software by changing the parameters of the digital FIR filter.

With a final sampling rate of 64 Hz or less (faster rates are not helpful given detector time constants on order of 5 ms), enough real-time computational power remains in the current AzTEC DSP to also produce a set of cosine demodulated bolometer signals. In general, these signals are 90 degrees out of phase with respect to the sine modulated astronomical signal. This signal can be used to properly align the reference modulation signal to the bolometer output, which become slightly out of phase through time delays and the capacitance in the signal lines. When in phase, the mean level of the sine demodulated signal is maximized while the cosine demodulated signal has a value of zero[6]. The cosine demodulated signal can also be used to monitor and trace systematic noise in the system. In practice, however, the systematic noise is insignificant compared to the atmospheric and shot noise sources, and any systematic noise that is prevalent is typically common-mode and easily removed without necessitating the cosine demodulated data.

[6]Since the demodulation is performed digitally, the phase of the signal can only be shifted by the resolution of the reference wave, i.e. the ratio of the sampling rate to the modulation frequency, or 16000 Hz/200 Hz for typical AzTEC operational settings; therefore, a very small amount of astronomical signal may remain in the cosine demodulated data.

All backend electronics reside in a standard VME crate, consisting of just three printed circuit boards (PCBs): a Motorola Power-PC general purpose computing and control card running the real-time VxWorks operating system; a custom digital data acquisition card (fiber optic connections to front end, FPGA, DSP); and a standard ADC I/O card for miscellaneous input and timing signals. The backend electronics can nominally be any distance from the frontend/cryostat, limited only by practical considerations to the length of the fiber optic connections.

Bias generation and Housekeeping (temperature monitoring and control) cards are part of the AzTEC frontend electronics. The bolometer bias signal is generated from a digital sine wave stored as a finite number of samples in memory. A series of digital to analog (DAC) converters generate the analog sine wave that biases the AzTEC detectors. Bias amplitudes are controlled digitally and in a real-time fashion. The bias frequency is defined by the digital wave stored in memory and can be any integer divisor of the native sampling rate of 16 kHz. As discussed, the nominal bias frequency has been chosen as 200 Hz; however, if AzTEC is ever installed in an environment where there is significant noise at 200 Hz, the modulation frequency can easily be modified. The Housekeeping card reads out internal thermometer voltages and provides power and automated control to the millikelvin adsorption refrigerator (Section 2.2.2).

AzTEC is controlled, and data is stored, using custom software in conjunction with the Large Millimeter Telescope Monitor and Control (LMTMC) system (Souccar et al., 2004), a software package developed at UMass-Amherst for general use at the LMT. This can all be run on a standard desktop PC running a Linux operating system. All communication and data transfer between the Linux machine and the backend computer is via dedicated Ethernet. When collecting both sine and cosine demodulated bolometer signals at 64 Hz, the total data rate of AzTEC is roughly

100 kB/s, depending on the amount and rate of external data sources (e.g. telescope pointing data, weather, etc.) being acquired.

2.5.3 Data product

AzTEC data collected by the controlling Linux machine are stored as self-describing, binary NetCDF (Network Common Data Form) files. Individual files coincide with the execution of an observing script, where typical observing scripts and strategies are often, but not limited to, 10–60 minutes of continuous data taking. Typical file systems limit files to a maximum size of 2 GB, therefore, a single observation is limited to a maximum length of ~ 5 hours (assuming a minimal telescope data stream and a sampling rate of 64 Hz). The dataset resulting from a real-time observation contains all necessary data in a single file, including bolometer and telescope data, instrument status and settings, and observing script parameters and requires no post-observation merging of data sets.

2.6 Discussion and Future

So far, AzTEC has operated at a bandpass centered at 1.1 millimeters; however, it could be converted to work at other millimeter atmospheric windows (e.g. 1.4 mm or 2.1 mm) by simply replacing the feedhorn array, backshorts, UHMWPE lens, and some of the optical filters. BOLOCAM has already demonstrated this by operating at both 1.1 mm and 2.1 mm (Glenn et al., 2003). Operation at other wavelengths opens doors to more scientific projects. Furthermore, working at wavelengths longer than 1.1 mm may prove to be an interesting option in the early days of the LMT, if the telescope surface should spend some time at less than target surface accuracy.

Not all of the AzTEC's 144 electrically live detectors were fully functional during the JCMT05B science observations. Approximately 20 bolometers are excessively noisy or appear to be shorted at or before the thermistor when at operational tem-

peratures (only two appeared as shorts at room temperature). An additional ~ 15 bolometers have poor or unstable noise properties that render their data highly undesirable and are generally ignored. It was initially believed that many of these problems could have been due to shorts between electrical traces on the surface of the detector array, therefore, the array was brought back to the production facility at JPL in January 2007 to see if these shorts could be identified and fixed. Upon inspection, material was often found between the traces of many bolometers that may, or may not, have been conductive at low temperatures. The lithographic process used to produce the array leaves a considerable amount of non-conductive residue on the array, which under the microscope is indistinguishable from other, potentially conductive, substances. In most cases where a substance was found between traces of problem bolometer, the material was etched away using a fine tip probe. In some cases, these potential shorts were found between the lead traces on the bolometer, which were not removed due to the high risk of permanently damaging the detector. Only a few (~ 4) definite shorts of a metallic substance were found and fixed on the array (including the two room temperature shorts). However, once installed on the ASTE telescope in May 2007, it was quickly obvious that only a few of the bad channels were fully recovered and operational. While the problems may still lie with the detectors, it should be noted that the points of failure could lie in other components of the instrument, including the JFETs, signal cables, or RF filters. These components have had limited testing in the past, but may have failing components, have been damaged, or fail at cryogenic temperatures. Detector status and estimated failure mode tables are listed in Appendix A; however, additional dedicated testing would still be required to definitively determine each point of failure.

As discussed in Chapter 3, the AzTEC system is generally not limited by detector noise, or any other intrinsic instrumental source, but rather by noise induced by atmospheric fluctuations and shot noise (i.e. background limited). This means that

these "traditional" NTD-Ge bolometers already represent near maximum sensitivity for ground-based $\sim$ 1 mm observations. Therefore, future/other experiments seek advancement through continued focal plane improvement in both total number and density of detectors. The primary limitation to the type of detectors used in AzTEC is that they are difficult to multiplex in a stable and low-noise way. That is, each detector needs it's own set of analog electronics and wiring within the cryostat. As the number of detectors is increased, the electronics and wiring become increasingly complex and cumbersome. To construct practical systems with significantly more detectors, a multiplexing serialized readout scheme, e.g. something akin to modern CCD devices, must be implemented. In fact, this has already been accomplished in recent years using bolometer arrays of superconducting transition-edge sensors (TESs) and superconducting quantum interference device (SQUID) readout schemes. Instruments employing these technologies have recently been successfully deployed with hundreds (e.g. APEX-SZ; Schwan et al., 2003) to 1,000 detectors (e.g. SPT receiver, Ruhl et al., 2004; ACT/MBAC, Niemack, 2006), and soon the ambitious 10,000 pixel SCUBA-2 receiver is expected to be commissioned on the JCMT (Holland et al., 2006). Arrays of Kinetic Inductance Detectors (KIDs) represent another promising technology that would be straightforward to multiplex (Day et al., 2003) and apply to (sub-)millimeter astronomy.

Another limitation is that the AzTEC detectors do not fill the focal plane ($1.4\,f\lambda$ detector spacing at 1.1 mm) and do not instantaneously Nyquist sample the sky, thus requiring careful observing strategies that ensure full sampling when map making (Section 3.3.1). Other detector technologies, in conjunction with direct focal plane illumination (i.e. no feedhorns), are able to improve this situation with a higher density of bolometers; for example the SHARC-II instrument (Dowell et al., 2003) uses an array of 'pop-up' bolometers to achieve a filling factor of >90% and detector spac-

ing of $0.65\,f\lambda$ (relatively close to the $0.5\,f\lambda$ necessary for instantaneously complete sampling of the sky).

CHAPTER 3

INSTRUMENT INTEGRATION AND PERFORMANCE

3.1 Introduction

AzTEC was built to be a first-generation facility instrument of the Large Millimeter Telescope (LMT; Schloerb, 2008), a new observatory currently under development in Mexico as a partnership between the University of Massachusetts and the Instituto Nacional de Astrofisica Optica y Electronica (INAOE) of Mexico. Since AzTEC was finished well ahead of the LMT schedule, AzTEC was commissioned on the James Clerk Maxwell Telescope (JCMT) in June 2005. After a successful commissioning, AzTEC was brought back to the JCMT for a 3-month scientific run in the winter of 2005/06, henceforward referred to as the JCMT05B observing run. AzTEC was later brought to the southern hemisphere and installed at the 10-m dish of the Atacama Submillimeter Telescope Experiment (ASTE), where AzTEC was in full-time operation for a total of approximately 12 months over the course of 2007-2008. In this chapter, I discuss observation strategies, calibration, and performance of the AzTEC instrument, with a heavy emphasis on AzTEC's time at the JCMT.

3.2 Telescope Coupling

The AzTEC cryostat was installed directly inside the JCMT and ASTE receiver cabins at the Cassegrain focus, which moves with the telescope in elevation. As a liquid cryogen instrument that has a somewhat limited range of motion (to avoid spilling cryogens) and requires regular maintenance (to fill the cryogens), and given the size and mass ($\sim 200\,\mathrm{kg}$) of the AzTEC cryostat, AzTEC required a relatively

complex mechanical support system, with the cryostat pre-tilted along the axis of motion such that cryogens did not spill out when observing at low elevation. Despite tilts up to 45°, cryogen capacity was maintained up to $\geq 90\%$, due to symmetry in the AzTEC cryostat which allowed rotation of the cryogen tanks relative to the focal plane and optimal placement of the cryogen fill tubes. Due to the limited access to the cryostat within JCMT receiver cabin, a system of rails and axles were designed for the AzTEC mount that allowed the cryostat to be pulled out of its receiver bay, tilted for cryogen fills, and then returned and locked in observing position with precision and repeatability. In addition, the JCMT receiver cabin simultaneously houses multiple other mm-wave instruments that source significant levels of noise within the receiver cabin, therefore, the AzTEC mount incorporated significant amounts of radiative (e.g. Eccosorb[1]) and mechanical isolation built into the mechanical support of the cryostat and external optical components.

3.3 Observing

AzTEC is a passive instrument that continually takes data regardless of telescope operations. However, the AzTEC system only saves data in logical groups that begin and end with the start and completion of a programmed set of telescope commands, i.e. an observation of a particular object or field. AzTEC data is stored in a machine-independent binary format known as Network Common Data Form (NetCDF). These files are "self-describing" in that each contains all the data required to interpret the data set (i.e. generate a map), including telescope pointing and observation parameters.

While observing, real-time monitoring is provided by tools in the LMT Monitor and Control (LMTMC) system (Souccar et al., 2004) and the real-time plotting

[1]http://www.eccosorb.com

package KST[2]. Quick-look software, utilizing the custom AzTEC software package (Chapter 4), is used to perform a quick and streamlined reduction of the data set following each observation. The resulting maps are used to verify the quality and parameters of the observation.

3.3.1 Observing Modes

The AzTEC hexagonal array does not instantaneously Nyquist sample the sky (Figure 3.1), therefore, an observing strategy that moves the array with respect to the sky must be adopted to generate fully sampled maps. The most desired observing mode is usually the most efficient, which is typically a function of the type of source(s) being observed, telescope capabilities, instrument parameters, and noise considerations. At the JCMT, AzTEC employed two primary observing modes: jiggle mapping and raster scanning. At ASTE, AzTEC also incorporated Lissajous scanning.

3.3.1.1 Jiggle mapping

Like its predecessor on the JCMT (SCUBA Holland et al., 1998), AzTEC used the combination of a nodding primary mirror and a chopping secondary in the observing strategy known as jiggle mapping. The secondary mirror moves the beams on the sky in small increments (a few arcseconds) in a predefined pattern (generally 25 points for AzTEC) that fills the sky. The secondary stops at each position to integrate for for a length of time, typically defined to be about one second. During this pattern, the secondary mirror is also chopped to an off-beam position (many arcseconds away) at relatively high rates (2–8 Hz) to provide a reference signal to the on-source position. The transit time of the secondary between chop positions is typically $\sim 30\,\mathrm{ms}$ (i.e. about two AzTEC samples). After completing this pattern, the primary mirror is nodded such that the off-source and on-source locations are reversed. This is necessary

[2]http://kst.kde.org/

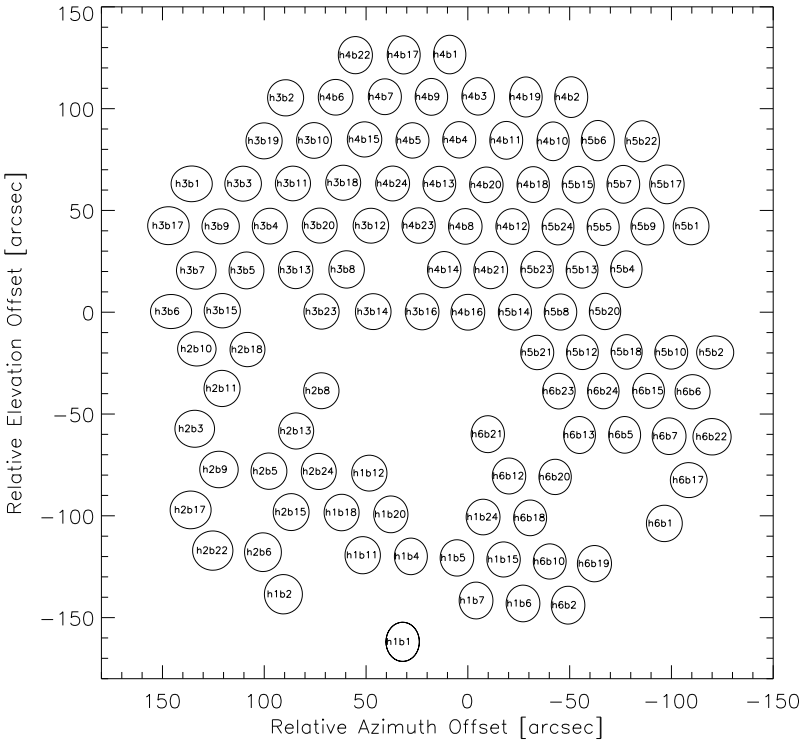

(a) JCMT Footprint

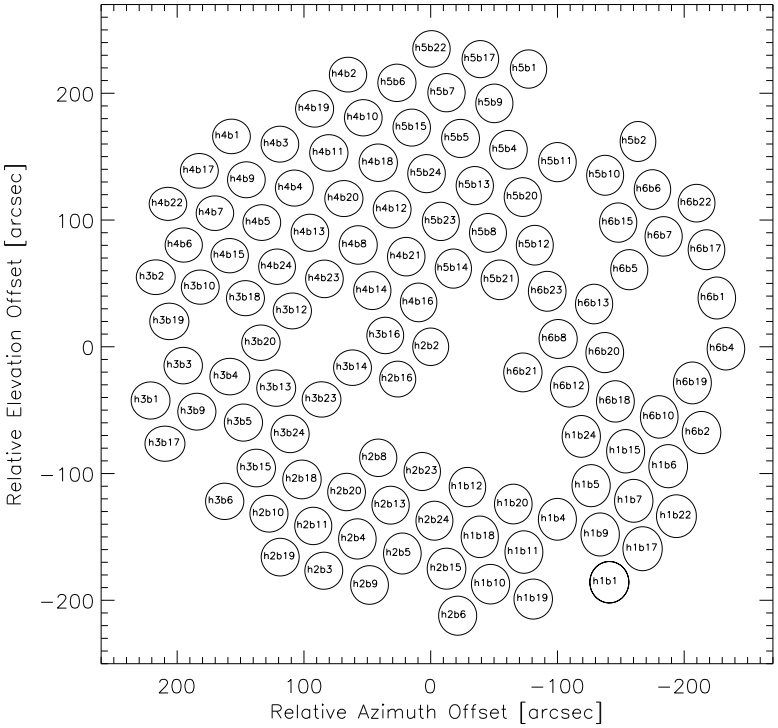

(b) ASTE Footprint

Figure 3.1. Footprint of AzTEC detector array as projected on the sky. Shown both when coupled to the: (a) JCMT; and (b) ASTE telescope. The relative bolometer positions are fixed in the horizontal Az/El coordinate system, however, the array was physically rotated between the JCMT and ASTE observing runs. Bolometer positions are relative to the arbitrarily defined reference pixel; h4b16 for JCMT and h2b2 for ASTE. The size and shape of each ellipse represents the FWHM of the two-dimensional Gaussian fit in the Az and El directions, as determined from beam map observations (Section 3.3.2.3). The array is divided into 6 hextants (h1–h6), each comprised of 24 bolometers (b1–b24). Inoperable bolometers during each run are omitted and are responsible for the gaps in the hexagonal array. There were 107 and 114 fully operational channels at the JCMT and ASTE, respectively.

to remove any signal introduced by the differential illumination of the primary mirror, the ground (spillover), and the secondary support structure by the detector beams in the "on" versus the "off" positions.

While at the JCMT, jiggle mapping was the preferred mode for photometry and mapping an area smaller than the AzTEC field-of-view (FOV ~ 5 arcminutes). Jiggle observations were the primary means of tracking AzTEC/JCMT pointing and provided secondary calibration observations. Unfortunately, most of the inoperable bolometers were clustered in one part of the array (Figure 3.1), which resulted in highly non-uniform coverage across the entire FOV (Figure 3.2). For photometric and pointing observations, the source was placed in the high coverage regions of the jiggle maps.

3.3.1.2 Raster scanning

Raster scanning was the primary strategy used at the JCMT for projects mapping areas much larger than the FOV. While raster scanning, the secondary mirror remains fixed as the primary moves the detector beams at constant velocity across the desired field. After each scan, the primary moves a small amount that is perpendicular to the scan direction, reverses, and moves back across the field. When the step size is relatively small (e.g. ¡ FWHM), this observation pattern produces a rectangular map with very smooth coverage (Figure 3.3), regardless of the location of the bad detectors. The co-addition of multiple raster scan maps taken with different position angles produces cross-linking of the data, thus helping reduce any scan-synchronous effects. Data taken during the turnarounds is saved, but is usually thrown out in the map making stage because the large accelerations of the telescope may induce excess noise through microphonic pickup and the telescope pointing may be unreliable.

The slowly varying nature of atmospheric emission (Figure 3.8) dictates that typical raster speeds should be at least a few beams/s, while mapping efficiency (telescope

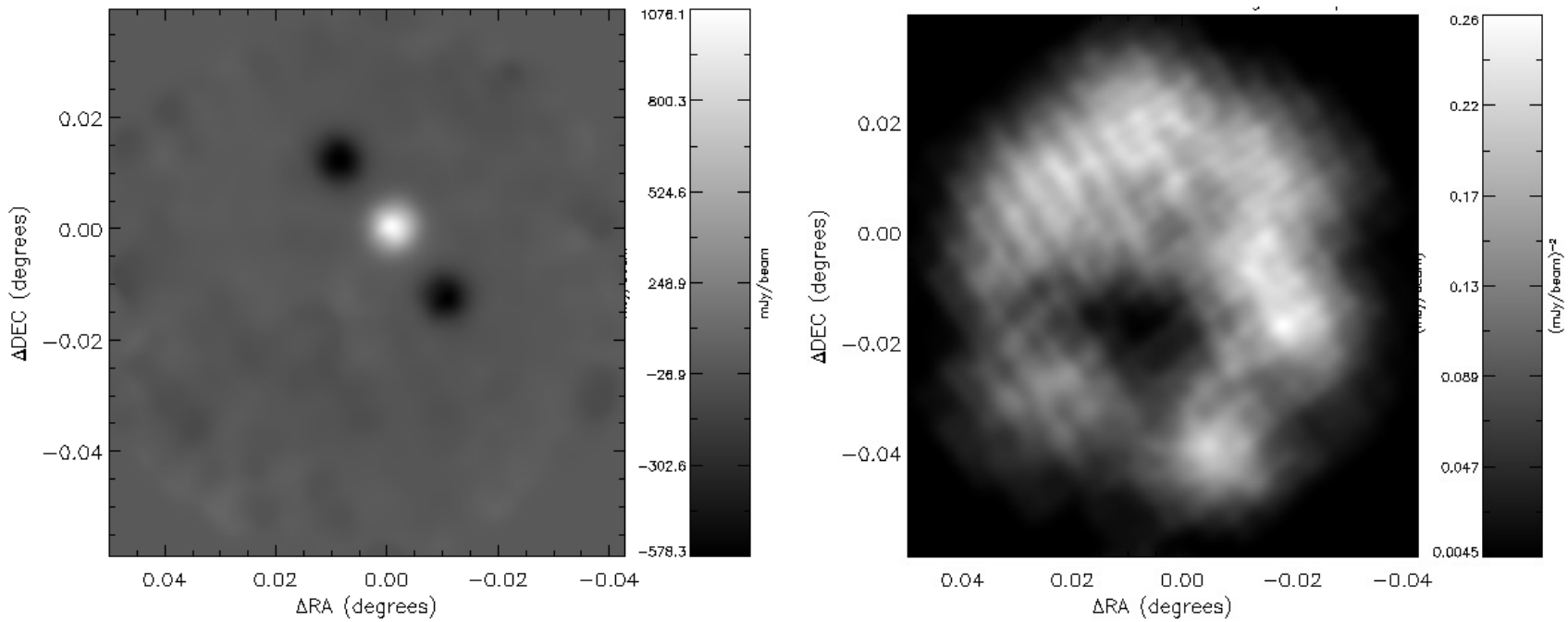

(a) Jiggle Signal Map

(b) Jiggle Coverage Map

Figure 3.2. Example jiggle map observation and associated coverage distribution. (a) Signal map of pointing target QSO J1048+7143 resulting from the typical jiggle mapping strategy employed by AzTEC at the JCMT. The combination of chopping and nodding of the secondary mirror (see text) results in the characteristic negative lobes in the source "off" positions. In practice, a two-dimensional Gaussian is fit to the peak positive flux to determine the pointing offset between the telescope boresight and the reference bolometer. (b) The corresponding coverage (i.e. weight) map. The lack of coverage near the center of the map is due to the cluster of inactive channels seen in Figure 3.1.

takes about 5 seconds to turn around between scans) and telescope stability suggest relatively slow scan speeds. Scanning speeds are also limited by the detector time constant ($\sim$ 4 ms) and the sampling rate (typically set to 64 Hz) in order to avoid time delay and smearing of signals. Given these considerations and a beamsize of 18 arcsec, typical AzTEC raster speeds at the JCMT were 60–180 arcseconds/s.

Raster scans were the preferred method for most science projects during the JCMT05B observing run, including the SMG surveys discussed in Chapters 5–6. Raster scanning strategies were also used for the nightly high-precision beam maps and primary calibration observations. At the JCMT, scans in elevation were preferred over azimuth scans, due to stability issues of the telescope's dome enclosure when moving at high speeds in azimuth, which lead to an induced noise signal at $\sim$ 2 Hz in the AzTEC timestream, possibly due to vibrations in the JCMT's Gortex shield. The nominal orientation of the AzTEC hexagonal detector array (Figure 3.1(a)) also meant that elevation scans provided an approximately fully sampled measurement in a single scan.

3.3.1.3 Lissajous scanning

The ASTE telescope is capable of any arbitrary scanning pattern (as long as within the telescope's allowable speeds and accelerations), which allowed AzTEC to scan in Lissajous patterns. The general Lissajous function can be applied to a scanning pattern as

$$x = A \sin at + \delta \tag{3.1}$$

$$y = B \sin bt, \tag{3.2}$$

where t is time; A and B are the amplitude of the scan in azimuth and elevation, respectively; a and b are the respective scan frequencies; and δ is the phase offset. The appearance of a Lissajous pattern is heavily dependent on the ratio a/b, and for

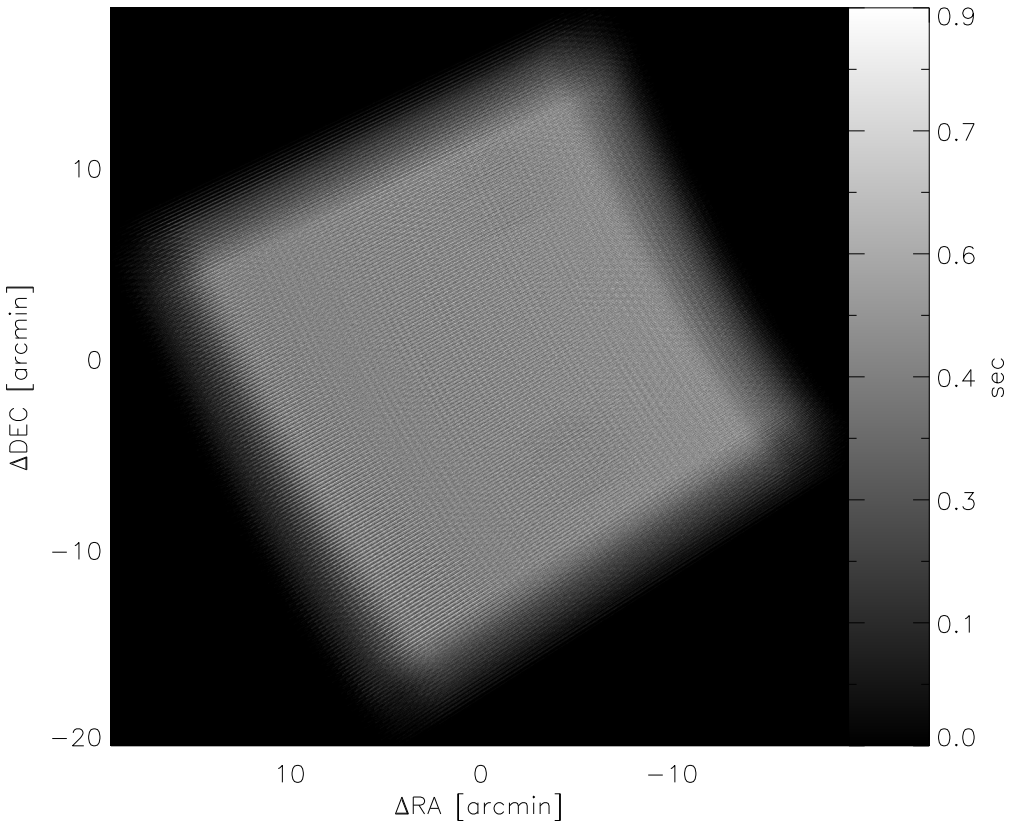

Figure 3.3. Coverage pattern of a typical raster scan observation. Coverage depends on the scanning strategy employed (e.g. spacing between scans), but is relatively smooth down to ~ 2 arcseconds (i.e. the plotted pixel size and 1/9 of the AzTEC/JCMT FWHM) for typical AzTEC observations at the JCMT. Typically, the scans are in the Az/El coordinate system while the coverage plot is in RA/DEC, resulting in the slight "fanning" seen in the plot due to sky rotation during the scan. If many of these square maps are taken at different times (i.e. different Az/El positions) and co-added together, sky rotation often causes the final map to be more circular in coverage.

the pattern to be closed, i.e. cyclical, the value of a/b must be rational. Unlike a raster scan, this Lissajous scan is nearly always accelerating with changing tangential velocity. However, these accelerations are generally much smoother and slower than that of the raster scan turnarounds; therefore pointing uncertainty and microphonic pickup are not significant issues.

The major advantage to using a Lissajous pattern is that all the data of the observation can be kept, thus increasing the overall efficiency of observation. For small maps (e.g. 10 arcmin x 10 arcmin) that may have otherwise spent over half the time in telescope turnarounds, Lissajous scanning can more than double the observing efficiency. However, given the footprint of the AzTEC array, the relatively simple Lissajous scans of Equation 3.1 often result in structured coverage patterns that are less smooth than that of a typical raster scan (e.g. Figure 3.3). This problem is easily rectified by adding a secondary harmonic oscillation to the pattern, i.e.

$$x = A \sin at + \delta + C \sin at/c \tag{3.3}$$

$$y = B \sin bt + D \sin bt/c, \tag{3.4}$$

where C and D are the azimuth and elevation amplitudes of the secondary oscillation, and c scales the frequency of oscillation. This secondary oscillation effectively moves the primary pattern relative to the sky, which acts to help fill in the gaps in coverage. When properly tuned to the map size desired, these scanning patterns result in maps that are as smoothly covered as a close-packed raster pattern (or better). Typically, the amplitudes and frequency of the secondary oscillation are smaller than that of the primary. An example Lissajous scanning pattern can be seen in Figure 3.4.

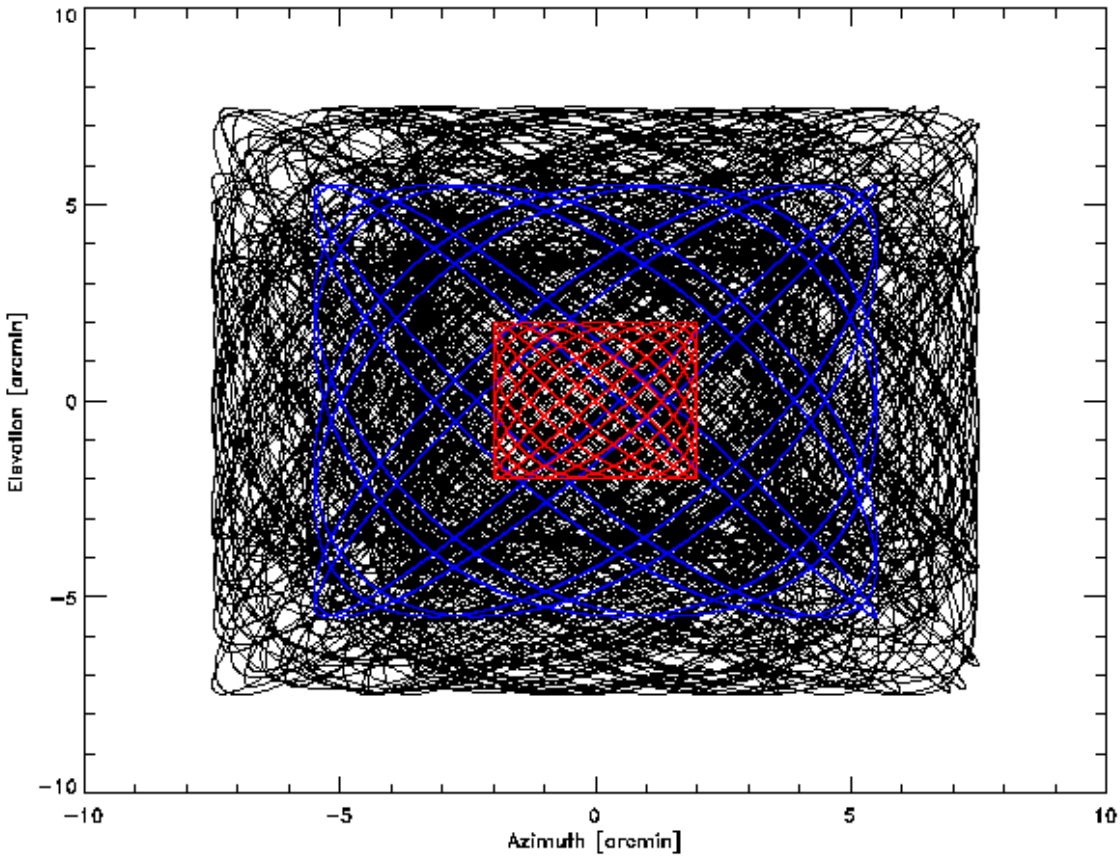

Figure 3.4. Lissajous scanning pattern and strategy. Example AzTEC Lissajous scanning pattern (black curve) as defined in Equation 3.3, with $A = B = 5.5$ arcmin, $C = D = 2$ arcmin, $a = 8z$, $b = 9z$, and $c = 30$, where z is a scaling factor used to control the peak velocity of the scan. The blue curve represents the primary oscillation and red represents the secondary, together resulting in true (black) pattern. Image courtesy of Grant Wilson.

3.3.2 Engineering and calibration observations

During routine operations, there are four types of engineering, or "overhead", observations that must be taken nightly in order to adequately tune and calibrate the AzTEC system.

3.3.2.1 Focus observations

For optimum resolution and straightforward flux determination, it is beneficial to have the system in focus. For AzTEC, focusing has typically been performed at the beginning and half-way through each night. Focus is determined by producing small and quick maps of a bright source (typically $> 1\,\mathrm{Jy}$) at a variety of secondary mirror positions. A two-dimensional Gaussian is fit to the source in each map and the optimum focus position is determined to be that corresponding to where the source FWHM is minimized and the peak amplitude is maximized. Jiggle-maps and small Lissajous maps were used for this purpose at the JCMT and ASTE, respectively.

3.3.2.2 Load curves

"Load curve" refers to a measurement of detector voltage as a function of detector bias while observing a blank piece of sky. The derivative, $\mathrm{d}V/\mathrm{d}P$, or responsivity, S, provides a conversion from detector voltage to power absorbed by the detector and is found by sweeping through all commandable bias settings while monitoring the detector output. The responsivity varies with total power loading; therefore, responsivity is measured under a variety of atmospheric conditions to provide a correction for the detectors' non-linear response (Figure 3.5).

3.3.2.3 Beam maps

High-resolution observations of a very bright millimeter source are made nightly (after focusing) such that individual maps can be made by each detector. These maps provide the relative positions and point spread functions (PSFs) of the detectors in

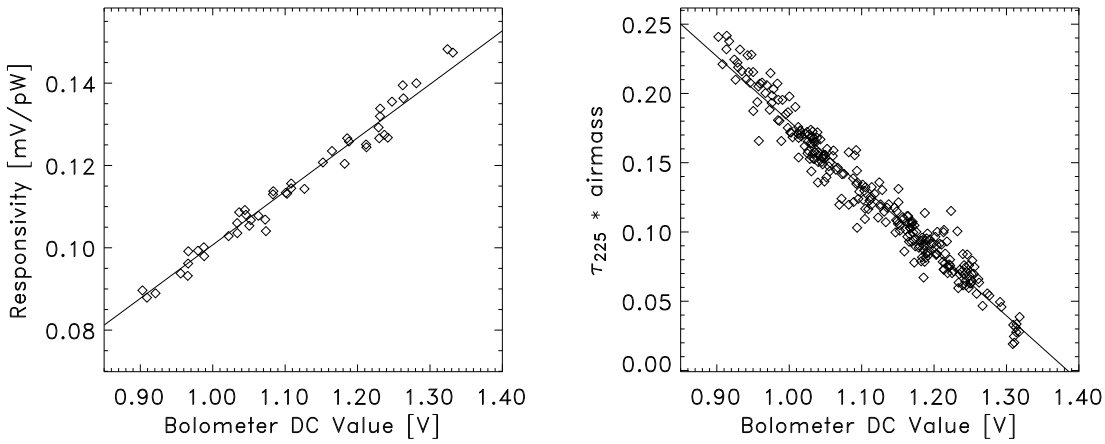

Figure 3.5. AzTEC detector responsivity and opacity calibrations. **Left:** responsivity versus bolometer DC voltage level for an example detector. Responsivity provides the conversion from raw detector voltage to incident power. Responsivity is determined from load curves taken under various atmospheric and optical loading conditions. For the bias setting used, and the range of optical loading experienced, the responsivity is well represented by a linear fit through the data (solid line). **Right:** opacity vs. bolometer DC voltage for the same detector. This relationship is also highly linear over the typical operating range. Figure reproduced from Wilson et al. (2008a).

the array. The detector array and all optics are fixed with respect to the telescope, therefore, the detectors have fixed relative positions in the horizontal Az/El coordinate system (Figure 3.1). Since these observations are typically of a source with a well known and stable flux (e.g. Uranus), these observations also provide absolute calibration of the detectors (i.e. optical power to flux density conversion).

3.3.2.4 Pointing observations

While beam maps provide the relative positions of bolometers in the array, further pointing observations are made throughout the night to measure and monitor the absolute pointing offset between the array and the telescope boresight. These observations are necessary to measure residual errors in the telescope pointing model and any changes in the AzTEC/JCMT coupling. A bolometer near the center of the detector array is chosen as a reference position to which the boresight offset is measured. These observations are ideally of a bright source ($\geq 1\,\mathrm{Jy}$) that is unresolved and located spatially near the science target of interest. A two-dimensional Gaussian is fit to the point-source image, with the best-fit peak locations providing the measurement of the boresight offset. These pointing offsets can change both as a function of time (e.g. thermal flexing) and position on the sky (e.g. gravitation flexing, errors in the motors and gears); therefore, pointing observations are typically made every 1–2 hours and nearby pointing targets are always observed before the first, and after the last, observations of the science target. A continuous pointing correction model is made by interpolating between these measurements in an attempt to account for slow drifts in the boresight offset. The distribution of pointing model offsets is shown in Figure 3.6. Pointing observations were primarily performed using jiggle-map and Lissajous observing strategies at the JCMT and ASTE, respectively.

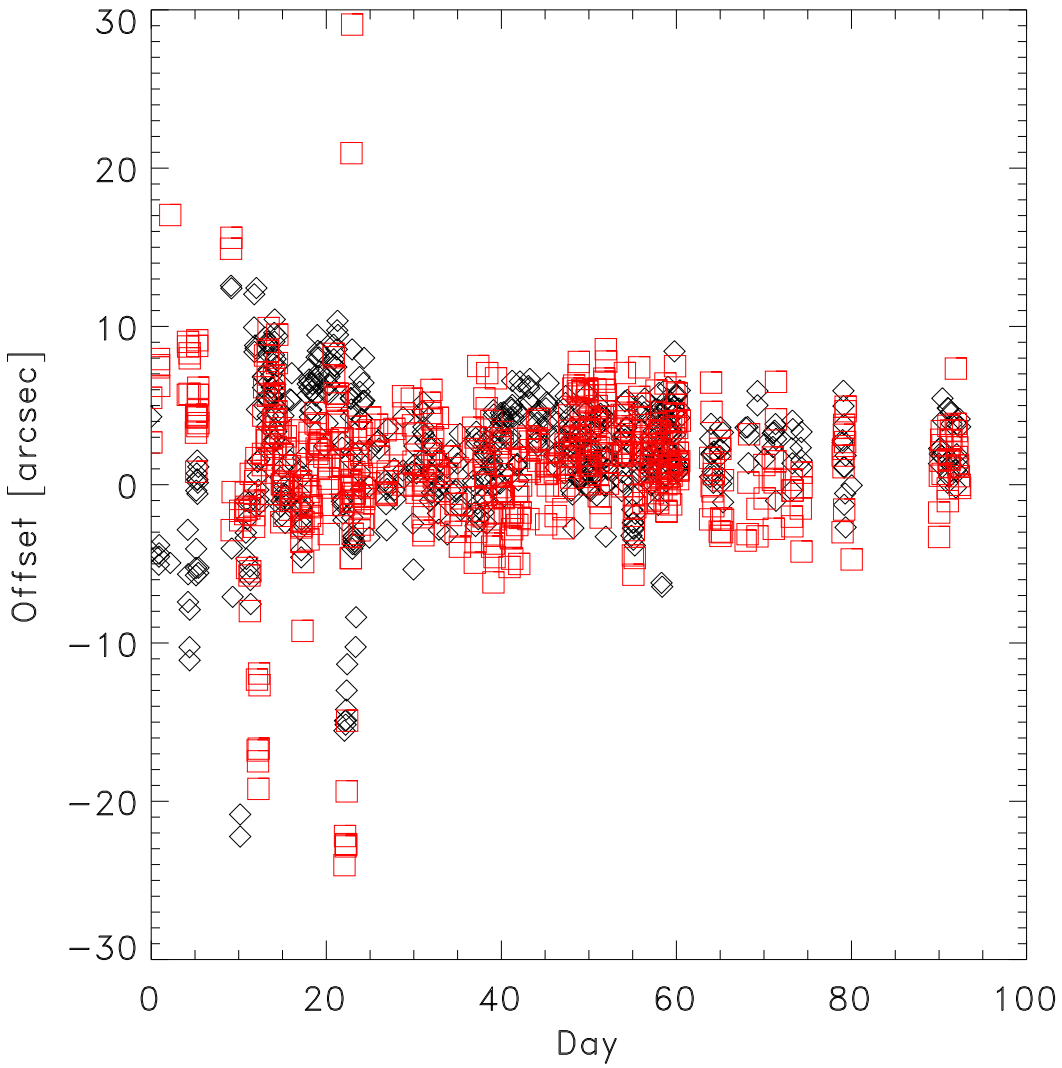

Figure 3.6. Boresight pointing offsets as measured during the JCMT05B observing run. Azimuth offsets are represented as black diamonds and elevation offsets as red squares. Note that these data represent the relative *correction* size and should not be interpreted as actual pointing uncertainty in AzTEC maps (i.e. residuals are much smaller). Each measurement is known to < 1 arcsecond. Time has been normalized to the start of the JCMT05B run. Strong variations in the first month are due, in part, to manual changes to an offset parameter in the actual telescope pointing model. This parameter was no longer changed after day 25.

3.4 Calibration

The output of bolometer i, $b_{i,\alpha}$ (in Volts), at sky position α is given by

$$b_{i,\alpha} = S_i(Q) A_{\rm eff} \eta \int_0^\infty d\nu f(\nu) \int_{\rm sky} d\Omega P_i(\Omega_\alpha - \Omega) e^{-\tau_{\rm eff}} I_\nu(\Omega), \tag{3.5}$$

where $S_i(Q)$ is the responsivity (in V/W), Q is the optical loading (in W) dominated by the telescope and atmosphere, $A_{\rm eff}$ is the effective telescope aperture, η is the optical efficiency, $f(\nu)$ is the peak-normalized AzTEC bandpass, $P_i(\Omega_\alpha - \Omega)$ is the peak-normalized AzTEC beam pattern for bolometer i at sky position Ω_α, $\tau_{\rm eff}$ is the opacity of the atmosphere, and $I_\nu(\Omega)$ is the source intensity on the sky (in $\mathrm{Jy\,beam^{-1}}$). As discussed below and in Figure 3.5, S_i and $\tau_{\rm eff}$, both of which depend on observational conditions (e.g. weather) and change significantly on the time scale of hours, are modeled as functions of the "DC" level of the bolometer signal.

3.4.1 Responsivity and extinction

Variations in atmospheric radiative loading produce non-linearity in the detector's response. Figure 3.5 shows the affect of changing atmospheric loading on bolometer output. Bolometer response to various power loads are calculated from the analysis of nightly load curves (Section 3.3.2.2), where a wide range of incident electrical power loads on the detectors are explored to measure their responsivities (local slope of the thermistor's electrical output as a function of incident power). The bolometer DC voltage level (i.e. fundamental amplitude of the modulated signal) is linearly correlated to the the detector responsivity. A unique linear fit between responsivity and the DC-level is made for each bolometer and this fit is used to convert the bolometer output to power units.

The atmospheric opacity is also linearly correlated to the bolometer DC-level, as shown in the right hand panel of Figure 3.5. At the JCMT, this relationship is calibrated to the 225 GHz opacity measurements of the CSO tau monitor, which records

$\tau_{225\mathrm{GHz}}$ for zenith at the same site as the JCMT. At ASTE, AzTEC similarly uses the on-site ASTE tau meter. Therefore, the measured DC values of each bolometer during an observation simultaneously provide a real-time measure of detector responsivity and atmospheric transmission ($e^{-\tau_{\mathrm{eff}}}$), both of which must be known to maintain proper calibration of the detectors and astronomical signals.

3.4.2 Flux conversion factor

Many of the factors in Equation 3.5 are a function of the combined telescope and instrument optics only, i.e. the effective aperture, AzTEC bandpass, beam pattern, and optical efficiency. In principle, all of these components are constant and their combined effect is sometimes collectively referred to as the flux conversion factor, or FCF (units of $\mathrm{Jy\,beam^{-1}\,W^{-1}}$), defined as

$$\mathrm{FCF}_i = \frac{1}{A_{\mathrm{eff}}\eta \int_0^\infty d\nu\, f(\nu) \int_{sky} d\Omega\, \mathrm{P}_i(\Omega_\alpha - \Omega)}. \tag{3.6}$$

With a known set of FCF_i values, the bolometer output (Equation 3.5) for a point-source at (θ_0,ϕ_0) with average flux density $\bar{I}$ over the observed bandpass can be simplified as

$$b_i(\theta_0, \phi_0) = \frac{S_i(Q)e^{-\tau_{\mathrm{eff}}}\bar{I}}{\mathrm{FCF}_i}. \tag{3.7}$$

An FCF is calculated for each bolometer from high-resolution, high-sensitivity beam maps (Section 3.3.2.3) of bright calibration sources of well-known flux. At the JCMT, all calibration observations were of Uranus. A small flux correction is necessary for Uranus due to its somewhat significant angular extent extent (3–4 arcsec) compared to the AzTEC/JCMT beam (18 arcsec). At the JCMT, there is a statistically significant increase in the FCF for measurements taken within one hour after sunset[3]. This is a possible sign that the telescope surface accuracy and/or instrument

[3]correlation between FCF and time after sunset was also seen for SCUBA at the JCMT (Wouterloot et al., 2004).

coupling to the telescope changes as the telescope cools down during/after sunset. All measurements taken more than one hour after sunset were found to have a constant FCF, as expected. Therefore, all calibration for science observations taken more than 1 hour after sunset use the average of all FCF measures more than 1 hour after sunset. Observations taken within one hour of sunset have their FCF values scaled by a correction factor, f $\equiv$ FCF$_i$/<FCF$_i$ >, that is modeled as a linear function of time, such that

$$\begin{aligned} f &= 1 && \text{if HAS} \geq 1 \\ &= 1 + m \cdot (\text{HAS} - 1) && \text{if HAS} < 1. \end{aligned} \tag{3.8}$$

where HAS is the time after sunset in hours and m is common to all bolometers. A fit of all available JCMT FCF measures to Equation 3.8 results in a value of $-0.115 \pm 0.002\,\mathrm{h}^{-1}$.

3.4.3 Calibration uncertainty

Using the definitions of this section, the calibrated bolometer time-stream signals, $\bar{I}_i(t)$, can be written as

$$\bar{I}_i(t) = \frac{b_i(t) \cdot < \mathrm{FCF}_i > \cdot f}{S_i \cdot e^{-\tau_{\mathrm{eff}}}}. \tag{3.9}$$

The error on the calibrated bolometer signals is equal to the quadrature sum of the uncertainties of all four factors in Equation 3.9 and is typically 6-13% for JCMT05B data. However, it is important to note that most projects produce final co-added maps that are comprised of multiple individual maps that span multiple days and calibrations and are each sampled by multiple bolometers; therefore, any random components of this uncertainty would be lower in a final map. The quoted uncertainty does not include the systematic 5% uncertainty in the flux density of Uranus (Griffin & Orton, 1993).

3.5 Performance Characterization

3.5.1 Optical characteristics

Detector beam parameters (Table 3.1) are characterized through two-dimensional Gaussian fits to high-resolution beam maps (Section 3.3.2.3) of a bright point-like (or known extent) source. When coupled to the JCMT, AzTEC's FWHM beamsize is 17 ± 1 arcsec and 18 ± 1 arcsec in Azimuth and Elevation, respectively, and 30 ± 1 arcsec and 30 ± 2 arcsec at the ASTE telescope, where the quoted uncertainties represent the distribution of beam widths for the entire array. The hexagonal array of detectors is roughly circular with a FOV diameter of ~ 5 (8) arcminutes at the JCMT (ASTE). The AzTEC beams highly are Gaussian down to the first sidelobe response at ~ 20 dB (1%), corresponding to a distance of ~ 1.3 FWHM (i.e. 23 arcsec at the JCMT). Beam maps also provide the relative positions of the bolometers (Figure 3.1). There were 107 operational, stable, and optically active bolometer channels during the JCMT05B observing run. After fixing a few electrical shorts on the detector array and swapping some of the cold JFET amplifiers (Chapter 2), the number of fully operational channels increased to 114 during the 2007 and 2008 ASTE observation runs.

3.5.2 Detector Sensitivity

Even an ideal detector with no intrinsic noise will be limited by the irreducible noise floor caused by photon statistics, or the photon background limit (BLIP). For ground-based (sub-)millimeter experiments, there is typically a large background load of photons from the atmosphere, as well as from the emissivity of the telescope and coupling optics. As shown in Table 2.1, photon noise dominates the intrinsic detector noise sources under typical atmospheric conditions.

The noise equivalent flux density (NEFD) is calculated as a function of temporal frequency by taking the Fourier transform of calibrated detector timestreams during

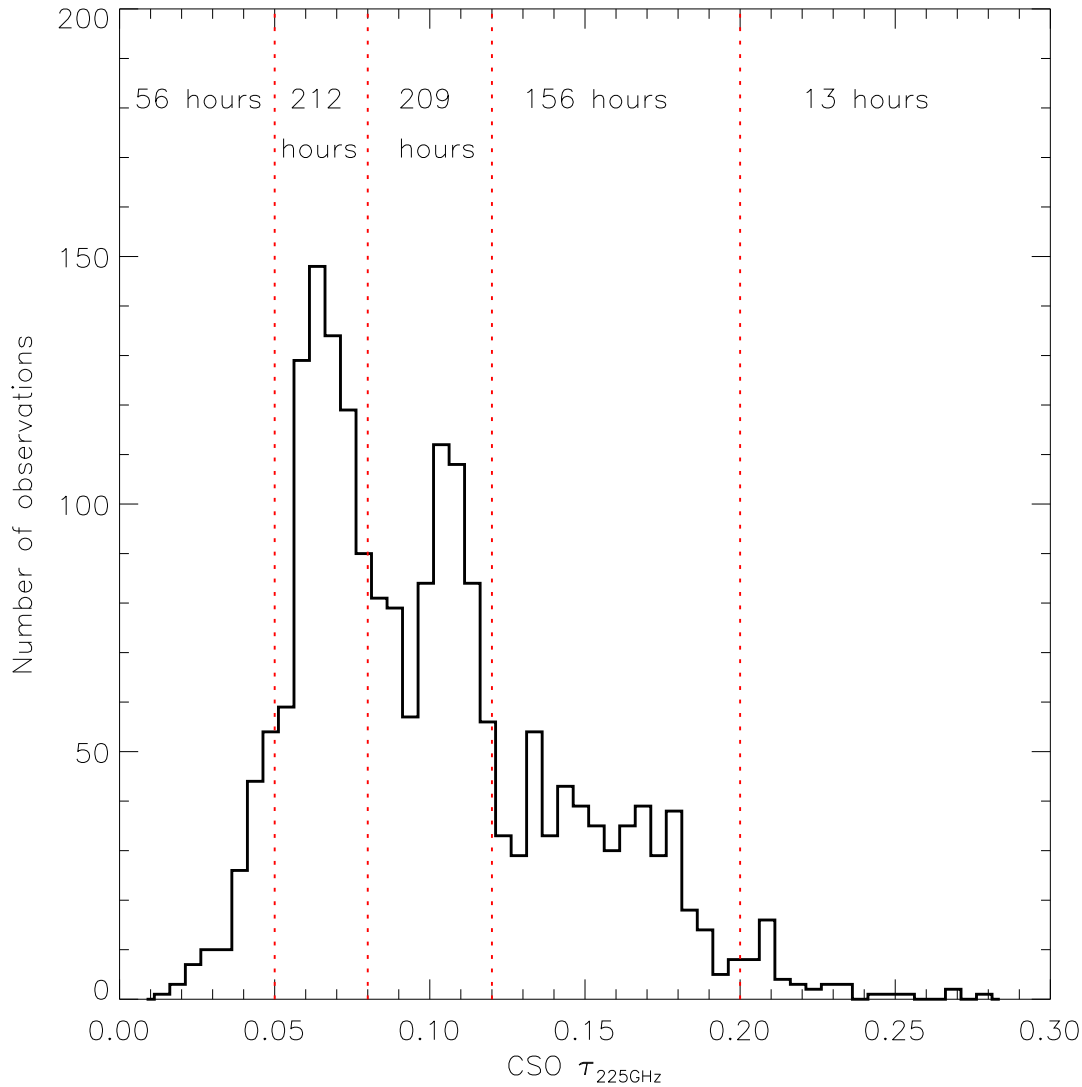

Figure 3.7. Distribution of atmospheric opacity during the JCMT05B observing run. Each sample represents the opacity at zenith during a single observation as measured by the CSO 225 GHz tau meter. The effective opacity of an observation is the zenith opacity multiplied by the number of "atmospheres", or the ratio of the column density at the observation angle to that at zenith. JCMT weather bands are separated by dotted lines and are defined as follows: Grade 1 ($\tau < 0.05$); Grade 2 ($0.05 < \tau < 0.08$); Grade 3 ($0.08 < \tau < 0.12$); Grade 4 ($0.12 < \tau < 0.20$); and Grade 5 ($\tau > 0.2$). Observations differ in duration, typically 5–60 minutes in length. The integrated times of these observations in the various weather bands are printed near the top of the figure.

Table 3.1. Optical Characteristics of AzTEC JCMT05B Observing Run

Optical Feature	Measured Value
Band center frequency	270.5 GHz
Effective bandwidth	49.0 GHz
Effective throughput ($A\Omega\eta$)	$0.2 \pm 0.014\,\mathrm{mm}^2$ sr.
Beam FWHM (azimuth)	$17'' \pm 1''$
Beam FWHM (elevation)	$18'' \pm 1''$

Note. — AzTEC 1.1 mm optical parameters during the JCMT05B observing run. The effective bandwidth is calculated assuming a flat-spectrum source. The effective throughput is calculated as described in Wilson et al. (2008a), and, when assuming a telescope emissivity of $\epsilon = 0.15$ (ratio of effective temperature and true temperature in the Rayleigh-Jeans limit), infers an instrumental optical efficiency of $\eta_{\mathrm{inst}} = 0.19$. The AzTEC 1.1 mm bandpass is discussed further in Chapter 2.

observation (e.g. scanning across) of a blank patch of sky. Figure 3.8 shows the NEFD of a typical detector under three effective atmospheric opacities (0.11, 0.16, and 0.21) that were typical of JCMT05B observations (Figure 3.7). The relatively "flat" noise spectrum at higher frequencies (~ 10 Hz) is attributed to the detector white noise floor (dominated by BLIP noise). A histogram of these idealized sensitivities of all operable detectors during JCMT05B is shown in Figure 3.9. However, fluctuations in the atmospheric emission result in the large signal seen at low frequencies in Figure 3.8, which ultimately limits the achievable detector sensitivities.

Fortunately, much of the atmospheric signal is correlated across portions, or all, of the detector array and can be removed, or "cleaned", from the timestream using various techniques (e.g. principal component analysis, or PCA; see Chapter 4). However, such cleaning typically does not remove all of the low-frequency noise, which remains at a dominant level (thin curves in Figure 3.8). Faster telescope scanning speeds can result in higher sensitivities by pushing the optical bandpass of the detectors to higher frequencies (dotted curve in Figure 3.8); however, the desire to scan quickly must be

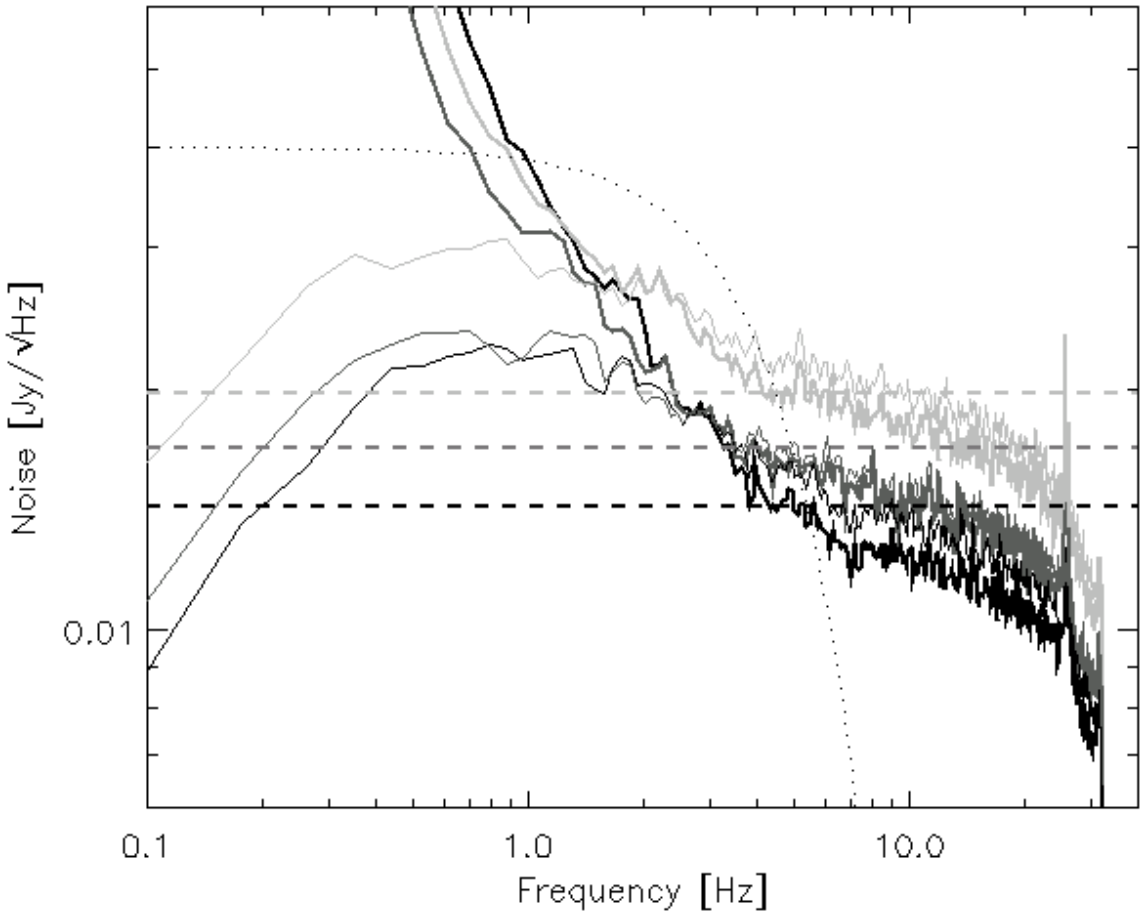

Figure 3.8. Noise Equivalent Flux Density (NEFD) for an average AzTEC bolometer channel under typical weather conditions. Plotted for three different optical loading conditions with effective 225 GHz opacities (τ_{225}) of 0.11, 0.16 and 0.21 represented as the dark, medium, and light shaded curves, respectively. Thick lines represent the raw (pre-cleaning) data, while thinner lines are post-cleaning (using PCA). The cleaned spectra are higher than the raw data at some frequencies due to a flat spectrum re-scaling that corrects for point-source flux attenuation incurred in the cleaning process. Horizontal dash lines represent the predicted NEFD's for a detector with the target physical parameters (Section 2.3), bias level, and estimated optical loading. The relatively high low-frequency NEFD post-cleaning is due to residual atmospheric fluctuations. The dotted curve represents the approximate response of a point source (in arbitrary units) for a linear scan velocity of 180 arcseconds/s and the AzTEC/JCMT FWHM beamsize of 18 arcseconds. Figure reproduced from Wilson et al. (2008a).

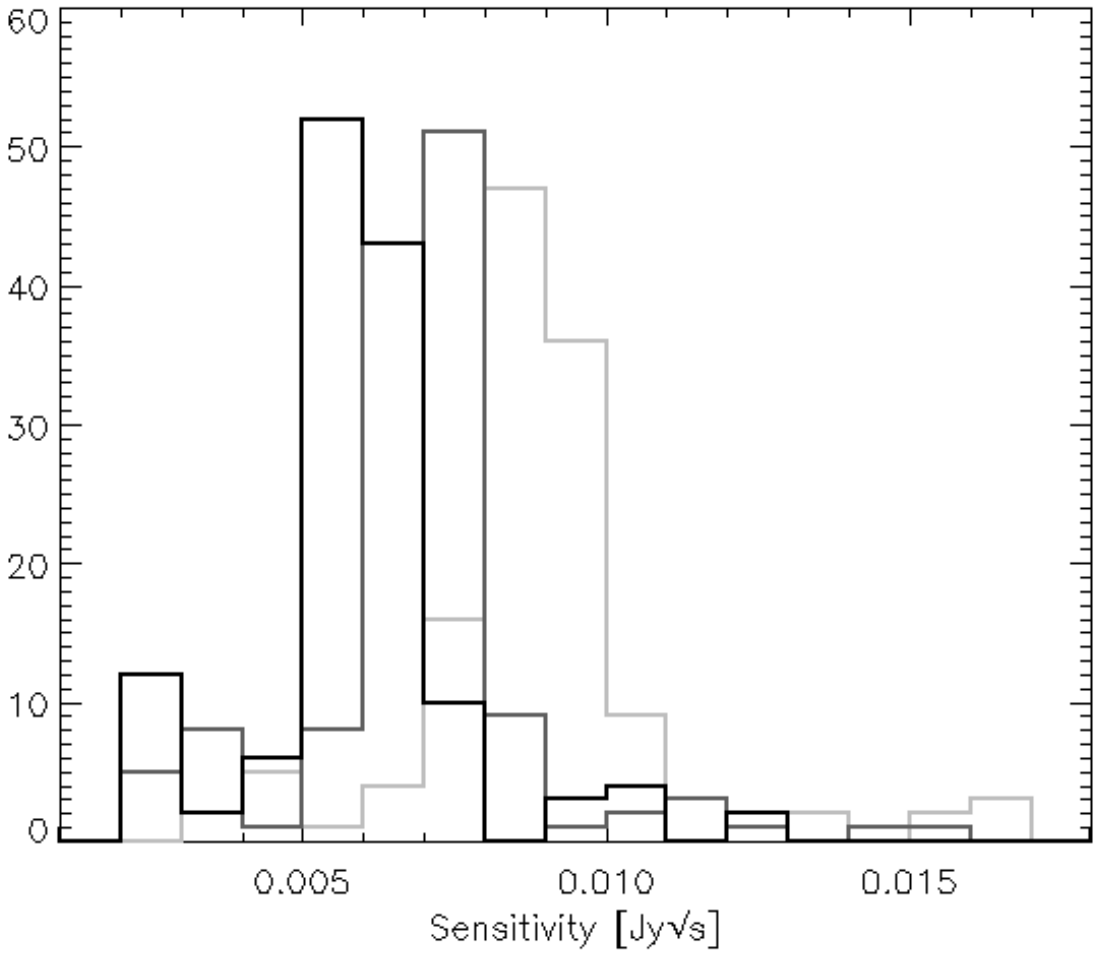

Figure 3.9. Distribution of AzTEC detector sensitivities under typical weather conditions. Histogram values represent the optimum potentially achievable sensitivities of the operational AzTEC detectors for the three opacities listed and described in Figure 3.8. Sensitivities represent the limit in which the low-frequency atmospheric signal can be removed/reduced to the white noise level represented by the relatively flat portion (e.g. $\sim 10\,\mathrm{Hz}$) of the PSDs in Figure 3.8. Plot reproduced from Wilson et al. (2008a).

tempered by considerations of observation efficiency and instrument/telescope limitations (Section 3.3.1.2).

The beginning of the effects of the cutoff frequency of the detector time constant ($f_c \sim 40\,\mathrm{Hz}$) can be seen in the slow rolloff of the NEFD spectra at $\gtrsim 20\,\mathrm{Hz}$. The abrupt cutoff in spectra just before 32 Hz is due to the digital block FIR filter that conditions the signals before 64 Hz decimation (Section 2.5.2). The line at 25 Hz is likely an aliased harmonic of the AC power source ($\sim 60\,\mathrm{Hz}$). Given the optical bandpass of typical scan speeds are at significantly lower frequencies than this noise feature, it has become common to apply an additional low-pass filter in software when performing off-line data reduction and analysis.

3.5.3 Mapping Speeds

The best indicator of future performance and capability for an array receiver is the instrument mapping speed. Mapping speed is a metric that can be summed linearly and simultaneously accounts for the variations in detector sensitivities, the effectiveness of the atmospheric cleaning algorithm, the individual optical efficiencies achieved by each detector, and most importantly, the residual correlations between detectors in the array. The effective mapping speeds for the JCMT raster-scanned maps are calculated as

$$M_{\mathrm{em}} = \frac{N_{\mathrm{det}}\Omega_{\mathrm{pix}}}{t_{\mathrm{int}}} \sum_{i=1}^{N_{\mathrm{pix}}} \frac{1}{\sigma_i^2}, \tag{3.10}$$

where σ_i represents the noise level of the ith pixel in a map with N_{pix} pixels, each of solid angle Ω_{pix}. N_{det} represents the number of functional detectors and t_{int} is the total integration time spent on the map.

Point-source mapping speeds achieved through raster scanning of the JCMT05B observations of large blank fields are plotted in Figure 3.10 as a function of effective opacity, τ_{225}. The best fit second-order polynomial is shown as a solid line and gives parameters such that $\mathrm{MS}(\tau_{225}) = 292\tau_{225}^2 - 206\tau_{225} + 45.9$ (applicable for $\tau_{225} <$

0.35). Most overheads and mapping efficiencies are ignored, making these idealized *point-source* mapping speeds generally applicable to scanned AzTEC maps at any observatory by scaling the mapping speed values by the ratio of the telescope areas[4] (assuming similar telescope efficiencies). Note that for extended (resolved) sources the mapping speed would be lower and does not scale with telescope area.

It is generally favorable to apply a point-source filter *after* the co-addition of multiple raster-scanned maps due to the benefits of cross-linking (Section 4.4.2). To estimate effective mapping speeds of the individual observations presented in Figure 3.10, σ_i values of the resulting map are estimated as the unfiltered pixel noise scaled by the average reduction factor due to the optimum filter when applied to a co-added map.

Mapping speed is correlated to the atmospheric conditions in two ways: atmospheric loading (shot noise) and atmospheric stability. The latter gives rise to residual fluctuations that are inseparable from astronomical signals which leads to much of the scatter in the mapping speeds. The high scatter in mapping speeds at the lowest opacities are in-part due to errors in the estimation of the opacity; however, it may also be indicative of reduced effectiveness of the standard atmospheric cleaning algorithm used and/or fundamentally different noise properties of the atmospheric noise fluctuations under these weather conditions.

Table 3.2 gives the expected and achieved noise performance of the instrument in a manner that allows one to compare ideal and achieved detector sensitivities and mapping speeds in terms of flux-density. In the table, the column of "Projected" sensitivities indicates the sensitivity predicted from the bolometer model and the measured optical loading at the JCMT. The three columns of measured sensitivities

[4]This is because the throughput, $A\Omega$, of a single-moded system is constant, while a true point-source stays fully within the beam. In terms of absorbed power, the instantaneous point-source signal-to-noise scales with telescope area, hence, the detector sensitivity, $\hat{s}$, scales inversely with area.

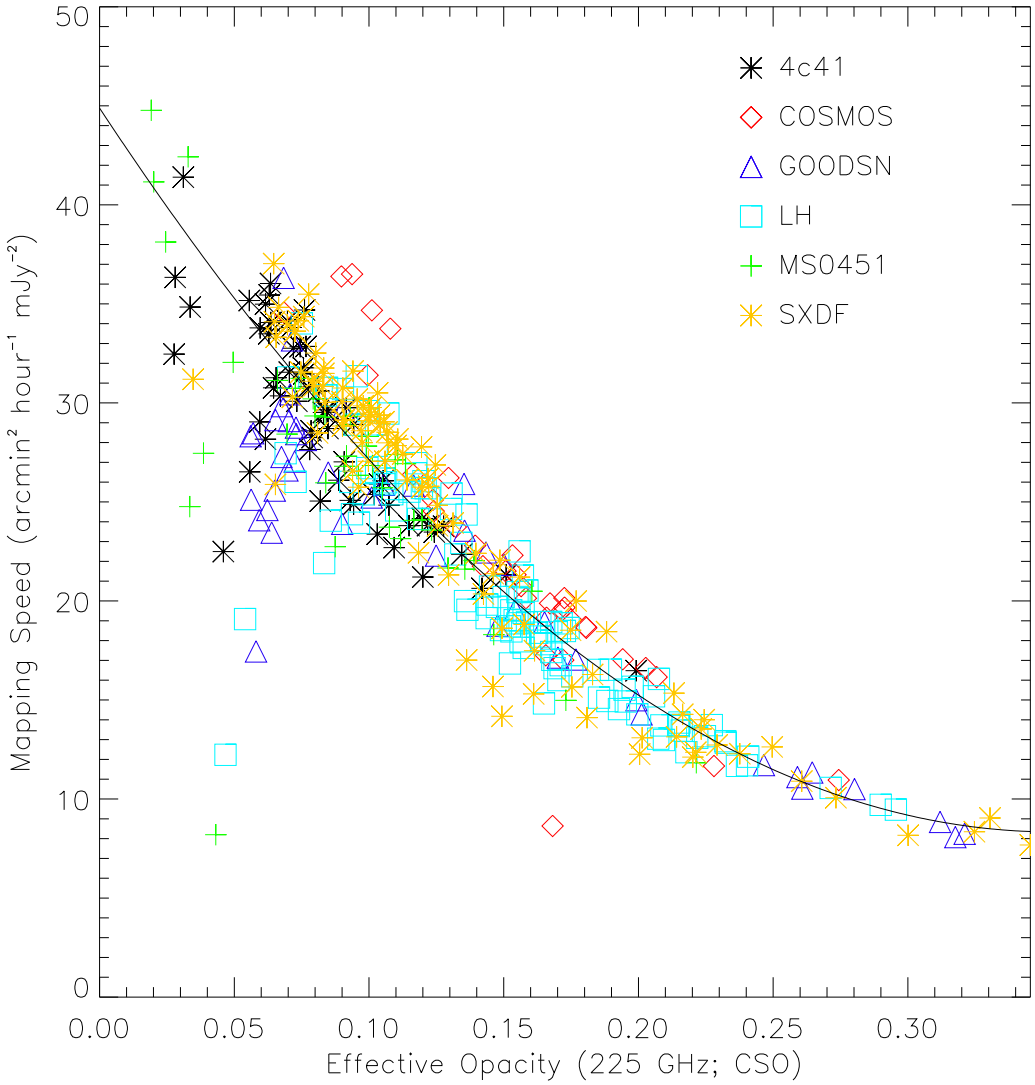

Figure 3.10. Empirical point-source mapping speeds for the AzTEC/JCMT system for a variety of effective atmospheric opacities and using the standard cleaning/mapping software. See Chapter 4 for descriptions of the mapmaking algorithms. These mapping speeds were calculated according to Equation 3.10 and do not include overheads and mapping efficiencies that are specific to the observing strategy employed. The mapping speeds plotted span surveys of various sizes and scanning strategies (speeds, length, spacing). The solid line represents the best fit second-order polynomial, such that MS $= 292\tau_{225}^2 - 206\tau_{225} + 45.9$. Here σ_i is taken as the raw (unfiltered) pixel noise scaled by the average gain due to an optimal point-source filter after co-addition. See text for details.

show the achieved sensitivities in the presence of atmospheric noise in three cases: A) if "perfect" atmospheric noise subtraction were possible as measured by the 10-Hz value of the time stream detector noise of Figure 3.8, B) with the achieved atmospheric noise subtraction indicated by the thinner power spectral density (PSD) curves of Figure 3.8 and the point-source response function (also shown as a dotted curve in that figure), and C) as inferred from empirical mapping speed estimates obtained with Equation 3.10. The following relationship is used between mapping speed and detector sensitivity $\hat{s}$ (in mJy$\sqrt{s}$) to calculate one where the other is known:

$$\mathrm{MS} = \frac{3600 N_{\mathrm{det}} \Omega_b}{2\hat{s}^2} \tag{3.11}$$

where $N_{\mathrm{det}} = 107$ and $\Omega_b = 0.096$ arcminutes^2, the area under a 18″-FWHM 2-d Gaussian, for JCMT05B observations. Equation 3.11 assumes the use of a simple beam smoothing filter on maps. The factor of $2\hat{s}^2$ in the denominator represents the square of $\hat{s}_{\mathrm{sm}}$ ($= \sqrt{2}\hat{s}$), the appropriate sensitivity post smoothing.

The degradation of sensitivity and mapping speed between columns 3 and 4 of Table 3.2 is believed to be due to non-idealities such as residual bolometer-bolometer correlations which are not apparent from the timestream PSDs. It should be emphasized that column 4, or more generally, Figure 3.10, properly scaled by telescope area, is the most accurate reference for planning point-source observations with AzTEC. Note that these mapping speed estimates do not include overheads such as calibration observations (Section 3.3.2) or map inefficiencies (Section 3.3.1). The values given in Table 3.2 are only meant to be illustrative of where the losses in sensitivity occur when beginning projections with raw detector sensitivities.

Table 3.2. Expected and Achieved Noise Performance

	Projected (bolometer model) JCMT (LMT)	Measured (white PSD level) JCMT	Measured (actual PSD) JCMT	Measured (map space) JCMT
Detector Sensitivity ($\mathrm{mJy}\sqrt{s}$)	10.02 (0.9)	8.55	**14.5**	26-28
Mapping Speed ($\mathrm{arcmin}^2\mathrm{mJy}^{-2}\mathrm{hr}^{-1}$)	184 (2013)	253	88	**23-28**

Note. — "Projected" is the (white) timestream PSD prediction based on the bolometer model and optical loading. Values in parentheses are calculated for the LMT by scaling according to telescope area assuming an effective LMT mirror diameter of 43 m as (very conservatively) truncated by AzTEC's Lyot stop. "Measured (white PSD level)" is the noise level measured from calibrated timestream PSDs at 10 Hz from the $\tau_{225} = 0.11$ *thicker* curve of Figure 3.8. "Measured (actual PSD)" is the inferred sensitivity based on the full cleaned time stream PSD of the $\tau_{225} = 0.11$ *thinner* curve of Figure 3.8. The quoted sensitivity is calculated by forming a weighted average of PSD/2, weighted by the square of the point-source response function of figure 3.8, and then taking the square root. "Measured (map space)" is the sensitivity inferred from mapping speeds estimated with Equation 3.10. Values given in bold are directly computed from AzTEC data. All other values are estimated as described in the text. Table also appears in Wilson et al. (2008a).

CHAPTER 4

AZTEC DATA REDUCTION SOFTWARE

4.1 Introduction

A sophisticated custom software package has been developed for reducing sets of raw AzTEC data into coherent maps of astronomical signal. This software is logically broken into dozens of sub-programs, most of which are transparent to the common user. Additional programs are available to provide diagnostics, quick-look maps, source identification, noise characterization, and simulations. The software package is designed to be versatile and general enough that it could be applied (with some initial effort) to data sets from other similar instruments (e.g. millimeter bolometer arrays) that employ similar observing strategies (e.g. scanning, chopping, etc). The entire AzTEC data reduction software package is written in IDL (Interactive Data Language[1]) and is freely available following the instructions listed on the AzTEC website (http://www.astro.umass.edu/aztec/).

In lieu of a full software manual, this chapter provides motivation and theory behind the major steps involved in reducing AzTEC data and defers detailed reference to the thorough descriptive headers included in every official AzTEC program[2]. In this chapter I provide an overview of the most prominent components involved in transforming raw bolometer timestreams to an optimally sensitive astronomical map.

---

[1]http://www.ittvis.com/idl/

[2]To help new users get started, example scripts for the standard reduction of data sets are provided in the software archive or are available from any AzTEC team member listed on the website.

The primary steps of the analysis pipeline are to organize the data, remove correlated noise (i.e. "cleaning"), produce maps of each observation, co-add all maps of the same region, and provide optimal source filtering. The analysis pipeline includes many cleaning and mapping options and algorithms, the choice of which depends primarily on the type of observation and source(s) being observed. The bulk of the programming effort to date has been directed towards the reduction and analysis of point source observations and surveys, motivated largely by the early science goals of the instrument; however, an advanced iterative approach (Section 4.3.2.3) to mapping bright and large-scale sources has been developed, and is still evolving. Finally, I note that an external software package developed for observation planning is described in Appendix B.

4.2 Pre-Processing and Data Standardization

AzTEC data sets typically differ slightly from one observing run to the next. This is particularly true when moving from one telescope to another, where the pointing signals and calibration may be significantly different. In addition, the number of working detectors sometimes changes as modifications are made to various components of the system. Therefore, before reducing a given data set, it must be standardized to the format expected by the rest of the software package. If one were to adapt the AzTEC software package for use with another instrument, the following section describes the critical components that would need careful adaptation to the specifics of that instrument's data configuration.

4.2.1 Data alignment

The first step in almost any data reduction is to properly align and correlate independently derived data sets, which in this case involves aligning bolometer and pointing data. This includes synchronizing the signals in time, determining relative

detector beam positions with respect to the telescope boresight, and correcting for any offsets between the actual and reported telescope pointing.

Bolometer data and telescope pointing signals are generated by independent systems whose electronics and real-time processing can introduce a small constant offset between the two data sets. This offset can be calculated by analyzing bi-directional raster scans across a bright astronomical source (a source should be fixed on the sky, regardless of the direction of the scan). This offset was found to be approximately 0.022 seconds for the JCMT/AzTEC setup and was found to be constant throughout the 3 months of observing. It is also noted that the JCMT pointing signals are updated at 8 Hz, and must be interpolated to 64 Hz to match the AzTEC bolometer data. These correction algorithms are automatically invoked when running any major AzTEC software application and are transparent to the user.

The relative positions of the detectors' beams on the sky are measured through high-resolution beam maps of a bright astronomical source (Section 3.3.2.3). At the JCMT, AzTEC and all of its optics move with the telescope in both azimuth and elevation, so the beam positions remain fixed with respect to each other in the horizontal (Az/El) coordinate system. These beam locations give the relative pointing offsets of each bolometer to a reference detector (e.g. the detector nearest the array center) that has been aligned with the nominal telescope boresight. These offsets are necessary to extract the pointing of all detector signals with respect to the telescope boresight position.

As with any telescope, the pointing accuracy and alignment of the JCMT/AzTEC system changes with time and position of the telescope. Numerous sources can contribute to such changes, such as gravitational and thermal flexing, wear and tear of the motors and gears, tectonic activity, etc. The bulk of the telescope-only related errors are modeled out by the telescope's own pointing model, however, small level residuals inevitably remain. Therefore, regular observations of bright sources with

well known positions that are located near to the science target are necessary to monitor and maintain the pointing accuracy of our observations (see Section 3.3.2.4). In practice, these pointing corrections are automatically applied to every observation in the map-making process (Section 4.4).

A continuous AzTEC pointing model is generated for the entirety of each observing run by interpolating between the entire set of available boresight offset measurements. This pointing model is constructed at the conclusion of every observing run using a separate AzTEC software package that largely automates the selection and mapping of pointing observations and filters out any observations with unusual source properties in the pointing maps (e.g. extended source, low signal-to-noise, unexpectedly large offset). An interactive option allows users to quickly scan through all available pointing maps and select maps that should, or should not, be included in the pointing model. Alternatively, the users can override the default pointing model and provide their own pointing offsets measured for their particular survey.

4.2.2 Calibration

As discussed in Section 3.4, nightly load curve measurements provide a measurement of detector responsivity as a function of the DC value of the bolometer readout. This allows continuous calibrated conversion of raw bolometer readout (in Volts) to incident power (in Watts). Observations of sources with well known flux then provide a measure of the flux conversion factor (FCF), which provides the conversion from power received to astronomical flux units (once corrected for atmospheric extinction). For a given set of coupling optics, and assuming constant optical efficiency of all components, the FCF is constant throughout an entire observing run (see Section 3.4.2 for exceptions). Finally, astronomical fluxes must be corrected for the extinction incurred through absorption by the Earth's atmosphere. As shown in Section 3.4.1, the effective atmospheric opacity, $\tau_{\rm eff}$ is linearly correlated to the overall loading of the

bolometers (DC level of output signal), which provides a continuous measurement of the atmospheric extinction, i.e. transmission = $e^{-\tau_{\rm eff}}$.

All of these corrections and conversions are typically invoked in the mapping stage (Section 4.4) and are fully automated and transparent to the user. Default conversion parameters are provided through parametrization files within the software package and are unique to each observing run. These parameter files also provide flags indicating which bolometer channels were non-functional during each particular run and should be ignored in any further analysis.

4.3 Noise Rejection: "Cleaning" of the Data

AzTEC is used as a differencing radiometer through the various observing modes discussed in Section 3.3.1. Along with signals from astronomical sources, other sources of varying signal can couple to the bolometers as noise. However, in many cases these signals can be separated from the astronomical signal using knowledge of the system and simple assumptions about the source(s) being observed. The AzTEC noise rejection (commonly referred to as "cleaning" the data) software generally works on subsets of data at a time, typically divided into individual scans for raster observations or a user-defined period of time for Lissajous scans (usually 5–10 seconds).

4.3.1 Spike Removal

Before attempting to remove the atmospheric signal, the detector timestreams are cleared of any spikes caused by cosmic ray hits, electronic glitches, or other unidentified sources of sudden changes in detector output. For AzTEC, the number of spike events over the entire array can vary drastically for different observations; from just a few to over 100 in a single hour long observation[3]. These spikes are identi-

[3]When experiencing a large number of spikes, most of the events are confined to just a few bolometers. It is not known what causes these strong variations in the spike event rate.

fied by sudden jumps in the detector signals that are too large and too fast to be of mm-wave astronomical origin, given the detector's continuous Gaussian-like beam and observing strategy (e.g. smoothly scanning across a source). Detector samples around an identified spike are flagged as bad and unused in most other processes, including mapping. The number of flagged samples is scaled by the amplitude and decay time of the spike signal given the detector time constant. To protect processes that demand a continuous data set from being corrupted by the spike, the flagged data samples are replaced by simulated data that are based on the noise properties of the detector and the averaged sky signal as measured by other (non-spike) detectors during the flagged period. To ensure smooth continuity, these simulated fluctuations are added to a linear interpolation between the last good sample before, and the first good sample after, the flagged spike region (see Figure 4.1).

The despiking algorithm searches for potential spikes in a differenced bolometer timestream, i.e. the raw timestream subtracted from the same timestream shifted in time by 1 sample (1/64 seconds). Spikes are defined as a differenced signal that is significantly larger than than the standard deviation of the differenced signal by a user-defined margin (default threshold of 7σ). Spikes are searched for and removed recursively in order to be sensitive to a large dynamic range of spikes, i.e. to keep large spikes from inducing a large sample-to-sample variance that makes smaller spikes fall under the spike detection threshold.

4.3.2 Correlated Noise Removal

Though today's mm-wavelength continuum cameras provide high raw sensitivity and fast mapping speeds, the ultimate sensitivity of any observation from the ground is limited by the stability and opacity of the atmosphere above the telescope. The dominant source of noise is the variable emission from water vapor in the atmosphere, which can be several orders of magnitude brighter than a typical astronomical target.

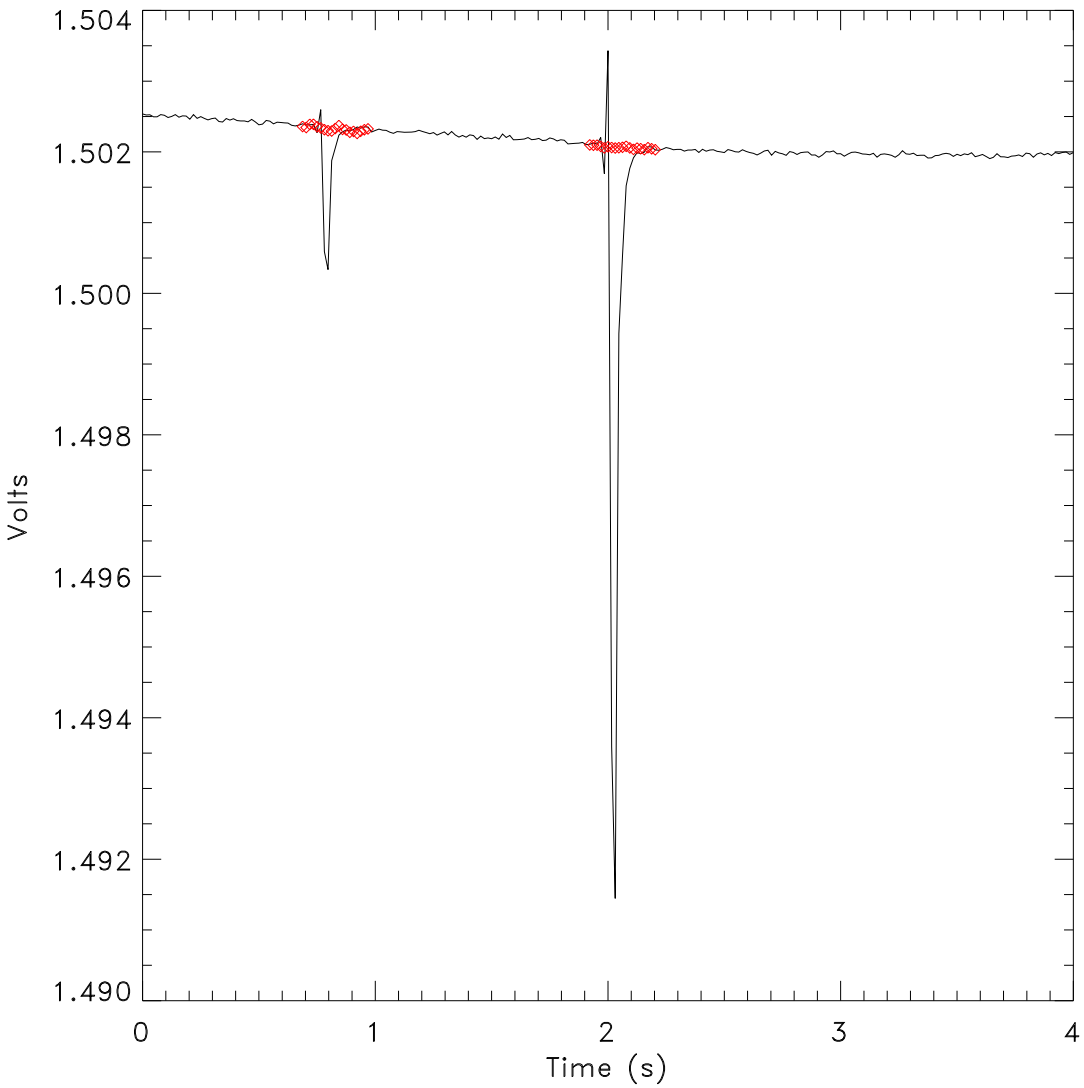

Figure 4.1. AzTEC raw bolometer timestream before and after spike removal. The black curve represents the raw bolometer timestream of a typical detector during spike events. These spikes are identified through the fast signal changes they induce, which are too large and fast to be from a typical astronomical source given the beamsize and scanning speed. Samples that are affected by the spike are replaced with simulated data (red diamonds) that match the bolometer's non-spike noise properties and the atmospheric signal (as measured by other detectors with no spikes) during the event. Although these samples are omitted from the final data set and map, the simulated replacement data is necessary to avoid contamination through any data processing that requires a continuous timestream (e.g. PCA cleaning; Section 4.3.2). Note that a lower raw bolometer voltage represents a *higher* power load.

The atmospheric noise fluctuates both spatially and temporally and generally displays 1/f-like behavior; however, the standard scanning strategies used (Section 3.3.1) allow us to treat the dominant instabilities on a largely temporal basis. The observer's greatest weapons to combat this noise lie in that: (a) the atmospheric signal is correlated across multiple (or all) detectors in the array, as the individual beams largely overlap in the lower atmosphere before separating in the far field; and (b) the atmospheric components are correlated in time, while the astronomical signal being measured is correlated in space. For brevity, this section will assume the data being processed are the results of scan maps only, which was the sole observing strategy of the AzTEC surveys discussed in Chapters 5 & 6.

Two general algorithms have been developed for the removal of correlated atmospheric noise in scan map data: (a) "average subtraction"; and (b) principal component analysis (PCA).

4.3.2.1 Average Subtraction

The first method is to remove the dominant common-mode signal seen by *all* detectors and is referred to as "average subtraction". A model of the atmospheric signal is generated from the sensitivity-weighted, and gain scaled, average of the detector array at each sample (1/64 of a second). To prevent bright astronomical sources or unidentified spikes from skewing the array average, significant outlier samples are masked from the model calculations using a user defined threshold (e.g. 4σ). The model is subtracted from each of the bolometer timestreams, scaled by their respective gains and correlations to the atmospheric model. This procedure is successful at removing signal from atmospheric fluctuations common to all the bolometers; however, any signals on scales significantly smaller than, or varying across, the full array size (FOV$\sim$ 5 arcmin) will largely remain. The average subtraction algorithm is the preferred method for bright source beam map measurements, as it generally results in

the least amount of distortion in source shape and amplitude compared to other more aggressive methods. This method is typically applied recursively – high S/N signal in the post-cleaning map is subtracted from the raw timestreams and the process is repeated until the result converges (similar to that described in Section 4.3.2.3) – in order to ensure an accurate representation of the beam response.

4.3.2.2 Principal component analysis (PCA)

The second algorithm takes a more statistical approach by identifying and removing correlated noise through the method known as Principal Component Analysis (PCA). PCA is also sometimes referred to as the Karhunen-Love transform (KLT) or the Hotelling transform. PCA linearly transforms the data onto a new coordinate system where the variance is maximized in each principal coordinate, or component, in ranked order. This is accomplished through Eigen decomposition of the covariance matrix of the bolometer data set, which provides the eigenvectors and eigenvalues of the covariance matrix. These eigenvectors are orthogonal and, in an ideal sense, each represents a different source of signal/noise, although these components may not have truly identifiable and independent sources in a real and physical sense. When transformed to the new basis set, the covariance matrix is diagonal and simply consists of the eigenvalues. The eigenvalues are directly proportional to the amount of total variance their respective eigenvectors are responsible for in the data set as a whole. Assuming some of the components can be identified as noise (or some other undesirable signal), they can be separated and removed from the data set by zeroing the respective eigenvectors before re-projecting the data back to the original bolometer timestream basis set. This reduces the variance of the data set and, assuming the desired astronomical signal is orthogonal to the removed eigenvectors and is relatively unaffected, increases the S/N of the desired measurement.

In practice, most scientific observations are of relatively dim astronomical sources (e.g. $\ll 1\,\mathrm{Jy}$) whose signal is very small compared to the powerful fluctuations in atmospheric emission. For AzTEC data, this means the atmospheric signal is typically responsible for the largest eigenvalues upon decomposition of the covariance matrix, as it is both powerful and correlated across much of the array. This important feature is enhanced further, in general, for point source observations, as the detector spacing of the AzTEC array ($1.4f\lambda$) results in a point source being seen by very few detectors at any given time, i.e. there is very little correlation of source signal across array. Therefore, when using PCA to reduce AzTEC data, it is common to remove (i.e. zero) the eigenvectors associated with the largest eigenvalues before projecting back to the original bolometer timestreams.

Deciding which, and how many, PCA components to remove depends on both the source and noise properties of the data set. Empirically, it is found that the log of the eigenvalues are roughly Gaussian in distribution, with a few large outliers representing strong correlated signal, while dim astronomical signal is typically associated with the lower Gaussian-like eigenvalues. Given these general relations, the AzTEC PCA software adaptively determines the number of eigenvectors to remove based on a user-supplied threshold that cuts out any eigenvalues that are above this threshold. This threshold is defined as an eigenvalue upper limit in units of standard deviations, which is adaptive in that the number of offending components depends on the overall distribution of eigenvalues. This selection process is run iteratively in order to prevent large eigenvalue outliers from skewing the standard deviation of the value set. This selection process is exemplified in Figure 4.2. For sub-millimeter galaxy (SMG) surveys (e.g. Chapters 5–6), where the source fluxes are very small (typically $<10\,\mathrm{mJy}$), an aggressively small "cut" threshold of 2.5σ is used.

The appropriate PCA threshold cut to use depends on the size and brightness of the source, but generally results in maps at a much lower noise level than when

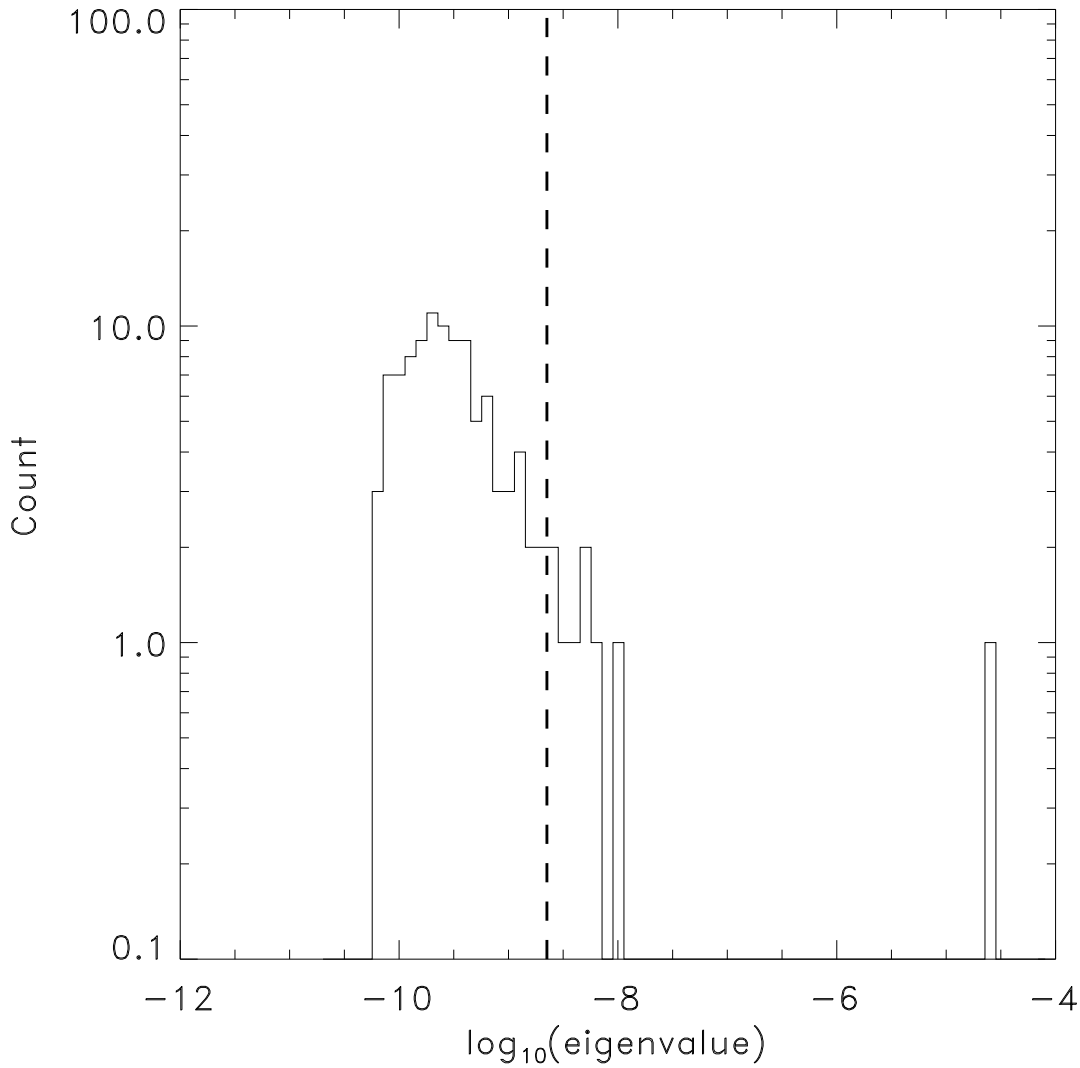

Figure 4.2. The distribution of eigenvalues for the covariance matrix of a typical AzTEC raster scan. In practice, strong positive outliers are identified as the "principal" components of correlated noise. Outliers are identified as those that are $\geq n\sigma$ the average eigenvalue, where n is user defined. The culling of outliers is done adaptively, with the mean and standard deviation re-calculated after the removal of any eigenvalues. This is repeated until no more components are removed. For data sets where astronomical sources are expected to be very dim (i.e. far below the raw noise level of a single scan), an aggressively low value of n can be chosen (typically $n = 2.5$ for AzTEC SMG surveys) without significantly affecting the source shape or amplitude. An adaptive $n = 2.5$ threshold is depicted as the vertical dashed line.

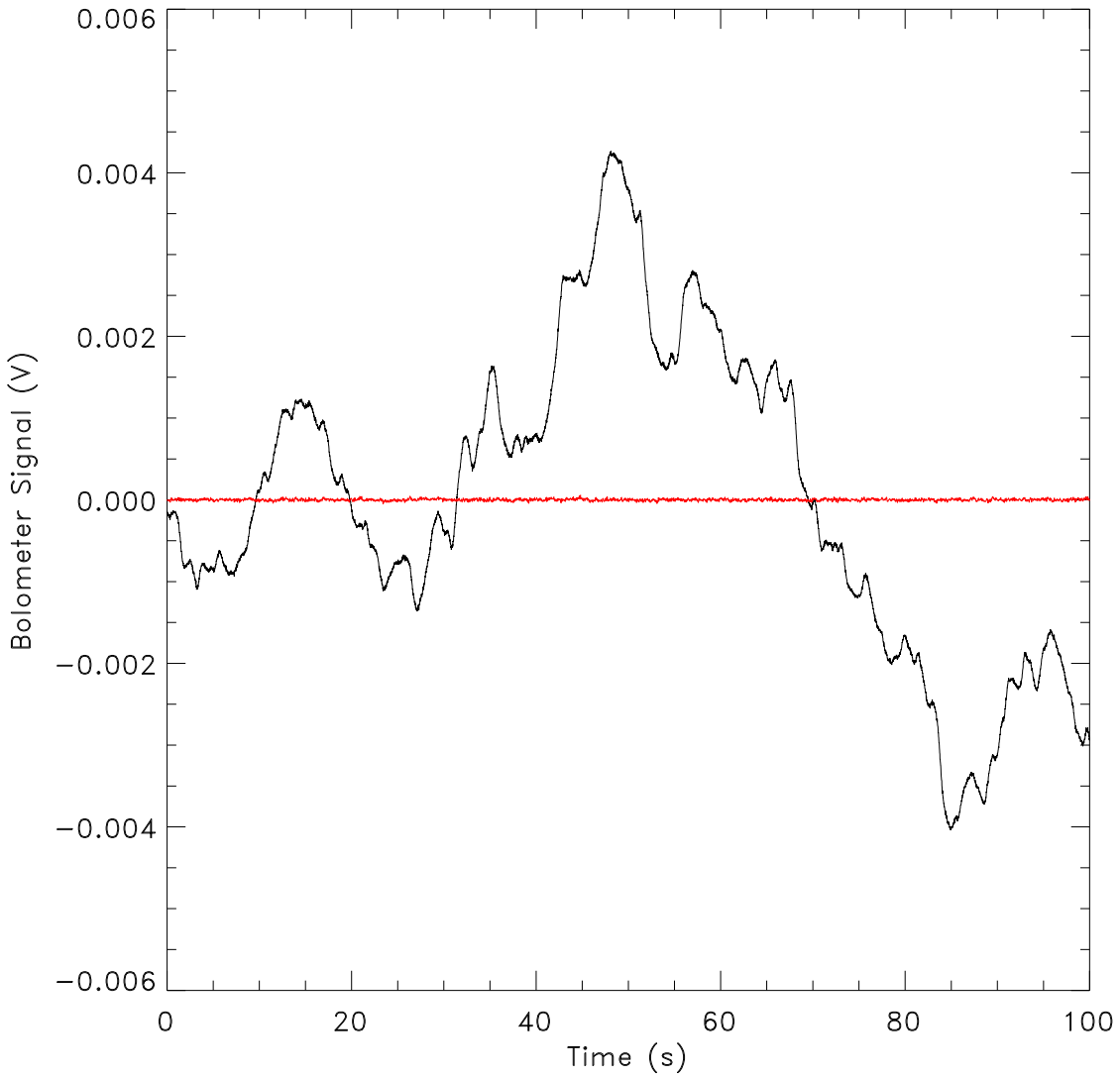

Figure 4.3. AzTEC timestream data before and after correlated noise removal. The mean-subtracted raw timestream of a typcial bolometer during a standard Lissajous scanning pattern at the ASTE telescope is plotted in black. This is compared to the same bolometer signal after the application of aggressive $n = 2.5$ PCA cleaning (red). The large fluctuations in the raw timestream are all due to changes in the absorbed atmospheric emission (some of the signals are induced by the elevation component of the scanning strategy). This atmospheric signal is heavily correlated across the array and easily identified and removed by the PCA algorithm.

cleaned with the average subtraction technique. For bright and/or extended astronomical sources, overly aggressive application of PCA techniques can cause severe flux attenuation and distortion in the source shape by projecting out eigenvectors that contain some source signal. Therefore, PCA is most generally applicable to observations of faint sources, where the signal is significantly buried in the noise of a single scan or observation. However, even faint sources are unlikely to be completely orthogonal to the removed eigenvectors, thus some level of source attenuation happens whenever using PCA. When the astronomical source shape is known (i.e. point sources), this attenuation and shape distortion can be accounted for through simulation (Section 4.5.2). Projecting a noiseless simulated source onto the same basis set as the cleaned data can generate a 'source kernel', with which the effects of each application of PCA can be recorded and corrected for.

In practice, the PCA algorithm is applied to a subset of data (e.g. a single scan) as follows:

1. Calculate the covariance matrix ($N_{\text{bolo}} \times N_{\text{bolo}}$) of the data (sub-)set ($N_{\text{bolo}} \times N_{\text{samples}}$).

2. Calculate eigenvalues (N_{bolo} vector) and eigenvectors ($N_{\text{bolo}} \times N_{\text{bolo}}$) of covariance matrix

3. Identify "undesired" components (e.g. largest eigenvalues if atmosphere dominated)

4. Project bolometer data (sub-)set onto the full eigen basis set, i.e. $\mathbf{F} = \mathbf{B}\mathbf{V}^{\mathrm{T}}$, where $\mathbf{B}$ is the original data (sub-)set, $\mathbf{V}^{\mathrm{T}}$ is the transpose of the eigenvector matrix such that $\mathbf{V}^{\mathrm{T}} = \mathbf{V}^{-\mathbf{1}}$ due to orthogonality of $\mathbf{V}$, and $\mathbf{F}$ is the projected data set.

5. Set all values along undesired components to zero

6. Project data (sub-)set back onto original basis set using eigenvector matrix, i.e. $\mathbf{B}_{\text{new}} = \mathbf{FV}$

4.3.2.3 Iterative techniques for extended sources

Bright and/or extended sources can work their way into the correlated noise model and consequently be significantly attenuated and/or distorted when that model is subtracted from the bolometer time streams. This attenuation and distortion generally cannot be modeled through simulation if the flux distribution is unknown (i.e. most extended sources) or is explicitly being measured (i.e. beam maps); therefore, a new approach to mitigating such artifacts is required. This is accomplished through iteration of the full cleaning and map-making (Section 4.4) processes. That is, significant detections of flux in the initial (potentially attenuated and distorted) map is translated back to bolometer timestream signals and subtracted from the raw data, i.e. the source model is subtracted from the initial data set. The data streams are then cleaned and mapped again. Any significant detections in the second map is added to the first map's source model and the summed model is subtracted from the *initial*, i.e. raw, bolometer timestreams. This process is repeated until the result converges to a model-subtracted map that is consistent with pure noise. Any induced artifacts of the cleaning process (for example, negative lobes near a bright source) are automatically compensated for by the inverse effect of subtracting non-real features in the timestream (e.g. subtracting negative flux from the raw data will correspond to positive flux in the resulting map, thus canceling the false negative in the previous incarnation of the source model).

This iterative technique is currently referred to as flux recovery using iterative techniques, or FRUIT. When applied to fully simulated data sets of a bright and geometrically complicated source, FRUIT proves to be exceptionally robust in recovering both source amplitude and shape. Since the surveys of this dissertation (Chapters 5–

6) consist solely of point-source surveys, a full description of the FRUIT algorithm is deferred to a more relevant publication.

4.4 Mapping

4.4.1 Individual Observations

Individual maps are made using the cleaned detector signals and associated pointing data of each bolometer. The data is weighted (and error estimated) by each bolometer's sensitivity, as calculated from the detector's PSD[4] during the observation or sub-sets of the data (e.g. each scan). This data is then binned in the desired coordinate system and resolution. The binned data is co-added using the sensitivity weights (i.e. a simple weighted mean calculation) to produce a single map for each observation. These weights are also binned and summed to produce effective coverage (integration time) and measurement error maps.

In practice, this is typically the analysis step where fine pointing corrections (Section 3.3.2.4) are applied and the bolometer signals are calibrated to flux units (Section 3.4), although corrections can be applied earlier, if desired. For example, pre-cleaning application of these steps could be potentially beneficial if a cleaning algorithm was implemented that was spatially dependent or more accurate if using fully calibrated bolometer signals. However, current AzTEC cleaning algorithms (Section 4.3) do not incorporate spatial relations and are relatively insensitive to absolute calibration (current algorithms automatically adapt to an array of detectors with different gains).

[4]For observations that include very bright source(s) that can significantly affect the RMS of the bolometer signal over the scales being considered (e.g. scan or whole observation), it is better to use the default relative bolometer sensitivities determined from that nights beam map observations, which will prevent estimation of spuriously high uncertainties for data containing the source.

4.4.2 Co-addition and optimal filtering

Most projects consist of many individual observations/maps, either because of the necessary integration time to beat down the noise, or the sheer size of the survey field dictates that the region is observed in pieces, i.e. a mosaic. In such cases, the individual maps are populated on the same underlying grid, defined through a common tangent point to which all data is projected on to a square grid of user-defined resolution. Having each map on a common pre-defined grid helps preserve pointing resolution when the maps are co-added, which is calculated as a simple weighted average of overlapping pixels. To avoid significant smoothing of the signal, all maps should be created with small pixel sizes, typically 1/6 of the beamsize (e.g. 3 arcsec for AzTEC at the JCMT), or smaller.

At this point, as pixels are made smaller, the pixel-to-pixel noise increases as less and less data falls into each pixel, or bin. Noise at such high spatial frequencies is clearly not of astronomical origin if it is on scales much smaller than the beamsize (18 arcsec at JCMT). Therefore, the map can be low-pass filtered in the spatial Fourier domain to remove the high-frequency noise while preserving the true astronomical signal. This can be performed by convolving the map with the true beam response of the instrument, which is traced as described in Section 4.5.2. This effectively "beam smoothes" the map and is appropriate for all kinds of maps (point or extended sources).

Additional filtering of the image to enhance astronomical signal can be performed based on detailed knowledge of the spatial noise properties in the map, as determined from the noise-only map realizations described in Section 4.5.1. The power spectral density (PSD) of the noise-only maps typically exhibit enhanced noise at low spatial frequencies (i.e. large scales). These long-wavelength modes are de-weighted in the map by defining a high-pass filter whose response is the inverse of the square root of the average PSD of the noise-only map realizations. Application of such a filter

to the survey map flattens, or "whitens", the noise power spectrum with frequency. Since this filter applies varied weights to different spatial scales, it can significantly affect the appearance of sources in the image in the presence of noise (a concern most relevant to extended source maps). For point source surveys, this whitening filter is also applied to the point source kernel (Section 4.5.2) which tracks the combined effects of all cleaning (e.g. PCA) and filtering processes on a point source in the map. The attenuation as measured by the point source kernel is then used to rescale the *entire* map, thus fully restoring the flux of point sources in the map while scaling the uncertainty of the measurement appropriately.

Together, these two components represent what is often referred to as an optimal filter[5]. The application of this filter to the signal map is mathematically equivalent to fitting a whitened version of the true point-source response to the center of every pixel in a whitened version of the map (Scott et al., 2008). As with fitting, it is important for the convolutions of the filters to account for the various uncertainties of the pixels involved, which may be non-uniform. Accounting for such non-uniformities is important both for arriving at the truly best fit amplitude and the propagation of uncertainty for every pixel. Proper accounting also allows for arbitrarily small pixel sizes when mapping. Past surveys (e.g. Laurent et al., 2005; Coppin et al., 2006) instead relied on a compromise pixel size that would be both small enough to avoid significant smoothing of flux over the finite pixel width and large enough to ensure roughly uniform coverage across all pixels. With full propagation and accounting of all weights, the pixel size can be as small as practical considerations (e.g. computation time) will allow.

[5]Sometimes loosely referred to as a Wiener filter, although wiener filters don't necessarily include explicit knowledge of the source response, which can be known to high precision for observations of point sources

4.5 Normalization and Simulation

4.5.1 Noise Characterization

Noise-only maps are generated from the actual data set through the process of jackknifing – randomly multiplying subsets of the bolometer timestreams by either $+1$ or -1. These data subsets must be chosen to be: (a) large enough to preserve all relevant noise scales; and (b) short enough to ensure a large number of subsets such that every pixel has a statistically large number of $+1$ and -1 multiplied samples. To the extent that these concerns are true, the resulting map is devoid of astronomical signal (due to the positive-definite nature of that signal), while preserving the noise properties (inherently positive and negative) of the full signal map. These noise-only maps are generated for every observation and can be co-added and filtered in the same manner as the signal maps (Section 4.4.2) in order to produce a direct noise-only analog of the final signal map.

In practice, the AzTEC data is jackknifed on the same data lengths used for cleaning (e.g. a single scan for JCMT raster observations). The random $+1$ and -1 are also randomly chosen for each individual bolometer, which further improves the statistics by increasing the total number of subsets with a randomized sign. To fully explore probability space for noise in the signal map, many realizations of the noise-only maps are created, both at the individual and fully co-added map scale. It has become standard practice to produce at least 100 fully co-added noise only maps for any given AzTEC survey.

A collection of a large number of fully co-added noise-only map realizations has many uses, including: defining the noise PSD used in creating the optimal filter of Section 4.4.2, ultimate normalization of the uncertainties in the signal map, and a testbed for various simulations. These noise maps are critical to the detailed simulations and statistical analyses of Chapters 5–6.

4.5.2 Point source response

Point sources are unique in that their beam response is known *a priori* and to high precision from beam map observations (Section 3.3.2.3). As alluded to in the previous sections, this allows for the careful tracking of the various effects (e.g. attenuation and distortion) inflicted upon such sources by the various data processing algorithms, most notably the cleaning (Section 4.3) and filtering (Section 4.4.2) steps. This is accomplished by starting with a *noiseless* model of the beam response before processing. This model is taken as a two-dimensional Gaussian matching the average detector beam characteristics. This model is then sent through the same cleaning, mapping, and filtering algorithms using the exact parameters applied to the real data set. The end result is what is referred to as the "point source kernel", which accurately represents the shape of a point source in the processed signal map.

The point source kernel is typically calculated for the center of the map. The actual kernel at any given location in the map may differ very slightly than that of the middle, as any given location is sampled by the array from a unique collection of scan angles (a function of the observing strategy used), which results in a unique collection of low-level scan-synchronous and cleaning artifacts. Therefore, the source kernel is rotationally symmetrized to provide an average kernel shape that is appropriate throughout the entire map. Variation across the map is no more than a few percent, which is relatively insignificant compared to the instantaneous uncertainty in calibration (Section 3.4) and the low S/N measurements of typical mm-wave point source surveys. As with the noise-only maps, accurate representation of the point source kernel is a critical component of the simulations used for statistical population analyses in Chapters 5–6.

4.6 Conclusions

In summary, a sophisticated and fully self-contained data reduction pipeline has been created specifically for the production of astronomical maps from raw AzTEC data sets; however, most components are general enough to be broadly applied to any instrument that produces similar timestream-based data sets, uses similar scanning-type strategies, and has similarly well-behaved noise properties. The various algorithms have been thoroughly vetted through tireless simulation and prove to be self-consistent through iteration. The current software package is both stable and robust, thus allowing third party users to create maps from raw AzTEC data sets with limited familiarity and knowledge of the data structure and software characteristics.

CHAPTER 5

SMG OVER-DENSITY AND CORRELATIONS WITH LARGE-SCALE STRUCTURE IN THE AZTEC/COSMOS FIELD

5.1 Introduction

Foreground structure, cosmic variance, and source environment can affect the observer's perception and interpretation of the source population being probed in a particular survey. For example, gravitational lensing by massive foreground clusters affects both the observed flux of sources and the areal coverage of the survey in the source plane. These aspects of gravitational lensing have been utilized to probe the very faint sub-millimeter galaxy (SMG) population below the confusion limit imposed by the high density of faint SMGs relative to the survey beam size (e.g. Smail et al., 1997; Chapman et al., 2002a; Cowie et al., 2002; Smail et al., 2002; Knudsen et al., 2006; Wilson et al., 2008b). The measured (sub)millimeter fluxes of sources found in the direction of very massive clusters can also be affected by, and confused with, the signal imposed through the Sunyaev-Zel'dovich effect on the cosmic microwave background (e.g. Wilson et al., 2008b). Furthermore, surveys can be affected by foreground structures with high galaxy-densities, which increase the likelihood of galaxy-galaxy lensing by intervening galaxies and complicate counterpart identification at other wavelengths (Chapman et al., 2002b; Dunlop et al., 2004).

Spectroscopic observations have shown that the vast majority of SMGs with detectable radio counterparts lie at an average redshift of $z \sim 2.2$ (Chapman et al., 2005), while spectroscopic (Valiante et al., 2007) and photometric (e.g. Younger et al., 2007) analysis put many radio-faint SMGs at even higher redshifts. The average

SMG is unlikely to be found at $z \lesssim 1$, however it remains to be seen if the $z \sim 1$ SMG population can be locally enhanced due to large-scale structure and cosmic variance. Some evidence exists for increased number densities of SMGs in mass-biased regions of the $z \gtrsim 1$ Universe. Surveys towards several $z \sim 1$ clusters (Best, 2002; Webb et al., 2005) find a number density of SMGs in excess of the blank-field counts that can not be explained by gravitational lensing alone. This implies that some of the SMGs are physically associated with the clusters, although the number statistics are small and the lensing could be underestimated (Webb et al., 2005). Similar over-densities have been found towards high-redshift radio galaxies (Stevens et al., 2003; De Breuck et al., 2004; Greve et al., 2007) and $z > 5$ quasars (Priddey et al., 2008), where lensing of background sources is less likely to be an issue. Spectroscopic observations have also found common redshifts amongst SMGs in the SSA22 and HDF fields, suggesting physical over-densities of SMGs at redshifts of 3.1 and 2.0, respectively (Chapman et al., 2005). Together, these surveys suggest that these massive dusty starbursts are prominent in moderate and high-redshift cluster/proto-cluster environments.

In this paper, we analyze the density and distribution of SMGs in the AzTEC/-COSMOS survey (Scott et al., 2008). The AzTEC/COSMOS survey covers a region within the COSMOS field (Scoville et al., 2007a) known to contain a high density of optical-IR galaxies and prominent large-scale structure at $z \lesssim 1.1$ (Scoville et al., 2007b), including a massive $M \sim 10^{15} M_{\odot}$ cluster at $z \approx 0.73$ (Guzzo et al., 2007). In § 5.2 we present the 1.1 mm source counts for the AzTEC/COSMOS field, revealing a strong over-density of bright SMGs compared to the blank-field. We explore the nature of this over-density through examination of the spatial correlation between SMGs and the known large-scale structures (§ 5.3). Positive correlation between SMG positions and low-redshift large-scale structure has been previously detected statistically in 3 disjoint SCUBA surveys (Almaini et al., 2003, 2005). We now present a wide-field investigation of such correlations using the AzTEC/COSMOS

survey, which has advantages in its contiguous size (0.15 deg^2), broad range of low-redshift environments, and the availability of deep multiband imaging and reliable photometric redshifts (Ilbert et al., 2009).

This is the second paper describing the 1.1 mm results of the AzTEC/COSMOS survey. Paper I (Scott et al., 2008) presented the data-reduction algorithms, AzTEC/COSMOS map and source catalog, and confirmation of robustness of the AzTEC/JCMT data and pointing. Additionally, seven of the brightest AzTEC/-COSMOS sources have had high-resolution follow-up imaging at 890 μm using the Sub-Millimeter Array (SMA) and are discussed in detail in Younger et al. (2007). Spitzer IRAC colors of these SMGs, and others, are discussed in Yun et al. (2008).

5.2 Number counts in the COSMOS field

The number density of SMGs provides constraints on galaxy evolution models (e.g. Kaviani et al., 2003; Granato et al., 2004; Baugh et al., 2005; Negrello et al., 2007) and insights to the dust-obscured component of star formation in the high-redshift Universe. The number density also describes how these discrete objects contribute to the cosmic infrared background (CIB), as discussed in Paper I. In this paper, we focus on how the localized SMG number counts reflect large-scale structure. Before presenting the number counts for the AzTEC/COSMOS survey (§ 5.2.3 & § 5.2.5), we describe the technical details of the flux corrections (§ 5.2.1) and methods (§ 5.2.2) that are vital to the construction of unbiased source counts from typical SMG surveys. Here we expand on the flux correction techniques of Coppin et al. (2006) and provide new tests of these methods through simulation.

5.2.1 Flux Corrections

Surveys of source populations whose numbers decline with increasing flux result in blind detections that are biased systematically high in flux. This bias is typically

referred to as "flux boosting" and results from the fact that detected sources have a higher probability of being an intrinsically dim source (numerous) coincident with a positive noise fluctuation than being a relatively bright source (scarce) coincident with negative noise. This effect is concisely described in Hogg & Turner (1998) and is extremely important for SMG surveys (see Figure 5.1) due to the relatively low S/N of the measurements and a population that is known to decline steeply with increasing flux (e.g. Scott et al., 2006; Coppin et al., 2006, and references therein).

We calculate an intrinsic flux probability distribution for each potential AzTEC source using the Bayesian techniques outlined in Paper I and Coppin et al. (2005, 2006). The probability of a source having intrinsic flux S_i when discovered in a blind survey with measured flux $S_m \pm \sigma_m$ is approximated as

$$p(S_i|S_m, \sigma_m) = \frac{p(S_i)p(S_m, \sigma_m|S_i)}{p(S_m, \sigma_m)} \tag{5.1}$$

where $p(S_i)$ is the assumed prior distribution of flux densities, $p(S_m, \sigma_m|S_i)$ is the likelihood of observing (S_m, σ_m) for a source of intrinsic flux S_i, and $p(S_m, \sigma_m)$ is a normalizing constant. The resulting probability distribution is referred to as the posterior flux distribution, or PFD, throughout this section. We assume a Gaussian (normal) noise distribution for $p(S_m, \sigma_m|S_i)$ that is consistent with the noise in our map at the location of the discovered source. The prior, $p(S_i)$, is generated from pixel histograms of 10,000 noiseless simulations of the astronomical sky – as would be seen in zero-mean AzTEC/JCMT maps – given our best estimate of the true underlying SMG population and distribution. For this paper, we assume the SMG population exhibits number count densities that are well described by a Schechter function (Schechter, 1976) of the form

$$\frac{dN}{dS} = \frac{N^*}{S'} \left(\frac{S}{S'}\right)^{\alpha+1} \exp(-S/S'). \tag{5.2}$$

This parametric form is a slight departure from that used in Paper I and in the SCUBA/SHADES survey (Coppin et al., 2006), with N^*/S' replacing the parameter N' found in Paper I. This form has the advantage of reducing the correlations between the normalizing parameter and the parameters S' and α. The normalizing factor, N^*, is in units of deg^{-2} and is independent of the observation wavelength when assuming the same source population and a constant flux ratio between the observing bands. For the Bayesian prior, we initially assume parameters of $[S', N^*, \alpha] = [1.34, 5280, -2]$, which represent the best-fit Schechter function to the SCUBA/SHADES number counts (Coppin et al., 2006) when reparameterized to the form of Equation 5.2 and scaled to 1.1 mm assuming an $850\,\mu$m/$1100\,\mu$m spectral index of 3.5 (flux ratio ~ 2.5).

A second systematic flux bias in low-S/N blind surveys results from source detections being defined as peak locations in the map. The measured source flux is, on average, biased high due to the possibility of large positive noise peaks lying nearby, but off-center from, the true source position. This bias is minimized through point-source filtering and is sub-dominant to the flux boosting described previously. It is significant only for the lowest S/N detections and is largely avoided by restricting our analysis to the most robust sources ($S/N \gtrsim 4$). The remaining small bias ($b_{peak} < 0.2\sigma_m$ for $S/N \geq 4$) is estimated through simulation and subtracted from the detected source flux (S_m) before calculating the PFD in Equation 5.1.

We validate these flux corrections through extensive simulation of the PFD. We generate 10,000 simulated maps by adding noiseless sky realizations to random noise maps using the prescription outlined in Paper I. Sources are randomly injected spatially (i.e. no clustering) and in accordance with the number counts prior assumed. We group recovered sources in the resulting maps according to their measured values (S_m, σ_m), with each being mapped back to an intrinsic flux, S_i, defined as the maximum input flux found within $\sigma_{beam} = 7.6''$ of the output source location. For each

bin of measured values (S_m, σ_m), the input S_i values are binned and normalized to produce a simulated PFD.

Example simulation results are presented in Figure 5.1. Overall, the Bayesian approximation of the PFD (solid curve) provides a good estimate of the simulated probability distribution (histogram) at most fluxes. The differences at low flux and low S/N are due to a combination of source confusion in the simulations, higher-order effects of the bias to peak locations, and other low level systematics. For the purposes of this paper, the Bayesian results are preferred to the simulated PFDs for their computational speed, resolution, and flexibility in priors. The strong differences between the simulated probability distributions (histograms) and the naive Gaussian distributions (dashed curves) demonstrate the significance of flux boosting in surveys of this type. It is important to note that flux boosting (as described above) is not related to the adopted detection threshold and that even the most robust detections can be significantly biased. For example, a source detected at $S/N = 8$ in the AzTEC/COSMOS map will have been boosted by an average of 1.2 mJy ($\sim 1\sigma_m$), assuming the scaled SCUBA/SHADES SMG population.

5.2.2 Number Counts Derivation

The relative robustness of each source candidate is encoded in the PFD and is a function of both S_m and σ_m, as opposed to merely S_m/σ_m, due to the population's steep luminosity function. As in Paper I, we use the total probability of a source candidate being de-boosted to negative flux as the metric of relative source robustness. Coppin et al. (2006) found that $P(S_i \leq 0|S_m, \sigma_m) < 0.05$ provided a natural threshold from which to select a large sample of robust SMGs without including a significant number of noise peaks, or "false detections". This threshold also marks the point where the Bayesian approximation begins to suffer from low-level systematics, as suggested by the comparison of the Bayesian and simulated PFDs (Figure 5.1).

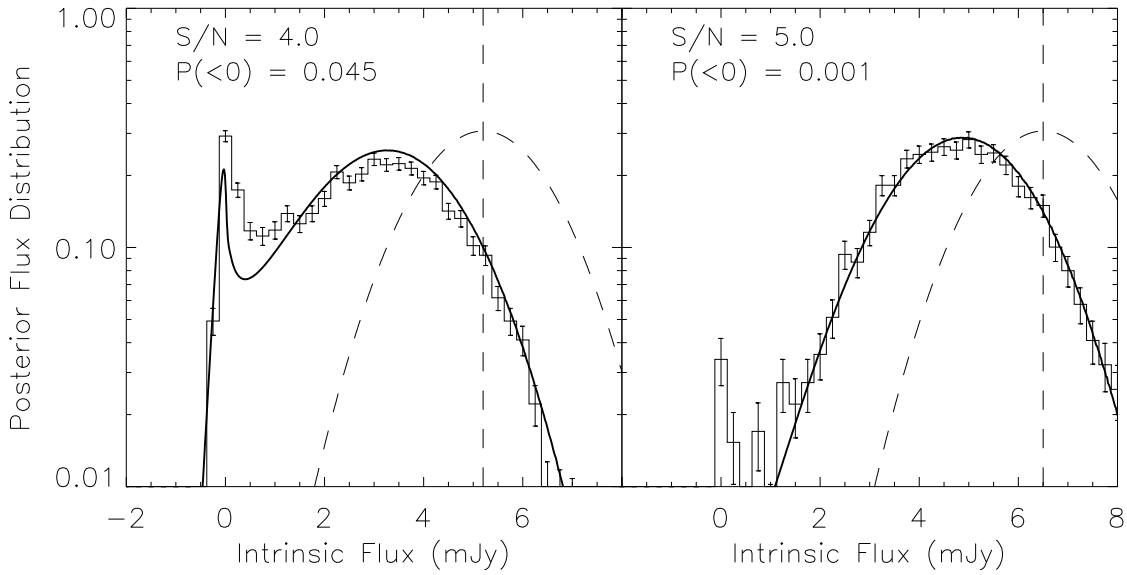

Figure 5.1. Example Posterior Flux Distributions (PFDs) as determined from Bayesian techniques. Plotted for $S/N = 4$ (left) and $S/N = 5$ (right) detections in a map with noise $\sim 1.3\,\mathrm{mJy}$ assuming an underlying source population consistent with the AzTEC/COSMOS results presented in § 5.2.3. The simulated probability distribution is shown as the histogram and is calculated as described in § 5.2.1. Error bars represent the 1σ Poisson errors of the simulation results, limited only by the number of simulations computed. The Bayesian approximation is depicted as a solid curve. The dashed vertical line represents the measured flux, S_m. The dashed curve is the Gaussian probability distribution, $p(S_m, \sigma_m|S_i)$, which represents the distribution that might otherwise be assumed without flux boosting and/or false detection considerations.

Therefore, we will use this "null threshold" of 5% to define our catalog of robust sources from which to estimate number counts. This threshold is equivalent to S/N values of 4.1 - 4.3 for our range of σ_m values, 1.2 - 1.4 mJy, assuming the scaled SCUBA/SHADES prior.

We derive the number counts from the catalog of robust sources and their associated PFDs using a bootstrap sampling method similar to that used in Coppin et al. (2006). In each step of this method, the selected sources are randomly assigned fluxes according to their respective PFDs (Equation 5.1). These samples are binned by flux to produce differential (dN/dS) and integral ($N(> S)$) source counts, with each bin being appropriately scaled for survey completeness and area. We introduce sample variance by sampling the robust source catalog *with replacement* (e.g. Press et al., 1992), and by Poisson deviating the number of times the catalog is sampled around the true number of detections. We repeat this process 20,000 times to determine uncertainty and correlation estimates for the number count bins.

Applying this sampling method to relatively small source catalogs results in a discretely sampled probability distribution for each number counts bin. This finite multinomial distribution can be non-Gaussian and asymmetric; therefore, we describe the uncertainty in the number counts as 68% confidence intervals that are approximated by linearly interpolating between the occupation numbers sampled in the bootstrap.

Survey completeness is estimated through simulation, in which sources of known intrinsic flux are randomly injected into noise map realizations one at a time and their output is tested against the null threshold source definition. Independent simulations confirm that this method provides excellent completeness estimations at all fluxes considered and that source confusion is not an issue given our beamsize (18") and map depth ($\sigma > 1.1$ mJy). Completeness is calculated as a function of intrinsic flux and averaged across the map to account for the slightly varying depth across the

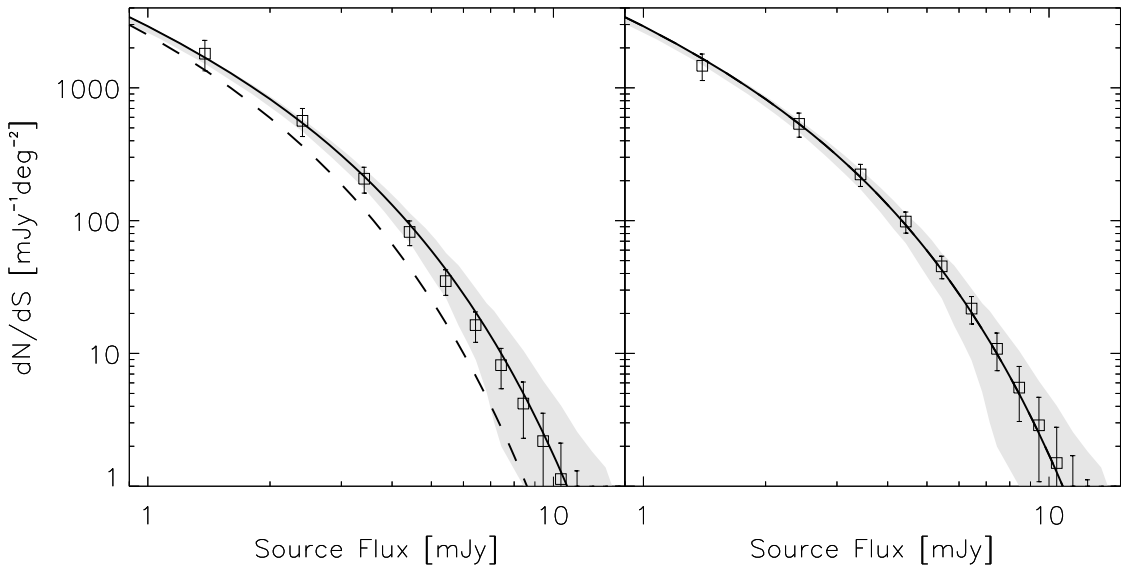

Figure 5.2. Simulated differential number count results (data points) using the extraction techniques described in § 5.2.2. The solid line represents the analytic source counts (Equation 5.2) used to populate the simulated maps, while the shaded region is the 1σ dispersion incurred by randomly populating maps of this size (0.15 deg^2). The left panel shows the results when assuming a prior based on the scaled SCUBA/-SHADES results (dashed curve), while the right panel is for the "ideal" prior that matches the underlying input population (solid curve). Error bars represent the 1σ dispersion from 1,000 simulations, while the errors in the means are typically smaller than the data symbols plotted.

survey region considered. We calculate the effective completeness of each differential number counts bin by averaging the simulated completeness function within the bin, weighted by the assumed relative abundance of sources (i.e. the prior).

We test these techniques by applying the same flux correction and number counts extraction algorithms to simulated maps with the same size and noise properties as those of the AzTEC/COSMOS survey. Figure 5.2 shows the extracted differential number counts from simulated maps using two different assumed priors. Both sets of simulated maps were populated with the same SMG population (solid line), which is similar to the final results of this AzTEC/COSMOS survey (§ 5.2.3). The right panel of Figure 5.2 shows the results of the ideal case where the Bayesian prior is the same distribution used to randomly populate the simulated maps, while the left

panel shows the results when using the scaled SCUBA/SHADES prior (dashed curve), which differs from the simulated input population (solid curve). For both priors the extracted number counts are in excellent agreement with the injected population. The relatively small differences between the input and output counts in the ideal case are used as systematic correction factors in our final calculations. The lowest flux bin (1–2 mJy) suffers from very low (and poorly defined) completeness and is, in general, the most sensitive to the assumptions in the prior. For these reasons we will restrict our analysis in this paper to the number count results for fluxes > 2 mJy, unless otherwise specified.

In Figure 5.2, the dispersion of the output source counts (error bars) is noticeably smaller than the dispersion of input source counts (shaded region) at high fluxes. This discrepancy reflects the correlation between output data points through our assumed prior. We characterize the overall bias to the assumed population by testing a wide range of priors against a static input population. For priors that are consistent with previous SMG surveys (e.g. Laurent et al., 2005; Coppin et al., 2006; Scott et al., 2006), the bias incurred is generally smaller than the formal 1σ errors of the extracted counts in a survey of this size and depth. Larger biases can result for exceptionally poor priors (e.g. $>$ order of magnitude differences from the true population); however, in most cases the extracted number counts better represent the actual source population than the initial prior, making it possible to mitigate this bias through an iterative process that adjusts the prior based on the extracted counts. We apply this iterative method to the AzTEC/COSMOS number counts estimate in the next section.

5.2.3 AzTEC/COSMOS Number Counts

The AzTEC/COSMOS integrated number counts are shown in Figure 5.3. This field shows an excess of sources at all fluxes when compared to the scaled SCUBA/-

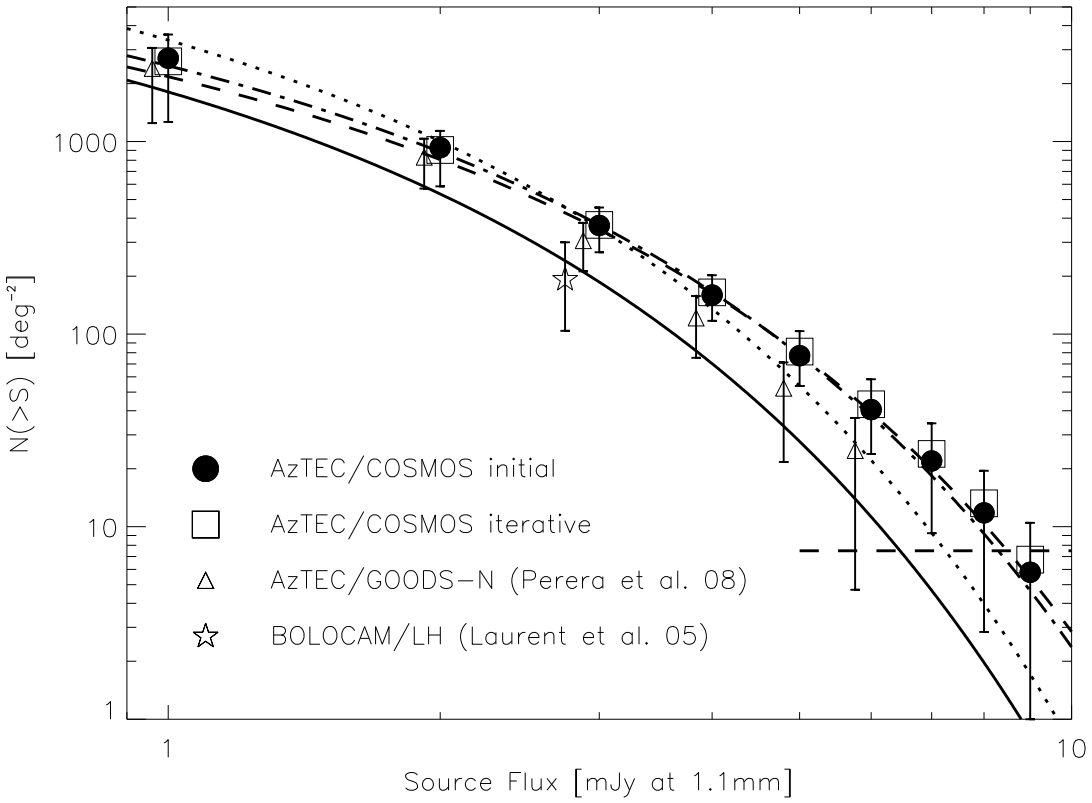

Figure 5.3. AzTEC/COSMOS integral source counts derived from the most robust AzTEC sources in the field using the techniques described in § 5.2.2. Filled circles (confidence bars omitted) represent the extracted counts using the initial assumed scaled SCUBA/SHADES prior (solid curve). Empty squares and 68% confidence bars represent the extracted counts after iteratively adjusting the prior to best represent the results of this survey. The dashed, dash-dotted, and dotted curves represent differential number counts fits to Equation 5.2 with free parameters [S',N^*], [S'], and [N^*], respectively. The horizontal dashed line represents the "survey limit", defined here as the source density that will Poisson deviate to zero sources (per 0.15 deg^2) 32.7% of the time. Open triangles and associated error bars represent the number counts found in the AzTEC GOODS-N survey (Perera et al., 2008) using the same techniques and have been shifted 4% to the left for clarity.

SHADES results (solid line). The number counts results are relatively insensitive to the choice of prior, with the initial analysis (filled circles) in agreement with those produced using an iterative prior (open squares). The "robust" source criterion of $P(S_i < 0|S_m, \sigma_m) < 0.05$ is somewhat more sensitive to the chosen prior, with the equivalent S/N threshold in a $\sigma_m = 1.3\,\mathrm{mJy}$ region being 4.2 and 4.0 for the initial and final iterative priors, respectively. The final iterative prior deems a larger number of sources as robust compared to the initial prior due to the number of sources lying in this S/N range. The corresponding effect on the survey completeness keeps this from being a runaway process, with the iterative number counts quickly converging within a few iterations.

The differential and integrated number counts of the AzTEC/COSMOS field are presented in Table 5.1. We fit the differential number counts to Equation 5.2 using Levenberg-Marquardt minimization, incorporating the data covariance matrix to account for correlations between flux bins. Various fits to the data are presented in Table 5.2 and are shown in Figure 5.3. Given the size and depth of this survey, we constrain the parametric fits to flux bins between 2 and 10 mJy to avoid bins that are poorly sampled and prone to systematic errors. This range of flux values is relatively insensitive to the power-law parameter α (Equation 5.2); therefore, we fit the data while holding α constant at values of -2 and -1, which represent the SCUBA/-SHADES result and a pure exponential, respectively. We also present similar fits to the SCUBA/SHADES number counts (Coppin et al., 2006) for comparison. The parametrized AzTEC/COSMOS results provide the maximum constraint on differential source counts at fluxes $\sim 4 - 5\,\mathrm{mJy}$ (depending on the parametrization). For example, a two parameter (S',N^*; α fixed to -2) fit to Equation 5.2 constrains the AzTEC/COSMOS differential counts at 4.5 mJy to $84 \pm 17\ \mathrm{deg}^{-2}\,\mathrm{mJy}^{-1}$.

Uncertainty in the flux calibration of the AzTEC/COSMOS survey is not included in these calculations and we believe it to be sub-dominant to the formal errors of the

Table 5.1. AzTEC/COSMOS Differential and Integral Number Counts

Flux Density (mJy)	dN/dS (mJy^{-1}deg^{-2})	Flux Density (mJy)	N(>S) deg^{-2}
1.40	$1706.^{+666.}_{-1534.}$	1.0	$2610.^{+987.}_{-1346.}$
2.42	$535.^{+235.}_{-292.}$	2.0	$904.^{+232.}_{-319.}$
3.43	$204.^{+88.}_{-82.}$	3.0	$369.^{+85.}_{-103.}$
4.43	$84.^{+37.}_{-33.}$	4.0	$165.^{+37.}_{-48.}$
5.44	$38.^{+18.}_{-18.}$	5.0	$81.^{+22.}_{-27.}$
6.44	$19.^{+10.}_{-12.}$	6.0	$43.^{+15.}_{-19.}$
7.44	$11.^{+6.}_{-9.}$	7.0	$24.^{+11.}_{-15.}$
8.44	$6.5^{+4.2}_{-6.0}$	8.0	$13.^{+6.}_{-10.}$
9.44	$3.9^{+3.8}_{-3.6}$	9.0	$6.7^{+3.7}_{-6.7}$

Note. — AzTEC/COSMOS differential and integral number counts using iterative adjustment of the prior. The differential number counts flux bins are 1 mJy wide and span integer flux values, with effective bin centers (first column) weighted according to the assumed prior. The lowest flux bin listed is particularly sensitive to uncertainties in the prior and such systematics are not included in the given 68% confidence intervals.

source flux, number counts, and fitted parameters. Calibration error estimates for individual observations during this observing season are 6-13% (Wilson et al., 2008a). Any normally distributed random component of this error will be reduced in the final co-added map since this survey is composed of multiple observations spanning many nights/weeks and calibration measurements. Systematic error in the calibration is believed to be dominated by the 5% uncertainty in the flux density of our primary calibrator, Uranus (Griffin & Orton, 1993).

5.2.4 Blank-Field Model

It is immediately apparent that the AzTEC/COSMOS field is rich in bright sources when compared to other 1.1 mm surveys (see § 5.2.5). In order to quantify the significance of this potential over-density, we must first adopt an accurate characterization of the true background ("blank-field") population. The tightest published constraint

Table 5.2. Parametric Fits to Differential Number Counts

Data Set	S' (mJy)	N^* (deg^{-2})	α	χ^2
AzTEC/COSMOS	1.83 ± 0.41	4420 ± 2720	-2	0.21
AzTEC/COSMOS	1.72 ± 0.12	5200	-2	0.28
AzTEC/COSMOS	1.36	9610 ± 1970	-2	1.89
SCUBA/SHADES	3.36 ± 0.49	5200 ± 1790	-2	0.23
AzTEC/COSMOS	1.31 ± 0.23	3570 ± 1790	-1	0.59
SCUBA/SHADES	2.39 ± 0.27	4370 ± 1170	-1	0.21
$\mathrm{MODEL}_{1.1\mathrm{mm}}$	1.34	5280	-2	$--$

Note. — Fit results to the differential number counts and respective covariance matrix of the AzTEC/COSMOS (1100 μm) and SCUBA/SHADES (850 μm; Coppin et al., 2006) surveys. All fits are to the modified Schechter function given in Equation 5.2 while holding various parameters constant (those with no uncertainty given). To avoid strong systematics at low flux, all fits are limited to data with $S_{1100\,\mu\mathrm{m}} \geq 2\,\mathrm{mJy}$ and $S_{850\mu\mathrm{m}} \geq 4\,\mathrm{mJy}$ for the AzTEC and SCUBA surveys, respectively. The last row represents our assumed 1.1 mm blank-field model for the initial prior (scaled SCUBA/SHADES). χ^2 values are unrealistically low, likely due to a combination of: (a) our uncertainties being assumed as Gaussian in the fit; and (b) additional correlation not accounted for in the linear Pearson covariance matrix constructed through the bootstrap sampling method (§ 5.2.2). These effects are also seen in the SCUBA/SHADES implementation of this algorithm (Coppin et al., 2006).

on the SMG population is provided by the 850 μm SCUBA/SHADES survey (Coppin et al., 2006), which we convert to 1100 μm assuming an 850 μm/1100 μm power-law spectral index of 3.5. This scaling is roughly consistent with the integrated number counts of the 1.1 mm Bolocam Lockman Hole survey (Laurent et al., 2005), which partially overlaps with the SCUBA/SHADES survey. Assuming the SCUBA and AzTEC observations are in the Rayleigh-Jeans regime of optically-thin thermal dust emission from the SMGs, our scaling is consistent with the sub-mm spectral indexes of bright IR galaxies in the local universe (Dunne et al., 2000; Dunne & Eales, 2001).

Using a scaled version of the number counts measured at a different observation wavelength carries the inherent risk that the two bands are sensitive to significantly different (although overlapping) source populations, as evidenced by the possible existence of sub-millimeter drop-outs (SDOs, Greve et al., 2008). The SCUBA 850 μm surveys would be relatively insensitive to these proposed SDOs due to a combination of high redshift ($z \gg 3$) and/or unusual spectral energy distributions (e.g. $T_{dust} \sim 10$ K). Therefore, it is important to verify the blank-field model with a direct measurement of 1.1 mm population.

The most robust characterization of the AzTEC/COSMOS over-density comes through comparison to similar analyses of other AzTEC 1.1 mm surveys, which eliminates systematics between different instruments and minimizes those related to calibration. The best AzTEC 1.1 mm blank-field constraints are being provided by the AzTEC 0.5 deg^2 survey of the SHADES fields (Chapter 6). Results of the AzTEC/-SHADES survey (using nearly identical algorithms as those applied to AzTEC/COSMOS) are consistent with our scaling of the SCUBA/SHADES counts. Our number counts model falls in the higher regions of the AzTEC/SHADES uncertainty interval (modeled differential counts are roughly $+0.5\sigma$ to $+2.0\sigma$ above the average AzTEC/-SHADES counts in the flux range explored here) and is within the field-to-field variations measured in those large surveys; therefore, we believe our model represents a

conservatively high estimate of the blank-field counts that is appropriate for robust qualification of the potential over-density.

We note that the AzTEC survey of the GOODS-N field (Perera et al., 2008) finds an SMG number density that is somewhat higher than our blank-field model; however, our model is within the $\sim 1\sigma$ uncertainty of that survey's integrated number counts (Figure 5.3; note that the data points are correlated). The AzTEC/GOODS-N results imply an S' parameter ($S' = 1.25 \pm 0.39\,\mathrm{mJy}$) that is consistent with our general scaling of the SCUBA/SHADES counts, but suggest systematically higher number counts (i.e. larger N^* parameter). The small size of the GOODS-N survey (0.068 deg^2) makes it highly susceptible to cosmic variance and clustering, thus reducing it's viability as a measurement of the average sky. It also does not significantly constrain the bright ($S > 5\,\mathrm{mJy}$) 1.1 mm source counts where the AzTEC/COSMOS over-density is most apparent (§ 5.2.5). The SCUBA survey of GOODS-N (Borys et al., 2003) already suggests the field may be overly rich in sub-millimeter sources, with number counts systematically higher than seen in the SCUBA/SHADES blank-field (Coppin et al., 2006), although the analyses of these two SCUBA surveys differ significantly and the difference in number counts could be partially systematic.

5.2.5 SMG Over-density

The source catalog presented in Paper I suggests that the AzTEC/COSMOS field has a significantly larger number of bright 1.1 mm sources than might otherwise be expected for a survey of this size and depth. The density of sources in the AzTEC/-COSMOS field with raw measured fluxes $\geq 6\,\mathrm{mJy}$ is 3 times higher (14 sources in 0.15 sq. deg. field) than in the 1.1 mm Bolocam Lockman Hole survey of similar depth (3 sources in 0.09 sq. deg.; Laurent et al., 2005). The seven brightest AzTEC sources in the COSMOS field have been imaged using the Submillimeter Array (SMA) at

890 μm, and they are shown to be single, unresolved sources at 2 arcsec resolution (Younger et al., 2007).

We compare the AzTEC/COSMOS number counts to the blank-field model discussed in § 5.2.4. Figure 5.3 shows that the AzTEC/COSMOS integrated source count estimates are clearly in excess of the scaled SCUBA/SHADES counts.

To estimate the probability of this excess happening by chance, we compare the number of robust sources detected in the AzTEC/COSMOS survey to the number recovered in simulated maps. In Figure 5.4 we show the distribution of the number of recovered sources in 10,000 simulations, each populated with a random realization of the scaled SCUBA/SHADES counts. On average, 12.1 sources are recovered from each of the simulated maps, which is in agreement with the semi-analytical expectation value of 11.2 (calculated from the scaled SCUBA/SHADES results and simulated completeness of this survey) and the expected number of false detections ($\langle N_{false} \rangle \approx 1.2$). Application of the same source criteria (5% null threshold, scaled SCUBA/SHADES prior) to the real map results in 23 robust sources (32 if using the iterative prior), which is greater than in 99.7% of the simulations. The AzTEC/-COSMOS source over-density is even more significant in the number of very bright sources, with 11 detected at $S/N \geq 5$ ($S_m \gtrsim 6.2$ mJy). Ten-thousand simulations of the blank-field model could produce no more than 6 such detections in a single map, thus inferring a $\gg 4\sigma$ significance in the number of bright sources.

Assuming the scaling of the SCUBA/SHADES counts accurately represents the blank-field SMG population at 1.1 mm, the parametric fits shown in Table 5.2 favor the over-density being described as a shift in the flux parameter S' over an increase in the normalization parameter N^*. This is consistent with an apparent over-density caused by uniform amplification of the source fluxes. However, this solution is degenerate with an alternative scaling of the SCUBA/SHADES results – scaling with a flatter spectral index of ~ 2.6 also produces a good fit to the AzTEC/COSMOS

number counts (dash-dotted curve of Figure 5.3). Therefore, an accurate representation of the blank-field population (§ 5.2.4) is critical to properly quantifying the over-density.

If taken alone, the over-density of SMGs in the AzTEC/COSMOS field would likely be explained away as simple cosmic variance in the SMG population as traced in a 0.15 deg^2 field. However, in the following sections we demonstrate that the over-density is due, in part, to *foreground* structure in the COSMOS field. Only with the rich multi-wavelength coverage of the COSMOS field and the relatively large size of the AzTEC map is this analysis possible.

5.3 Correlation Between AzTEC sources and Large Scale Structure in the COSMOS field

Author's note: Many of the figures and statistical analyses presented in this section were generated by Itziar Aretxaga, a co-author of the publication of this chapter (Austermann et al., 2009).

Having shown that the AzTEC/COSMOS field exhibits a significant excess of bright SMGs with respect to our adopted blank-field model, we explore the possibility that this over-density is due, in part, to a correlation of AzTEC sources with the prominent large-scale structures at $z \lesssim 1.1$ identified in this portion of the COSMOS field (Scoville et al., 2007b). All correlation tests in this section are limited to the inner 0.15 deg^2 region of the AzTEC map where the uniformity in coverage simplifies the analysis.

The smoothed galaxy density map produced by the COSMOS consortium (Scoville et al., 2007b, see Figure 5.5) shows a collection of dense regions in the the AzTEC covered area. We first look for coincidence with AzTEC sources by cross-correlating the surface-density of optical-IR galaxies in this map with the AzTEC source positions using a bi-dimensional Kolmogorov-Smirnov (K-S) test of similarity (Peacock, 1983;

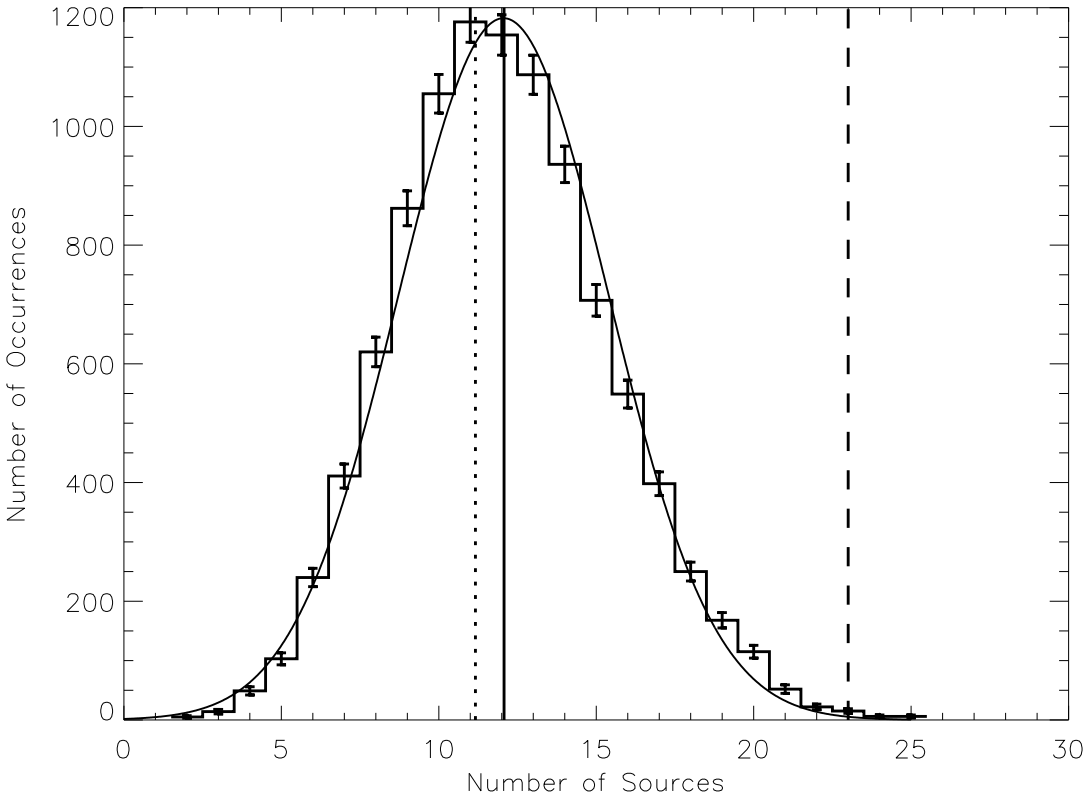

Figure 5.4. Distribution of the number of robust sources detected in 10,000 simulations (using 300 unique noise realizations) of the AzTEC/COSMOS observations when randomly populating the astronomical sky with the scaled SCUBA/SHADES number counts (solid histogram). Using the same source criteria, there are 23 robust sources detected in the AzTEC/COSMOS map (dashed vertical), which is greater than 99.7% of the simulations. A Gaussian fit to the simulation results (thin solid curve) shows 23 sources to be a 3.3σ outlier. The difference between the simulation mean (solid vertical) and the semi-analytic expectation value (dotted vertical) reflects the number of false detections (i.e. ~ 1 per map) for the scaled SCUBA/SHADES prior and chosen source threshold.

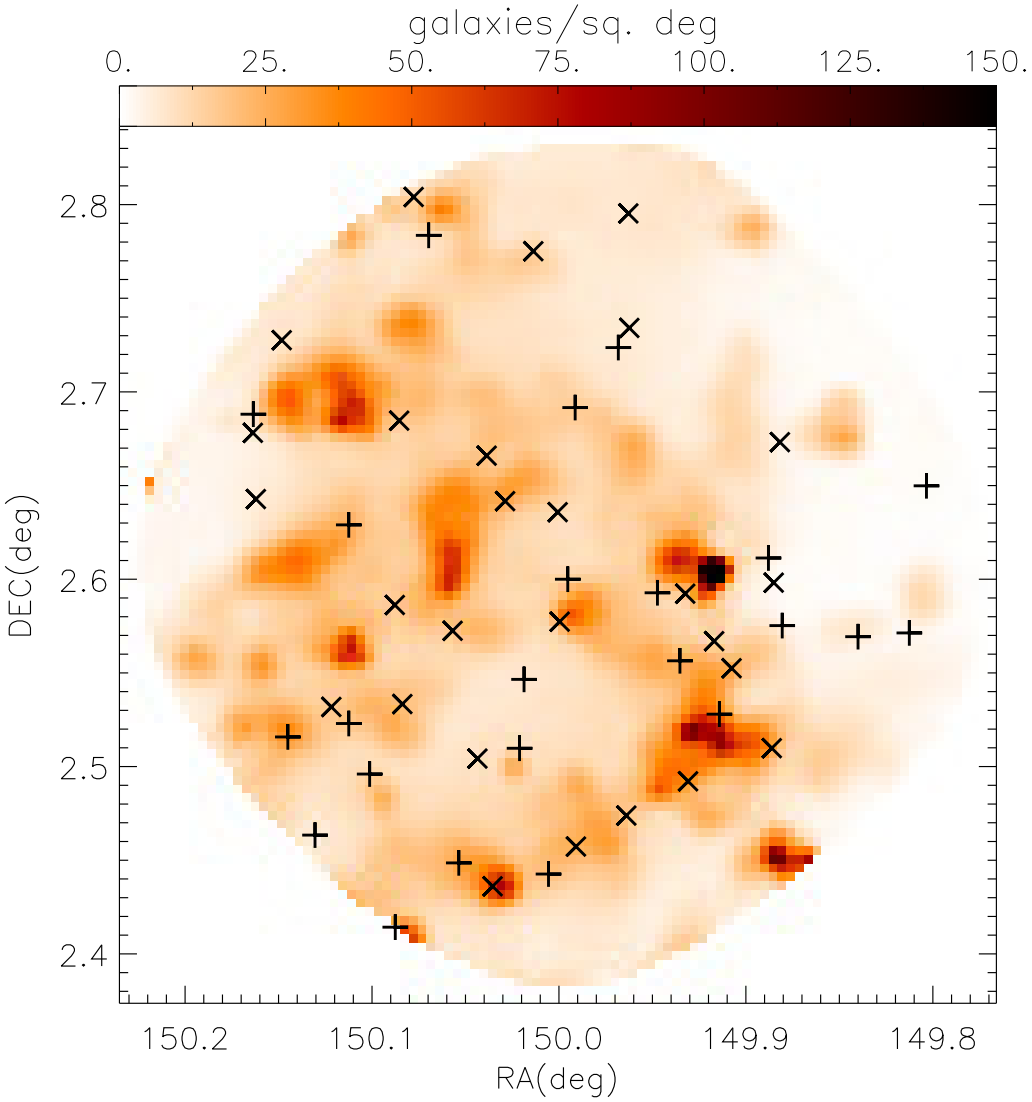

Figure 5.5. Smoothed surface density map of galaxies derived from the optical-IR catalog of COSMOS galaxies (Scoville et al., 2007b) in the 0.15 sq. deg area surveyed by AzTEC, where darker colors indicate more densely populated areas of the sky. The cross and plus symbols represent AzTEC sources detected at signal-to-noise ratios $S/N \geq 4$ and $4 > S/N \geq 3.5$ (Scott et al., 2008), respectively.

Fasano & Franceschini, 1987). Restricting this analysis to the 30 robust AzTEC sources detected at a $S/N \geq 4$, which have an estimated false detection rate of less than 7% (Scott et al., 2008), we find that the test cannot reject the null hypothesis that the distribution of AzTEC-source positions follows the surface density distribution of optical-IR galaxies. The test concludes that the difference between the SMG and optical-IR populations is smaller than 93.7% of the differences expected at random due to sample variance, often referred to as rejecting the null hypothesis at the 6.3% level, thus suggesting the distributions could indeed be similar.

The significance of the SMG positional correlation with the large-scale structure is further quantified by comparing the K-S D-statistic of the SMG catalog to that of a homogeneous random distribution of the same number of sources, under the null hypothesis that they follow the surface density of optical-IR galaxies. This test determines that the AzTEC/COSMOS source distribution follows the optical-IR distribution more strongly than 98.9% ($\sim 2.5\sigma$) of the random-position catalogs. The result is somewhat less significant, 91.1%, if we expand the comparison to the full $S/N \geq 3.5$ AzTEC/COSMOS catalog, which is likely due to the increased number of false detections (from ~ 1 to ~ 11) at this lower S/N threshold. These false detections (noise peaks) are inherently random and homogeneous in their distribution and dilute the correlation signal.

It is possible that only a fraction of the AzTEC source positions are correlated with the prominent large-scale structures detected in the COSMOS galaxy density map while a subset of randomly distributed source positions dilutes the sensitivity of the quadrant-based bi-dimensional K-S statistic discussed above. Therefore, we further test the hypothesized correlation by comparing the surface density of optical-IR galaxies within a small area surrounding AzTEC positions to that surrounding random positions in the map. Figure 5.6 shows the distribution of the galaxy densities at $z \lesssim 1.1$ projected within 30" (1.7 pixels in the smooth galaxy density map)

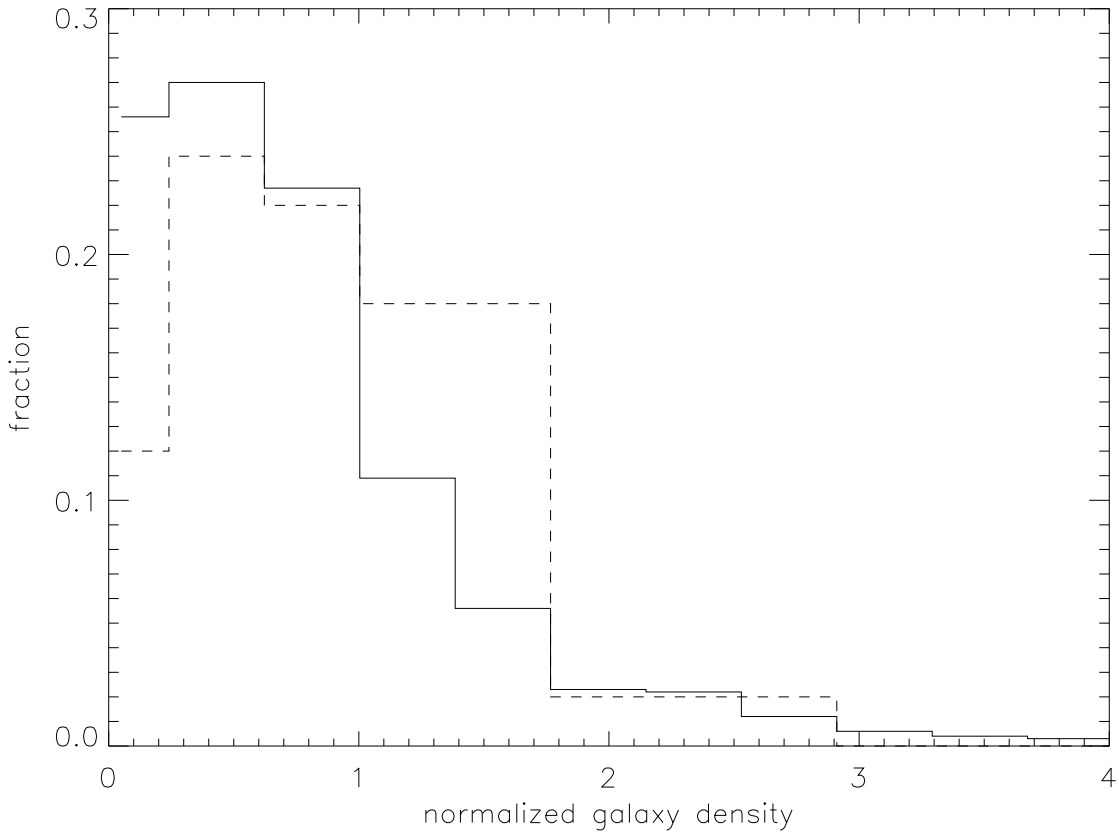

Figure 5.6. Histogram of the galaxy density at $z \lesssim 1.1$ found within 30 arcsec of (a) AzTEC/COSMOS source candidates detected at $S/N \geq 3.5$ (dashed line) and (b) random positions in the AzTEC mapped area of COSMOS (solid line). The two populations are different at the 97.2% confidence level, using a one-dimensional K-S test. The galaxy densities are normalized to the mean galaxy density in the full AzTEC-covered area.

of the AzTEC source positions, compared to the galaxy densities found around random positions within the AzTEC survey region. The two distributions are clearly different, with a one-dimensional K-S test rejecting the null hypothesis of identity at $> 99.99\%$ and 97.2% levels for the $S/N \geq 4$ and $S/N \geq 3.5$ catalogs, respectively. The mean number of nearby optical-IR galaxies at $S/N \geq 4$ ($S/N \geq 3.5$) AzTEC source positions is larger than that at random positions in the map at a significance of 99.99% (99.5%) according to the non-parametric Mann-Whitney (MW) U-test.

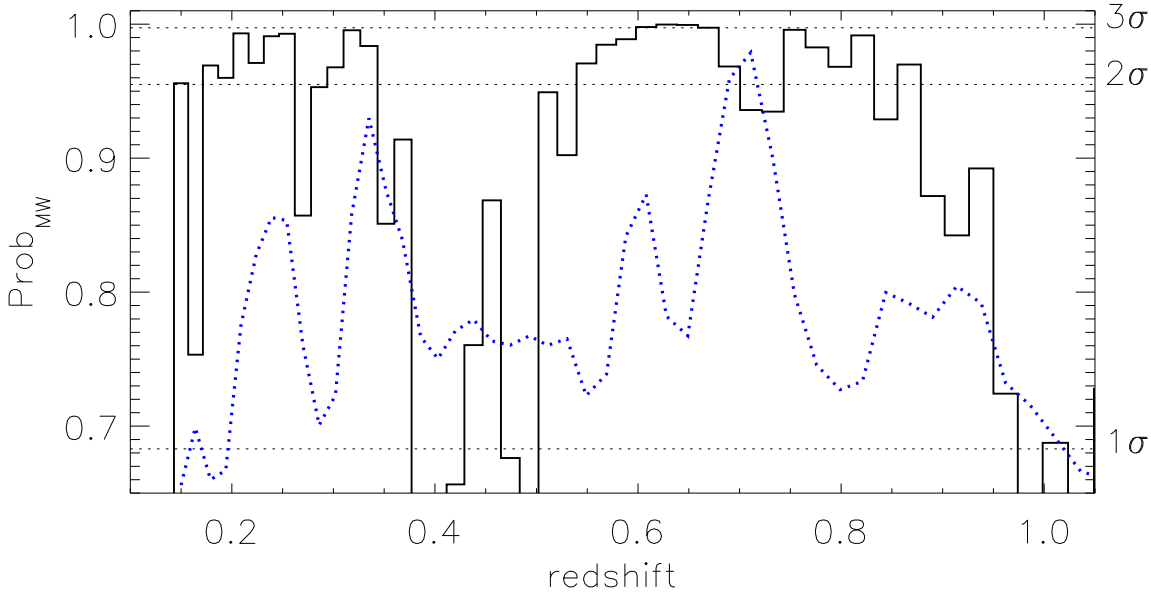

Figure 5.7. Bar-representation of the Mann-Whitney probability that the mean galaxy density around AzTEC sources at a given redshift slice is significantly larger than the mean galaxy density around random positions. Horizontal dotted lines represent the 1σ, 2σ, and 3σ significance levels, respectively. The blue-dotted curve shows the relative number of optical/IR galaxies contained within each redshift slice within the AzTEC covered area ($N_{\rm gal}(z)/N_{\rm total} * 10. + 0.60$).

We can search in redshift space for the structures that contribute the most to the coincidence between AzTEC sources and the galaxy density in their "line of sight" using the photometric redshifts of the optical-IR population (Ilbert et al., 2009), which have a mean accuracy of $|\Delta z|/(1+z) \approx$ 0.01-0.02. Figure 5.7 shows a bar-representation of the MW probabilities that the mean integrated galaxy density around AzTEC sources is significantly larger than that around random positions in the map for various redshift slices. There is positive signal ($\gtrsim 2\sigma$) arising at different redshift slices, most notably at $z \sim 0.65$. At redshifts $z > 1.1$, the number of galaxies detected at optical-IR wavelengths decreases significantly, and the level of correlation found with AzTEC sources is well below the 2σ threshold.

The most prominent contribution to the AzTEC-optical/IR correlation lies at $0.6 \lesssim z \lesssim 0.67$, with the redshift slices within this range having MW probabilities

of difference up to 99.98%. The smoothed galaxy density map for this redshift range is shown in Figure 5.8. Two prominent large-scale structures have been identified (Structures #1 and #24 in Scoville et al., 2007b) within this redshift slice. Structure #1 at $z = 0.73 \pm 0.27$ has 1767 optical-IR galaxy members and approximately spans (FWHM) Δ RA = 0.22 deg and Δ Dec = 0.17 deg. Structure #24, a less massive but very compact system that is X-ray detected, has 85 galaxy members and is at z $\sim$ 0.61. Structure #24, however, does not appear to contribute to the correlation, as no AzTEC sources fall within its primary extension. Structure #1 contains a rich core and represents a massive cluster ($\sim 10^{15} M_{\odot}$) at $z \approx 0.73$, which is clearly seen in the COSMOS weak-lensing convergence map (Massey et al., 2007) and in X-ray emission (Guzzo et al., 2007). This cluster lies outside the redshift span of strong correlation, but the filamentary structure that leads to it is part of the redshift slice under analysis (see Figure 5.8).

We next assess whether the substructures within Structure #1 are the main contributors to the observed correlation. Figure 5.9 shows the distribution of galaxy densities around AzTEC sources and around random positions in the collapsed $0.6 \lesssim z \lesssim 0.67$ map. The means differ at the 99.8% confidence level according to the MW U-test. If we exclude a circular region around the cluster center with radius $\theta = 1.5'(\sim 0.6\,\mathrm{Mpc})$, which contains both the cluster-core and the cluster-outskirt regions seen by the X-ray temperature profile (Guzzo et al., 2007), the significance of the difference is 99.94%. Excluding a larger circular region of radius $\theta = 6'(\sim 2.4\,\mathrm{Mpc})$, which represents the FWHM of the full Structure #1, the MW significance decreases to only 98.6%. This demonstrates that although AzTEC sources do correlate with the galaxy densities associated with the extended Structure #1, the less prominent large-scale structure across the rest of the map is also well-correlated with the AzTEC positions.

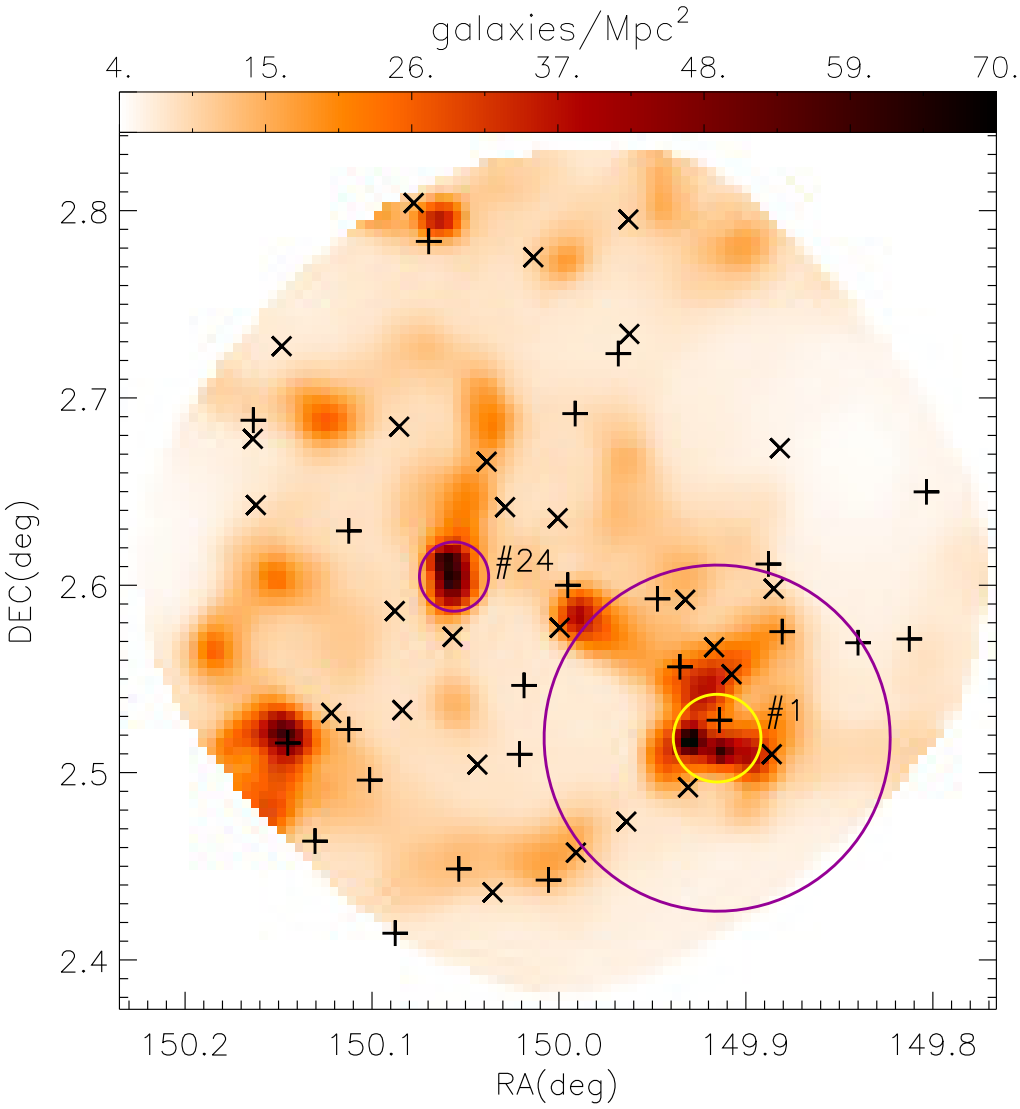

Figure 5.8. Smoothed surface density map of Optical-IR galaxies at $0.60 \lesssim z \lesssim 0.67$ compared to AzTEC/COSMOS source locations. The large-scale structure at $z = 0.73 \pm 0.26$ detected by Scoville et al. (2007b) is marked as Structure #1 and the large circle (6' diameter). This large-scale structure has a peak over-density at $z \sim 0.73$, outside of the redshift range of this figure, and is identified as a massive cluster (Guzzo et al., 2007). The yellow circle (1.5' diameter) marks the spatial extent of this cluster as traced by the X-ray contours. Another rich cluster, at $z \sim 0.61$, is marked as Structure #24. Symbols are the same as in Figure 5.5.

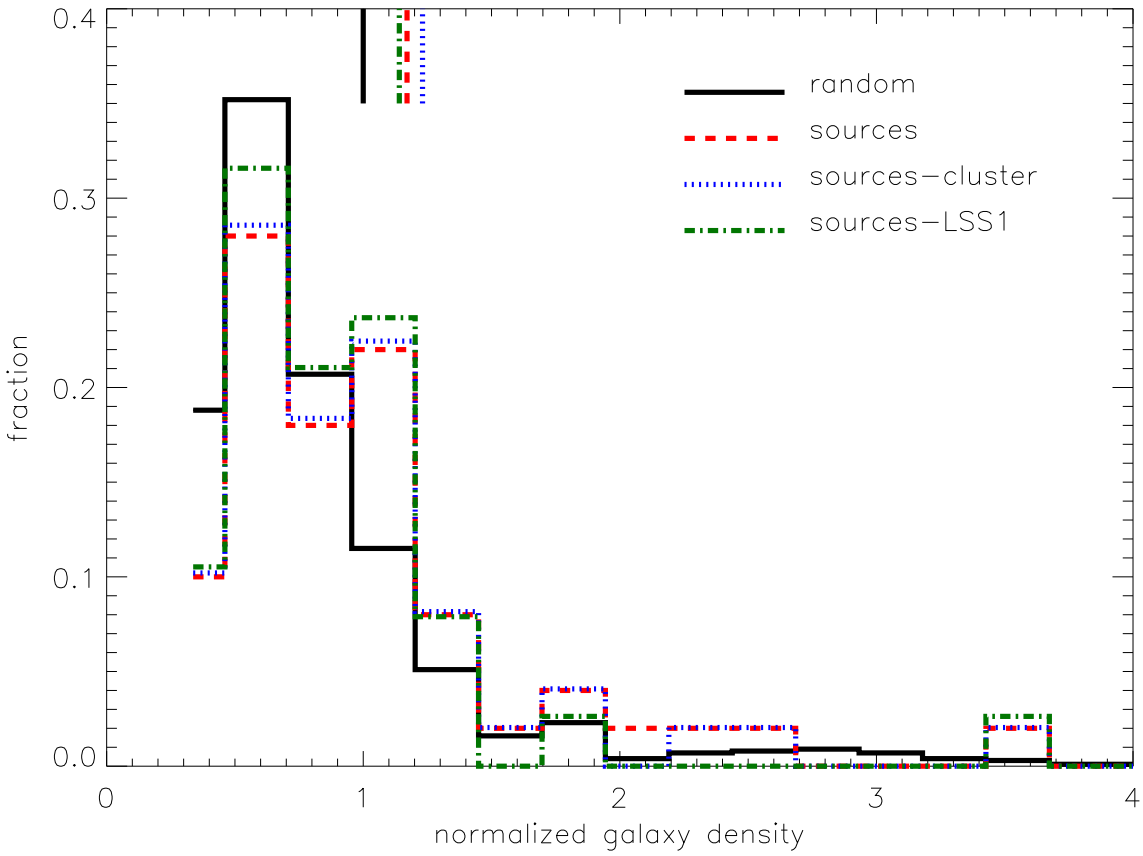

Figure 5.9. Histogram of the fraction of optical-IR selected galaxies at $0.60 \lesssim z \lesssim 0.67$ found within 30 arcsec of AzTEC source candidates (red dashed line), and around random positions within the AzTEC-mapped area of COSMOS (black solid line). The blue dotted-line histogram represents the number of optical-IR galaxies around AzTEC sources, excluding the single AzTEC source that falls within the X-ray traced cluster-outskirt region ($\theta \lesssim 1.5$ arcmin from the cluster center, Guzzo et al., 2007), while the green dash-dotted histogram excludes the full 6 arcmin radial structure identified as Structure #1. The mean values of these histograms are represented at the top of the figure as vertical bars. The galaxy densities are normalized to the mean galaxy density in the full AzTEC-covered area such that the mean density of random positions is 1.

Figure 5.10 shows the optical/IR galaxy density map for the redshift slice $0.24 \lesssim z \lesssim 0.26$, which is also a large contributor to the overall correlation between the large-scale-structure of the field and AzTEC sources (Figure 5.7). Structure #22 from Scoville et al. (2007b), with ~ 67 possible galaxy members at $z \approx 0.26 \pm 0.11$, is the main cluster in this redshift slice and is also detected in X-ray. However, as with the portion of Structure #1 in the $0.60 \lesssim z \lesssim 0.67$ slice, this system does not dominate the overall correlation with AzTEC sources: the mean galaxy density around AzTEC sources differs from random locations at the 99.1% level after exclusion of the Δ RA $\approx$ 0.06 deg and Δ Dec $\approx$ 0.14 deg area of influence of the cluster. Similarly, we find that the prominent contributions of other redshift slices (e.g. $z \sim 0.33$ and $z \sim 0.8$) to the overall spatial correlation are not due to single compact structures.

It appears that the observed correlations are not dominated by the clusters in the field, thus it is not surprising that the AzTEC positions are, in general, less correlated with the weak-lensing mass map of COSMOS (Massey et al., 2007), which is particularly sensitive to the most massive structures like the $z \approx 0.73$ cluster (see Figure 5.11). The null hypothesis that the distribution of masses found within 30" of AzTEC positions is the same as that found around random positions in the weak-lensing map is "rejected" at only the 60% level (K-S test), and their means differ at the 91.5% level (MW U-test).

5.4 Discussion

The distribution of AzTEC sources is correlated with the large-scale distribution of optical/IR galaxies at $z \lesssim 1.1$ and the primary (but not unique) contributors to this signal are located at redshifts $0.60 \lesssim z \lesssim 0.65$ and $0.24 \lesssim z \lesssim 0.26$ (section § 5.3). The correlations in these redshift regimes are robust, with mean optical/IR densities differing from random distributions at the 99.1 to 99.98% level (MW U-test). For the seven AzTEC sources that have been followed up with SMA interferometry (Younger

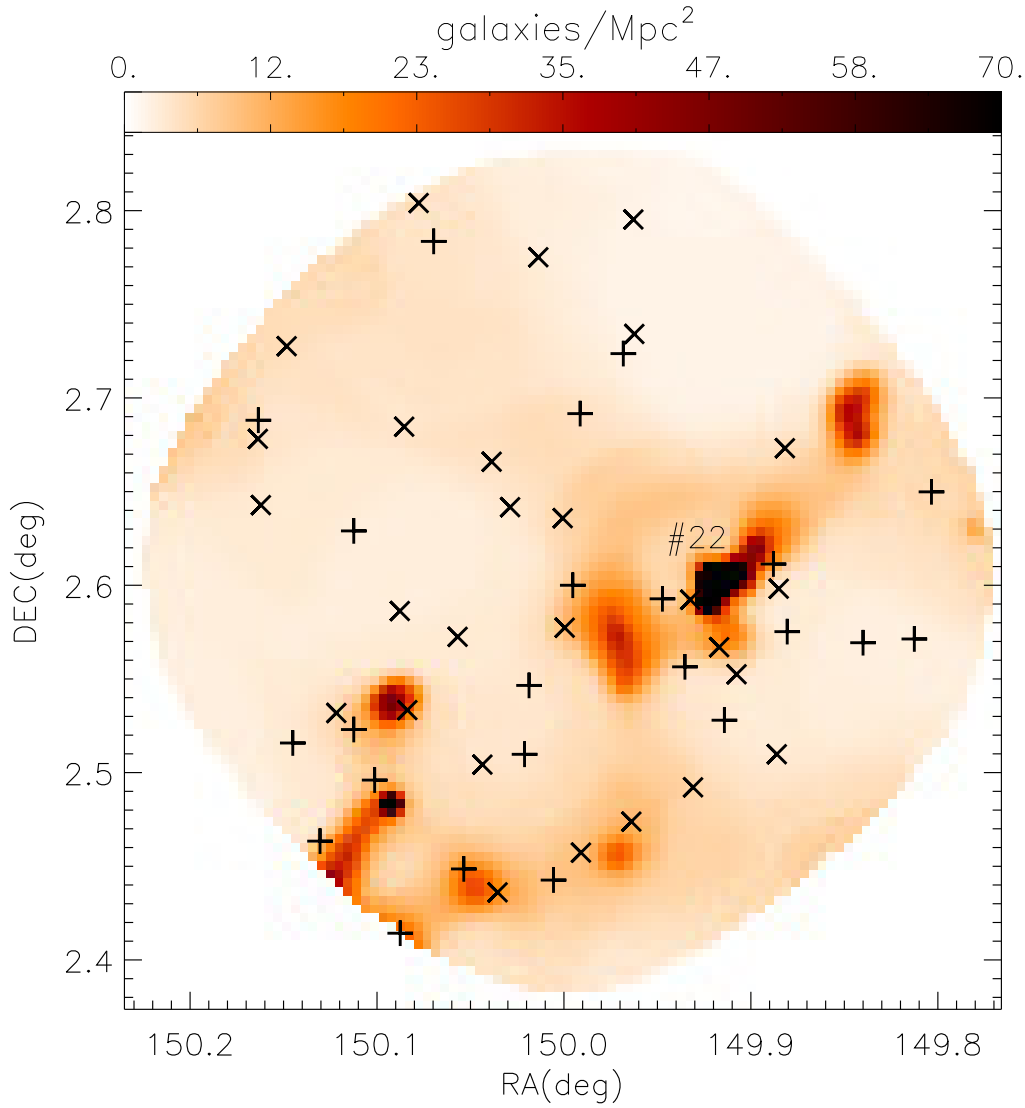

Figure 5.10. Smoothed surface density map of galaxies at $0.24 \lesssim z \lesssim 0.26$ detected at optical-IR wavelengths by the COSMOS survey, which includes Structure #22 of Scoville et al. (2007b). Symbols are the same as in Figure 5.5
.

et al., 2007) and the additional 14 that have radio detections (Scott et al., 2008), secure optical/IR counterparts have been identified. The optical-IR and FIR-mm-radio photometric redshifts of these sources place the majority of these objects at $z \gtrsim 3$; therefore, AzTEC detected sources are most likely background systems to the $z \lesssim 1.1$ galaxy densities shown in Figure 5.5. This is not surprising, given that the population of SCUBA SMGs with radio counterparts have a median redshift of 2.2 (Chapman et al., 2003, 2005; Aretxaga et al., 2003, 2007; Pope et al., 2005).

The amplification caused by massive clusters at intermediate redshifts ($z \sim 0.2 - 0.4$) has been used to detect and study the sub-millimeter galaxy population since the first SMG surveys (e.g. Smail et al., 1997). Lensing is expected to occur also in and around the $z \approx 0.73$ cluster detected in the COSMOS field, but only 4 of the 50 $S/N \geq 3.5$ AzTEC source-candidates are projected within 2' of the dense cluster core. Removing these sources/regions from the analysis of § 5.3 has little effect on the correlation strength. Thus the correlations seem to be tied to the general $z \lesssim 1.1$ large-scale structure in the field. The same result holds if we exclude the other prominent structures in this field, Structures #24 at $z \approx 0.61$ and #22 at $z \approx 0.26$. Furthermore, the bulk of AzTEC sources do not significantly correlate with the weak-lensing map, which is particularly sensitive to the mass contained in rich clusters.

Lensing of the sub-mm galaxy population by foreground low-redshift structures has been claimed in the correlation analysis of 39 sub-millimeter galaxies detected in 3 disjoint fields with the density of $R < 23\,\mathrm{mag}$ galaxies (Almaini et al., 2005), which statistically lie at $\langle z \rangle \sim 0.5$. It was argued that the bright $S_{850\mu\mathrm{m}} > 10\,\mathrm{mJy}$ sources are found to cluster preferentially around the highest-density areas, and Almaini et al. (2005) estimate that 20-25% of the sub-millimeter galaxy population is subject to lensing by foreground structures. We note that a similar study performed in the GOODS-N region (Blake et al., 2006) found no detectable correlation

between 35 SCUBA-selected SMGs and the optically-selected galaxy populations at $z \leq 0.8$. This difference in correlation strength may be related to cosmic variance of foreground structure on the scale of these maps. There also exist potential cases of lensing by individual galaxies, with some SCUBA sources being incorrectly identified as low-redshift galaxies due to intervening foreground galaxies that lie directly along the line of sight (Chapman et al., 2002b; Dunlop et al., 2004). Since it includes a high-density region within the COSMOS field, the AzTEC survey is sensitive to all of these types of amplification, and we have demonstrated that there is a positive correlation with the large-scale structure. Inspection of the optical/IR counterparts of the 21 AzTEC galaxies with radio and/or sub-mm interferometric positional accuracy, including the 7 sources known to have sub-millimeter emission on scales $\theta < 1.2$" (Younger et al., 2007), show no obvious signs of strong galaxy-galaxy lensing and hence any amplification of this sub-sample must be attributed to weak-lensing.

If our blank-field number counts model (§ 5.2.4) accurately represents the intrinsic (non-amplified) SMG population in the AzTEC/COSMOS field, then the observed number density of sources is also consistent with weak-lensing of the background SMG population. Parametric fits to the flux-corrected number counts (§ 5.2.3, see also Table 5.2 and Figure 5.3) show that the relative over-density of sources can be fully explained as a systematic increase in the parameter S', which is consistent with an average flux amplification (e.g. lensing) of the source population by $\sim 30\%$. Conversely, the number counts data are only marginally consistent with a simple increase in the normalization parameter N^*, thus disfavoring a uniform physical over-density (e.g. cosmic variance) of sources in this field as the sole cause of the observed over-density. Additionally, any over-density due to variance and/or clustering can not explain the correlation of AzTEC sources to the $z \lesssim 1.1$ structure, as the AzTEC sources are likely background sources and not physically associated with the $z \lesssim 1.1$ structure.

An alternative cause of the number counts over-density can be imagined as an additive flux source (e.g. dense screen of faint foreground sources) confused with the blank-field sources. However, the AzTEC/COSMOS map has been filtered for point source detection and has a mean of zero (Scott et al., 2008), which leaves the map insensitive to high-density or uniform millimeter flux sources that span large spatial scales. Furthermore, the positions of AzTEC sources are not strongly correlated with the most dense and compact foreground regions (i.e. clusters) that could otherwise be potential sources of additional mm-wave flux in our map (e.g. the Sunyaev-Zel'dovich effect).

The significance of the spatial correlation between AzTEC sources and the intervening large-scale structure contrasts with the lack of a similar detectable signal among the sources discovered by COSBO (Bertoldi et al., 2007), the 1.2 mm MAMBO survey to the south and adjacent to the AzTEC surveyed area (see Figure 5.11). If we repeat the analysis performed in § 5.3 with the MAMBO catalog, we do not find a significant correlation with the COSMOS optical/IR galaxy surface density; the probability that the galaxy densities around MAMBO sources are different from that around random positions in the map is only 87% (K-S test). This lack of a significant correlation signal may be due in part to the smaller catalog of significant sources in the COSBO field and the overall lack of significant foreground structure in much of the COSBO covered area.

The association between COSBO sources and the weak-lensing derived mass-map, however, is stronger with a 99.4% probability (K-S test) that the distribution of mass around MAMBO source locations is different from that of random positions in the COSBO survey region. This signal is dominated by a group of $\sim 7-8$ of the most significant MAMBO sources close to two compact mass spikes, which are identified with X-ray bright over-densities consisting of a total of ~ 127 galaxies at $z \approx 0.24$ (Structure #17 in Scoville et al., 2007b) and are likely clusters. The possible spatial

correlation of COSBO sources with foreground structures, therefore, might be of a somewhat different nature than that of AzTEC sources. The COSBO region may be witnessing amplification caused by the two clusters revealed by the weak-lensing map, while the AzTEC sources are more likely amplified by galaxies contained within the more tenuous filamentary large-scale structure, which is so tenuous in the COSBO field that it provides no significant signal in the sample of MAMBO sources.

5.5 Conclusions

The central 0.15 deg^2 of the AzTEC/COSMOS survey shows a significant over-density of bright 1.1 mm-detected SMGs when compared to the background population inferred by other surveys. We find that this over-density cannot be explained as sample variance of the blank-field SMG population. The SMG positions are significantly correlated with the $z \lesssim 1.1$ optical/IR galaxy density on the sky, which is believed to be in the foreground of nearly all AzTEC/COSMOS SMGs. Both the spatial correlation and the AzTEC/COSMOS SMG number counts are consistent with gravitational amplification of the blank-field SMG population. The lack of strong correlation to the weak-lensing maps of Massey et al. (2007) indicates that this amplification is primarily due to weak-lensing by the large-scale structure as opposed to lensing by the compact and massive clusters in the field. SMGs detected in a different part of the COSMOS field by the 1.2 mm COSBO survey are also spatially correlated to the $z \lesssim 1.1$ structure, however, this correlation is dominated by two compact structures (likely clusters) in the field. The lack of significant large-scale structure (i.e. lensing opportunities) in the rest of the COSBO survey region results in COSBO number counts that are consistent with the blank-field (Bertoldi et al., 2007) – a strong contrast to the significant SMG over-density and rich foreground structure found in the nearby AzTEC/COSMOS field.

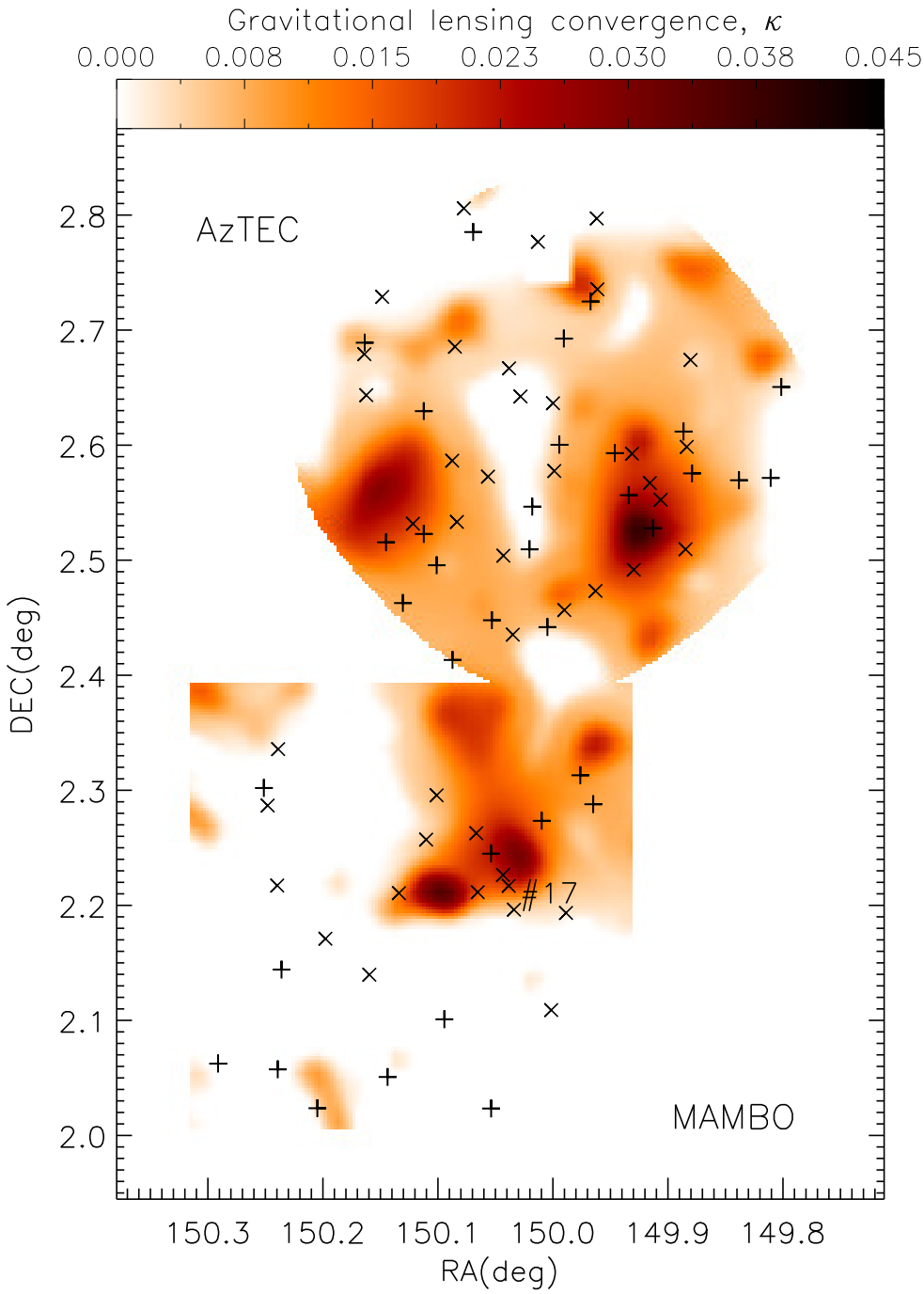

Figure 5.11. Weak-lensing convergence mass map (Massey et al., 2007) of the AzTEC and MAMBO surveyed regions of COSMOS. Crosses mark the millimeter source positions from the two catalogs and follow the notation of Figure 5.5.

CHAPTER 6

CHARACTERIZING THE BLANK-FIELD SMG POPULATION: THE AZTEC/SHADES SURVEY

6.1 Introduction

Since the first blind sub-millimeter detections of high-redshift dusty starburst galaxies (Smail et al., 1997; Hughes et al., 1998; Barger et al., 1998), 'blank-field' (i.e. no known mass/structure bias in field selection) surveys have been the workhorse in the study of these so-called sub-millimeter galaxies (SMGs). Significant surveys have been undertaken at 850 μm (e.g. Scott et al., 2006 and references therein, Pope et al., 2006, Coppin et al., 2006), 1100 μm (Laurent et al., 2005; Scott et al., 2008; Perera et al., 2008), and 1200 μm (e.g. Greve et al., 2004; Bertoldi et al., 2007; Greve et al., 2008). These surveys have helped establish a baseline understanding of the SMG population and number counts, to which the results of targeted surveys of biased regions can be compared (e.g. Stevens et al., 2003; Greve et al., 2007; Priddey et al., 2008; Austermann et al., 2009). The blank-field surveys have provided the community with hundreds of (sub-)mm targets to study in detail through counterpart identification and multi-wavelength analysis (e.g. Clements et al., 2008), mid-IR spectroscopy (e.g. Menéndez-Delmestre et al., 2007; Pope et al., 2008), and redshift measurements/estimation (e.g. Chapman et al., 2005; Aretxaga et al., 2007). These data help lead to estimates of dust masses, dust temperatures, IR luminosities, and star-formation rates (e.g. Kovács et al., 2006; Coppin et al., 2008), as well as clustering strength (e.g. Blain et al., 2004; van Kampen et al., 2005; Chapman et al., 2009) and stellar masses, morphologies, and star-formation history (e.g. Dye et al., 2008).

In turn, this information provides constraints on the formation and evolution of massive galaxies and illuminates the dust-enshrouded component of the star-formation history of the Universe (see the review paper by Blain et al., 2002).

Most SMG surveys have been relatively modest in size ($< 0.1\,\mathrm{deg}^2$) which generally results in the characterization of the overall SMG population being limited by both sample size and cosmic variance. Such small surveys are also unable to constrain the brightest and rarest SMGs. The situation has been improved by both the combined analysis of multiple surveys (e.g. Scott et al., 2006) and by the relatively large 850–μm SCUBA/SHADES survey (Coppin et al., 2006), which mapped $0.2\,\mathrm{deg}^2$ to depths of $\sigma_{850} \sim 2\,\mathrm{mJy}$.

Here we present another step in constraining the blank-field SMG population using the $1100\,\mu$m AzTEC/SHADES survey, which covers $0.5\,\mathrm{deg}^2$ to depths of $\sigma_{1100} \sim 1\,\mathrm{mJy}$. This survey dramatically improves our understanding of the 1100μm blank-field population, with previous $1100\,\mu$m surveys being limited by size (e.g. Perera et al., 2008), depth (e.g. Laurent et al., 2005), and/or structure in the field (e.g. Austermann et al., 2009). In this paper we describe the largest $1100\,\mu$m SMG catalog available (Section 6.3), provide the tightest constraints on the 1100μm blank-field number counts (Section 6.4), and compare these results to other surveys and models (Section 6.5). This paper is the first in a series of papers using the AzTEC/SHADES maps and catalogs to study the sub-millimeter population of galaxies.

6.2 Observations

We have completed the SCUBA Half-Degree Extragalactic Survey (SHADES; Mortier et al., 2005) by mapping over one-half square degree of sky using the AzTEC 1.1-mm camera (Wilson et al., 2008a) mounted on the 15-meter James Clerk Maxwell Telescope (JCMT). The AzTEC/JCMT system results in an approximately Gaussian beam with FWHM $\approx 18\,\mathrm{arcsec}$. The SHADES survey is split between the Lockman

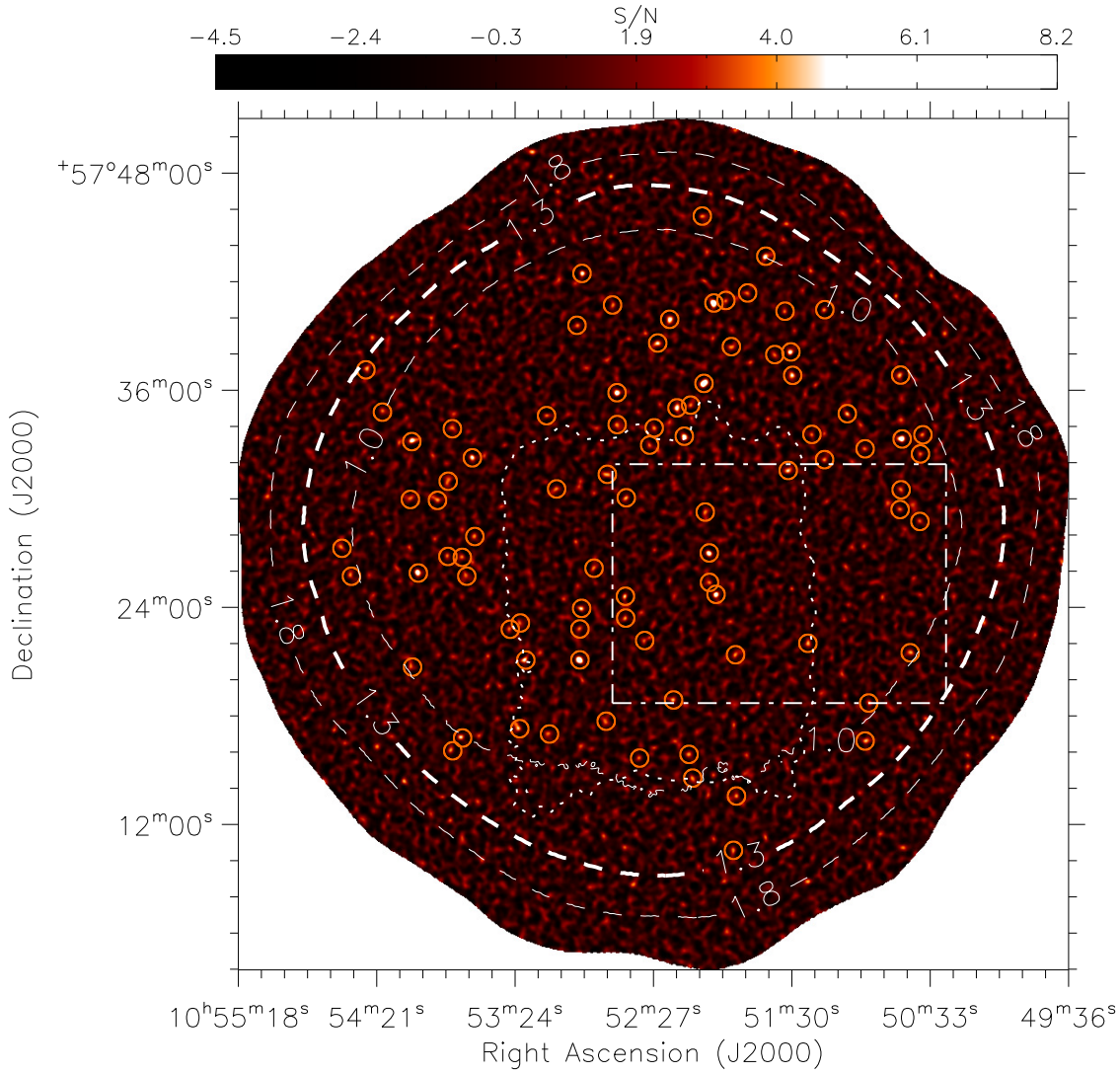

Figure 6.1. AzTEC Signal-to-Noise map of the Lockman Hole East field, observed with an AzTEC/JCMT beamsize of FWHM ≈ 18 arcsec. The most significant source candidates, as defined in the text and listed in Table 6.1, are circled. The observing pattern results in maps that are deepest in the center, with noise increasing towards the edges. Reference contours show the distribution of 1σ depth, in mJy. The maximal extent ($\sigma_{850} \leq 6$ mJy) of the overlapping 850–μm SCUBA/SHADES survey is depicted by the dotted curve. AzTEC/LH has 0.45 deg^2 of total displayed area. For analysis purposes, the survey area is trimmed to the region of relatively uniform coverage (thick 1.3 mJy contour), resulting in a 0.31 deg^2 map with noise levels 0.9–1.3 mJy. For comparison in Section 6.5, the approximate size of the similar depth 1.1–mm AzTEC/GOODS-N survey (0.068 deg^2; Perera et al., 2008) is represented by the dash-dotted rectangle; however, these surveys do not actually overlap on the sky.

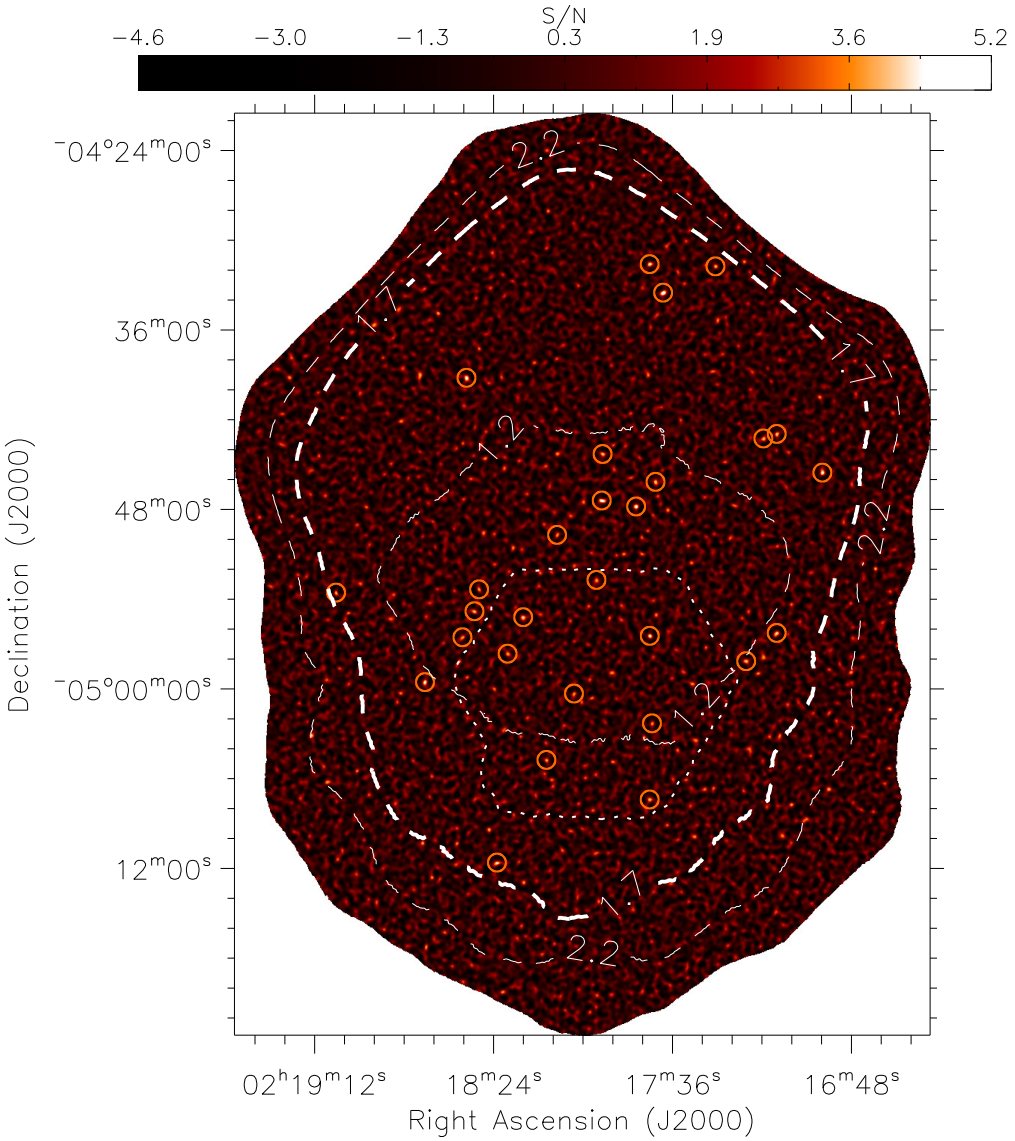

Figure 6.2. AzTEC Signal-to-Noise map of the Subaru/XMM-Newton Deep Field (SXDF), observed with an AzTEC/JCMT beamsize of FWHM $\approx$ 18 arcsec. The most significant source candidates, as defined in the text and listed in Table 6.2, are circled. The observing pattern results in maps that are deepest in the center, with noise increasing towards the edges. Reference contours show the distribution of 1σ depth, in mJy. The maximal extent ($\sigma_{850} \leq 6$ mJy) of the overlapping 850–μm SCUBA/SHADES survey is depicted by the dotted curves. AzTEC/SXDF S/N map covers a total of 0.59 deg^2, with the trimmed analysis region (thick 1.7 mJy contour) covering 0.37 deg^2 with noise levels 1.0–1.7 mJy. Note that flux scale is different than the AzTEC/LH map in Figure 6.1.

Hole East field (LH; $10^{\rm h}52^{\rm m}$, $+57°00'$) and the Subaru/XMM-Newton Deep Field (SXDF; $02^{\rm h}18^{\rm m}$, $-05°00'$). AzTEC has mapped over 0.7 deg^2 to 1.1 mm depths of 0.9–1.7 mJy between the LH and SXDF fields, including the central 0.13 and 0.11 deg^2, respectively, mapped by SCUBA at 850 μm (Coppin et al., 2006). All AzTEC/-SHADES observations were carried out between November 2005 and January 2006, with over 180 hours of telescope time dedicated to this project, including all overheads.

The AzTEC/SHADES observing strategy is similar to that used for other AzTEC blank-field surveys at the JCMT and is described in detail in previous publications (Scott et al., 2008; Perera et al., 2008). All observations were made while scanning the telescope in elevation in a raster pattern (see Wilson et al., 2008a). Initially, the AzTEC/SHADES observations were made as small 15 arcmin $\times$ 15 arcmin mosaic maps with scan speeds of 90–120 arcsec s^{-1}. Later observations were extended to cover an entire field in one continuous observation of size 35 arcmin $\times$ 35 arcmin, which served to reduce observational overheads. Faster scan speeds of 180–220 arcsec s^{-1} were used for these longer scans, which increased the effective sensitivity of the observations due to AzTEC's greater sensitivity at these higher temporal frequencies (Wilson et al., 2008a). After full reduction, the larger maps with faster scan-speeds have an observing efficiency of $\sim$ 150 per cent, relative to the smaller maps. In the end, 46 (63) mosaic maps and 65 (34) full maps were used to create the final LH (SXDF) map. These observations were performed over a wide range of atmospheric conditions and elevations (effective opacity at 225 GHz: $0.05 < \tau_{225\rm GHz} < 0.35$) resulting in instantaneous mapping speeds ranging from 8–37 arcmin^2 mJy^{-2} hr^{-1}.

Nightly overhead observations included focusing, load curves, beam maps and pointing observations, all of which are described in the AzTEC instrument paper (Wilson et al., 2008a). Pointing observations of bright point sources (typically $>$ 1 Jy) that lie near the science field being targeted were made every two hours. These

measurements provide small corrections to the JCMT pointing model and are applied using a linear interpolation between the nearest pointing measurements taken before and after each science observation. Flux calibration is performed as described in Wilson et al. (2008a) using the nightly load curves and beam maps of our primary calibration source, Uranus. The error in flux calibration is estimated to be 6–13 per cent on an *individual* observation (Wilson et al., 2008a). The actual error in the final co-added AzTEC/SHADES maps, which comprise observations spanning many nights and calibrations, will be smaller, assuming the calibration uncertainty is normally distributed. These individual error estimates do not include the systematic 5 per cent absolute uncertainty in the flux density of Uranus (Griffin & Orton, 1993).

6.3 Maps and Catalogs

In this section we describe the methods used to construct the 1.1–mm maps and source catalogs. We test the astrometry and calibration of our maps against complementary radio data. We also describe expanded and improved methods for estimating and correcting for flux biases inherent to these surveys and test these estimates against simulations.

6.3.1 Map Making

The time streams of each observation are cleared of intermittent spikes (e.g. cosmic-ray events, instrumental glitches) and have the dominant atmospheric signals removed using the techniques described in Scott et al. (2008). Each observation is then mapped to a 3 arcsec x 3 arcsec grid in RA-Dec that is tangent to the celestial sphere at ($10^{\rm h}51^{\rm m}59^{\rm s}$, $+57°21'43''$) for Lockman Hole and ($02^{\rm h}18^{\rm m}01^{\rm s}$, $-04°59'54''$) for SXDF. These are the same pixel sizes and tangent points used for the SCUBA/-SHADES 850–μm maps, allowing for straightforward comparison of maps in upcom-

ing SHADES publications. All observations are then 'co-added' on the same grid to provide a weighted-average signal map and weight map for each field.

In parallel, we pass a simulated point source (as defined through beam map observations) through the same algorithms to trace and record the effective PSF, or 'point source kernel', in our final maps. We also create five noise-only map realizations of each observation by jack-knifing (randomly multiplying by 1 or -1) each scan (5–15 seconds of data) of the time stream. This process works to remove astronomical signal while preserving the dominant noise properties in the map. One-hundred fully co-added noise maps are then created by randomly selecting a noise realization for each observation and calculating the weighted average in the same manner used to create the co-added signal maps.

An optimal point source filter is applied to our maps utilizing the information contained within the point source kernel and noise map realizations. The filtering techniques used are described in detail in previous AzTEC publications (Scott et al., 2008; Perera et al., 2008). The resulting AzTEC signal-to-noise maps of Lockman Hole and SXDF are shown in figures 6.1–6.2. The thick dashed contour of each map depicts the 50 per cent coverage level, representing a uniformly-covered region that has a noise level within $\sqrt{2}$ of that found in the deep central region of that map and beyond which the survey depth drops off sharply – a consequence of the particular observation modes employed. The AzTEC/SHADES maps are trimmed at this 50 per cent coverage level for all analysis in the following sections. The trimmed maps have total sizes of $0.31\,\mathrm{deg}^2$ and $0.37\,\mathrm{deg}^2$ for LH and SXDF, respectively, and correspond to depths of $0.9 < \sigma_{\mathrm{lh}} < 1.3\,\mathrm{mJy}$ and $1.0 < \sigma_{\mathrm{sxdf}} < 1.7\,\mathrm{mJy}$. The SXDF map is larger and shallower than that of Lockman Hole due to an observation script error that led to some individual maps being offset in declination. We continued to observe the resulting extended SXDF region after discovery of the error in order to maximize the usefulness of our entire data set.

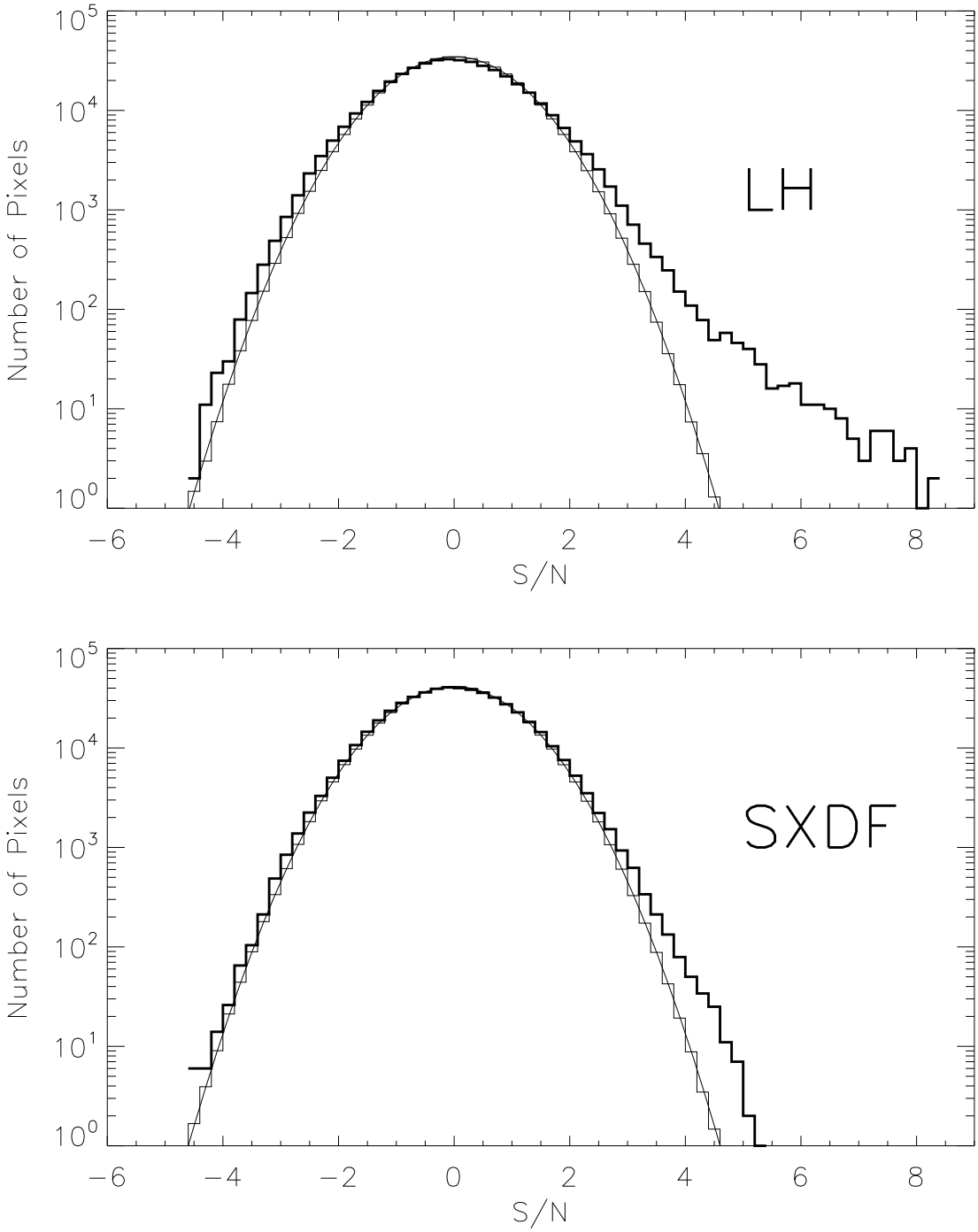

Figure 6.3. Pixel signal-to-noise (S/N) histograms of the LH and SXDF maps (thick histograms) and average of their respective noise map realizations (thin histograms). The noise-only maps are well described as a Gaussian (smooth curve), while the signal maps are distorted by the presence of sources. Sources affect both the positive and negative flux distribution due to the AC-coupled nature of AzTEC maps and, consequently, sources have a zero mean response. Histograms are of pixels falling within the 'well covered' region, as depicted in the thick contours of Figures 6.1–6.2.

The optimal filter is also applied to the co-added point source kernel and noise maps in order to provide the best model of the point source response and accurate estimates of the noise properties in our final maps. As shown in Figure 6.3 and for previously published AzTEC/JCMT maps (Scott et al., 2008; Perera et al., 2008), these noise-only maps confirm a highly Gaussian nature of the underlying noise in the AzTEC/SHADES data. Accurate representations of the filtered point source kernel and the noise properties of the maps are critical components of the simulations described throughout this paper.

6.3.2 Astrometry

We have checked the astrometric accuracy of the AzTEC/SHADES maps by stacking (i.e. averaging) the AzTEC flux at the positions of radio sources in these fields (techniques described in detail in Scott et al., 2008). We use a re-reduction of the archival VLA 1.4 GHz continuum data in the Lockman Hole field (Ibar et al., 2009) to generate a catalog of radio sources in the AzTEC/LH field and we utilize the 100 μJy catalog of Simpson et al. (2006) in the AzTEC/SXDF field. These catalogs result in stacked detections of significance $11\,\sigma$ and $7\,\sigma$ for AzTEC/LH and AzTEC/SXDF, respectively. The stacked data are consistent with no systematic astrometric offset in either map (e.g. Figure 6.4) with the possible exception of a small offset in declination, $+2.9 \pm 1.3$ arcsec, in the AzTEC/SXDF field. Due to the low significance and relatively small size of this potential offset, no correction is applied to the map.

We can also constrain the random astrometric errors across the AzTEC maps by measuring the broadening of the stacked signal compared to the AzTEC point-source response (see Scott et al., 2008). This broadening suggests that the random radial pointing error RMS is $\sigma_{\rm p} \lesssim 4$ arcsec for both fields. Broadening of the stacked signal is also caused by pointing errors in individual AzTEC observations (final maps are co-additions of dozens of such observations) and clustering of the radio sources; therefore,

$\sigma_{\rm p} < 4\,$arcsec provides a strong upper limit to the random astrometric errors in the AzTEC/SHADES maps.

6.3.3 Calibration Checks

Flux density calibration was performed on a nightly basis as described in Section 6.2. All steps in producing the AzTEC/SHADES maps were performed by the AzTEC instrument team (Wilson et al., 2008a) and are identical to those employed for other published AzTEC data sets (Scott et al., 2008; Perera et al., 2008), thus minimizing systematic differences between these AzTEC surveys. Flux calibration is expected to be consistent across all regions of the final AzTEC/SHADES maps, with each point being sampled numerous times by each of a large set ($\gg 10$) of observations that span a wide range of atmospheric conditions and calibrations.

We find no significant systematics between individual observations, including between the small mosaic and large full-map observations. Noise properties are consistent across individual observations, with mapping speeds following the correlation with atmospheric opacity described in Wilson et al. (2008a). The methods used to remove atmospheric signal (Perera et al., 2008) produce consistent point source kernels (shape and amplitude) across all observations, with the resulting attenuation of point sources (which is corrected for in the final map based on the average attenuation) varying about the mean with an RMS of 3.6 per cent.

We also use the stacking analysis of Section 6.3.2 as a check of the relative calibrations between fields based on the average mm-wave flux of known radio populations. We find that the calibrations of the AzTEC/SHADES fields are consistent; the average 1.1–mm fluxes at the location of $S_{1.4\rm GHz} > 100\,\mu$Jy radio sources are $0.59 \pm 0.09\,$mJy and $0.50 \pm 0.07\,$mJy for the LH and SXDF maps, respectively. If we remove radio sources that fall within 9 arcseconds of significant AzTEC 'sources' with $S/N \geq 3.5$ or $S/N \leq -3.5$ from the stacking analysis, we find that the stacked average

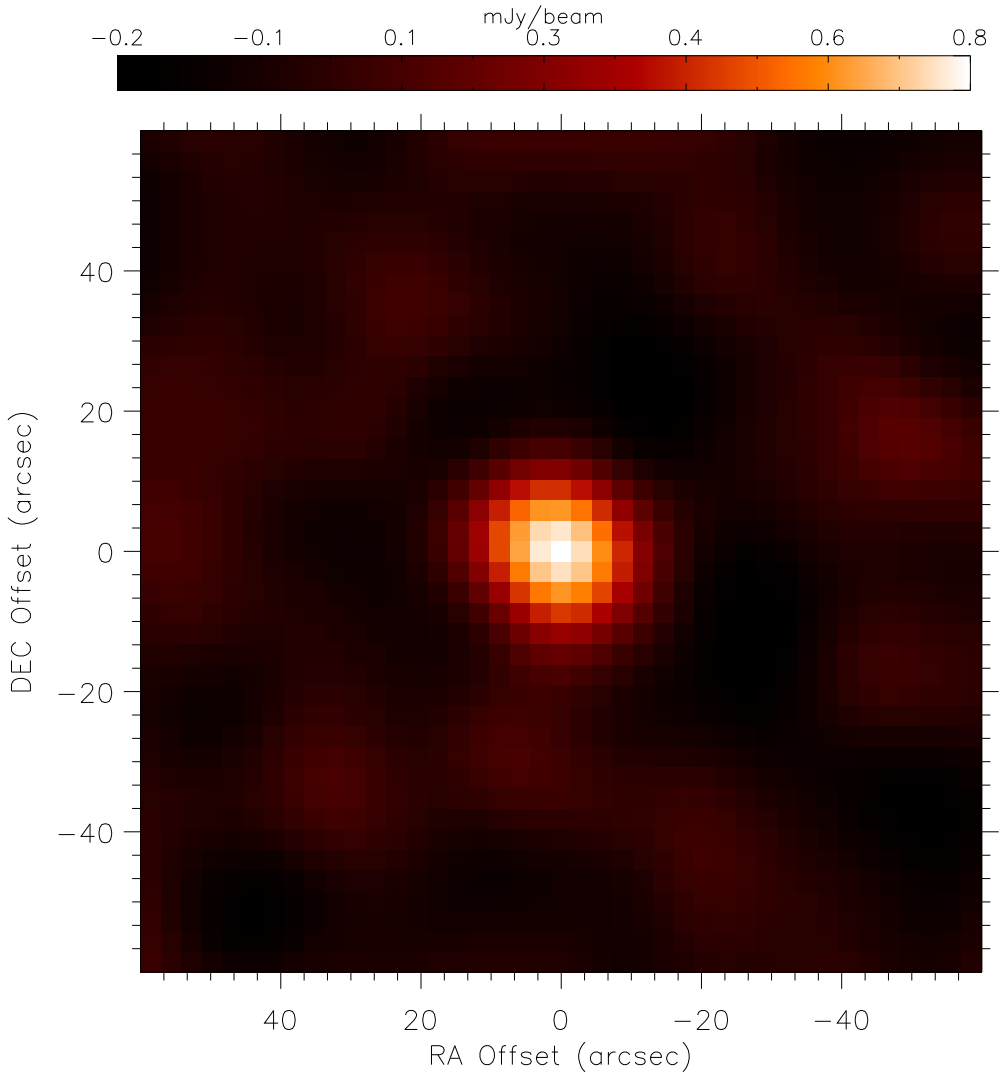

Figure 6.4. Stacked 1.1 mm flux (i.e. noise weighted average) of radio identified sources in the AzTEC/LH map. Only radio sources with 1.4 GHz fluxes $> 66\mu$Jy are considered for this particular stack, with radio sources taken from the catalog of Ibar et al. (2009). This (and other) stacked images on previously known populations help confirm that there are no systematic offsets in the astrometry of AzTEC/SHADES maps (Section 6.3.2). The stacked (i.e. averaged) flux of a well defined population can be compared to that found in other 1.1 mm surveys as a sanity check on the overall calibration, although there is no guarantee that the various surveyed regions host the same source populations (Section 6.3.3).

1.1–mm flux becomes $400 \pm 100\,\mu$Jy and $430 \pm 70\,\mu$Jy for LH and SXDF, respectively. We also utilize the deeper radio catalog available for the LH field to determine that the average 1.1–mm flux of millimeter-dim $S_{1.4\mathrm{GHz}} > 66\,\mu$Jy radio sources is $528 \pm 71\,\mu$Jy, which is consistent with similar stacks of the AzTEC/COSMOS ($530 \pm 87\,\mu$Jy; Scott et al., 2008) and AzTEC/GOODS-N ($439 \pm 107\,\mu$Jy; using the radio catalog of Biggs & Ivison, 2006 and the AzTEC map of Perera et al., 2008) surveys. Assuming the various fields have similar radio populations, which may not be strictly true for fields with significant structure (e.g. AzTEC/COSMOS; Austermann et al., 2009), these tests show that the calibration across various AzTEC surveys is consistent within the measurement errors of the stacks. Note that since the available radio catalog does not cover the entire AzTEC/LH field, we stack only on radio sources found in deep regions of the radio survey ($\sigma_{1.4\mathrm{GHz}} < 13\,\mu$Jy) to ensure a uniform sampling of $S_{1.4\mathrm{GHz}} > 66\,\mu$Jy sources.

6.3.4 Catalogs

The AzTEC/SHADES maps clearly show the signature of significant mm-wave sources, as shown in Figure 6.3. Candidate mm-wave sources are identified as local maxima in the optimally filtered maps that pass a chosen threshold. Although it is possible that some local maxima could be due to multiple neighboring sources (relative to the FWHM ≈ 18 arcsec beamsize) that blend into one peak, the low S/N of most detections prohibits deconvolution of potential multi-source peaks. AzTEC maps are mean-subtracted (i.e. the background has a zero net contribution) and SMGs are expected to be sparse, with less than one source per AzTEC/JCMT beam down to < 0.1 mJy; therefore, source blending is expected to be rare for bright sources in the AzTEC/SHADES survey, unless the SMG population is significantly clustered on scales smaller than 18 arcseconds.

The most robust AzTEC/SHADES source candidates are given in Tables 6.1–6.2. Source candidates are listed in descending order of detected S/N. Centroid source positions are determined using flux-squared weighting of the pixels within 9 arcsec (FWHM/2) of the local maxima. The AzTEC/SHADES survey detects 43 and 21 robust sources with $S/N \geq 4$ in the LH and SXDF fields, respectively. Additional significant detections, as defined in Section 6.3.6, are also listed in the source tables and considered in the analysis of Section 6.4. Multi-wavelength analysis of sources found in the AzTEC/SHADES survey, including combined 850 μm/1100 μm properties of sources within the overlapping AzTEC and SCUBA SHADES surveys (Negrello et al., in prep.), is deferred to future publications.

6.3.5 Flux corrections

Sources discovered in these blind surveys experience two notable flux biases, both of which cause the average measurement of the flux density of a source to be high relative to its true intrinsic flux, $S_{\rm i}$. These flux biases can be very significant ($\sim$ 10–50 per cent for sources listed in Tables 6.1–6.2), particularly for the low-significance detections that typify SMG surveys. Therefore, it is important to characterize and correct for these biases before fluxes and number counts can be compared to measurements at other wavelengths. Since these biases are a function of survey depth, these corrections are also necessary before detailed comparisons can be made with other 1.1 mm surveys.

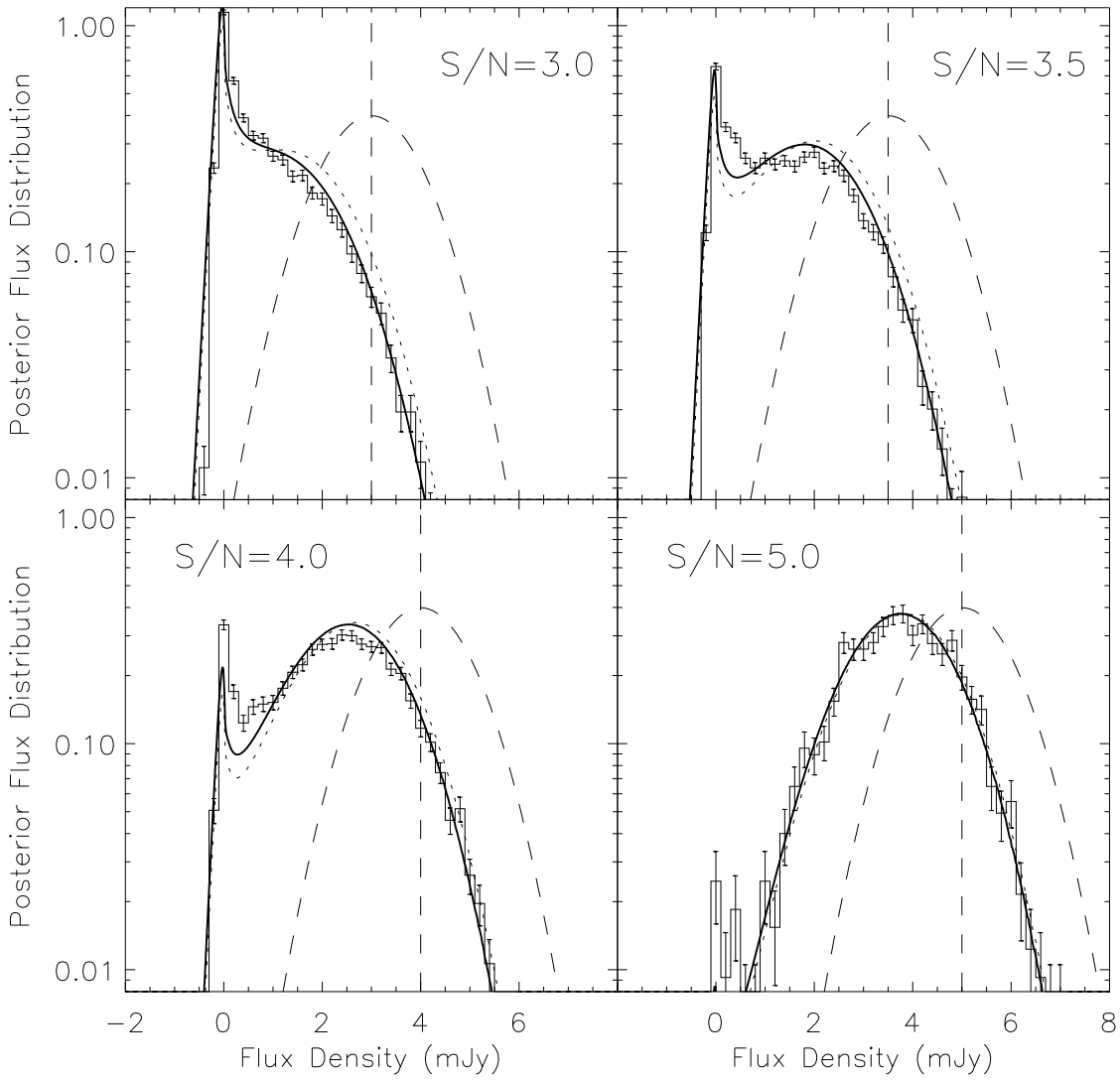

Figure 6.5. Bayesian posterior flux density (PFD; solid curve) compared to the intrinsic flux distribution recovered through simulation (histogram with 1σ Poisson errors of simulation) for sources detected at the significance listed and at a noise level of $\sigma_{\rm m} = 1.0\,{\rm mJy}$. Also shown are the Bayesian predictions without the correction for the bias to peak locations in the map (dotted curves). The dashed vertical line represents the raw measured flux, $S_{\rm m}$, while the dashed curve represents the Gaussian probability distribution that might otherwise be assumed without flux boosting and/or false detection considerations. Negative flux probabilities are allowable through the zero-mean AzTEC point-source kernel and effectively represent the probability of a null detection.

Table 6.1. AzTEC Lockman Hole East (LH) Sources

Source Location	Nickname	S/N	$S_{1.1\mathrm{mm}}$ (measured) (mJy)	$S_{1.1\mathrm{mm}}$ (corrected) (mJy)	$P(S_{1.1} < 0)$	SCUBA Counterpart
J105201.98+574049.3	AzLOCK.1	8.2	7.4 ± 0.9	$6.6^{+0.9}_{-1.0}$	0.000	
J105206.08+573622.6	AzLOCK.2	8.2	7.2 ± 0.9	$6.4^{+0.9}_{-0.9}$	0.000	
J105257.18+572105.9	AzLOCK.3	7.5	7.2 ± 1.0	$6.2^{+1.1}_{-0.9}$	0.000	LOCK850.02
J105044.47+573318.3	AzLOCK.4	6.7	6.2 ± 0.9	$5.3^{+0.9}_{-1.0}$	0.000	
J105403.76+572553.7	AzLOCK.5	6.4	5.9 ± 0.9	$4.9^{+1.0}_{-0.9}$	0.000	
J105241.89+573551.7	AzLOCK.6	6.2	5.6 ± 0.9	$4.8^{+0.8}_{-1.0}$	0.000	
J105203.89+572700.5	AzLOCK.7	6.0	5.7 ± 0.9	$4.8^{+0.9}_{-1.1}$	0.000	LOCK850.04
J105201.14+572443.0	AzLOCK.8	6.0	5.6 ± 0.9	$4.7^{+1.0}_{-1.0}$	0.000	LOCK850.01
J105214.22+573327.4	AzLOCK.9	5.7	5.0 ± 0.9	$4.1^{+0.9}_{-0.9}$	0.000	LOCK850.34
J105406.44+573309.6	AzLOCK.10	5.5	5.1 ± 0.9	$4.1^{+0.9}_{-1.0}$	0.000	
J105130.29+573807.2	AzLOCK.11	5.4	4.8 ± 0.9	$3.8^{+1.0}_{-0.9}$	0.000	
J105217.23+573501.4	AzLOCK.12	5.4	4.7 ± 0.9	$3.8^{+0.9}_{-1.0}$	0.000	
J105140.64+574324.6	AzLOCK.13	5.3	5.3 ± 1.0	$4.1^{+1.0}_{-1.1}$	0.000	
J105220.24+573955.1	AzLOCK.14	5.2	4.6 ± 0.9	$3.6^{+0.9}_{-0.9}$	0.000	
J105256.32+574227.5	AzLOCK.15	5.2	4.8 ± 0.9	$3.7^{+0.9}_{-1.0}$	0.000	
J105341.50+573215.9	AzLOCK.16	5.2	4.7 ± 0.9	$3.7^{+1.0}_{-1.0}$	0.000	
J105319.47+572105.3	AzLOCK.17	5.0	4.7 ± 0.9	$3.6^{+1.0}_{-1.0}$	0.001	LOCK850.15
J105225.16+573836.7	AzLOCK.18	4.8	4.2 ± 0.9	$3.2^{+1.0}_{-0.9}$	0.001	
J105129.55+573649.2	AzLOCK.19	4.8	4.3 ± 0.9	$3.2^{+1.0}_{-0.9}$	0.002	
J105345.53+571647.0	AzLOCK.20	4.7	4.7 ± 1.0	$3.4^{+1.1}_{-1.1}$	0.004	
J105131.41+573134.1	AzLOCK.21	4.7	4.1 ± 0.9	$3.1^{+0.9}_{-1.0}$	0.003	LOCK850.13
J105256.49+572356.7	AzLOCK.22	4.7	4.5 ± 1.0	$3.2^{+1.1}_{-1.0}$	0.004	LOCK850.43
J105321.96+571717.8	AzLOCK.23	4.5	4.4 ± 1.0	$3.1^{+1.0}_{-1.1}$	0.007	
J105238.46+572436.8	AzLOCK.24	4.5	4.3 ± 0.9	$3.0^{+1.0}_{-1.1}$	0.007	LOCK850.03
J105107.06+573442.2	AzLOCK.25	4.4	3.9 ± 0.9	$2.7^{+1.0}_{-0.9}$	0.008	
J105059.75+571636.7	AzLOCK.26	4.3	4.6 ± 1.0	$3.1^{+1.1}_{-1.3}$	0.016	
J105218.64+571852.9	AzLOCK.27	4.3	4.3 ± 1.0	$2.9^{+1.1}_{-1.1}$	0.013	
J105045.11+573650.4	AzLOCK.28	4.3	4.1 ± 1.0	$2.7^{+1.1}_{-1.1}$	0.015	
J105123.33+572200.8	AzLOCK.29	4.2	4.0 ± 0.9	$2.7^{+1.1}_{-1.1}$	0.016	
J105238.09+573003.4	AzLOCK.30	4.2	3.8 ± 0.9	$2.6^{+0.9}_{-1.1}$	0.014	
J105425.31+573707.8	AzLOCK.31	4.2	5.2 ± 1.2	$3.1^{+1.4}_{-1.6}$	0.038	
J105041.16+572129.6	AzLOCK.32	4.2	4.1 ± 1.0	$2.7^{+1.1}_{-1.2}$	0.020	
J105245.93+573121.2	AzLOCK.33	4.2	3.8 ± 0.9	$2.5^{+1.0}_{-1.0}$	0.016	LOCK850.52
J105238.35+572324.4	AzLOCK.34	4.1	4.0 ± 1.0	$2.6^{+1.0}_{-1.2}$	0.023	
J105355.84+572954.7	AzLOCK.35	4.1	3.7 ± 0.9	$2.5^{+1.0}_{-1.1}$	0.021	
J105349.58+571604.3	AzLOCK.36	4.1	4.3 ± 1.1	$2.7^{+1.2}_{-1.3}$	0.032	
J105152.72+571334.5	AzLOCK.37	4.1	4.1 ± 1.0	$2.6^{+1.1}_{-1.3}$	0.033	
J105116.44+573209.9	AzLOCK.38	4.0	3.5 ± 0.9	$2.4^{+1.0}_{-1.1}$	0.025	
J105212.26+571552.5	AzLOCK.39	4.0	4.0 ± 1.0	$2.5^{+1.1}_{-1.3}$	0.035	
J105226.58+573355.0	AzLOCK.40	4.0	3.5 ± 0.9	$2.3^{+1.0}_{-1.0}$	0.026	
J105116.34+574027.3	AzLOCK.41	4.0	3.7 ± 0.9	$2.4^{+1.1}_{-1.2}$	0.036	
J105058.27+571842.8	AzLOCK.42	4.0	3.9 ± 1.0	$2.4^{+1.2}_{-1.2}$	0.042	
J105153.10+572122.7	AzLOCK.43	4.0	3.8 ± 1.0	$2.4^{+1.1}_{-1.2}$	0.039	LOCK850.79

Table 6.1. (continued)

Source Location	Nickname	S/N	$S_{1.1\mathrm{mm}}$ (measured) (mJy)	$S_{1.1\mathrm{mm}}$ (corrected) (mJy)	$P(S_{1.1} < 0)$	SCUBA Counterpart
J105241.87+573406.1	AzLOCK.44	3.9	3.5 ± 0.9	$2.3^{+1.0}_{-1.1}$	0.033	
J105154.82+573824.6	AzLOCK.45	3.9	3.5 ± 0.9	$2.2^{+1.0}_{-1.1}$	0.035	
J105210.75+571433.8	AzLOCK.46	3.9	3.9 ± 1.0	$2.4^{+1.2}_{-1.3}$	0.047	
J105306.80+573032.7	AzLOCK.47	3.9	3.6 ± 0.9	$2.3^{+1.0}_{-1.2}$	0.037	
J105431.31+572543.3	AzLOCK.48	3.9	4.0 ± 1.0	$2.4^{+1.3}_{-1.3}$	0.052	
J105340.49+572755.0	AzLOCK.49	3.9	3.6 ± 0.9	$2.2^{+1.1}_{-1.1}$	0.039	
J105205.59+572916.1	AzLOCK.50	3.9	3.5 ± 0.9	$2.2^{+1.0}_{-1.2}$	0.042	
J105035.90+573332.1	AzLOCK.51	3.9	3.7 ± 1.0	$2.2^{+1.2}_{-1.2}$	0.050	
J105206.79+574537.5	AzLOCK.52	3.9	4.2 ± 1.1	$2.4^{+1.3}_{-1.6}$	0.070	
J105435.20+572715.9	AzLOCK.53	3.9	4.0 ± 1.0	$2.4^{+1.2}_{-1.5}$	0.062	
J105351.57+572648.8	AzLOCK.54	3.8	3.5 ± 0.9	$2.1^{+1.1}_{-1.2}$	0.050	
J105153.94+571034.3	AzLOCK.55	3.8	4.6 ± 1.2	$2.4^{+1.3}_{-2.0}$	0.094	
J105203.84+572522.7	AzLOCK.56	3.8	3.6 ± 0.9	$2.1^{+1.1}_{-1.3}$	0.055	LOCK850.06
J105251.38+572609.9	AzLOCK.57	3.8	3.6 ± 0.9	$2.1^{+1.2}_{-1.2}$	0.056	
J105243.78+574042.6	AzLOCK.58	3.8	3.4 ± 0.9	$2.1^{+1.1}_{-1.2}$	0.053	
J105044.92+573030.0	AzLOCK.59	3.8	3.4 ± 0.9	$2.1^{+1.1}_{-1.2}$	0.054	
J105345.63+572645.8	AzLOCK.60	3.8	3.5 ± 0.9	$2.1^{+1.1}_{-1.2}$	0.056	
J105257.19+572248.5	AzLOCK.61	3.8	3.7 ± 1.0	$2.1^{+1.2}_{-1.3}$	0.063	
J105211.61+573510.7	AzLOCK.62	3.8	3.3 ± 0.9	$2.0^{+1.0}_{-1.2}$	0.056	
J105406.14+572042.0	AzLOCK.63	3.7	3.7 ± 1.0	$2.1^{+1.2}_{-1.4}$	0.074	
J105310.94+573435.6	AzLOCK.64	3.7	3.3 ± 0.9	$2.0^{+1.1}_{-1.2}$	0.059	
J105258.39+573935.4	AzLOCK.65	3.7	3.4 ± 0.9	$2.0^{+1.1}_{-1.2}$	0.061	
J105351.46+573058.2	AzLOCK.66	3.7	3.4 ± 0.9	$2.0^{+1.1}_{-1.2}$	0.064	
J105045.33+572924.4	AzLOCK.67	3.7	3.4 ± 0.9	$1.9^{+1.1}_{-1.2}$	0.065	
J105325.86+572247.3	AzLOCK.68	3.7	3.5 ± 0.9	$2.0^{+1.1}_{-1.3}$	0.071	
J105059.74+573245.6	AzLOCK.69	3.7	3.3 ± 0.9	$1.9^{+1.1}_{-1.2}$	0.064	
J105121.65+573333.6	AzLOCK.70	3.7	3.2 ± 0.9	$1.9^{+1.0}_{-1.2}$	0.064	
J105407.02+572957.7	AzLOCK.71	3.7	3.4 ± 0.9	$1.9^{+1.1}_{-1.3}$	0.071	
J105132.73+574022.1	AzLOCK.72	3.7	3.4 ± 0.9	$1.9^{+1.1}_{-1.2}$	0.069	
J105157.08+574057.6	AzLOCK.73	3.7	3.3 ± 0.9	$1.9^{+1.1}_{-1.2}$	0.068	
J105246.38+571742.5	AzLOCK.74	3.7	3.6 ± 1.0	$1.9^{+1.2}_{-1.4}$	0.087	
J105309.72+571700.1	AzLOCK.75	3.7	3.6 ± 1.0	$1.9^{+1.2}_{-1.4}$	0.087	
J105228.45+573258.0	AzLOCK.76	3.7	3.2 ± 0.9	$1.9^{+1.0}_{-1.2}$	0.067	
J105148.13+574122.5	AzLOCK.77	3.7	3.3 ± 0.9	$1.9^{+1.1}_{-1.3}$	0.073	
J105349.75+573352.4	AzLOCK.78	3.7	3.4 ± 0.9	$1.9^{+1.1}_{-1.3}$	0.076	
J105232.60+571540.3	AzLOCK.79	3.7	3.6 ± 1.0	$1.9^{+1.2}_{-1.5}$	0.088	
J105418.55+573447.5	AzLOCK.80	3.7	3.7 ± 1.0	$1.9^{+1.1}_{-1.5}$	0.093	
J105321.70+572308.3	AzLOCK.81	3.6	3.4 ± 0.9	$1.9^{+1.1}_{-1.4}$	0.083	
J105136.91+573758.1	AzLOCK.82	3.6	3.2 ± 0.9	$1.8^{+1.0}_{-1.3}$	0.079	
J105343.81+572543.6	AzLOCK.83	3.6	3.3 ± 0.9	$1.8^{+1.0}_{-1.4}$	0.090	
J105230.53+572210.0	AzLOCK.84	3.6	3.4 ± 1.0	$1.8^{+1.0}_{-1.6}$	0.099	LOCK850.14
J105036.93+573228.9	AzLOCK.85	3.6	3.3 ± 0.9	$1.8^{+1.0}_{-1.5}$	0.096	
J105037.18+572844.9	AzLOCK.86	3.6	3.3 ± 0.9	$1.7^{+0.9}_{-1.5}$	0.099	

Table 6.1. (continued)

Source Location	Nickname	S/N	$S_{1.1\mathrm{mm}}$ (measured) (mJy)	$S_{1.1\mathrm{mm}}$ (corrected) (mJy)	$P(S_{1.1} < 0)$	SCUBA Counterpart

Note. — The columns give: 1) AzTEC source location as the RA/DEC centroid position; 2) Nickname; 3) Signal-to-noise of the detection in the AzTEC map; 4) Measured 1.1–mm flux density and error; 5) Flux density and 68 per cent confidence interval, as defined in Section 6.3.6, after corrections for flux boosting and the bias to peak locations in the map; 6) Probability that the source will de-boost to $S_{\mathrm{i}} < 0$ when assuming the AzTEC/SHADES Bayesian prior; and 7) SCUBA identification, if applicable.

The primary flux bias in SMG surveys is commonly referred to as 'flux boosting' and is due to the combination of a source density that increases sharply with decreasing flux and the blind nature of the survey (i.e. sources have previously unknown positions); see Hogg & Turner (1998) for a full description of this effect. We employ an advanced version of the Bayesian methods of Coppin et al. (2005, 2006) to correct for flux boosting and generate a full posterior flux density (PFD) probability distribution for each source candidate. The Bayesian approach requires a prior in the form of the assumed number density of sources projected on the sky (i.e. 'number counts') as a function of flux. We use the iterative method of Austermann et al. (2009) to determine the most appropriate prior. We begin by using the SCUBA/SHADES (Coppin et al., 2006) 850 μm number counts, scaled to 1.1 mm through an initial assumption of the 850/1100 μm flux ratio, as the initial prior. The prior is then iteratively adjusted using the empirical number counts of this survey (Section 6.4.1), which quickly converges within a few iterations. As the widest-area deep millimeter survey to date, these iterative AzTEC/SHADES results provide the best 1.1–mm blank-field source number density prior available.

A second notable flux bias results from sources being defined as local maxima in the map. Since the position of the source is not independently known, nearby positive

Table 6.2. AzTEC Subaru XMM/Newton Deep Field (SXDF) Sources

Source Location	Nickname	S/N	$S_{1.1\mathrm{mm}}$ (measured) (mJy)	$S_{1.1\mathrm{mm}}$ (corrected) (mJy)	$P(S_{1.1} < 0)$	SCUBA Counterpart
J021738.52−043330.3	AzSXDF.1	5.2	7.4 ± 1.4	$5.3^{+1.4}_{-1.7}$	0.002	
J021745.76−044747.8	AzSXDF.2	4.8	5.4 ± 1.1	$4.0^{+1.1}_{-1.3}$	0.003	
J021754.97−044723.9	AzSXDF.3	4.8	5.3 ± 1.1	$3.8^{+1.2}_{-1.2}$	0.004	
J021831.27−043911.9	AzSXDF.4	4.8	6.9 ± 1.4	$4.4^{+1.7}_{-1.6}$	0.011	
J021742.10−045626.7	AzSXDF.5	4.7	5.1 ± 1.1	$3.6^{+1.2}_{-1.2}$	0.005	SXDF850.03
J021842.39−045932.7	AzSXDF.6	4.6	5.8 ± 1.3	$4.0^{+1.3}_{-1.6}$	0.010	
J021655.80−044532.2	AzSXDF.7	4.6	6.3 ± 1.4	$4.0^{+1.6}_{-1.7}$	0.019	
J021742.13−043135.6	AzSXDF.8	4.5	6.4 ± 1.4	$4.0^{+1.6}_{-1.8}$	0.025	
J021823.10−051136.7	AzSXDF.9	4.3	6.9 ± 1.6	$3.8^{+1.9}_{-2.4}$	0.061	
J021816.07−045512.2	AzSXDF.10	4.3	4.7 ± 1.1	$3.1^{+1.2}_{-1.3}$	0.018	SXDF850.29
J021708.04−045615.3	AzSXDF.11	4.3	5.5 ± 1.3	$3.3^{+1.5}_{-1.7}$	0.039	
J021708.03−044256.8	AzSXDF.12	4.2	5.9 ± 1.4	$3.3^{+1.7}_{-1.9}$	0.053	
J021829.13−045448.2	AzSXDF.13	4.2	4.4 ± 1.1	$2.8^{+1.2}_{-1.4}$	0.028	
J021740.55−044609.1	AzSXDF.14	4.1	4.8 ± 1.2	$2.9^{+1.3}_{-1.5}$	0.037	
J021754.76−044417.5	AzSXDF.15	4.1	4.8 ± 1.2	$2.9^{+1.3}_{-1.5}$	0.037	
J021716.24−045808.4	AzSXDF.16	4.1	5.0 ± 1.2	$2.9^{+1.5}_{-1.6}$	0.044	
J021711.62−044315.1	AzSXDF.17	4.1	5.6 ± 1.4	$3.1^{+1.6}_{-2.0}$	0.064	
J021724.48−043144.5	AzSXDF.18	4.1	6.1 ± 1.5	$3.1^{+1.5}_{-2.6}$	0.091	
J021906.24−045333.4	AzSXDF.19	4.0	6.5 ± 1.6	$3.3^{+0.9}_{-3.3}$	0.118^{a}	
J021742.13−050723.4	AzSXDF.20	4.0	5.7 ± 1.4	$2.9^{+1.3}_{-2.6}$	0.096	
J021809.81−050444.8	AzSXDF.21	4.0	5.0 ± 1.3	$2.6^{+1.6}_{-1.8}$	0.070	
J021827.89−045320.5	AzSXDF.22	3.9	4.2 ± 1.1	$2.5^{+1.2}_{-1.5}$	0.057	
J021820.23−045738.7	AzSXDF.23	3.9	4.3 ± 1.1	$2.5^{+1.3}_{-1.6}$	0.060	
J021832.33−045632.7	AzSXDF.24	3.8	4.1 ± 1.1	$2.3^{+1.3}_{-1.5}$	0.065	
J021802.42−050018.4	AzSXDF.25	3.8	4.2 ± 1.1	$2.3^{+1.2}_{-1.7}$	0.081	
J021756.39−045242.5	AzSXDF.26	3.8	4.0 ± 1.1	$2.1^{+1.3}_{-1.5}$	0.076	
J021741.50−050218.0	AzSXDF.27	3.8	4.4 ± 1.2	$2.3^{+1.1}_{-2.0}$	0.096	
J021806.97−044941.9	AzSXDF.28	3.7	3.9 ± 1.1	$2.0^{+1.1}_{-1.7}$	0.091	

Note. — The columns give: 1) AzTEC source location as the RA/DEC centroid position; 2) Nickname; 3) Signal-to-noise of the detection in the AzTEC map; 4) Measured 1.1–mm flux density and error; 5) Flux density and 68 per cent confidence interval, as defined in Section 6.3.6, after corrections for flux boosting and the bias to peak locations in the map; 6) Probability that the source will de-boost to $S_{\mathrm{i}} < 0$ when assuming the AzTEC/SHADES Bayesian prior; and 7) SCUBA identification, if applicable.

a) Source is included in order to have a complete list of candidates with $S/N \geq 4$, despite its relatively high null probability.

noise inevitably induces positional errors and this noise can combine with the off-center beam-convolved flux of the source to outshine the true source being measured, thus resulting in an average positive flux bias in the local maxima being measured. The bias is independent of the aforementioned 'flux boosting' (the Bayesian prior is a noiseless calculation) and is instead a systematic of the actual measurement, as opposed to an effect of the luminosity function being surveyed. This bias to peaks (or 'noise gradient bias', e.g. Ivison et al., 2007) is minimized by optimally filtering the map for point sources, but can still be a significant factor for low-significance sources.

We characterize and quantify the bias to peak locations through 10,000 simulations of the LH and SXDF maps. These simulated maps are generated by populating the noise-only maps with the flux-scaled point source kernel at random locations drawn from a uniform distribution and in accordance with a number counts distribution that is consistent with the final AzTEC/SHADES counts (Section 6.4.1). We generate simulated PFDs by cataloging the input flux ($S_{\rm i}$) associated with each source measurement ($S_{\rm m}$,$\sigma_{\rm m}$) recovered in the simulated maps. These simulated PFDs are compared to the Bayesian estimate to characterize the remaining bias (e.g. Figure 6.5), which comes primarily from the bias to peak locations. Through comparison of the PFDs over the flux range under investigation here ($S_{\rm i} > 1\,{\rm mJy}$) and for detections with $S/N \geq 3$, we find that the average flux bias incurred for an AzTEC/JCMT measurement of ($S_{\rm m}$,$\sigma_{\rm m}$) is well described by the equation

$$b_{\rm peak}(S_{\rm m}, \sigma_{\rm m}) = \frac{\alpha\sigma_{\rm m}}{\sqrt{2\pi}} \exp\left(\frac{-\beta^2 S_{\rm m}^2}{2\sigma_{\rm m}^2}\right) \tag{6.1}$$

with $\alpha = 1$ and $\beta = 0.4$. In this form, the bias is modeled as α effective independent noise elements that lie at a radial distance from the true source that is equivalent to that where the fractional flux of the Gaussian beam (relative to maximum) is β. Although this bias is relatively small in flux, it can have a strong effect on the Bayesian probability densities of low S/N detections (e.g. 50 per cent overestimate

in probability that $S_{\rm i} = S_{\rm m}$ for a $S_{\rm m} = 3 \pm 1\,{\rm mJy}$ measurement; see Figure 6.5). We note that the estimates provided by Equation 6.1 are significantly smaller than the generalized case provided by Equation B19 of Ivison et al. (2007) and are specifically tailored to AzTEC/JCMT scanning observations through simulation. Maps with a significantly different response to point sources (e.g. different beamsize or mapping strategy) may require a reevaluation of the functional form and parameter values of Equation 6.1.

We correct for the bias to peak locations by subtracting $b_{\rm peak}$ from the measured flux, $S_{\rm m}$, before calculating the Bayesian estimated PFD. The differences between the Bayesian PFDs with (solid curves) and without (dashed curves) this secondary bias correction can be seen in Figure 6.5 for several S/N detection levels. Analysis of past surveys typically ignored this bias, but largely avoided its effects by restricting the analysis to only the most significant sources (e.g. $S/N \gtrsim 4$).

The de-boosted flux value listed for each source in Tables 6.1–6.2 is taken as the flux at the PFD local maximum nearest the detected flux, $S_{\rm m}$ (see Figure 6.5). Our improved estimate of the significant biases at work for low significance detections leads to accurate PFDs down to at least $S/N = 3$, thus allowing us to utilize more of the maps' information when conducting the source-list driven number counts analysis of Section 6.4.

6.3.6 Source robustness and false detections

The effects of flux boosting (Section 6.3.5) make S/N a less than ideal measure of source robustness; therefore, we include an estimate of the total probability that the source will de-boost to $S_{\rm i} < 0$, $P(S_{1.1{\rm mm}} < 0)$, as determined from the integrated Bayesian PFD, in the source lists of Tables 6.1–6.2. This provides a better metric than just S/N for the *relative* robustness of the source detections, due to its dependence on both $S_{\rm m}$ and $\sigma_{\rm m}$, rather than just the ratio $S_{\rm m}/\sigma_{\rm m}$ (see also Coppin et al., 2006).

We have restricted Tables 6.1–6.2 to include only the most robust AzTEC/SHADES sources with $P(S_{1.1\mathrm{mm}} < 0) \leq 0.1$. The effective S/N, as a function of σ_{m}, of this 10 per cent 'null-threshold' is plotted in Figure 6.6. We note that the *absolute* value of $P(S_{1.1\mathrm{mm}} < 0)$ is highly sensitive to the Bayesian prior used. For example, if we instead assumed the results of the relatively source-rich AzTEC/GOODS-N survey (Perera et al., 2008) as the Bayesian prior, the number of sources in AzTEC/LH passing the 10 per cent null-threshold increases from 86 to 221. Therefore, it is important to consider the priors used when comparing the number of 'detections' in various surveys of this type. However, we note that the effect of the choice of prior on the resulting number counts (Section 6.4) is much less substantial, as the apparent change in the number of 'detections' is largely counteracted by the survey completeness corresponding to the particular prior used.

The number of false detections in a given source catalog depends strongly on the chosen threshold for what is, and what is not, defined as a source. Due to the relatively large 18 arcsecond beamsize of AzTEC on the JCMT, the AzTEC/SHADES maps are expected to become significantly 'full' of sources (on average one source per beam) when considering the expected high density of sources with 1.1–mm fluxes < 0.1 mJy. Various estimates of the false detection rate of AzTEC/JCMT maps are explored in Perera et al. (2008), who conclude that the average number of significant noise peaks in the jack-knifed noise-only maps provide a conservative overestimate of the number of false detections in the map. The ratio of number of sources in the signal map to the average number found in the corresponding noise-only maps is plotted as a function of null-threshold in Figure 6.7 for the LH and SXDF fields.

6.4 SMG Number Counts

In this section, we present the sky-projected densities of 1.1–mm sources in the AzTEC/SHADES survey and the methods by which they are determined. These

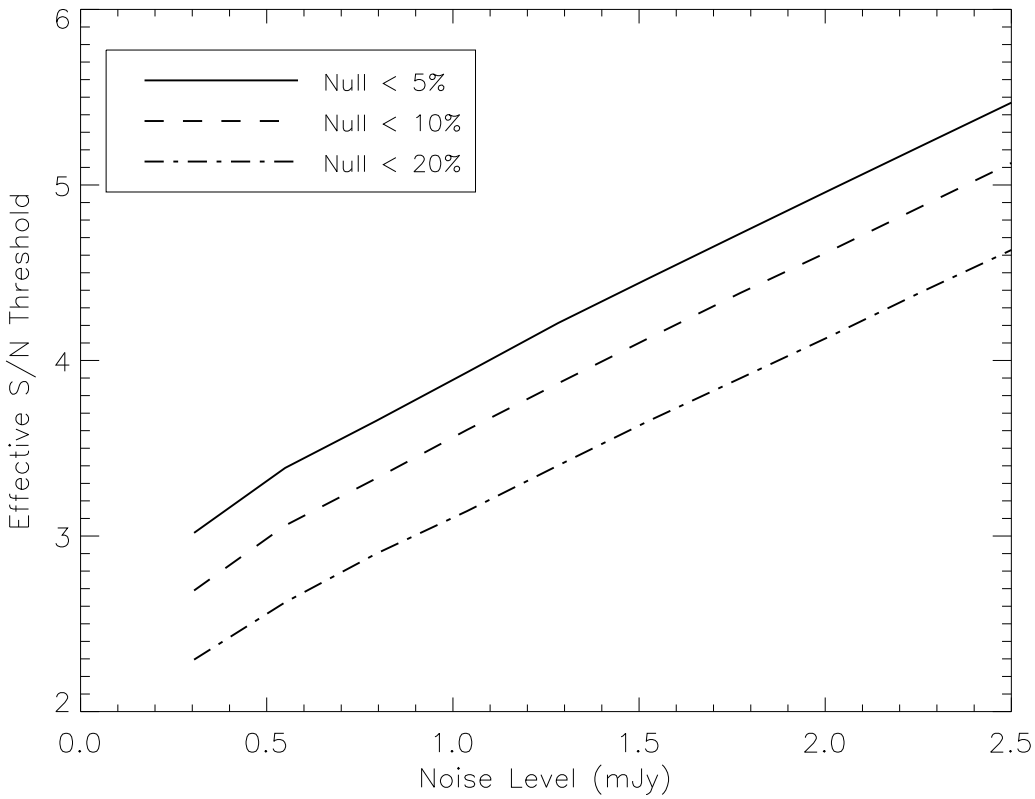

Figure 6.6. Effective S/N threshold as a function of noise level for the given null-threshold values when assuming the AzTEC/SHADES number counts as the Bayesian prior. These curves represent constant levels of robustness for an SMG detection using AzTEC/JCMT data. These values are unique to the particular Bayesian prior (number counts) assumed.

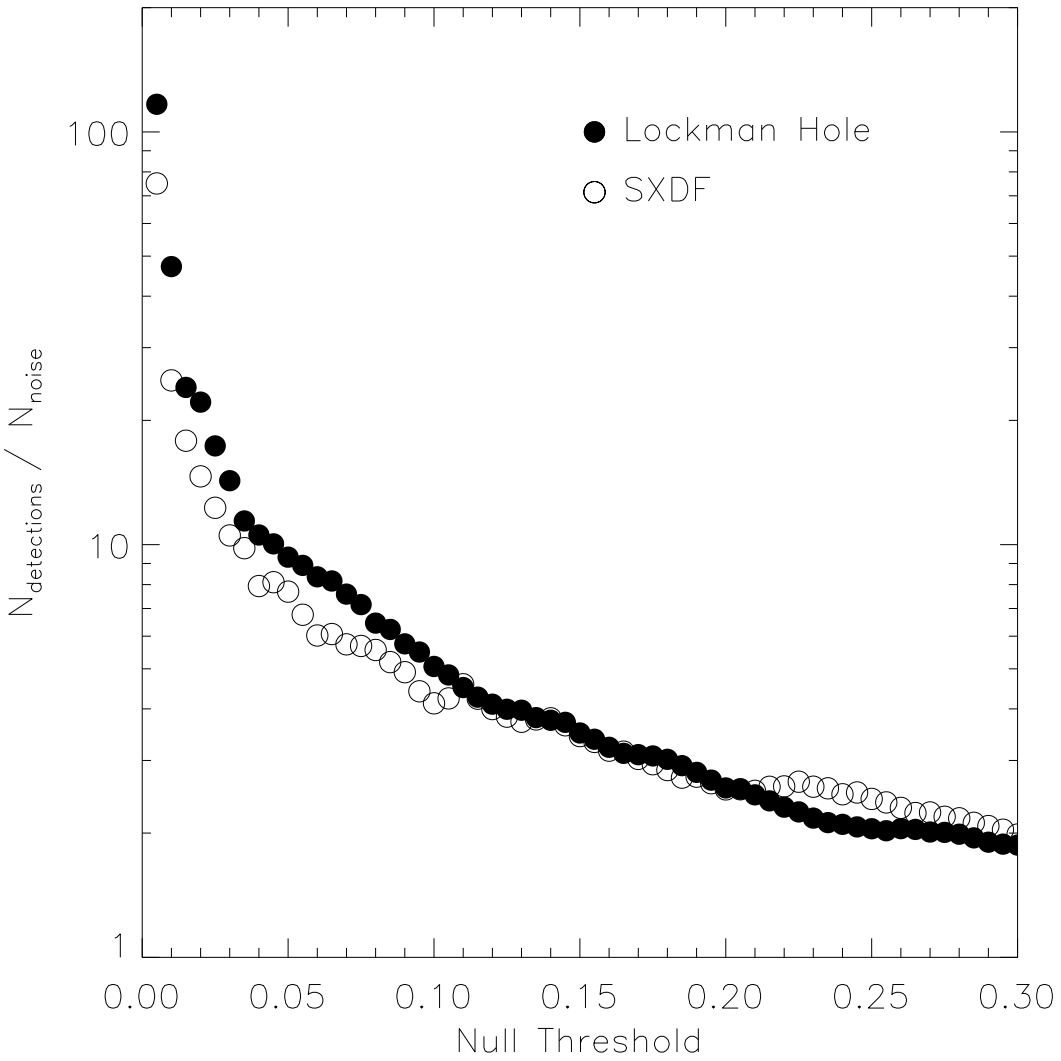

Figure 6.7. Ratio of the total number of detections to the number of significant noise-only peaks as a function of null-threshold for the 50 per cent coverage region of AzTEC/LH and AzTEC/SXDF. This provides an estimate of the relative number of false detections expected beyond a given source threshold, i.e. below a given null-threshold.

methods represent an extended and improved version of the algorithms outlined in the SCUBA/SHADES number counts paper (Coppin et al., 2006). In Section 6.4.3 we provide parametric fits to the number count results of the combined surveys. These number count results provide a useful measure of the SMG population through which we compare those found in other fields, at different wavelengths, and that predicted by various models and simulations (Section 6.5).

6.4.1 Number counts: algorithm and results

We calculate source number counts using the bootstrap sampling methods outlined in Austermann et al. (2009), which are motivated by those used to determine the SCUBA/SHADES number counts (Coppin et al., 2006). In this method, the catalogs of continuous source PFDs are sampled at random and with replacement (e.g. Press et al., 1992) in order to determine specific intrinsic fluxes for the sources in the catalog. These samples are binned to produce both differential and integral source counts as a function of intrinsic flux. This sampling process is repeated 100,000 times to provide sufficient sampling of the source count probability distribution. Sampling variance is injected by Poisson deviating the number of sources sampled in each of the 100,000 iterations around the actual number of sources detected in the map. Number count results are taken as the mean of each bin and the distribution across the iterations is used to characterize the associated uncertainty. The counts are then corrected for completeness, using estimates derived from simulation, and scaled for survey area. The resulting number counts are then taken as the new Bayesian prior and the entire process, including producing new catalogs of sources and their PFDs, is repeated in the iterative-prior process described in Section 6.3.5. For each iteration of the prior, the number counts are calculated for both the LH and SXDF surveys independently and also for the two surveys combined. The Bayesian prior chosen for the next iteration is always taken as the best fit to the combined result.

This iterative procedure minimizes our bias to the number counts assumed in the Bayesian calculations.

Previous surveys using a similar bootstrapping technique (Coppin et al., 2006; Perera et al., 2008; Austermann et al., 2009) limited the source catalog to those sources with negative flux probability of $P(S_{\rm i} < 0) < 0.05$, i.e. a null-threshold of 5 per cent. This null-threshold value was historically used to limit the number of false detections to a near negligible amount and to render the bias to peak locations relatively insignificant. However, the false detection probability is inherently accounted for in the bootstrap sampling method if accurate PFDs are used. As discussed in Section 6.3, our bias corrections result in PFDs that are accurate for all source candidates with $S/N \geq 3$, and possibly lower significance (currently untested below $S/N = 3$). The PFDs are particularly accurate in the $S_{\rm i} \geq 1\,{\rm mJy}$ flux range considered in this analysis. Since the traditional null-threshold of 5 per cent would limit the AzTEC/-SHADES source candidate list to just those with $S/N \gtrsim 4$ (Figure 6.6), we explore fainter sources in the data set with the use of higher null-thresholds that incorporate a larger catalog of source candidates in the derivation of source count densities.

We derive combined AzTEC/SHADES number counts using null-thresholds of 5, 10, and 20 per cent. The 20 per cent threshold represents the lowest significance tested in our simulations (effective $S/N \gtrsim 3$) and safely avoids complications related to source confusion by keeping the density of detections sufficiently low. The results are consistent for all three threshold values tested and the variations between the results are, in general, much smaller than the formal 68 per cent uncertainty of the number count estimates. We have verified through simulation that the use of the higher null-threshold values supplies additional data without introducing any significant biases or systematics (Section 6.4.2).

The combined AzTEC/SHADES differential number counts using 5 per cent (open circles) and 20 per cent (filled circles) thresholds are compared in Figure 6.8. The

two results are nearly identical at high fluxes, but differ slightly in the lower flux bins. The variation at low flux is not surprising given that the additional sources being considered when using the softer 20 per cent threshold are all relatively low in flux, thus providing significantly more data in the lower flux bins. All AzTEC/-SHADES number count uncertainties represent the 68 per cent confidence interval derived from the distribution of bootstrap iterations. All uncertainties assume a spatially random distribution of sources and, therefore, do not account for the effects of cosmic variance/clustering. The differential number counts data points are strongly correlated, as described in Appendix C.1.

Figure 6.9 presents the integral source counts, $N(> S)$, for both the LH and SXDF surveys using the 20 per cent null-threshold. Unlike the finite-bin differential counts measurements, the integral counts are threshold measurements (i.e. number of sources greater than flux, S) and can be derived at continuous values of flux. Therefore, the final combined AzTEC/SHADES results are depicted as a continuous 68 per cent confidence region. The combined differential and integral number counts are also given in Table 6.3, with integral counts listed at integer flux limits.

6.4.2 Simulations and tests

We test for biases and systematics in these techniques by applying the same number count algorithms to simulated maps of model source populations. Simulated maps are constructed as described in Section 6.3.5 and we test a range of input model populations motivated by past 1.1–mm and 850–μm surveys.

Our simulations show that the number counts estimates for any flux bin can be significantly biased towards the assumed value in the Bayesian prior, particularly if that bin is poorly sampled by the catalog of source PFDs used to construct the number counts. We significantly reduce this bias in the lower flux bins by extending the sampled catalog to include fainter source candidates with $P(S_{\rm i} < 0)$ values up to

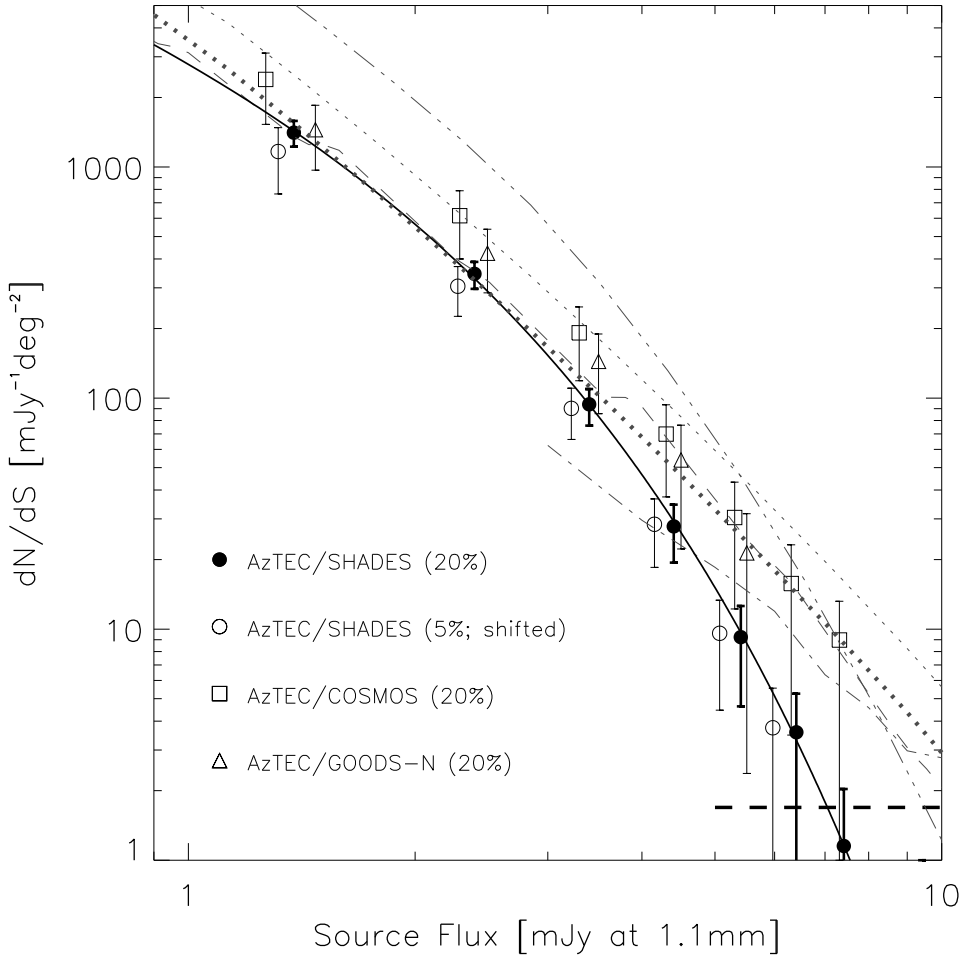

Figure 6.8. Differential number counts for the combined AzTEC/SHADES survey in 1 mJy wide bins. The per cent value in parentheses represents the null-threshold used for each data set. The 5 per cent threshold results of AzTEC/SHADES have been artificially displaced to the left for clarity, but represent the same bins as the 20 per cent threshold results. Number counts for the AzTEC/COSMOS and AzTEC/GOODS-N surveys have been re-calculated using the final AzTEC/SHADES prior (solid curve), while applying the methods of this paper to the data sets of Scott et al. (2008) and Perera et al. (2008), respectively, and are calculated for slightly different bins (i.e. not shifted) for improved clarity. Error bars represent 68 per cent confidence intervals. Bin centers are weighted by the assumed prior (solid curve). The thick horizontal dashed line represents the 'survey limit', defined as the source density that will Poisson deviate to zero sources 32.7 per cent of the time in a survey this size. The dot, dash, dash-dot, and dash-dot-dot-dot curves represent the predictions of Rowan-Robinson (2009), Granato et al. (2004), van Kampen et al. (2005), and Baugh et al. (2005), respectively. The thick and thin dotted curves represent models with high-redshift formation limits of $z_{\rm f} = 4$ and $z_{\rm f} = 5$, respectively.

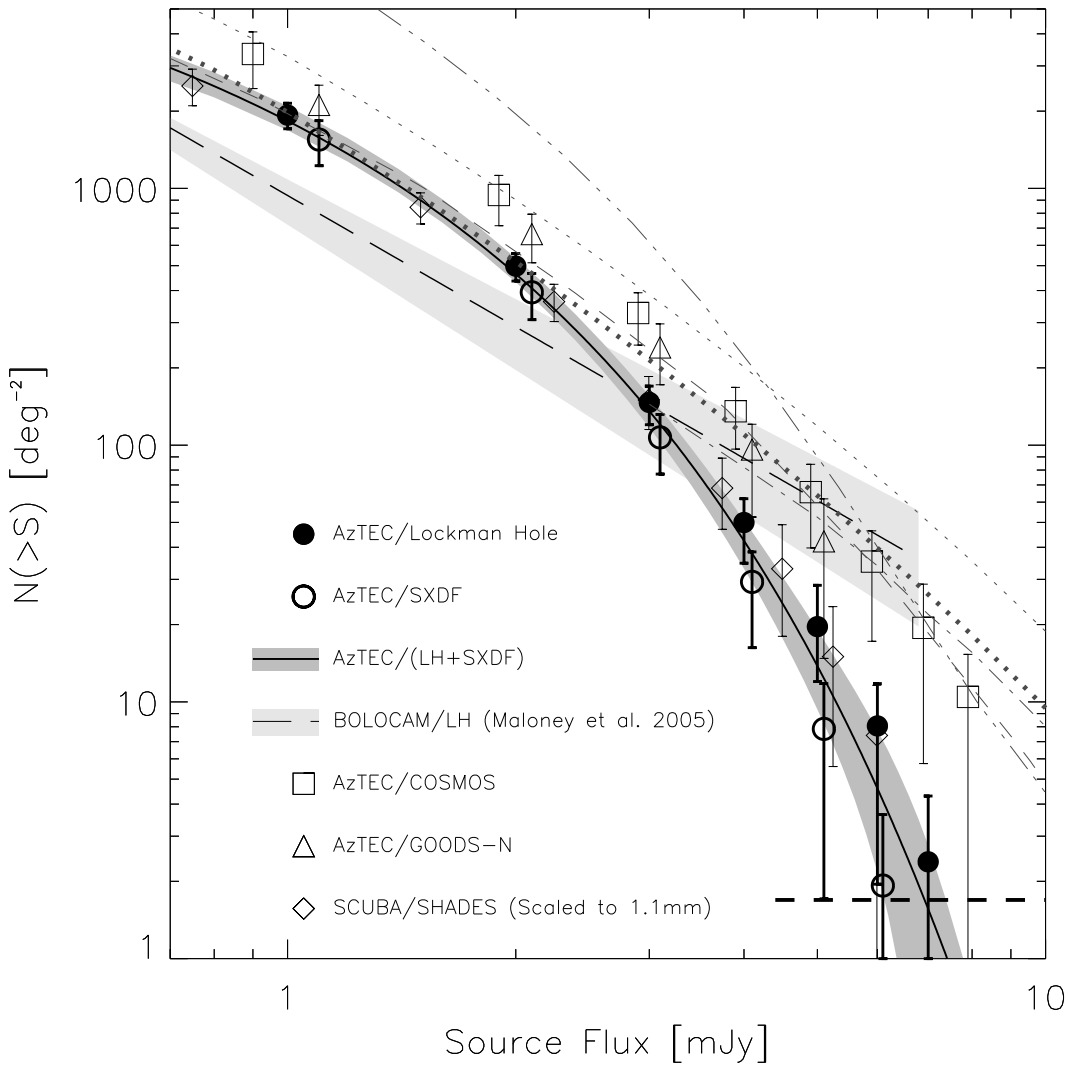

Figure 6.9. Integrated number counts for the AzTEC/LH and AzTEC/SXDF surveys with 68 per cent confidence intervals. Their combined constraint on the average blank-field number counts is shown as a continuous 68 per cent confidence region. A 3-parameter Schechter fit to the combined differential counts (Figure 6.8) is shown as the solid curve. Results of other 1.1–mm surveys are plotted for comparison, with the AzTEC/GOODS-N and AzTEC/COSMOS results being recalculated using the AzTEC/SHADES prior and a 20 per cent null-threshold. The SCUBA/-SHADES results (Coppin et al., 2006) are scaled to 1.1 mm using the combined fits of Section 6.4.3. Discrete integrated number counts data points are calculated at varying flux values (i.e. not shifted) for increased clarity. Model predictions plotted as described in Figure 6.8.

Table 6.3. AzTEC/SHADES Differential and Integral Number Counts

Flux Density (mJy)	dN/dS (mJy^{-1}deg^{-2})	Flux Density (mJy)	N($> S$) (deg^{-2})
1.38	1410^{+170}_{-180}	1.0	1890^{+190}_{-190}
2.40	345^{+44}_{-48}	2.0	481^{+49}_{-51}
3.40	94^{+15}_{-18}	3.0	136^{+18}_{-20}
4.41	28^{+7}_{-8}	4.0	42^{+9}_{-9}
5.41	$9.2^{+3.4}_{-4.6}$	5.0	14^{+4}_{-5}
6.41	$3.6^{+1.7}_{-2.8}$	6.0	$4.9^{+2.5}_{-3.0}$
7.41	$1.2^{+0.9}_{-1.2}$	7.0	$1.3^{+0.5}_{-1.3}$

Note. — The differential number counts flux bins are 1-mJy wide with effective bin centers (first column) weighted according to the assumed prior. Correlations amongst data points are described in Appendix C.1.

20 per cent, thus providing more data in these otherwise poorly sampled bins. This is shown through example in Figure 6.10. Although significant bias to the chosen prior can still be seen in the lowest flux bin (1-2 mJy), this bin is still very sensitive to the 'true' population. Therefore, by iteratively adjusting the prior based on the results (Section 6.3.1), we find that the bulk of this bias can be removed. This general result is also supported through full simulations with a precisely known input population. As expected, the results based solely on the brightest source candidates (null-threshold = 5 per cent; open squares) are more severely biased by the assumed prior at low fluxes.

The primary concerns when considering low-significance sources (e.g. S/N = 3.0) are: (a) false detections (noise peaks); and (b) source confusion (significant contribution from multiple sources in each measurement). However, false detections are inherently accounted for by having accurate PFDs at the intrinsic fluxes being probed, and our simulations show that confusion does not play a significant role at

fluxes $S_{\rm i} > 1\,{\rm mJy}$, based on an extrapolation of measured SMG number counts (e.g. Coppin et al., 2006; Perera et al., 2008; this paper) and the AzTEC/JCMT beamsize (FWHM = 18 arcsec). Using the fitted results of Section 6.4.3, the traditional rule of thumb confusion 'limit' of 1 source per 30 beams ($\Omega_{\rm beam} = \pi\sigma^2_{\rm beam}$; e.g. Hogg, 2001) is $\sim 0.8\,{\rm mJy}$ for AzTEC/JCMT 1.1 mm data and is below the most likely intrinsic fluxes of the individual sources considered here. Most importantly, our simulations find no significant systematics or biases between the input and output number counts of the constructed maps, thus confirming that neither of the above concerns present a problem for the AzTEC/SHADES results as given.

6.4.3 Parametric fits

For simulation and modeling of the SMG population, it is often useful to have a functional form for the number counts result. We fit the AzTEC/SHADES differential number counts to the 3-parameter Schechter function

$$\frac{dN}{dS} = N' \left(\frac{S}{S'}\right)^{\alpha+1} e^{-S/S'}, \tag{6.2}$$

using Levenberg-Marquardt minimization. We convert the normalization parameter N' to the more easily interpreted $N_{\rm 3mJy}$ (the differential counts at $S_{\rm 1.1mm} = 3\,{\rm mJy}$) using the relation

$$N_{\rm 3mJy} = N' \left(\frac{3\,{\rm mJy}}{S'}\right)^{\alpha+1} e^{-3\,{\rm mJy}/S'}. \tag{6.3}$$

The best-fit AzTEC/SHADES parameters are listed in Table 6.4. The table also includes the results of a combined analysis of the currently available AzTEC 'blank-field' surveys AzTEC/SHADES and AzTEC/GOODS-N; however, the addition of the relatively small GOODS-N survey provides only a slight increase in the constraint of the average SMG population. These results are relatively insensitive to the Schechter parameter α, which is strongly anti-correlated to, and somewhat degenerate with, the

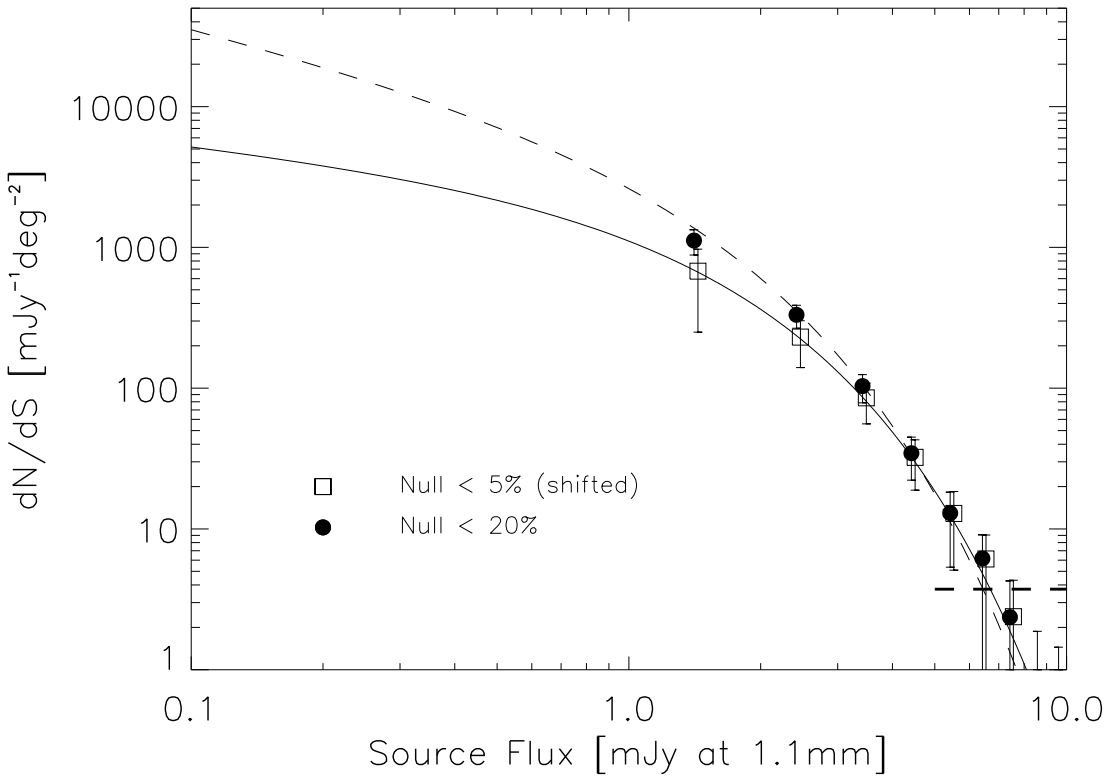

Figure 6.10. Differential number counts of the AzTEC Lockman Hole survey (symbols) for different null-threshold values when assuming a significantly different (and incorrect) prior that predicts a much lower number of faint sources (solid curve). The dashed curve represents the prior used throughout the rest of this paper, which is very near to our best estimate of the true AzTEC/Lockman-Hole number counts. The open symbols have been artificially displaced by +5 per cent along the x-axis for improved clarity.

parameter S' in the flux range sampled ($S_{\rm i} > 1\,{\rm mJy}$). Therefore, we find that the AzTEC/SHADES number counts are nearly as well described by a Schechter function with the α parameter fixed to a reasonable value that is consistent with previous data sets (e.g. $\alpha = -2$; Coppin et al., 2006).

In previous incarnations of the bootstrap sampling method outlined in Section 6.4.1 (Coppin et al., 2006; Perera et al., 2008; Austermann et al., 2009), formal fits to the differential number counts resulted in unrealistically low χ^2 values, due to an underestimate of the correlations between bins. We have now improved the algorithm for calculating the correlation matrix, which is described in Appendix C.1. However, the large correlations amongst the 1 mJy wide AzTEC/SHADES flux bins lead to a level of degeneracy that significantly complicates the application of typical fitting algorithms that incorporate the covariance matrix.

We avoid such complications in the derivation of best-fit statistics by implementing a bootstrap sampling method of parameter uncertainty estimation that is similar to what is used in the error estimation for the individual number count data points (Section 6.4.1). In this method, parameter space is explored by calculating best-fit parameters for *each* of the 100,000 number count bootstrap iterations. Figure 6.11 shows the resulting parameter space for a two-parameter fit to the AzTEC/SHADES results using Equation 6.2 with Schechter parameter α fixed to a value of -2. Marginalized 68 per cent confidence intervals are used for the parameter uncertainties presented in Table 6.4. We find that this alternative approach gives results that are comparable to that of formal fits, while providing a better characterization of the true parameter probability distributions by avoiding assumptions of Gaussian distributed uncertainty in the fitted parameter and number count errors. Since an explicit flux value is chosen for each source upon an individual iteration of the bootstrap (i.e. a single flux is chosen from the source's PFD), the number counts found by each realization have flux bins that are effectively independent; therefore, this method provides a direct

Table 6.4. Parametric Fits to SHADES Number Counts

Data Set	S' (mJy)	$N_{3\mathrm{mJy}}$ ($\mathrm{deg}^{-2}\mathrm{mJy}^{-1}$)	α	α_{dust}
AzTEC/SHADES	$1.11^{+0.09}_{-0.09}$	153^{+9}_{-17}	-2	–
AzTEC/SHADES	$1.03^{+0.11}_{-0.43}$	158^{+16}_{-21}	$-1.8^{+1.1}_{-0.6}$	–
AzTEC/(SHADES+GOODS-N)	$0.96^{+0.25}_{-0.33}$	170^{+15}_{-20}	$-1.56^{+0.65}_{-0.9}$	–
Two-Frequency Fits				
AzTEC+SCUBA SHADES	1.15 ± 0.07	153 ± 12	-2	$(3.81 - 0.24) \pm 0.17$
AzTEC+SCUBA SHADES	1.04 ± 0.21	157 ± 15	-1.75 ± 0.48	$(3.83 - 0.25) \pm 0.17$

Note. — Parametric fits to differential number counts of Table 6.3 using Equation 6.2. Uncertainties of AzTEC-only fits represent the marginalized 68 per cent confidence intervals derived from the distribution of bootstrap iterations (Section 6.4.3). The Schechter parameter α is given in Column 4, and is held constant for fit results given without a confidence interval. The quantity α_{dust} is a free parameter representing the spectral index inferred by the simultaneous fit of the AzTEC/SHADES (1100μm) and SCUBA/SHADES (850 μm) results, as described in the text. Uncertainties of the combined AzTEC and SCUBA fit are the formal 1σ parameter errors when using Levenberg-Marquardt minimization. The additional negative correction listed for α_{dust} represents an estimated correction for the systematic error induced by the SCUBA/SHADES choice of prior, as described in the text. All parameter values are for number counts at 1100μm.

exploration of parameter space without necessitating an explicit calculation of the bin-to-bin correlations that exist amongst the final averaged results of Table 6.3.

Table 6.4 also includes the results of simultaneous fits to the AzTEC/SHADES and published SCUBA/SHADES (Coppin et al., 2006) results, where we have assumed the two surveys are sampling the same source population and that the number counts of the two bands are consistent within an average scaling of flux density. These fits are accomplished through the introduction of a free spectral index parameter, α_{dust}, which we have defined to reflect the average flux ratio between the two observing bands through the relation

$$\frac{S_{850}}{S_{1100}} = \left(\frac{\lambda_{850}}{\lambda_{1100}}\right)^{-\alpha_{\mathrm{dust}}}, \tag{6.4}$$

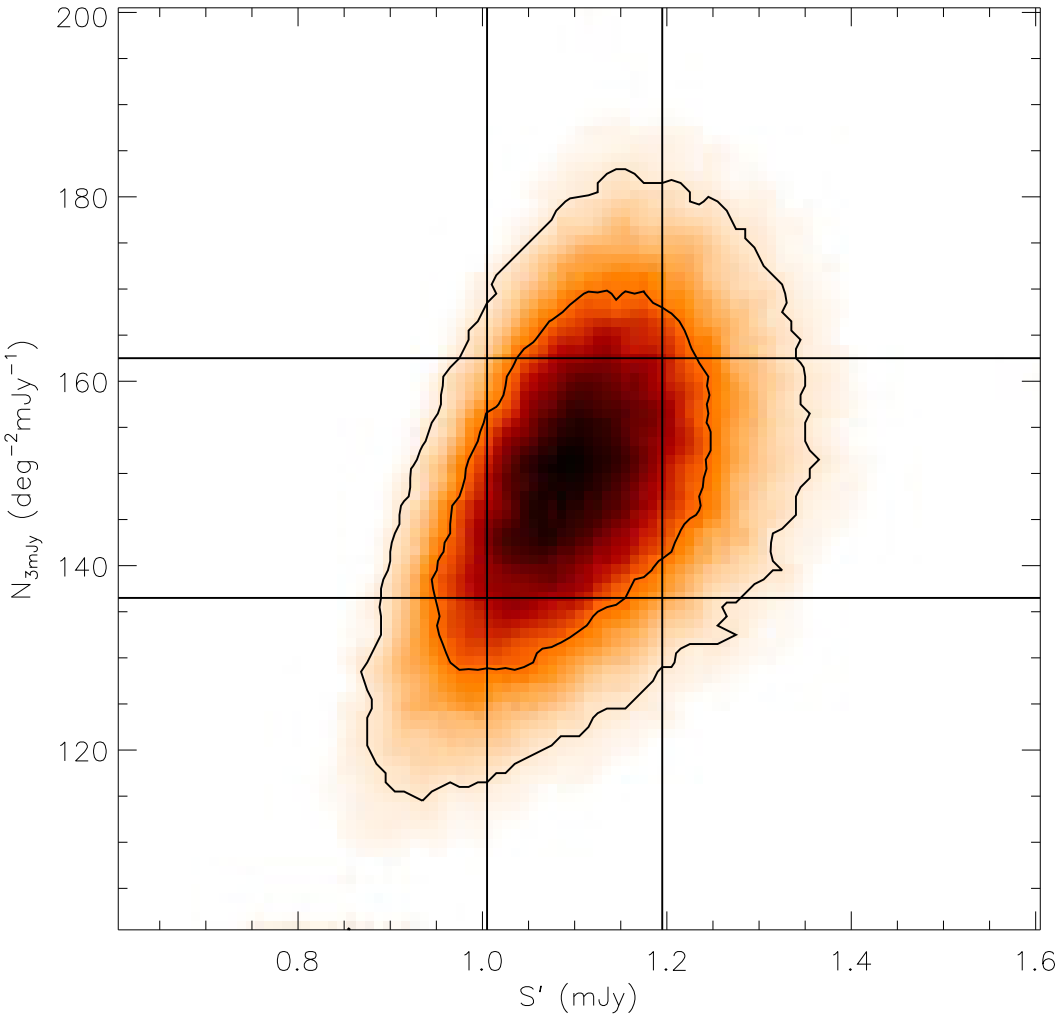

Figure 6.11. Example distribution of best fit results of each iteration of bootstrapped AzTEC/SHADES number counts. Fits are to Equation 6.2 with the Schechter parameter α fixed to -2. Contours represent the 68 and 95 per cent confidence regions. Vertical and horizontal lines represent the marginalized 68 per cent confidence intervals of S' and $N_{3\mathrm{mJy}}$, respectively.

where λ_{850} and λ_{1100} represent the effective center wavelengths of AzTEC and SCUBA, respectively (see also Perera et al., 2008). The combined SHADES fit, assuming the nominal band centers of 850 μm and 1100 μm and using Levenberg-Marquardt minimization, gives $\alpha_{\rm dust} = 3.81 \pm 0.17$ ($S_{850}/S_{1100} = 2.67 \pm 0.12$). The quoted uncertainties do not include systematic errors due to spectral differences between the SMGs and flux calibrators, which is expected to be smaller than the formal 1σ uncertainty given, or the systematic calibration uncertainty of each data set. For optically thin thermal dust emission in the Rayleigh-Jeans limit ($\lambda \gg hc/kT$), $\alpha_{\rm dust}$ represents the dust emissivity index ($\alpha_{\rm dust} = 2 + \beta$); however, the Rayleigh-Jeans approximation is not strictly applicable at these wavelengths due to the expected temperature ($T_{\rm d} \sim 35\,{\rm K}$; e.g. Chapman et al., 2005; Kovács et al., 2006; Coppin et al., 2008) and redshift ($\langle z \rangle \sim 2.2$; e.g. Chapman et al., 2005) of the typical SMG.

We have tested for various other systematics between the two instruments' data sets by recalculating the AzTEC number counts under conditions and assumptions closely matching those existing for the SCUBA/SHADES analysis (Coppin et al., 2006). Since the AzTEC/SHADES survey includes additional mapped area not covered by SCUBA, the comparison of the two surveys may be susceptible to cosmic variance on large scales (i.e. $\gtrsim 0.1\,{\rm deg}^2$). However, we find that there are no significant differences in the results when restricting the AzTEC analysis to only those regions covered by SCUBA. We also find no significant differences when applying the same 5 per cent null-threshold (Section 6.4.1) used in the SCUBA/SHADES analysis. The SCUBA analysis lacks a correction for the bias to peak map locations (Section 6.3.5), however, their use of the conservative 5 per cent null-threshold should keep this bias relatively small and it is expected to have no significant effect on the resultant number counts.

Finally, we note that the SCUBA analysis uses an external Bayesian prior that was based on 850–μm results of the Hubble Deep Field North (Borys et al., 2003), as

opposed to the self-consistent iterative prior used in this paper. This prior represents a slight overabundance of bright SMGs when compared to the SCUBA/SHADES number counts, probably resulting in a small, but systematic, overestimate of the SCUBA/SHADES counts. Although we cannot use the exact same prior as SCUBA without inherently assuming an $850\,\mu$m/$1100\,\mu$m scaling relation (e.g. a value of $\alpha_{\rm dust}$), we can adopt a similar prior that assumes the results of an $1100\,\mu$m survey of the same approximate field (AzTEC/GOODS-N; Perera et al., 2008). We recalculate the AzTEC/SHADES counts with this prior, as well as other matched systematics (5 per cent null-threshold, no correction for peak bias) to re-estimate $\alpha_{\rm dust}$. These values are compared to the previous fits to determine the systematic error estimates given in Table 6.4 and result in a final corrected scaling index of $\alpha_{\rm dust} \approx 3.6 \pm 0.2$. As will be discussed in Section 6.5, this value of $\alpha_{\rm dust}$ is larger than that inferred by current measurements of the SMG redshift distribution (Chapman et al., 2005) and the SEDs of local starbursts (Dunne & Eales, 2001), as well as measurements of SMG 350μm/850μm flux ratios (Kovács et al., 2006; Coppin et al., 2008). This suggests that there may be further systematics between the AzTEC and SCUBA number counts analyses or that our assumptions (i.e. uniform flux ratio and the two wavebands track the same SMG population) are invalid. Analysis of the 850μm/1100μm flux density ratios of individual SHADES sources is deferred to Negrello et al. (in prep.).

6.5 Discussion

6.5.1 Comparison of 1.1 mm surveys

To appreciate the contribution of AzTEC/SHADES to our understanding of the SMG population, it must be compared to previous SMG surveys. The AzTEC/-SHADES integral number counts are in strong disagreement with the parametric results derived from a fluctuation analysis of the 1.1–mm BOLOCAM Lockman Hole survey (dashed line in Figure 6.9, Maloney et al., 2005). The BOLOCAM survey is sig-

nificantly smaller and shallower than this AzTEC/SHADES survey and consequently contains fewer sources and is more susceptible to sample variance. Furthermore, the BOLOCAM fluctuation analysis is likely to be skewed by their requirement that the source population be well described by a single power law, which diverges at zero flux and has since been shown to poorly describe the SMG population over a wide range of flux densities (e.g. Scott et al., 2006; Coppin et al., 2006; this data set) Therefore, the BOLOCAM/LH single power-law result may represent a compromise between the relatively steep drop in SMG number counts at high flux density and the inevitably more moderate slope at the faint end.

Figure 6.9 also shows the integral number counts for the individual AzTEC/LH (filled circles) and AzTEC/SXDF (open circles) fields at specific flux density limits. The two fields' number counts are consistent within their respective uncertainties; however, the overall trend suggests that the AzTEC/LH field is rich in bright ($S_{1.1} \gtrsim 4\,\mathrm{mJy}$) sources relative to AzTEC/SXDF. This difference of bright AzTEC source counts is consistent with the differences seen between the regions of LH and SXDF surveyed by SCUBA at $850\,\mu$m (Coppin et al., 2006).

The effects of cosmic variance appear more prevalent when comparing the results of this survey to the $0.15\,\mathrm{deg}^2$ AzTEC/COSMOS survey (Scott et al., 2008), which targeted a region with significant structure, as traced by the optical/IR galaxy population at $z \lesssim 1.1$ (Scoville et al., 2007b). The average blank-field number counts of AzTEC/SHADES confirm the significant over-density of bright 1.1–mm sources in the AzTEC/COSMOS region first reported in Austermann et al. (2009), who conclude that the observed over-density is probably due to gravitational lensing by foreground ($z \lesssim 1.1$) structure. We have recalculated the AzTEC/COSMOS number counts using the AzTEC/SHADES prior and a 20 per cent null-threshold (Figure 6.9), affirming that the AzTEC/COSMOS over-density is significant regardless of the chosen prior.

We similarly find that the AzTEC/GOODS-N region is relatively rich in 1.1–mm sources compared to the much larger AzTEC/SHADES survey. This is consistent with the relative abundances found in the comparable 850–μm surveys of GOODS-N (Borys et al., 2003) and SHADES (Coppin et al., 2006). The higher number counts of AzTEC/GOODS-N may be due to cosmic variance on the scale of the GOODS-N map ($0.068\,\mathrm{deg}^2$), which can be exemplified by moving a box the size of AzTEC/GOODS-N to different locations within the well-covered, and similar depth, regions of the AzTEC/LH map (e.g. dash-dotted rectangle in Figure 6.1). This simple exercise shows that the total number of source candidates within the GOODS-N sized box can change by a factor of ~ 2 for any of the source definitions explored here (i.e. null-threshold 5–20 per cent). The high number of bright SMGs seen in GOODS-N may be due to structures in the field that have been found to be rich in SMGs (Chapman et al., 2009; Daddi et al., 2009). This richness of (sub-)millimeter sources in the GOODS-N field relative to SHADES is probably responsible for the relatively small value of α_{dust} (2.84 ± 0.32, Perera et al., 2008) derived from these two disjoint surveys (AzTEC/GOODS-N and SCUBA/SHADES) compared to that derived from the overlapping AzTEC/SHADES and SCUBA/SHADES surveys ($\alpha_{\mathrm{dust}} \approx 3.6 \pm 0.2$, Table 6.4), which actually sample much of the same fields.

Recently, evidence has been found that bright SMGs can trace high-redshift mass structures in another AzTEC survey (Tamura et al., accepted to Nature). Upon visual inspection, the sources in the AzTEC/LH map seem to have a potentially structured distribution. This is largely driven by the relative dearth of sources in the north-east and south-west regions of the map (see Figure 6.1), which is particularly true for the distribution of the brightest sources (e.g. $S/N > 4.5$, see Figure 6.12(a)).

While a thorough examination of the possible structured distribution of SMGs in AzTEC/LH is left to a future analysis (e.g. looking for spatial correlations to other high-redshift populations), I present the following first order look into the existence

of a single dominant linear distribution within the map. First a source flux weighted center position is determined for the map. Then the number of sources falling within a rectangular box of a given width (e.g. 4 arcmin) and infinite length is calculated as a function of position angle as the box pivots on the previously determined center position. This same calculation is then done on a large number of simulated maps with a random distribution of the *same* number of sources as the real map. The maximum number of sources falling within the box (any angle) is taken for each simulation to provide the probability distribution for the maximum in-box count expected at random. The number of in-box sources in the real map is then compared to this distribution to determine the probability that the box contains more sources than a random spatial distribution. The results for the $S/N > 4.5$ source distribution and a 4 arcmin wide rectangular test box is shown in Figure 6.12(b), resulting in a maximum probability of an over-density of 98.6%. This general result is relatively insensitive to box width and S/N threshold, with most combinations with a S/N threshold around $\gtrsim 4$ (to avoid randomly distributed false detections) and a width of at least a few arcmin (statistically necessary to keep enough sources in the box at any given time) resulting in maximum probabilities of $\gtrsim 95\%$ at the ~ 120 degree position angle.

6.5.2 Comparison to 850 μm counts

As shown in Figure 6.9, the SCUBA 850 μm and AzTEC 1100 μm SHADES counts are consistent within a uniform scaling of flux density (Section 6.4.3). Under the assumption that AzTEC and SCUBA are sampling the same source population, $\alpha_{\rm dust}$ represents a power law approximation to the Rayleigh-Jeans tail of these galaxies. The relatively steep 850 μm/1100 μm spectral index derived from the SMG populations of SHADES (after correction of systematics due to chosen priors), $\alpha_{\rm dust} \approx 3.6 \pm 0.2$, is roughly consistent with the 450 μm/850 μm spectral index, $\alpha_{\rm dust} \approx 3.6$–$3.7$, found by the SCUBA Local Universe Galaxy Survey (SLUGS) of IR bright galaxies in

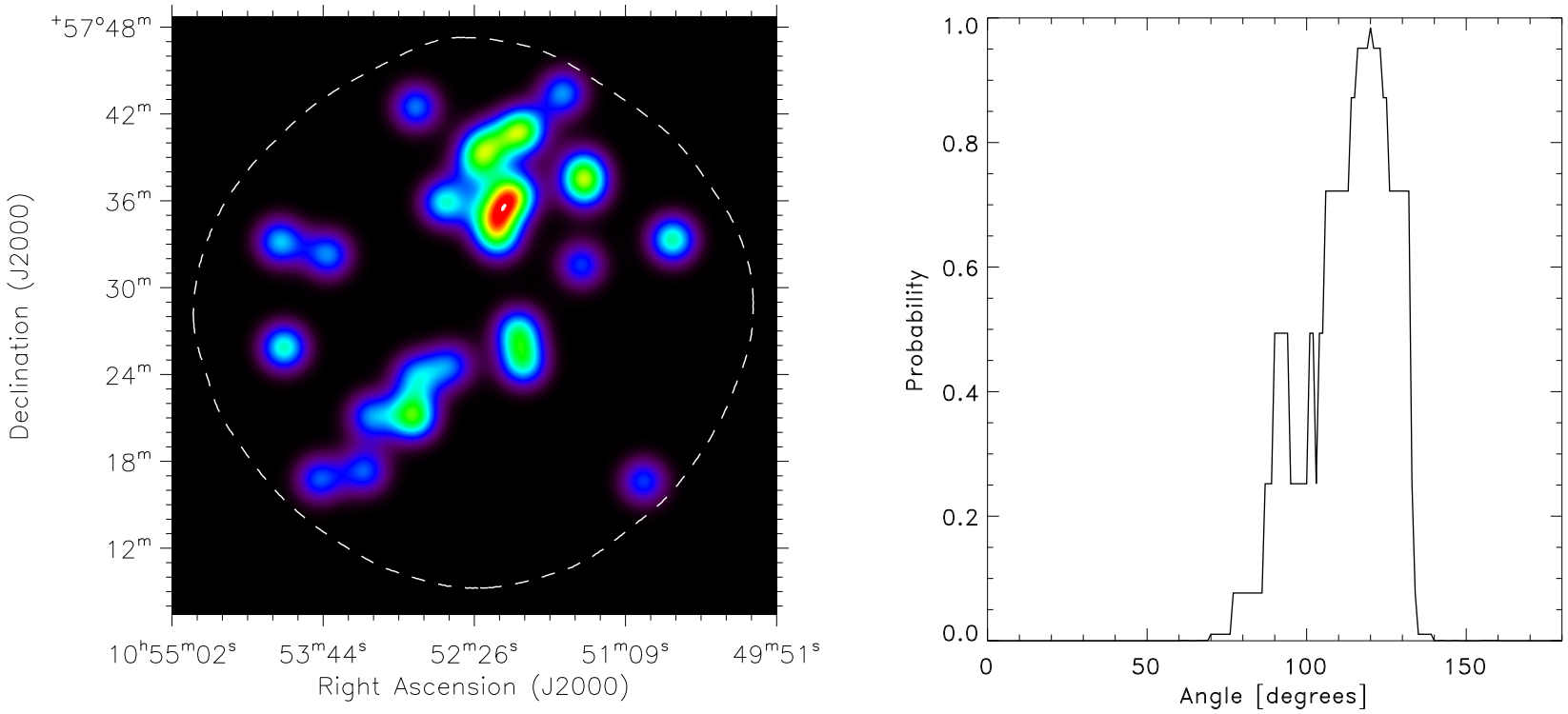

(a) Smoothed $S/N > 4.5$ AzTEC/LH

(b) Over-Density Significance

Figure 6.12. Potential signs of structure in the bright SMG distribution in the AzTEC/LH survey. (a) Distribution of $S/N > 4.5$ sources in AzTEC/LH, scaled linearly in flux and smoothed to a FWHM of 1 arcminute. The nominal 50% coverage survey area is depicted by the dashed curve. (b) Significance of over-density as a function of bi-directional position angle (i.e. measured from north towards east) from north-south (0 degrees) to east-west (90 degrees), as calculated as defined in the text. A maximum 98.6% over-density is aligned at 120 degrees.

the local Universe (Dunne & Eales, 2001) after correcting for an average CO(3–2) contamination of 25 per cent in the 850–μm band at $z = 0$ (Seaquist et al., 2004). The 450 μm measurements from SLUGS are already shortward of the Rayleigh-Jeans limit in the local Universe; particularly as local galaxy SEDs require two or more dust temperature components, with the cooler component being ~ 20 K. For a population of SMGs residing at the typical redshift of $z \sim 2$, the observed 850–μm SCUBA band is sampling a rest-frame wavelength of $\sim 280\,\mu$m. To produce a similar $\alpha_{\rm dust}$ to the SLUGS galaxies in the local Universe, a much hotter temperature is required for the SED ($T \geq 50$ K with $\beta = 2$), as depicted in Figure 6.13. Alternatively, these SMGs could have similar SEDs to the local galaxies but reside at lower redshifts ($z \lesssim 1$). The submm/mm flux ratio is at odds with the flux ratios from 350 μm/850 μm, which are consistent with the SLUGS SEDs for $z \sim 2$ (Kovács et al., 2006; Coppin et al., 2008).

It thus appears that our estimate of $\alpha_{\rm dust}$ is somewhat large given the expectation that $\beta \lesssim 2$ (Dunne & Eales, 2001, and references therein) and that the majority of our sources are unlikely to be fully in the Rayleigh-Jeans limit. The corresponding flux ratio, $S_{850}/S_{1100} = 2.52 \pm 0.11$, is also slightly high compared to that inferred by the S_{850}/S_{1200} flux ratio found for SMGs detected in the GOODS-N field (Greve et al., 2008) and to the semi-analytic model predictions of Swinbank et al. (2008). In addition, the existence of a population of sub-millimeter drop-outs (SDOs; e.g. Greve et al., 2008) – sources with a combination of high-redshift and/or low dust temperature such that the 850–μm band samples near, or shortward, of the peak emission – would act to *lower* the average value $\alpha_{\rm dust}$ for millimeter detected sources. If SDOs represent a significant fraction of the 1.1–mm population, it further suggests that our estimate of $\alpha_{\rm dust}$ is unrealistically high for the *average* (sub-)millimeter detected galaxy and may point to unknown systematics between the AzTEC and SCUBA number counts measurements. A straight comparison of the AzTEC and

SCUBA SHADES maps (Negrello et al., in prep.) will explore the SDO population as well as provide a more direct measure of $\alpha_{\rm dust}$ that is based on individual sources and fluxes in the maps, which are free of some of the systematics inherent to the comparison of number counts.

6.5.3 Predictions from models

Finally, we compare the AzTEC/SHADES number counts to those predicted at $1100\,\mu$m by various IR/sub-mm formation and evolution models in figures 6.8 and 6.9. The predictions of the IR/sub-mm evolution models of Rowan-Robinson (2009) are shown for high-redshift formation limits of $z_{\rm f} = 4$ and $z_{\rm f} = 5$. The AzTEC/-SHADES number counts agree with the $z_{\rm f} = 4$ model at fluxes $S_{1100} \lesssim 4\,$mJy, but are systematically lower than the predictions at higher fluxes. A semi-analytical model for the joint formation and evolution of spheroids and QSOs (Granato et al., 2004; Silva et al., 2005) predicts very similar number counts at $1100\,\mu$m. These models are in better overall agreement with the high flux number counts seen in the AzTEC/COSMOS and AzTEC/GOODS-N fields; however, those fields have significant biases and/or limitations, as discussed above. Also compared are the counts predicted by the semi-analytical galaxy formation model of Baugh et al. (2005, see also Lacey et al., 2008; Swinbank et al., 2008), which systematically over-predicts the number of sources seen in AzTEC/SHADES by a factor of 3–4 at all measured fluxes. Finally, we compare our results to the early predictions for SHADES (van Kampen et al., 2005) – models constrained to the SCUBA 8-mJy (i.e. $S_{1100} \geq 3\,$mJy) survey (Scott et al., 2002) – which forecast a shallower slope in the number counts than seen in the AzTEC/-SHADES fields. Assuming the bright sources are uniformly distributed across the sky, the AzTEC/SHADES survey suggests that all of these models significantly over-predict the number of intrinsically bright SMGs. If, instead, these relatively rare sources are strongly clustered, the true all-sky average number density of the brightest

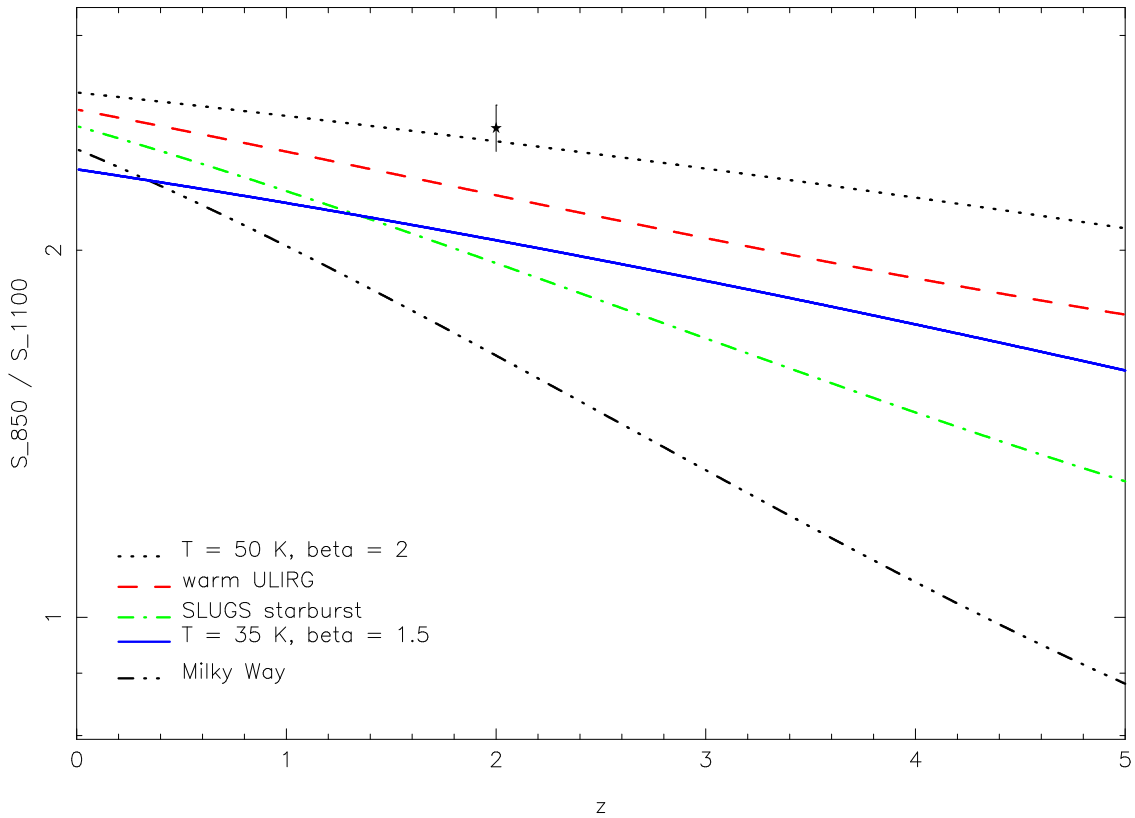

Figure 6.13. The S_{850}/S_{1100} flux ratio inferred from SCUBA and AzTEC SHADES number counts (data point) compared to relevant SED models of different galaxy types as a function of redshift. The SCUBA/AzTEC data point is plotted at $z = 2$ as a rough approximation to the average SMG redshift (Chapman et al., 2005). The 'SLUGS starburst' model has two temperature components (each isothermal) and is fit to the SLUGS data (Dunne et al., 2000; Dunne & Eales, 2001) with $\beta = 2$, $T_{\rm warm} = 40\,{\rm K}$, $T_{\rm cold} = 20\,{\rm K}$, and a warm/cold ratio of 30. Note that the SLUGS fit is before a correction for CO contamination (Seaquist et al., 2004), which would raise the S_{850}/S_{1100} ratio up slightly. Other models are single temperature isothermal models, as listed in the figure. Figure courtesy of Loretta Dunne.

SMGs could be higher than indicated by this survey, potentially bridging the gap between model and observation.

6.6 Conclusions

AzTEC/SHADES is the largest extragalactic millimeter-wave survey to date, with over $0.7\,\mathrm{deg}^2$ mapped to depths of $0.9 < \sigma_{1.1} < 1.7\,\mathrm{mJy}$. This survey, split between the Subaru/XMM-Newton Deep Field and the Lockman Hole, provides over 100 significant individual detections at 1.1 mm, with most representing newly discovered mm-wave sources. These maps also provide information on the fainter SMG population through the signature of numerous dimmer sources that are partially buried in the noise.

Combined with our improved methods for number count estimates, AzTEC/-SHADES provides the tightest available constraints on the average SMG population in the flux range $1\,\mathrm{mJy} \lesssim S_{1.1} \lesssim 10\,\mathrm{mJy}$. In particular, the AzTEC/SHADES results represent a significant advance in our knowledge of the blank-field population at 1.1 mm, showing that there are significantly lower densities of bright SMGs than that suggested by smaller 1.1–mm surveys published previously. An accurate understanding of the average SMG population is critical for comparisons to source counts found in biased and/or over-dense regions. The AzTEC/SHADES blank-field counts confirm the over-density of $S_{1.1} > 2\,\mathrm{mJy}$ sources found in the AzTEC/COSMOS field (Austermann et al., 2009) and show that the GOODS-N field is also relatively rich in bright SMGs, thus suggesting that cosmic variance can significantly affect the observed number density of SMGs in mass-biased regions (AzTEC/COSMOS) and/or on relatively small scales (AzTEC/GOODS-N; $0.068\,\mathrm{deg}^2$). We find that the variance in number counts seen across the four available AzTEC/JCMT survey fields (LH, SXDF, COSMOS, GOODS-N) is significantly larger than that expected from Poisson

statistics alone, particularly at $S_{1.1} > 4\,\mathrm{mJy}$, thus suggesting that bright SMGs may be strongly clustered.

The AzTEC/SHADES results are consistent with the predictions of the formation and evolution models of Granato et al. (2004) and the $z_{\mathrm{f}} \sim 4$ evolution models of Rowan-Robinson (2009) for blank-field 1.1 mm source counts at $S_{1.1} \lesssim 4\,\mathrm{mJy}$; however, these models systematically over-predict the number of AzTEC/SHADES sources seen at higher fluxes, although the relative scarcity and potential clustering of bright sources leaves even this unprecedentedly large SMG survey susceptible to the effects of cosmic variance. A truly unambiguous characterization of the $S_{1.1} \gtrsim 6\,\mathrm{mJy}$ SMG population will require significantly larger-area surveys at (sub-)mm wavelengths, such as those expected to be conducted in the coming year(s) by SCUBA-2 on the JCMT and AzTEC when mounted on the Large Millimeter Telescope (LMT).

We find that the SCUBA/SHADES and AzTEC/SHADES number counts are consistent within a uniform scaling of flux density. Assuming that the $850\,\mu$m and $1100\,\mu$m wavebands sample the same underlying source population, this scaling corresponds to an average source flux ratio of $S_{850}/S_{1100} = 2.52 \pm 0.11$, once corrected for known systematics between the data sets. This ratio is significantly larger than that expected for the high-redshift SMG population and we find that the systematics induced by small differences in the number count analyses of the two surveys limit the robustness of this measurement. The S_{850}/S_{1100} flux ratio is explored further in a direct comparison of individual sources lying in the overlapping regions of the SCUBA and AzTEC surveys (Negrello et al., in prep.).

APPENDIX A

DETECTOR REFERENCE AND STATUS TABLES

A.1 Channel Reference Translation

Due to the relatively independent development of the detector array (JPL) and the AzTEC readout electronics (UMass-Amherst), two different naming conventions exist for the respective detector/channel. AzTEC readout electronics and data sets refer to each hextant (1–6) and channel (1–24) by a number, resulting in names like 'h2b17'. Conversely, the array itself is physically labeled as having hextants A–F and detectors 1–24, which do not correspond to the AzTEC channels. A conversion chart is listed in Table A.1.

A.2 Status of Detectors and JFET Amplifiers

The AzTEC detector array was manufactured just in time for the winter 2005/06 observing run and shipped directly to the telescope. This schedule did not allow for thorough characterization and testing of the new detectors before being coupled to the telescope, where their functionality and sensitivities were determined while in operation.

The following tables represent an attempt to determine the failure mode for non-functional or overly noisy channels, i.e. bad bolometer, electrical short, bad JFET amplifier, or other. These tables are compiled from various initial tests when the AzTEC instrument was first installed on the JCMT (October 2005) and ASTE (May 2007) telescopes. Between these observing runs, the JFET/Hextant associations (Ta-

Table A.1. AzTEC Channel and Hextant Nomenclature

AzTEC Channel	Detector Number
1	23
2	16
3	18
4	13
5	14
6	21
8	20
9	5
10	19
11	11
12	12
13	4
14	9
15	3
16	15
17	1
18	24
19	7
20	17
21	8
22	25
23	6
24	10
Hextant Number	**Hextant Letter**
1	D
2	E
3	F
4	A
5	B
6	C

Note. — Conversion chart between AzTEC channel to physical detector number, followed by a conversion from hextant number to hextant number. AzTEC hextant numbers are preceded by the letter 'h' and the channel number is proceeded by 'b'. For example, AzTEC channel 'h2b23' is equivalent to physical bolometer 'E6'.

ble A.4) were rearranged (with one control segment) to help differentiate between bad bolometers (Table A.2) and bad JFET channels (Table A.3).

Table A.2. Detector Functionality and Status

Channel	Hex 1/D	Hex 2/E	Hex 3/F	Hex 4/A	Hex 5/B	Hex 6/C
1	1	1	1	1	1	1
2	1	1	1	1	1	1
3	0	1	1	1	1	1
4	1	1	1	1	1	1
5	1	1	1	1	1	1
6	1	1	1	1	1	1
7	1	-1	1	1	1	1
8	1	1	0	1	1	1
9	1	1	1	1	1	1
10	1	1	1	1	1	1
11	1	1	1	1	1	1
12	1	2	1	1	1	1
13	2	1	1	1	1	1
14	0	-1	1	1	1	2
15	1	1	1	1	1	1
16	0	1	1	1	-1	-1
17	1	1	1	1	1	1
18	1	1	1	1	-1[a]	1
19	1	1	1	1	2	1
20	1	1	1	1	1	1
21	0	2	-1	1	1	1
22	1	1	-1	1	1	1
23	0	1	1	1	1	1
24	1	1	1	1	1	0

Note. — Summary of our best estimate as to the functionality or type of fault associated with each detector. Each detector is coded as follows: (1) Optically active and seemingly normal response, to bright modulated source; (2) Optically active but has excess noise (-1) Bolometer channel acts as a short when cold; (0) Unknown fault or bad JFET amplifier (see Table A.3). (a) This bolometer once worked normally, but now is a clear short even at room temperature. This may be due to electrically conductive debris shorting the leads somewhere on the wafer.

Table A.3. JFET Amplifier Pair Functionality and Status

Channel	JFET 81	JFET 76	JFET 75	JFET 77	JFET 08	JFET 05
1	1	1	1	1	1	1
2	1	1	1	1	1	1
3	0	1	1	1	1	1
4	1	1	1	1	1	1
5	1	1	1	1	1	1
6	1	1	1	1	1	1
7	1	1	1	1	1	1
8	1	1	-1	1	1	1
9	1	1	1	1	1	1
10	1	1	1	1	1	1
11	1	1	1	1	1	1
12	1	2	1	1	1	1
13	2	1	1	1	1	1
14	0	1	1	1	1	2
15	1	1	1	1	1	1
16	0	1	1	1	2	1
17	1	1	1	1	1	1
18	1	1	1	1	2	1
19	1	1	1	1	2	1
20	1	1	1	1	1	1
21	-1	2	1	1	1	1
22	1	1	1	1	1	1
23	0	1	1	1	1	1
24	1	1	1	1	1	-1

Note. — Summary of our best estimate as to the functionality or type of fault associated with each JFET pair. Data is broken down into columns of JFET modules, each consisting of 24 pairs of matched JFETs. Each JFET pair is coded as follows: (1) Believed to be functional JFET amplifier; (2) Possibly noisy, troubled, or inconsistent JFET; (-1) Broken/Bad JFET; (0) Unknown, may be bad JFET or bolometer.

Table A.4. Hextant Wiring Table

JCMT 2005/06	
Hextant	JFET Module
1/D	81
2/E	08
3/F	05
4/A	77
5/B	76
6/C	75
ASTE 2007/08	
Hextant	JFET Module
1/D	81
2/E	76
3/F	75
4/A	77
5/B	08
6/C	05

Note. — AzTEC JFET modules and array hextants have a unique one-to-one relationship at each telescope, as defined in the table. JFET/Hextant association was changed for 5 of the 6 segments between observing runs for debugging purposes.

APPENDIX B

AZTEC MAPPING SIMULATOR: USER MANUAL

Disclaimer

AzTEC MapSim was built for planning AzTEC observations at the James Clerk Maxwell Telescope (JCMT) and is currently limited to raster scan patterns. The bulk of this document assumes observations at the JCMT. Depending on the observation modes available, this program may need significant modification before use in planning observations at the Large Millimeter Telescope (LMT). Although the program is stable and gave reasonable results for the JCMT, the program has limited testing and some bugs and limitations may be present. The program is currently limited to observation parameters (e.g. scanning speed) believed to be possible for the AzTEC/JCMT system; however, it may be possible for the user to design an observing strategy that is not physically feasible.

B.1 Introduction

When in operation, AzTEC is typically available to external observers through competitive proposal. These potential observers may not have experience with the AzTEC instrument or be familiar with its capabilities. The AzTEC mapping simulator is designed to provide an efficient means by which these potential observers can: (a) calculate the necessary time for their project and proposal; and (b) design the most efficient scanning strategy for their project.

AzTEC is a large-format bolometer array camera under development at the University of Massachusetts in collaboration with researchers at Caltech, Cardiff, INAOE, Sejong University, and Smith College. This document describes how to obtain, install, and use AzTEC MapSim, including the Mapping Simulator and Integration Time Calculator Tool, to plan observations with AzTEC. All software is freely available at the instrument home page, `http://www.astro.umass.edu/AzTEC/`.

B.2 System Requirements

- Supported platforms: Linux, Unix, Windows (untested on Macintosh)
- AzTEC MapSim runs in IDL Virtual Machine. If you do not have IDL v6.0 or later, you will need to download and install it (don't worry, there is a free version of Virtual Machine; see below).

- **Warning:** Older computers may run slowly for simulating large maps, as this program requires a large amount of computer memory. It is recommended that you have at least 256 MB of RAM.

B.3 Installing and Starting AzTEC MapSim

AzTEC MapSim is available as a zipped package that includes an IDL binary saveset and other supporting files. It can be downloaded from the instrument home page,
`http://www.astro.umass.edu/AzTEC/`.

1. Download the file to your computer and unzip it. It doesn't matter where you install it, as long as you keep all of the files in the same directory.

2. If you don't have IDL (or already have IDL -VM):

   (a) Download IDL-Virtual Machine (IDL-VM) from `http://www.rsinc.com/idlvm/` and install it. It is free!

   (b) Run IDL VM (if non-windows type "idl -vm"). You will be prompted to press "click to continue"

   (c) Browse to the directory where you unzipped the AzTEC MapSim software and run the program aztec_mapsim_v1.sav file

   (d) The AzTEC MapSim graphical user interface (GUI) should appear

3. If you already have IDL v.6.0 or above:

   (a) Start up IDL.

   (b) Type the following two commands:

      - IDL> `restore, ''<mydir> /aztec_mapsim_v1.sav''`
        where <mydir> represents the directory where you have the program stored. (Note double quotation marks.)
      - IDL> `aztec_mapsim_v1`

   (c) The AzTEC MapSim graphical user interface (GUI) should appear

B.4 Using AzTEC MapSim

The tool is run from only one GUI. There are a few basic parameters to change (map mode, scan length, scan speed, etc.), and two graphical output options (time of observation and mapping simulation). Fig. B.1 shows the GUI with the default parameters. The GUI will have a slightly different look depending on which OS you are running on.

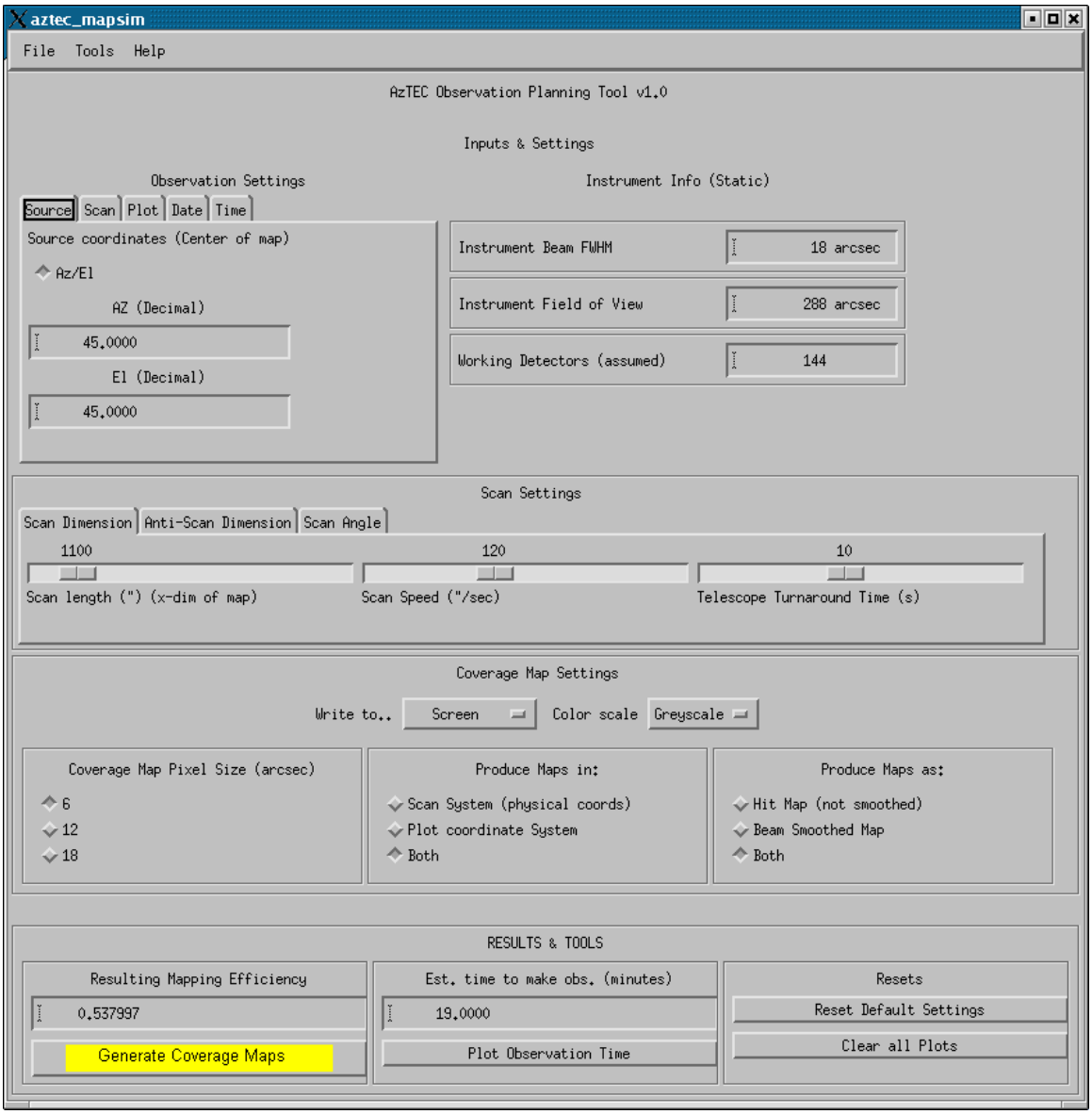

Figure B.1. The AzTEC MapSim GUI, showing default input values when the tool is first started.

B.4.1 Observing Modes

There are currently two observing modes supported for observing with AzTEC at the JCMT:

1. **Scan mapping:** The telescope is scanned, or swept, back and forth across the sky horizontally (i.e. in azimuth), with a vertical (i.e., altitude) offset between successive scans. Use this mode for making maps significantly larger than one AzTEC field of view (4.8 arcmin diameter). The optimal scan-speeds, step-sizes between scans and maximum scan-lengths will be determined for maps of different sizes during the commissioning run in June 2005. AzTEC MapSim default parameter values reflect either our preliminary best guess at the optimum values or just some arbitrary starting point.

2. **Jiggle mapping:** The telescope is "jiggled" on the sky to provide fully-sampled images by moving the secondary mirror in a jiggle-pattern while tracking the image center. This mode should be used for small maps (on order the size of the FOV) and photometry. Jiggle mapping mode is **not currently integrated** into this AzTEC MapSim software, but we're hoping to add it some time in the future. To estimate jiggle map exposure times and signal-to-noise ratios, please refer to the raw sensitivities listed on the AzTEC website.

B.4.2 Input Parameters

Following is a description of some key parameters you are likely to want to change (default values [**in square brackets**]):

I. Observation Settings

There are five categories of Observation Settings, accessed by clicking on the tabs under the "Observation Settings" title at the upper left of the GUI. Each category brings up a different set of parameter slider bars.

1. **Source**

   - **Source Az/El [45, 45]:** The azimuth and altitude in decimal degrees of your target at the start of the observation. This represents the position of the map center.

2. **Scan**

   - **Scan coordinate system [Az/El]** This is currently the only option.

3. **Plot**

   - **Plot coordinate system [Az/El]** This is currently the only option.

4. **Date** and

5. **Time**

- **Date/Time:** Date and Time are irrelevant when doing everything in Az/El coordinates, so ignore this for now. When RA/DEC functionality is introduced to the software, this will become important.

II. Scan Settings

There are six input parameters in the Scan Settings section, each one changed via a slider bar, accessible via three tabs:

1. **Scan Dimension:** Parameters along each telescope scan

   - **Scan length [1100]:** Desired length in arcseconds of each pass of the telescope across the map. This is limited by the detector time constant and scanning speed (below). ScanLength/ScanSpeed should be less than 100 seconds.
   - **Scan speed [120]:** Desired scanning speed of telescope across map in arcseconds/sec.
   - **Telescope turnaround time [10]:** At the end of each azimuth scan, the telescope has to stop moving, step in a direction perpendicular to the scan, and start a new scan in the opposite direction. The turnaround time for this operation will be measured during the commissioning run in June 2005; we currently assume 10 seconds.

2. **Anti-Scan Dimension:** Parameters perpendicular to each telescope scan.

   - **Scan step size [18]:** Desired separation in arcseconds (in the "anti-scan direction") between successive scans across the map. This parameter will affect the final coverage of the map; the default value of 18 arcseconds corresponds to one full instrument beam FWHM. Larger values will yield lower coverage, while smaller steps will yield a higher level of sampling of the sky.
   - **Number of scans [60]:** Desired total number of scans. Combined with step size, defines the y-dimension ('anti-scan dimension') size of map.

3. Scan Angle

   - **Scan Direction [90]:** The angle of the scan relative to the elevation direction. For reference, Scan Direction = 0 degrees corresponds to scans along elevation (first scan down from highest elevation to lowest, then back up). Scan Direction = 90 degrees corresponds to scans along azimuth (first scan along positive azimuth, i.e., from north through east). Although the final installation of the detector array has not happened as of the writing of this document, it is expected that the array will be mounted such that scans in azimuth (Scan Direction = 90) will produce the highest level of sampling of the sky, due to symmetries in the array. The array has six-fold symmetry; therefore, any increment of 60 degrees from an azimuth scan should also produce near optimal coverage. Feel free to try many different scan directions to see the difference it can make in the resultant coverage.

B.4.3 Output Options

There are several options you can change that affect the output, under the "Coverage Map Settings" heading (default values **in bold**):

1. **Write to...** Choose to produce coverage plots to **screen** or postscript files. This will produce files 'coverage_hist.eps' and 'coverage_map.eps' in to the directory you are running the software from. Be sure to re-name these files before you create new ones, or the originals will be overwritten!

2. **Color scale:** Choose **greyscale** or color scale plots.

3. **Coverage Map Pixel Size (arcsec):** Choose **6**, 12, or 18 arcsec pixels for the output simulation. This is effectively the 'binsize' for the coverage maps produced. Smaller pixels will make larger plot filesizes.

4. **Produce maps in:** Choose Scan System, Plot system, or **Both**. These are the coordinate systems chosen in the tabs in the upper left hand side of the GUI. For now, these are locked to Az/El. The Scan system plots will be in physical coordinates (as the scan parameters are defined in), while the plot system plots will produce them in the natural coordinate system (az/el in this case).

5. **Produce maps as:** Choose Hit Map (not smoothed), Beam Smoothed Map, or **Both**. Beam smoothed map is the Hit map smoothed by the beamsize of 18 arcseconds FWHM.

B.4.4 Primary Output

When you have set the parameters to represent the observations you wish to simulate, click on either the "Plot Observation Time" or the "Generate Coverage Map" button in the Results & Tools section at the bottom of the GUI.

- **Plot Observation Time:** This will simply produce a plot showing the total observation time as a function of assumed turnaround time at the end of each scan (Fig. B.2). This will show you how the turnaround time is affecting the total time required to make your map. The turnaround time is not currently known but various times will be tested during the AzTEC engineering run in June 2005.

- **Generate Coverage Maps:** The Coverage Map option will produce several plots and histograms including a simulation of the proposed map showing the total exposure time per pixel and all the individual scans, or passes of the telescope across the map(Fig. B.3). This is the primary tool of this software, so the button is in color so you don't miss it!

  The resulting coverage maps show the level of coverage (in seconds per pixel) via a shaded plot of the mapped field. The blue box in the map represents the 'full coverage' area of the map, which corresponds to the area that all bolometers have scanned across. This roughly defines the portion of the map where coverage

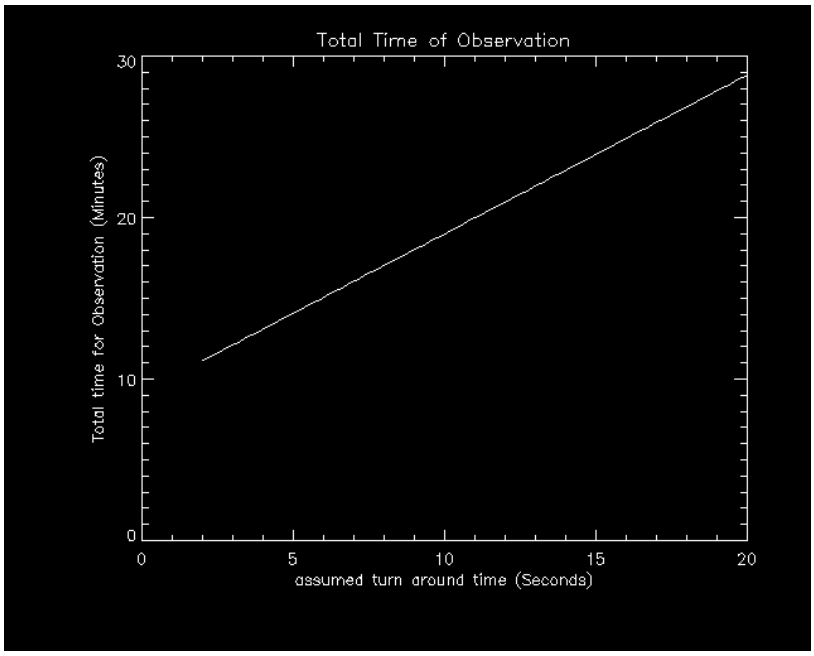

Figure B.2. Sample observation time estimates for raster scan observations. Shown for the default values of the mapping simulator.

is more or less uniform. The red lines represent a tracking of the center of the array as it scanned through the field. They are labeled with 'start' and 'end' to show direction.

The number of coverage maps produced is controlled by the "Produce Maps in:" and "Produce Maps as" options. If 'both' is selected in both fields, a total of 8 plots will be produced; 4 coverage maps and 4 corresponding histograms. The coverage scale can be depicted in color or greyscale (default), chosen by the "color scale" droplist.

- **Reset Default Settings:** This button simply resets ALL fields, sliders and lists to the default values seen when the program is first started.
- **Clear All Plots:** Since this program has the ability to produce a lot of plots and windows quickly, this will come in handy to quickly get rid of them all. Be careful, though, as this will delete ALL IDL plot windows that may be open through your current IDL session.

B.4.5 Ancillary Output

- **Resultant y-dimension of map (arcseconds):** This is the range you've mapped over in the "anti-scan direction". This value represents how far the telescope has moved in the y-dimension. This value is equal to (number of scans - 1)*(step size). This value appears under the "Anti-Scan Dimension" tab in the Scan Settings section (above).

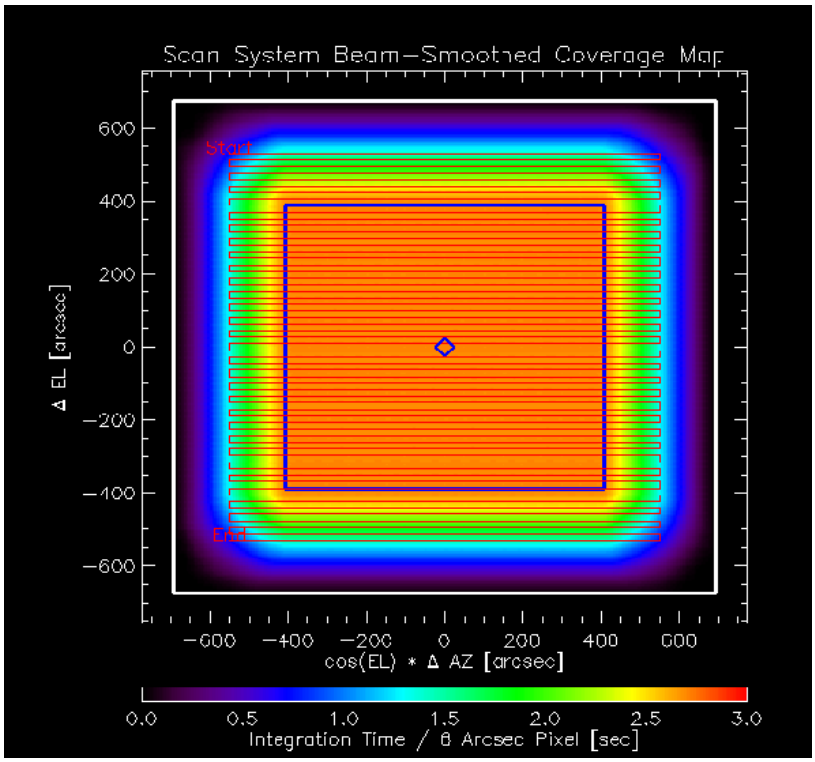

Figure B.3. Example Coverage Map Provided by the AzTEC Mapping Simulator. Shown for the default map values.

- **Resulting Mapping Efficiency:** The usable fraction of the map to be produced. This is basically the ratio of "good coverage" area over full scanned area. If l_x is the scan length, and l_y is the y-dimension defined above, then the resulting mapping efficiency is approximately: $\varepsilon = (l_x - FOV)(l_y - FOV)/(l_x \times l_y)$.

- **Estimated time to make observation (minutes):** This is a rough estimate of how long it will take to produce a map as you've defined, using the assumed telescope turnaround time you've chosen in the 'anti-scan dimension' tab. Effective turnaround times will not be determined until the engineering run of June 2005, but for now we highly suggest to assume a turnaround time of no less than 10 seconds. Physically, the JCMT dish should be capable in turning around in a minimum of 2 seconds, however such high acceleration will likely introduce noise into the system, so 10 seconds will likely prove to be a more useful turnaround time.

APPENDIX C

CORRELATION OF NUMBER COUNTS DATA POINTS

C.1 Correlation Matrix

The bootstrap sampling method of § 6.4.1 induces significant correlation between differential number counts bins through discrete sampling of continuous PFDs that have significant probability on scales comparable, or larger, than the bin size (1 mJy in this paper). Previous incarnations of this sampling method (e.g. Coppin et al., 2006) estimated covariance and correlation matrices directly from the variation in number counts results seen across the iterations of the bootstrap. This sampling method collapses each source's probability distribution (PFD; e.g. Figure 6.5) to a single flux upon each iteration, which acts to hide significant correlation by throwing away much of the information contained within the PFD. This resulted in severely underestimated bin-to-bin correlations amongst the differential number counts, as was evidenced by the unrealistically low χ^2 values of formal fitting (Coppin et al., 2006; Perera et al., 2008; Austermann et al., 2009).

We present an alternative method of calculating the correlation matrix which better captures these correlations amongst differential number counts bins. We begin by integrating the PFD of each source over the span of each flux bin. These binned probabilities can be summed over all sources to provide a number counts estimate that matches the final results of the full bootstrapping method, but without the robust uncertainty estimates that the bootstrap method is designed to provide. We apply this alternative number counts estimate to *each* of the 100,000 unique catalogs produced by the bootstrap. The Poisson deviation and replacement sampling used to produce each catalog (§ 6.4.1) act to perturb this new estimate of the number counts around the the most likely values. This collection of perturbed number counts is then used to estimate the correlation between the differential number counts bins.

We present the resulting correlation matrix for the AzTEC/SHADES differential results (§ 6.4) in Table C.1. These correlations apply directly to the differential results provided in Table 6.3 and Figure 6.8 (20% threshold counts). The last row of Table C.1 provides the standard deviation of the differential counts of each flux bin, as estimated in the bootstrap sampling method. These values can be applied to the correlation matrix to produce a covariance matrix for the data. However, the standard deviation is not an ideal representation of the true uncertainty distribution (Table 6.3) due to the finite sampling of each bin, which results in an asymmetric multinomial probability distribution.

Table C.1. Correlation matrix of the AzTEC/SHADES Differential Number Count Bins of Table 6.3

FLUX (mJy)	1.38	2.40	3.40	4.41	5.41	6.41	7.41
1.38	1.00	0.92	0.61	0.26	0.08	0.02	0.01
2.40	0.92	1.00	0.84	0.47	0.18	0.04	0.01
3.40	0.61	0.84	1.00	0.82	0.44	0.12	0.05
4.41	0.26	0.47	0.82	1.00	0.78	0.32	0.17
5.41	0.08	0.18	0.44	0.78	1.00	0.77	0.61
6.41	0.02	0.04	0.12	0.32	0.77	1.00	0.97
7.41	0.01	0.01	0.05	0.17	0.61	0.97	1.00
σ	179.77	46.40	16.69	7.55	3.98	2.38	1.33

Note. — The last row gives the standard deviation of each bin as determined through the bootstrap sampling method of § 6.4.1. Together, these values can be used to create a covariance matrix; however, we note the true uncertainty of each bin is non-Gaussian and best represented by the asymmetric uncertainty intervals of Table 6.3.

BIBLIOGRAPHY

Ade, P. A. R., Pisano, G., Tucker, C., & Weaver, S. 2006, Proc. SPIE, 6275

Almaini, O., et al. 2003, MNRAS, 338, 303

Almaini, O., Dunlop, J. S., Willott, C. J., Alexander, D. M., Bauer, F. E., & Liu, C. T. 2005, MNRAS, 358, 875

Aretxaga, I., Hughes, D. H., Chapin, E. L., Gaztañaga, E., Dunlop, J. S., & Ivison, R. J. 2003, MNRAS, 342, 759

Aretxaga, I., et al. 2007, MNRAS, 379, 1571

Austermann, J. E., et al. 2009, MNRAS, 123

Barger, A. J., Cowie, L. L., Sanders, D. B., Fulton, E., Taniguchi, Y., Sato, Y., Kawara, K., & Okuda, H. 1998, Nature, 394, 248

Baugh, C. M., Lacey, C. G., Frenk, C. S., Granato, G. L., Silva, L., Bressan, A., Benson, A. J., & Cole, S. 2005, MNRAS, 356, 1191

Bertoldi, F., et al. 2007, ApJS, 172, 132

Best, P. N. 2002, MNRAS, 336, 1293

Bhatia, A. K., & Saba, J. L. R. 2001, ApJ, 563, 434

Biggs, A. D., & Ivison, R. J. 2006, MNRAS, 371, 963

Bin, M., Benford, D. J., Gaidis, M. C., Buttgenbach, T. H., Zmuidzinas, J., Serabyn, E., & Phillips, T. G. 1999, International Journal of Infrared and Millimeter Waves, 20, 383

Blain, A. W., Kneib, J.-P., Ivison, R. J., & Smail, I. 1999, ApJ, 512, L87

Blain, A. W., Smail, I., Ivison, R. J., Kneib, J.-P., & Frayer, D. T. 2002, Phys. Rep., 369, 111

Blain, A. W., Chapman, S. C., Smail, I., & Ivison, R. 2004, ApJ, 611, 725

Blake, C., Pope, A., Scott, D., & Mobasher, B. 2006, MNRAS, 368, 732

Bock, J. J., Delcastillo, H. M., Turner, A. D., Beeman, J. W., Lange, A. E., & Mauskopf, P. D. 1996, Submillimetre and Far-Infrared Space Instrumentation, 388, 119

Borys, C., Chapman, S., Halpern, M., & Scott, D. 2003, MNRAS, 344, 385

Chapman, S. C., Scott, D., Borys, C., & Fahlman, G. G. 2002a, MNRAS, 330, 92

Chapman, S. C., Scott, D., Smail, I., Ivison, R. J., & Blain, A. W. 2002b, MNRAS, 335, L17

Chapman, S. C., Blain, A. W., Ivison, R. J., & Smail, I. R. 2003, Nature, 422, 695

Chapman, S. C., Blain, A. W., Smail, I., & Ivison, R. J. 2005, ApJ, 622, 772

Chapman, S. C., Blain, A., Ibata, R., Ivison, R. J., Smail, I., & Morrison, G. 2009, ApJ, 691, 560

Clements, D. L., et al. 2008, MNRAS, 387, 247

Coppin, K., Halpern, M., Scott, D., Borys, C., & Chapman, S. 2005, MNRAS, 357, 1022

Coppin, K., et al. 2006, MNRAS, 372, 1621

Coppin, K., et al. 2008, MNRAS, 384, 1597

Cowie, L. L., Barger, A. J., & Kneib, J.-P. 2002, AJ, 123, 2197

Crill, B. P., et al. 2003,ApJS, 148, 527

Daddi, E., et al. 2009, ApJ, 694, 1517

Day, P. K., LeDuc, H. G., Mazin, B. A., Vayonakis, A., & Zmuidzinas, J. 2003, Nature, 425, 817

De Breuck, C., et al. 2004, A&A, 424, 1

Dobbs, M., et al. 2006, New Astronomy Review, 50, 960

Dowell, C. D., et al. 2003, Proc. SPIE, 4855, 73

Dunlop, J. S., et al. 2004, MNRAS, 350, 769

Dunne, L., Eales, S., Edmunds, M., Ivison, R., Alexander, P., & Clements, D. L. 2000, MNRAS, 315, 115

Dunne, L., & Eales, S. A. 2001, MNRAS, 327, 697

Dye, S., et al. 2008, MNRAS, 386, 1107

Efstathiou, G., Kaiser, N., Saunders, W., Lawrence, A., Rowan-Robinson, M., Ellis, R. S., & Frenk, C. S. 1990, MNRAS, 247, 10P

Fasano, G., & Franceschini, A. 1987, MNRAS, 225, 155

Glenn, J., et al. 1998, Proc. SPIE, 3357, 326

Glenn, J., et al. 2002, Applied Optics, 41, 136

Glenn, J., et al. 2003, Proc. SPIE, 4855, 30

Goldsmith, P. 1998, Quasioptical Systems. IEEE, 345 East 47th St. NY, NY 10017

Granato, G. L., De Zotti, G., Silva, L., Bressan, A., & Danese, L. 2004, ApJ, 600, 580

Greve, T. R., Ivison, R. J., Bertoldi, F., Stevens, J. A., Dunlop, J. S., Lutz, D., & Carilli, C. L. 2004, MNRAS, 354, 779

Greve, T. R., Stern, D., Ivison, R. J., De Breuck, C., Kovács, A., & Bertoldi, F. 2007, MNRAS, 382, 48

Greve, T. R., Pope, A., Scott, D., Ivison, R. J., Borys, C., Conselice, C. J., & Bertoldi, F. 2008, MNRAS, 389, 1489

Griffin, M. J., & Orton, G. S. 1993, Icarus, 105, 537

Griffin, M. J., Swinyard, B. M., & Vigroux, L. G. 2003, Proc. SPIE, 4850, 686

Guzzo, L., et al. 2007, ApJS, 172, 254

Haig, D. J., et al. 2004, Proc. SPIE, 5498, 78

Hogg, D. W., & Turner, E. L. 1998, PASP, 110, 727

Hogg, D. W. 2001, AJ, 121, 1207

Holland, W. S., Cunningham, C. R., Gear, W. K., Jenness, T., Laidlaw, K., Lightfoot, J. F., & Robson, E. I. 1998, Proc. SPIE, 3357, 305

Holland, W. S., et al. 1999, MNRAS, 303, 659

Holland, W., et al. 2006, SPIE, 6275, 45

Hughes, D. H., et al. 1998, Nature, 394, 241

Ibar E., et al., 2009, MNRAS, submitted

Ilbert, O., et al. 2009, ApJ, 690, 1236

Ivison, R. J., et al. 2007, MNRAS, 380, 199

Kaviani, A., Haehnelt, M. G., & Kauffmann, G. 2003, MNRAS, 340, 739

Knudsen, K. K., et al. 2006, MNRAS, 368, 487

Kovács, A., Chapman, S. C., Dowell, C. D., Blain, A. W., Ivison, R. J., Smail, I., & Phillips, T. G. 2006, ApJ, 650, 592

Kreysa, E., et al. 1998, Proc. SPIE, 3357, 319

Lacey, C. G., Baugh, C. M., Frenk, C. S., Silva, L., Granato, G. L., & Bressan, A. 2008, MNRAS, 385, 1155

Laurent, G. T., et al. 2005, ApJ, 623, 742

Maloney, P. R., et al. 2005, ApJ, 635, 1044

Massey, R., et al. 2007, ApJS, 172, 239

Mather, J. C., 1984, Applied Optics, 23, 584

Menéndez-Delmestre, K., et al. 2007, ApJ, 655, L65

Mortier, A. M. J., et al. 2005, MNRAS, 363, 563

Mauskopf, P. D., et al. 1997, Applied Optics, 36, 765

Negrello, M., Perrotta, F., González-Nuevo, J., Silva, L., de Zotti, G., Granato, G. L., Baccigalupi, C., & Danese, L. 2007, MNRAS, 377, 1557

Niemack, M. D. 2006, Proc. SPIE, 6275

Peacock, J. A. 1983, MNRAS, 202, 615

Perera, T. A., et al. 2008, MNRAS, 391, 1227

Pope, A., Borys, C., Scott, D., Conselice, C., Dickinson, M., & Mobasher, B. 2005, MNRAS, 358, 149

Pope, A., et al. 2006, MNRAS, 370, 1185

Pope, A., et al. 2008, ApJ, 675, 1171

Press, W. H., Teukolsky, S. A., Vetterling, W. T., & Flannery, B. P. 1992, Cambridge: University Press, —c1992, 2nd ed.,

Priddey, R. S., Ivison, R. J., & Isaak, K. G. 2008, MNRAS, 383, 289

Rowan-Robinson, M. 2009, MNRAS, 394, 117

Ruhl, J., et al. 2004, Proc. SPIE, 5498, 11

Runyan, M. C. 2003, Ph.D. Thesis

Schloerb, F. P. 2008, Proc. SPIE, 7012,

Schneider, N., Urban, J., & Baron, P. 2009, arXiv:0902.1642

Schwan, D., et al. 2003, New Astronomy Review, 47, 933

Schechter, P. 1976, ApJ, 203, 297

Scott, S. E., et al. 2002, MNRAS, 331, 817

Scott, S. E., Dunlop, J. S., & Serjeant, S. 2006, MNRAS, 370, 1057

Scott, K. S., et al. 2008, MNRAS, 385, 2225

Scoville, N., et al. 2007a, ApJS, 172, 1

Scoville, N., et al. 2007b, ApJS, 172, 150

Seaquist, E., Yao, L., Dunne, L., & Cameron, H. 2004, MNRAS, 349, 1428

Siebenmorgen, R., & Krügel, E. 2007, A&A, 461, 445

Silva, L., De Zotti, G., Granato, G. L., Maiolino, R., & Danese, L. 2005, MNRAS, 357, 1295

Simpson, C., et al. 2006, MNRAS, 372, 741

Smail, I., Ivison, R. J., & Blain, A. W. 1997, ApJ, 490, L5

Smail, I., Ivison, R. J., Blain, A. W., & Kneib, J.-P. 2002, MNRAS, 331, 495

Souccar, K., Wallace, G., & Malin, D. 2004, Proc. SPIE, 5496, 241

Stevens, J. A., et al. 2003, Nature, 425, 264

Swinbank, A. M., et al. 2008, MNRAS, 391, 420

Sunyaev, R. A., & Zeldovich, Y. B. 1970, Ap&SS, 7, 3

Turner A. D., et al. 2001, Applied Optics, 40, 4921

Valiante, E., Lutz, D., Sturm, E., Genzel, R., Tacconi, L. J., Lehnert, M. D., & Baker, A. J. 2007, ApJ, 660, 1060

van Kampen, E., et al. 2005, MNRAS, 359, 469

Webb, T. M. A., Yee, H. K. C., Ivison, R. J., Hoekstra, H., Gladders, M. D., Barrientos, L. F., & Hsieh, B. C. 2005, ApJ, 631, 187

Waterloot, J. 2004, JCMT Newsletter, 22

Wilson, G. W., et al. 2008a, MNRAS, 386, 807

Wilson, G. W., et al. 2008b, MNRAS, 390, 1061

Younger, J. D., et al. 2007, ApJ, 671, 1531

Yun, M. S., et al. 2008, MNRAS, 389, 333